# Full three flavor oscillation analysis of atmospheric neutrino data observed in Super-Kamiokande

Chizue Ishihara

February 5, 2010

## Abstract

This thesis presents the first-time neutrino oscillation studies considering entire oscillation parameters, two mass differences $\Delta m_{12}^2$, $\Delta m_{23}^2$, three mixing angles $\theta_{12}$, $\theta_{23}$, $\theta_{13}$, and one CP phase parameter ($\delta_{cp}$), by the atmospheric neutrino data observed in Super-Kamiokande.

The Super-Kamiokande, a 50 kt water Cherenkov detector, started taking data in 1996 and has been observed a large number of atmospheric neutrino events. About 3,000 day neutrino data is collected through the data taking phases, Super-Kamiokande-I, II and III. This analysis is performed using the amount of this data for the first time.

The neutrino data selection and observed data quality for the analysis are summarized in this thesis. The analysis examines for both the normal and inverted mass hierarchy cases. In the normal (inverted) mass hierarchy case, $\Delta m_{23}^2$, $\sin^2 \theta_{23}$ and $\sin^2 \theta_{13}$ are constrained at 90 % C.L. to 1.88 (1.98) $\times 10^{-3} < \Delta m_{23}^2 < 2.75$ (2.81) $\times 10^{-3}$ eV$^2$, 0.406 (0.426) $< \sin^2 \theta_{23} < 0.629$ (0.644), $\sin^2 \theta_{31} < 0.066$ (0.122). No significant constraint on CP phase at 90 % C.L. is obtained for both mass hierarchies and there is no clear preference of mass hierarchy.

# ** ACKNOWLEDGMENTS **

# Contents

# Chapter 1

# Introduction

The present-day universe contains large number of baryons in the form of matter, but almost no antibaryons. According to the big bang model, quarks and untiquarks had existed in a comparable number in the initial explosion of the universe. However, since there was a small asymmetry of quarks and untiquarks at that time, quarks remain excessively through the universe expanding and cooling processes. This asymmetry could have developed with CP violation [1]. In fact, CP invariance are violated in weak interaction process of quarks [2]. But CP violation in lepton sector, which is considered to be related to the origin of the matter in the universe directly, have not been observed yet. A viable way of observing CP violation in the lepton sector is to use the phenomenon of neutrino oscillation. Thus, the discovery of neutrino oscillations had carried the issue of leptonic CP violation onto one of the central agenda of the particle physics.

## 1.1 Neutrino Oscillation

In the Standard Model of elementary particles, neutrinos are regarded as exactly massless particles [3, 4, 5]. However, there is no fundamental reason to forbid the finite masses of neutrinos. Some experiments set a limit of neutrinos' mass. Electron neutrino $\nu_e$ mass was measured by beta spectra in Tritium $\beta$-decay. The electron neutrino mass is constrained to be less than 2.2 eV/c$^2$ at 95% C.L. [6]. The upper limit of muon neutrino $\nu_\mu$ is set to be 190 keV/c$^2$ from the measurement of two body decay of $\pi^+$ at rest $\pi^+ \rightarrow \mu^+ + \nu_\mu$ [7]. Tau neutrino $\nu_\tau$ mass was obtained to be less than 18.2 MeV/c$^2$ from the measurement of the hadronic final states $\tau \rightarrow n\pi + \nu_\tau$ ($n > 2$) [8]. There had been no evidence of finite mass for neutrinos from these experiments.

On the other hand, a consequence of finite mass for neutrinos appears in neutrino oscillation because a weak eigenstate (flavor eigenstate) $|\nu_\alpha\rangle$ produced in weak interaction is a linear combination of the mass eigenstates $|\nu_i\rangle$ when neutrinos have mass. Neutrino oscillation is proposed by Maki, Nakagawa and Sakata in 1962 [9]. And see also Pontecorvo [10]. Their flavor eigenstates can be written as the superpositions of the mass eigenstates as follows :

$$|\nu_\alpha\rangle = \sum_{i=1}^{3} U_{\alpha i}|\nu_i\rangle, \tag{1.1}$$

where $|\nu_\alpha\rangle$ represents the flavor eigenstates $\nu_e, \nu_\mu$ and $\nu_\tau$ and $|\nu_i\rangle$ represents the mass eigenstates

$\nu_1$, $\nu_2$ and $\nu_3$. $U$ is a 3×3 unitary mixing matrix known as the MNSP matrix. The mixing matrix $U$ can be written as a product of three rotation matrices using the mixing angles $\theta_{12}$, $\theta_{23}$ and $\theta_{13}$ and a CP-violating phase $\delta$ as follows :

$$U = \begin{pmatrix} 1 & 0 & 0 \\ 0 & c_{23} & s_{23} \\ 0 & -s_{23} & c_{23} \end{pmatrix} \begin{pmatrix} c_{13} & 0 & s_{13}e^{-i\delta} \\ 0 & 1 & 0 \\ -s_{13}e^{i\delta} & 0 & c_{13} \end{pmatrix} \begin{pmatrix} c_{12} & s_{12} & 0 \\ -s_{12} & c_{12} & 0 \\ 0 & 0 & 1 \end{pmatrix}, \tag{1.2}$$

where $c_{ij} \equiv \cos\theta_{ij}$, $s_{ij} \equiv \sin\theta_{ij}$. The time evolution of the flavor eigenstates is represented as :

$$|\nu_\alpha(t)\rangle = \sum_i U_{\alpha i} \exp(-iE_i t) |\nu_i(t=0)\rangle \tag{1.3}$$

$$= \sum_i \sum_{\alpha'} U_{\alpha i} U_{\alpha' i}^* \exp(-iE_i t) |\nu_\alpha'(t=0)\rangle, \tag{1.4}$$

where $E_i$ is an eigenvalue of the mass eigenstate $|\nu_i\rangle$. Therefore the probability for flavor eigenstate $\nu_\alpha$ at t=0 to change the state $\nu_\beta$ at time t, is calculated as :

$$P(\nu_\alpha \to \nu_\beta) = |\langle\nu_\beta(t)|\nu_\alpha(0)\rangle|^2 \tag{1.5}$$

$$= \left|\sum_i U_{\beta i} U_{\alpha i}^* \exp(-iE_i t)\right|^2 \tag{1.6}$$

$$= \sum_i |U_{\alpha i} U_{\beta i}|^2 + \sum_{i \neq j} U_{\alpha i} U_{\beta i}^* U_{\alpha j}^* U_{\beta j} \exp(-i(E_i - E_j)t). \tag{1.7}$$

Due to the flavor mixing of massive neutrinos, the flavor transition phenomenon, called neutrino oscillation, could occur.

In the two-flavor mixing case, the mixing matrix $U$ is simplified as follows :

$$U = \begin{pmatrix} \cos\theta & \sin\theta \\ -\sin\theta & \cos\theta \end{pmatrix}. \tag{1.8}$$

The transition probability for $\nu_\alpha \to \nu_\beta$ (Eq. (1.7)) is expressed in much simpler form :

$$P_{(\nu_\alpha \to \nu_\beta)} = \sin^2 2\theta \sin^2\left(\frac{(E_i - E_j)t}{2}\right). \tag{1.9}$$

If neutrinos have finite masses, the following approximation can be used :

$$E_i - E_j = \sqrt{m_i^2 + p_i^2} - \sqrt{m_j^2 + p_j^2}$$

$$\simeq \left(p + \frac{m_i^2}{2p}\right) - \left(p + \frac{m_j^2}{2p}\right)$$

$$\simeq \frac{\Delta m_{ij}^2}{2E}, \tag{1.10}$$

where $\Delta m_{ij}^2 \equiv m_i^2 - m_j^2$ is the mass-squared difference of neutrino mass eigenstates. Finally using the neutrino flight length $L_\nu$ and the neutrino energy $E_\nu$, the survival probability of $\nu_\alpha$ in

the two-flavor mixing case is written as follows :

$$P(\nu_\alpha \rightarrow \nu_\alpha) \;\; = \;\; 1 - \sin^2 2\theta \sin^2 \left( \frac{\Delta m_{ij}^2 L_\nu}{4E_\nu} \right) \tag{1.11}$$

$$= \;\; 1 - \sin^2 2\theta \sin^2 \left( \frac{1.27 \Delta m_{ij}^2 (\text{eV}^2) L_\nu (\text{km})}{E_\nu (\text{GeV})} \right), \tag{1.12}$$

The oscillation probability is characterized by the mixing angle, the mass squared difference $\Delta m_{ij}^2$, the neutrino flight length $L_\nu$ and the neutrino energy $E_\nu$. So the oscillation amplitude is maximum when $L_\nu[\text{km}]/E_\nu[\text{GeV}] \sim \pi/(2.54 \cdot \Delta m_{ij}^2[\text{eV}^2])$. Putting experimentally conceivable numbers in this relation, one easily finds that neutrino oscillation experiment can explore the neutrino mass square difference below the eV$^2$ range.

## 1.2 Neutrino oscillation experiments

There are many experiments which have observed neutrino oscillations and measured oscillation parameters; the mass-squared difference and the mixing angle. In this section, the current status of our knowledge of neutrino oscillations is summarized.

### 1.2.1 Solar neutrino and Reactor neutrino

Electron neutrinos are produced via $4p \rightarrow^4 He + 2e^+ + 2\nu_e + \gamma$ in the Sun. The Homestake chlorine experiment [11], which was the first experiment to observe solar neutrinos, measured neutrinos by using the reaction $\nu_e +^{37}\text{Cl} \rightarrow \text{e}^- +^{37}\text{Ar}$. The produced Ar atoms were counted by a chemical technique. The measured count rate of solar neutrinos is 2.56 per $10^{36}$ target atoms per second, 2.56 SNU (SNU: Solar Neutrino Unit), against a prediction of 7.6 SNU from the standard solar model (SSM) [13]. Other experiments SAGE [14] and GALLEX [15], using $^{71}\text{Ga}$ target, and Kamiokande [12], H$_2$O target, also observed this flux deficit which became subsequently known as the "solar neutrino problem". This flux deficit is mostly solved by the neutrino oscillation, but the analysis using only the flux deficit cannot produce a unique solution for the neutrino oscillation.

Super-Kamiokande (SK) experiment [16, 18], which is a successor of Kamiokande experiment, started in 1996, and SNO experiment [17], which uses the Cherenkov detector filled with heavy water D$_2$O, started in 1999. SK and SNO measure solar neutrino flux from $^8$B in different neutrino reactions, charged current interaction (CC), $\nu_e + D \rightarrow e^- + p + p$, neutral current interaction (NC), $\nu_x + D \rightarrow \nu_x + p + n$, and elastic scattering (ES), $\nu_x + e^- \rightarrow \nu_x + e^-$. NC can be initiated with equal cross sections by neutrinos of all active flavors. Therefore NC measures $\phi(\nu_e) + \phi(\nu_\mu, \nu_\tau)$, where $\phi(\nu_\mu, \nu_\tau)$ is the flux of $\nu_\mu$ and/or $\nu_\tau$ from the Sun, while CC only measures the $\phi(\nu_e)$ flux from the Sun. From both NC and CC measurements, the $\nu_e$ flux deficit can be explained by $\nu_e$ oscillations into the other active neutrino flavors ($\nu_\mu$ and $\nu_\tau$). On the other hand, ES can measure a neutrino of any flavors. But the cross-section $\sigma(\nu_x)$ is different for each neutrino; $\sigma(\nu_{\mu,\tau} e \rightarrow \nu_{\mu,\tau} e) \simeq \sigma(\nu_e e \rightarrow \nu_e e)/6.5$. From the measurements of SNO and SK, $\nu_e \rightarrow \nu_\mu$ oscillation was discovered during 2001 and 2002. Combining all the results from solar neutrino experiments, the LMA-MSW solution [21] of the solar neutrino problem was indicated [16].

3

To confirm these results, the KamLAND experiment [20] played an important role. Kam-LAND is a liquid scintillator detector and searches for anti-electron-neutrino ($\overline{\nu}_e$) oscillations. The $\overline{\nu}_e$s are generated at distant power reactors. They are detected by the reaction $\overline{\nu}_e$+p$\rightarrow$ $e^+$+n, where the prompt signal from the positron and the delayed coincidence of characteristic gammas from neutron capture allow an efficient reduction of backgrounds. The $\overline{\nu}_e$ flux at the detector site is dominated by a number of reactors at an average distance of $\sim 180$ km. Since the energy of the produced $\overline{\nu}_e$s is around 3 MeV, the experiment is sensitive to $\Delta m^2$ down to several $10^{-6}$ eV$^2$. KamLAND observed a very clean energy dependent $\overline{\nu}_e$ disappearance, constraining the oscillation parameters precisely. The combined analysis of the solar neutrino data and the KamLAND data leads to the oscillation parameters [19]:

$$7.38 \times 10^{-5} < \Delta m_{12}^2 < 7.78 \times 10^{-5} eV^2,$$
$$0.30 < \sin^2 \theta_{12} < 0.34 \ \ (1\sigma). \tag{1.13}$$

### 1.2.2 Atmospheric neutrino and Accelerator neutrino

Atmospheric neutrinos are produced by the decays of pions and kaons which are generated when primary cosmic rays interact with the nuclei in the Earth's atmosphere :

$$\begin{aligned} \pi^+ &\rightarrow \mu^+ + \nu_\mu \\ &\hookrightarrow e^+ + \nu_e + \overline{\nu}_\mu, \end{aligned} \tag{1.14}$$
$$\begin{aligned} \pi^- &\rightarrow \mu^- + \overline{\nu}_\mu \\ &\hookrightarrow e^- + \overline{\nu}_e + \nu_\mu. \end{aligned} \tag{1.15}$$

Neutrinos $\nu_e$, $\overline{\nu}_e$, $\nu_\mu$ and $\overline{\nu}_\mu$ are generated as the atmospheric neutrino. The energy spectrum of the atmospheric neutrinos peaks around 40 MeV and extends to the energy range above TeV. The neutrino flight length ranges from $\sim 10$ to $\sim 10^4$ km, corresponding to the production height of about 15 km and the diameter of the Earth (13000 km), respectively. Since typical atmospheric neutrino experiments have enough event statistics for neutrino energies above several hundreds MeV, the observation of atmospheric neutrinos is sensitive to $\Delta m^2 \sim E_\nu/L_\nu = 10^{-1} \sim 10^{-4}$ eV$^2$. The predicted total flux of atmospheric neutrinos has $\sim 10\%$ uncertainty in the GeV energy range, which mostly comes from the uncertainties on cross sections of hadronic interactions and on fluxes of primary cosmic ray components [22]. However, the flavor ratio $(\nu_\mu + \overline{\nu}_\mu)/(\nu_e + \overline{\nu}_e)$ is predicted within only $3\%$ uncertainty. This ratio has been measured by several underground experiments (SK [23, 24], IMB [25, 26] and Soudan 2 [27]) and reported in terms of a double ratio R$\equiv (N_\mu/N_e)_{Data}/(N_\mu/N_e)_{MC}$, where $N_\mu$ ($N_e$) is the number of muon (electron) events produced by charged current interactions. The measured double ratio R was significantly lower than 1.

In 1998, Super-Kamiokande reported that the zenith angle distributions of muon neutrino events were asymmetric, and concluded that their results gave an evidence for neutrino oscillation [28]. In addition, MACRO [29] and Super-Kamiokande [30] have studied upward-going muons produced by energetic $\nu_\mu$ charged current interactions in the rock surrounding the detector and their data are consistent with the two-flavor neutrino oscillation $\nu_\mu \leftrightarrow \nu_\tau$. Super-Kamiokande also reported the observation of an oscillation signature with $L/E$ dependence [33], which is well described by the hypothesis that $\nu_\mu$ oscillates to $\nu_\tau$ with a nearly maximal mixing. In the two-flavor mixing framework, the neutrino oscillation parameters from SK $L/E$ result [35]
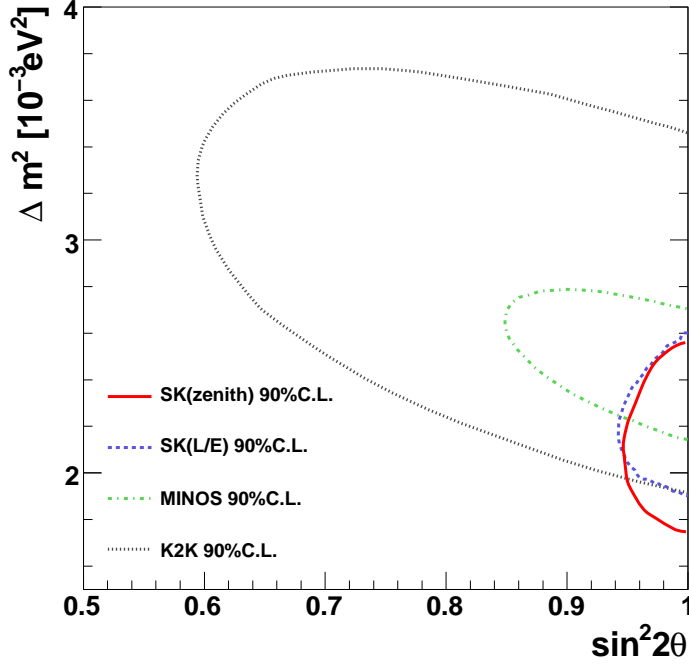
Figure 1.1: 90 % confidence level allowed regions of oscillation parameters for $\nu_\mu \leftrightarrow \nu_\tau$ oscillation. The horizontal axis shows $\sin^2 2\theta$ and the vertical axis shows $\Delta m^2$. The results are taken from latest Super-Kamiokande [35] zenith angle analysis result (solid line), $L/E$ result (dotted line), K2K experiment [31] (dashed line) and MINOS experiment[32] (dash-dotted line).

are constrained to be :

$$1.9 \times 10^{-3} < \Delta m^2_{23} < 2.6 \times 10^{-3} eV^2,$$
$$0.94 < \sin^2 2\theta_{23} \quad \text{at } 90\,\% \text{ C.L..} \tag{1.16}$$

The atmospheric neutrino oscillation was confirmed by long-baseline experiments using the muon neutrino beam produced by accelerators, such as K2K [31] and MINOS [32]. These experiments measure the spectral distortion and the decreasing $\nu_\mu$ flux during the travel. Figure 1.1 shows the allowed parameter regions from the $\nu_\mu \leftrightarrow \nu_\tau$ oscillation measurement experiments.

### 1.2.3 Mixing angle $\theta_{13}$

The third mixing angle $\theta_{13}$ was tested by the CHOOZ reactor experiment. This experiment looked for distortions in the energy spectrum of $\overline{\nu}_e$ produced by a nuclear reactor 1 km away by using liquid scintillator in conjunction with $\overline{\nu}_e$s from inverse $\beta$-decay process. $\overline{\nu}_e$ survival probability can be expressed :

$$\mathrm{P}(\overline{\nu}_e \to \overline{\nu}_e) \;\; = \;\; 1 - \sin^2 2\theta_{13} \sin^2 \left( \frac{1.27 \Delta m^2_{13} L}{E} \right). \tag{1.17}$$
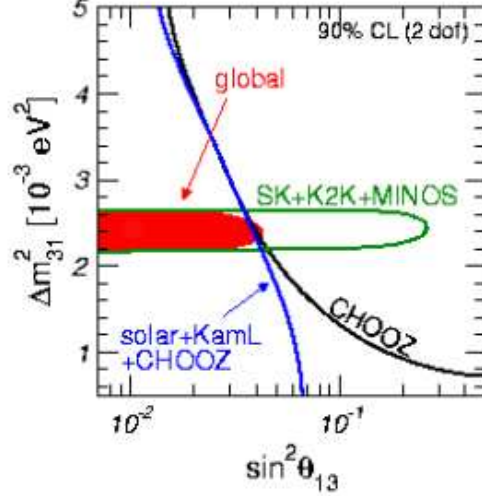
Figure 1.2: Allowed region on 1-3 parameter is plotted for each experiment. Combined analysis of the global data is shown as filled region. This plot taken from [37]

The CHOOZ experiment ended without any evidence for $\overline{\nu}_e$ oscillation in large mass splittings $\Delta m^2 = 10^{-2} \sim 10^{-3}$. Thus, it implies that the $\nu_e$ fraction in $\nu_3$ mass eigenstate would have been too small to be detected. The current upper limit on $\theta_{13}$ is given by the CHOOZ experiment [36] :

$$\sin^2 \theta_{13} < 0.04 \qquad (1.18)$$

at 90 % C.L.(assuming $\Delta m_{23}^2 = 2.0 \times 10^{-3}\,\mathrm{eV}^2$).

The atmospheric neutrino data have also been used to constrain $\theta_{13}$ in the three-flavor mixing framework with the one mass scale dominance approximation ($|m_2^2 - m_1^2| \ll |m_3^2 - m_2^2| \sim |m_3^2 - m_1^2|$). In this framework, oscillations of atmospheric $\nu_e$s are expressed by :

$$
\begin{aligned}
\mathrm{P}(\nu_e \to \nu_e) &= 1 - \sin^2 2\theta_{13} \sin^2 \left( \frac{1.27 \Delta m_{23}^2 L}{E} \right), & (1.19) \\
\mathrm{P}(\nu_\mu \to \nu_e) &= \mathrm{P}(\nu_e \to \nu_\mu) \\
&= \sin^2 \theta_{23} \sin^2 2\theta_{13} \sin^2 \left( \frac{1.27 \Delta m_{23}^2 L}{E} \right). & (1.20)
\end{aligned}
$$

Consistent results with CHOOZ experiment have been obtained [34, 35]. Detail of the analysis with atmospheric neutrino data will be discussed in Section 1.3.

### 1.2.4  Summary for neutrino oscillation parameters and Remaining issues

In this way, neutrino oscillation has been well understood and consolidated the existing of massive neutrinos. The global best fit results of neutrino oscillation parameters are summarized in Table 1.1. At the same time, there remain a few open questions.

Since oscillation experiments are measuring mass differences, $\Delta m_{12}^2$ and $\Delta m_{23}^2$, not the absolute neutrino masses, it is not known what the mass ordering is. Figure 1.3 shows the

6

| parameter | best-fit $\pm$ 1$\sigma$ C.L. |
|---|---|
| $\Delta m^2_{12}$ | $7.65\ ^{+0.23}_{-0.20} \times 10^{-5}$ eV$^2$ |
| $|\Delta m^2_{13}|$ | $2.40\ ^{+0.12}_{-0.11} \times 10^{-3}$ eV$^2$ |
| $\sin^2\theta_{12}$ | $0.304\ ^{+0.022}_{-0.016}$ |
| $\sin^2\theta_{23}$ | $0.50\ ^{+0.07}_{-0.06}$ |
| $\sin^2\theta_{13}$ | $0.01\ ^{+0.016}_{-0.011}$ |

Table 1.1: Summary table of the global best-fit to neutrino oscillation data from [37]
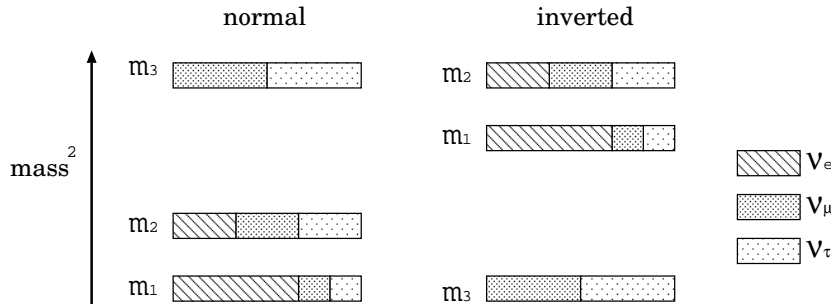


Figure 1.3: A three-neutrino mass-squared spectrum, which accounts for the observed flavor changes, for two mass hierarchy schemes

conceptual diagram for two types of the mass order. This is the first question which the mass hierarchy is, normal or inverted.

Whether or not $\theta_{13}$ is zero is the important question. If $\theta_{13}$ is found to be non-zero, it becomes possible to address the question of CP-violation in the lepton sector, because a CP-violating phase $\delta$ appears as a combination with $\theta_{13}$ parameter as shown in Eq. (1.2).

Typical atmospheric neutrino experiments cover a wide range of $L/E_\nu$ and can detect $\nu_e$ interactions. Therefore it is possible for those experiments to measure the effect of three-flavor oscillation including $\theta_{13}$ and 1-2 parameters. In the next section, it is described how these oscillation effects can be measured in Super-Kamiokande.

## 1.3 Sub-dominant effects of atmospheric neutrino oscillation

Atmospheric neutrino data are well fitted to pure $\nu_\mu \to \nu_\tau$ 2-flavor oscillation. When 3-flavor oscillation, electron neutrino oscillation, is considered, sub-dominant oscillation effects appear due to $\theta_{13}$ mixing and/or the $\Delta m^2_{12}$-induced oscillation wavelength. In these oscillation schemes, matter effect [21] plays an important role.

For neutrino traversing the Earth, oscillation probability is calculated taking into account Earth's matter potential due to the forward scattering amplitude of charged current $\nu_e$ and $\bar{\nu}_e$ interactions with electrons. The Earth contains a large number of electrons, electron neutrinos

interact with them via $W^{\pm}$ boson while muon and tau neutrinos do not.

When taking into account the matter effect in the $P(\nu_\mu \to \nu_e)$ oscillation with the approximation of $\Delta m_{12}^2 \sim 0$ as shown in Eq. (1.20), it can described by replacing $\theta_{13}$ and $\Delta m_{23}^2$ by the corresponding mixing parameters in matter. For constant matter density, $P(\nu_\mu \to \nu_e)$ ($= P(\nu_e \to \nu_\mu)$) is described as follows:

$$P(\nu_\mu \leftrightarrow \nu_e) \quad = \quad \sin^2\theta_{23} \sin^2 2\theta_{13,M} \sin^2\left(\frac{1.27\Delta m_{23,M}^2 L_\nu}{E_\nu}\right), \tag{1.21}$$

where

$$\Delta m_{23,M}^2 \quad = \quad \Delta m_{23}^2 \sqrt{(\cos 2\theta_{13} - A_{CC}/\Delta m_{23}^2)^2 + \sin^2 2\theta_{13}} \tag{1.22}$$

$$\sin^2 2\theta_{13,M} \quad = \quad \frac{\sin^2 2\theta_{13}}{(\cos 2\theta_{13} - A_{CC}/\Delta m_{23}^2)^2 + \sin^2 2\theta_{13}} \tag{1.23}$$

$$A_{CC} \quad = \quad 2\sqrt{2}G_F N_e E_\nu \tag{1.24}$$

$A_{CC}$ : the matter potential term

$G_F$: the Fermi constant

$N_e$: the electron densities in the medium.

When $|A_{CC}/\Delta m^2| = \cos 2\theta_{13}$, a resonant enhancement of the oscillation probability, called Mikheyev-Smirnov-Wolfenstein (MSW) resonant enhancement, occurs and holds for either neutrinos or anti-neutrinos depending on the mass hierarchy. Figure 1.4 shows oscillation probability of $\nu_\mu \to \nu_e$ for neutrinos traveling the Earth as a function of energy and zenith angle with a more realistic matter density distribution. The oscillation probability in vacuum is also shown in Fig. 1.4 for comparison. The resonance enhancement can be seen in the 2-10 GeV energy region and the upward direction with some assumptions written in the caption. Note that the enhancement occurs in normal (inverted) hierarchy case for the neutrinos (anti-neutrinos).

When the oscillation driven by the LMA-MSW effect obtained from solar neutrino parameters ($\Delta m_{12}^2$ and $\theta_{12}$) is considered, the oscillation effect of low energy electron neutrinos will be observable even if $\theta_{13} = 0$. In case of $\theta_{13} \sim 0$, the neutrino oscillation probabilities can be written in the constant matter density as follows:

$$P(\nu_e \leftrightarrow \nu_e) \quad = \quad 1 - P_{ex} \tag{1.25}$$

$$P(\nu_e \leftrightarrow \nu_\mu) \quad = \quad \cos^2\theta_{23} P_{ex} \tag{1.26}$$

$$P(\nu_\mu \leftrightarrow \nu_\mu) \quad = \quad 1 - \cos^4\theta_{23} P_{ex} - \sin^2 2\theta_{23}(1 - \sqrt{1 - P_{ex}}\cos\phi)$$

$$\phi \quad \sim \quad \left(\Delta m_{31}^2 + s_{12}^2 \Delta m_{21}^2\right)\frac{L}{2E_\nu}$$

$$P_{ex}(\nu_e \to \nu_x) \quad = \quad \sin^2 2\theta_{12,M} \sin^2\left(\frac{\Delta m_{21}^2 L_\nu}{4E_\nu}\frac{\sin^2 2\theta_{12}}{\sin^2 2\theta_{12,M}}\right)$$

where

$$\cos 2\theta_{12,M} \quad = \quad \frac{\cos 2\theta_{12}}{\sqrt{(\cos 2\theta_{12} - A_{CC}/\Delta m_{12}^2)^2 + \sin^2 2\theta_{12}}}. \tag{1.27}$$
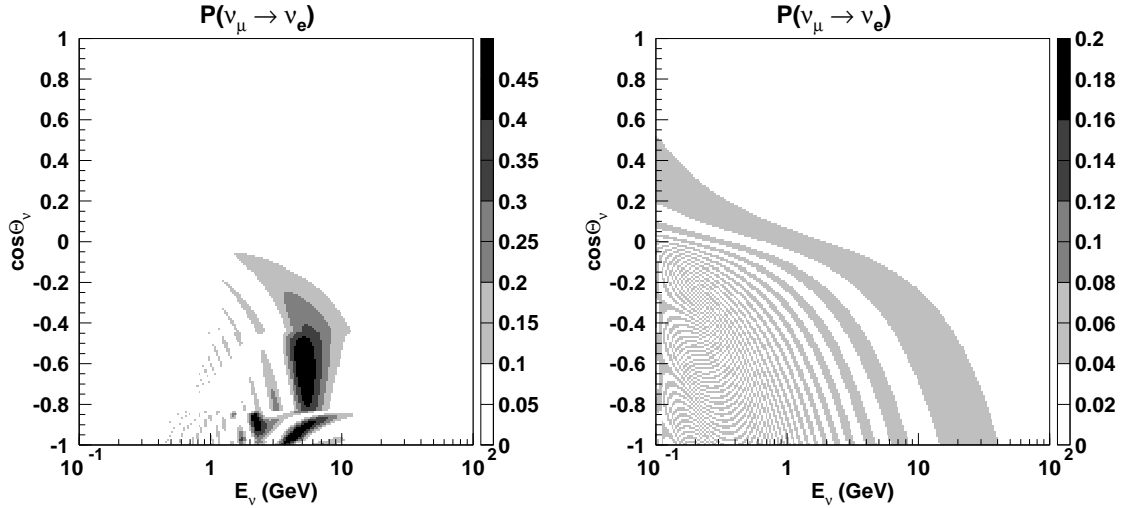
Figure 1.4: The $\nu_\mu$ to $\nu_e$ (or $\nu_e$ to $\nu_\mu$) transition probability in the Earth (left) and in vacuum (right) for atmospheric neutrinos as a function of energy $E_\nu$ and neutrino zenith angle. $\cos\Theta_\nu = -1$ and $\cos\Theta_\nu = 0$ correspond to upward-going and horizontal directions, respectively. The plots assume the oscillation parameters $(\Delta m_{23}, \sin^2\theta_{23}, \sin^2\theta_{13}) = (2.1 \times 10^{-3}eV^2, 0.5, 0.04$ (Chooz limit)).

Figure 1.5 shows the $P_{ex}$ as a function of energy and zenith angle with a more realistic matter density distribution. The oscillated atmospheric $\nu_e$ flux is expressed as :

$$
\begin{aligned}
F_e^{osc} &= F_e^0 \cdot P(\nu_e \to \nu_e) + F_\mu^0 \cdot P(\nu_\mu \to \nu_e) \\
&= F_e^0 \left(1 + P_{ex}(r\cos_{23}^2 - 1)\right) \\
\frac{F_e^{osc}}{F_e^0} - 1 &= P_{ex}(r\cos^2\theta_{23} - 1)
\end{aligned}
\tag{1.28}
$$

The observable $\nu_e$ oscillation is due to $r\cos^2\theta_{23} - 1$ in Eq. (1.28). Since $r$ in Eq. 1.28 is about 2 for low energy region, the $\nu_e$ oscillation effect can be seen by the flux deficit or excess in case of $\cos^2\theta_{23} \neq 0.5$. If $\cos^2\theta_{23}$ is greater than 0.5 ($\theta_{23} < 45°$), enhancement of flux is expected. On the other hand, if $\cos^2\theta_{23}$ is less than 0.5 ($\theta_{23} > 45°$), deficit of flux is expected. Figure 1.5 also shows the flux ratio for each case $\sin^2\theta_{23} = 0.4$, $\sin^2\theta_{23} = 0.5$ and $\sin^2\theta_{23} = 0.6$.

Two sub-dominant oscillation schemes are described above considering approximation of $\Delta m_{12}^2 \sim 0$ or $\theta_{13} \sim 0$. However, if we describe the effect due to the interference between $\theta_{13}$- and $\Delta m_{12}^2$-induced oscillations, full oscillation parameters should be taken into account without any approximations. The full oscillation parameters mean all relevant oscillation parameters including the CP violating phase. In constant matter density, $\nu_\mu \leftrightarrow \nu_e$ transition probability considering all oscillation parameters is described as follows:

$$
\begin{aligned}
P(\nu_\mu \leftrightarrow \nu_e) =\ & \cos^2\widetilde{\theta}_{13}\cos^2\theta_{23}P_{e2} \\
+\ & \sin^2\widetilde{\theta}_{13}\cos^2\widetilde{\theta}_{13}\sin^2\theta_{23}(2 - P_{e2}) \\
-\ & 2\sin\widetilde{\theta}_{13}\cos^2\widetilde{\theta}_{13}\sin\theta_{23}\cos\theta_{23}(\cos\delta R_2 - \sin\delta I_2)
\end{aligned}
$$

9
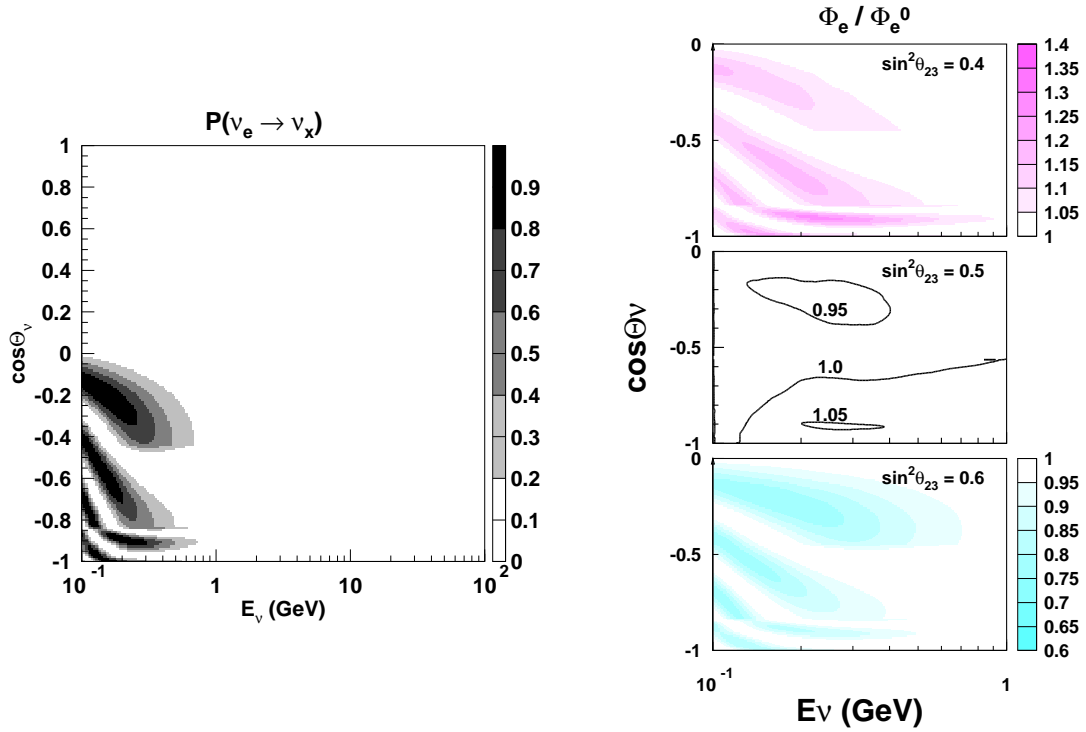
Figure 1.5: The left side panel shows the $\nu_e$ transition probability $P_{ex}$ for atmospheric neutrinos as a function of energy $E_\nu$ and neutrino zenith angle, assuming oscillations with $(\Delta m_{12}, \Delta m_{23}, \sin^2 \theta_{12}, \sin^2 \theta_{23}) = (7.7 \times 10^{-5} eV^2, 2.1 \times 10^{-3} eV^2, 0.3, 0.5)$. The right side panels show the electron neutrino flux ratio $F_e^{osc}/F_e^0$. An expected excess (deficit) for $\sin^2 \theta_{23}$ in the first (second) octant is shown in the upper (bottom) panel while the center panel for $\sin^2 \theta_{23} = 0.5$ is seen with small both deficit and excess.

where

$$P_{e2} = \sin^2 2\theta_{12,M} \sin^2 \frac{\phi_m}{2}$$

$$R_2 = -\sin 2\theta_{12,M} \cos 2\theta_{12,M} \sin^2 \frac{\phi_m}{2}$$

$$I_2 = -\frac{1}{2} \sin 2\theta_{12,M} \sin \phi_m$$

$\phi_m$ is the phase oscillation in matter and $\widetilde{\theta}_{13}$ is basically the mixing angle in matter; $\widetilde{\theta}_{13} \approx \theta_{13,M}$ [39]. If the full oscillation scheme is considered, the electron neutrino oscillations occur with the CP violating phase. Figure 1.6 shows $P(\nu_\mu \to \nu_e)$ as a function of energy and zenith angle in case of the oscillations $(\Delta m_{12}, \Delta m_{23}, \sin^2 \theta_{12}, \sin^2 \theta_{23}, \sin^2 \theta_{13}, \delta_{cp}) = (7.7 \times 10^{-5}, 2.1 \times 10^{-3}, 0.3, 0.5, 0.04, 0°)$ with realistic matter density. It is obvious that the electron neutrino oscillation may appear in both Sub- and Multi-GeV energy range. Here "Sub-GeV" ("Multi-GeV") is defined to be less (more) than 1.33 GeV in visible energy in a water Cherenkov detector. In Super-Kamiokande, a particularly important observation is the change of expected electron events. The expected electron events ($N_e$) as compared to no oscillated events ($N_e^0$) can be written in three terms :

$$\frac{N_e}{N_e^0} - 1 = (P_{ee} - 1) + r P_{e\mu}$$
$$\simeq \Delta_1(\theta_{13}) + \Delta_2(\theta_{12}, \Delta m_{12}^2) + \Delta_3(\theta_{13}, \theta_{12}, \Delta m_{12}^2, \delta_{cp})$$

where $r$ is the ratio of atmospheric $\nu_\mu$ and $\nu_e$ fluxes, $r \sim 2$ to $\sim 3.5$ in a few MeV to 10 GeV. $\Delta_1(\theta_{13})$ arises for $\theta_{13} > 0$ and is independent of $\Delta m_{12}^2$. $\Delta_2(\theta_{12}, \Delta m_{12}^2)$ arises for $\Delta m_{12}^2 > 0$ and is independent of $\theta_{13}$. Only $\Delta_3(\theta_{13}, \theta_{12}, \Delta m_{12}^2, \delta_{cp})$ depends on both $\Delta m_{12}^2$ and $\theta_{13}$. It is the only term which includes the effect from CP phase values. These three terms affect different energy regions; $\Delta_1(\theta_{13})$ induces the electron excess in Multi-GeV region due to $\theta_{13}$; $\Delta_2(\theta_{12}, \Delta m_{12}^2)$ induces an excess or deficit in Sub-GeV region due to an octant of $\sin^2 \theta_{23}$; $\Delta_3(\theta_{13}, \theta_{12}, \Delta m_{12}^2, \delta_{cp})$ occurs for both energy regions due to the interference between $\theta_{13}$- and $\Delta m_{12}^2$-induced oscillations. Figure 1.6 also shows the $\nu_e$ flux ratio $N_e/N_e^0$ assuming the same oscillation parameters. Figure 1.7 shows the numerical examples of the effects from various CP phases at the observed zenith angle distributions. The number of observed events is expected to change a few % due to CP phase. Therefore, looking for the interference sub-dominant effects of the atmospheric neutrino enables us to examine the CP phase.


This thesis aims to examine the full neutrino oscillation and to obtain the parameter values, which are $\Delta m_{12}^2$, $\Delta m_{23}^2$, $\theta_{23}$, $\theta_{13}$, and CP phase ($\delta_{cp}$), by considering sub-dominant effects in the atmospheric neutrinos. This is the first analysis in the Super-Kamiokande experiment and the first attempt to obtain the information of CP phase in the neutrino oscillation studies. The thesis's contents are as follows : Chapter 2 describes the Super-Kamiokande detector, Chapter 3 explains the simulation for the atmospheric neutrinos observed in Super-Kamiokande, Chapter 4 describes the detector calibrations which are important for precise measurements, Chapter 5 describes the measurement methods and the data of atmospheric neutrinos. The analysis and the results are explained in Chapter 6.
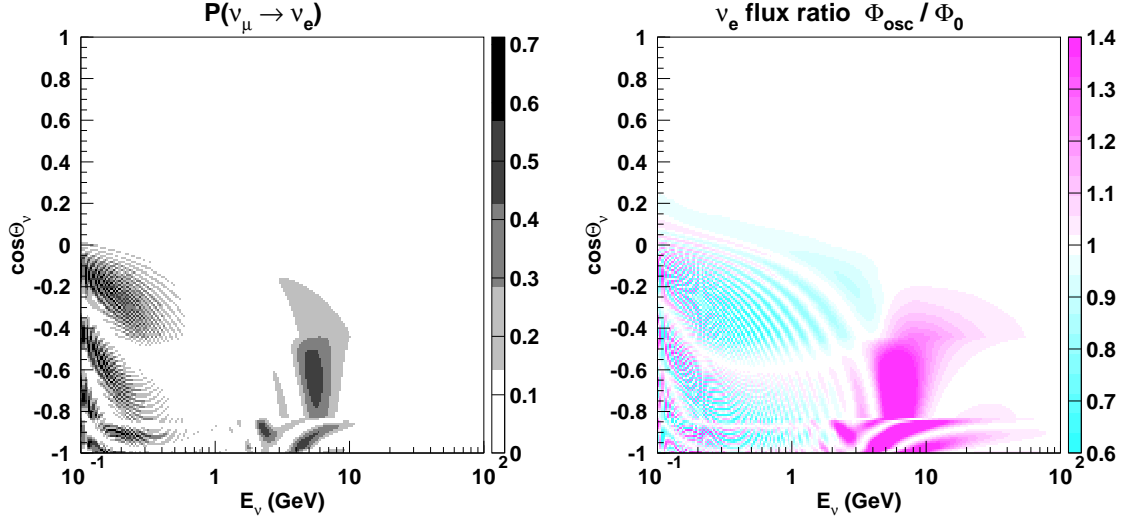
Figure 1.6: The left panel shows the probability $\nu_\mu \to \nu_e$ oscillation as a function of zenith angle and energy in case of $(\Delta m_{12}, \Delta m_{23}, \sin^2 \theta_{12}, \sin^2 \theta_{23}, \sin^2 \theta_{13}, \delta_{cp}) = (7.7 \times 10^{-5}, 2.1 \times 10^{-3}, 0.3, 0.5, 0.04, 0°)$. The right panel shows the $\nu_e$ flux ratio $N_e/N_e^0$ assuming the same oscillation parameters.
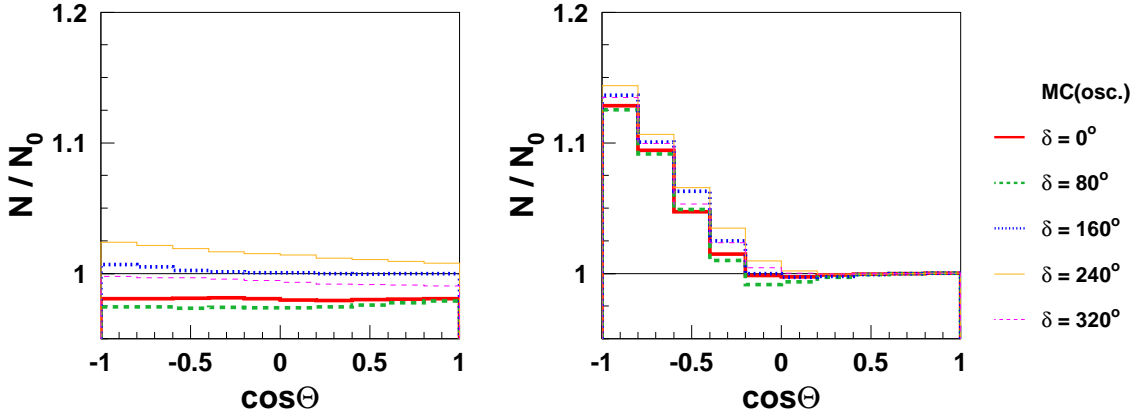


Figure 1.7: Zenith angle distributions of the expected MC events for Sub-GeV 1-ring e-like (left) and Multi-GeV 1-ring e-like (right) samples assuming the oscillation parameters $(\Delta m_{12}, \Delta m_{23}, \sin^2 \theta_{12}, \sin^2 \theta_{23}, \sin^2 \theta_{13}) = (7.7 \times 10^{-7}, 2.1 \times 10^{-3}, 0.30, 0.55, 0.04)$ in normal hierarchy case. Each line indicates the different CP phase value. All plots are normalized by the number of events without the oscillations.

# Chapter 2

# The Super-Kamiokande Detector

Super-Kamiokande is a cylindrical 50 kt water Cherenkov detector located at Kamioka Observatory of Institute for Cosmic Ray Research in Gifu Prefecture, Japan. A schematic view of the Super-Kamiokande detector is shown in Figure 2.1. The geographic coordinates of the site are 36°25'N and 137°18'E, and the altitude above sea level is 370 m. The detector lies in a zinc mine under the top of Mt.Ikenoyama, where the mean rock overburden is $\sim$ 1000 m (2700 m water equivalent). This overburden plays a role of a shield against cosmic ray muon background in the detector. The cosmic ray muon flux at the Super-Kamiokande site is reduced by 5 orders of magnitude compared to that on the surface of the earth. The detector construction is the water tank with the photomultiplier tubes(PMTs) which can detect weak lights due to Cherenkov radiation.

The main scientific purposes of the Super-Kamiokande experiment are the searches for nucleon decays and the studies of various types of neutrinos: atmospheric neutrinos, solar neutrinos, and the neutrinos from supernovae and the other astrophysical sources. The Super-Kamiokande detector is also used as a target of the artificial neutrino beam in long-baseline neutrino oscillation experiments.

The Super-Kamiokande experiment started taking data in April, 1996 and continued the observation for five years within the running period referred to SK-I till the detector maintenance in July, 2001. During refilling water after the maintenance, an accident occurred in November, 2001 in which more than a half of the PMTs were destroyed. The Super-Kamiokande detector was rebuilt after the accident with the half of the original PMT density in the inner detector and resumed observation from October, 2002, which is referred to the SK-II running period. The SK-II continued the physics measurement for three years and finished in October 2005 for the reconstruction work to put the PMT density back to the SK-I level. The Super-Kamiokande detector has restarted observation in June, 2006, which is referred to the SK-III period. Meanwhile, new electronics module for the Super-Kamiokande detector had been developed. New electronics was installed on the detector in September 2008, starting the SK-IV running period.

In this thesis, the data observed in the SK-I (1996-2001),the SK-II (2002-2005) and SK-III (2006-2008) running periods are used.

In this chapter, the construction and technical details of the Super-Kamiokande detector are described.
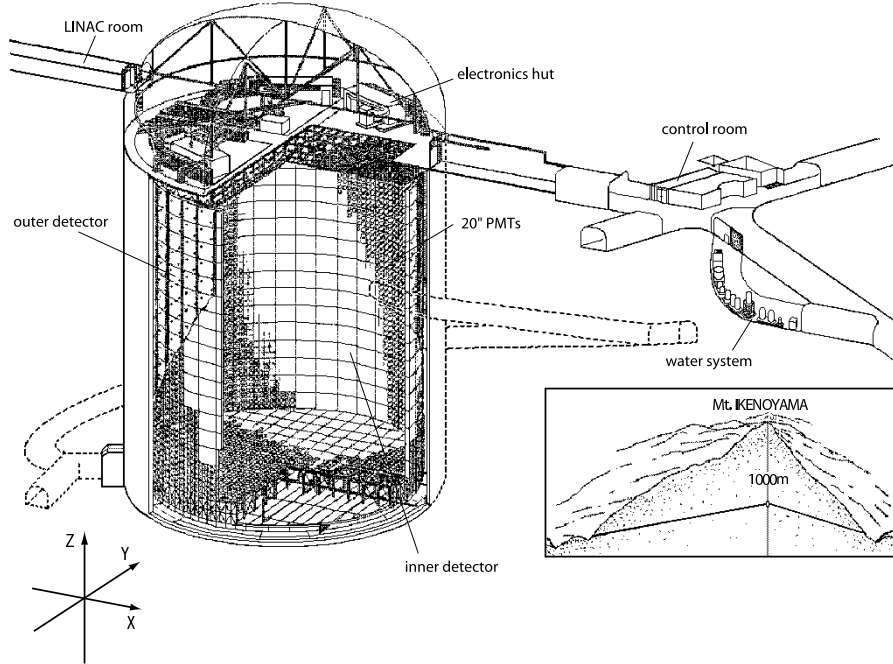
Figure 2.1: Super-Kamiokande detector and its location.

## 2.1 Cherenkov Radiation

The Super-Kamiokande detector observes relativistic charged particles in water by detecting the emitted Cherenkov light. The Cherenkov photons are radiated when the velocity of a charged particle exceeds the light velocity in the medium :

$$v \geq \frac{c}{n}, \tag{2.1}$$

where $v$ is the velocity of the charged particle, $n$ is the refractive index of the medium and $c$ is the light velocity in vacuum [40]. The momentum threshold of Cherenkov radiation is determined by the refractive index of the medium and the mass of the particle. Since the refractive index of water is about 1.34, the momentum thresholds of Cherenkov radiation for electrons, muons, charged pions and protons are 0.57, 118, 156 and 1051 MeV/$c$, respectively.

Cherenkov light is emitted on a cone with a characteristic half opening angle $\theta_C$ along the direction of the particle. The opening angle, called Cherenkov angle, is determined as follows :

$$\cos \theta_C = \frac{1}{n\beta}, \tag{2.2}$$

where $\beta = v/c$. For the particle with $\beta \simeq 1$ in water, the Cherenkov angle is about $42°$.

The number of photons emitted by Cherenkov radiation is given as a function of the wavelength $\lambda$ as follows :

$$\frac{d^2 N}{dx d\lambda} = \frac{2\pi\alpha}{\lambda^2} \left( 1 - \frac{1}{n^2\beta^2} \right), \tag{2.3}$$

14
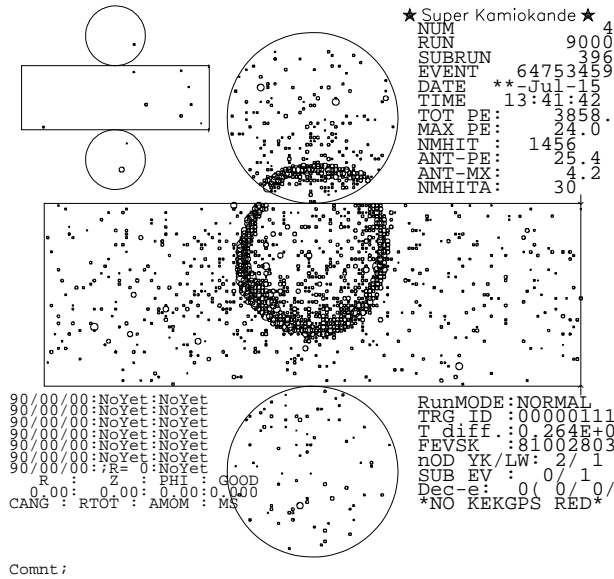
Figure 2.2: A visual display of a typical observed neutrino event in Super-Kamiokande. The size of small circles in the unrolled cylinder represents the amount of Cherenkov photons detected in each photo-multiplier tube. The Cherenkov ring image is clearly visible.

where $x$ is the path length of the charged particle and $\alpha$ is the fine structure constant. About 340 photons/cm are emitted between the wavelength of 300 nm to 600 nm, which is the sensitive wavelength region to the PMTs used in the Super-Kamiokande detector.

Particles emitting Cherenkov light project ring images on the wall inside the detector. Super-Kamiokande detects the Cherenkov photons by the PMTs arranged on the wall and the Cherenkov rings can be recognized. Figure 2.2 shows a visual display of a typical neutrino event in the Super-Kamiokande detector.

## 2.2   Detector

### 2.2.1   Water Tank

The whole size of the water tank is 41.4 m in the hight and 39.3 m in the diameter, in which 50 kt highly pure water is filled. The water tank is optically separated into two concentric cylindrical regions by a PMT support structure and a pair of opaque sheets as shown in Figure 2.3.

The detector part in the inner region of the tank is referred to the inner detector (ID). The inner region contains 32 kt water with the size of 36.2 m in the hight and 33.8 m in the diameter. 11,146 inward-facing 20-inch PMTs are attached to the supporting frame uniformly at intervals of 70 cm for SK-I. The effective photocathode coverage of the ID is about 40 %, and the rest of the surface is covered with black polyethylene terephthalate sheet, called "black sheet". 5,182 20-inch PMTs are attached at one intervals to the supporting frame and the photocathode coverage of the ID is about 20 % for SK-II. In the SK-III, the photocathode coverage is returned to about 40% level with 11,129 PMTs.
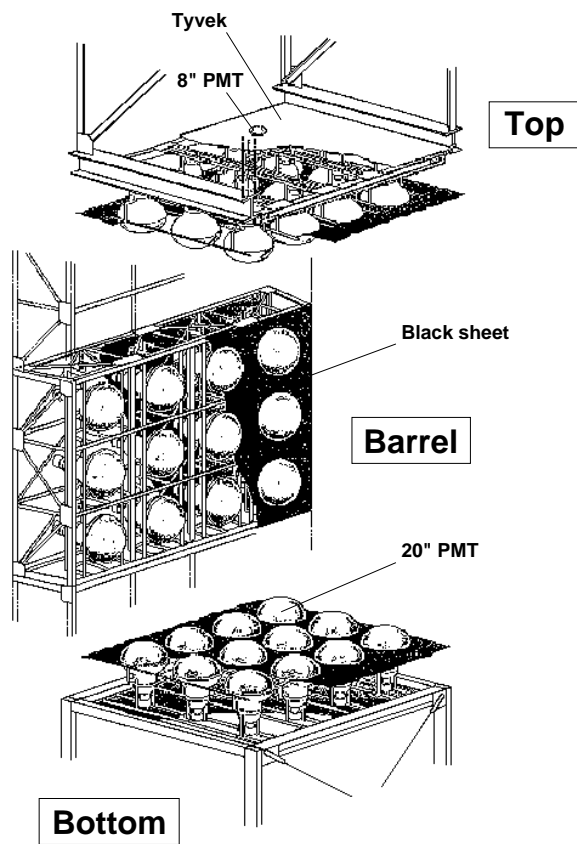
Figure 2.3: Supporting frame of PMTs.

The outer region completely surrounds the ID with the thickness of 2.05 m on top and bottom and 2.2 m along the barrel wall. This region, called the outer detector (OD), is monitored by 1,885 outward-facing 8-inch PMTs attached to the outer side of the supporting frame. To improve the light collection efficiency, a 60 cm × 60 cm wavelength shifting plate is attached to each OD PMT and the walls are covered with reflective material called "tyvek sheet". The OD is used as veto counter for entering cosmic ray muons and to tag the outgoing charged particles. Furthermore, the 2 m thickness water layer itself serves as a shield to attenuate gamma ray and neutron fluxes from the rock. The inner and outer volumes are separated by a 55 cm thick dead region. This region is not instrumented with any PMT. Stainless steel frames and signal and HV cables of the ID and OD PMTs are contained in this dead region.

### 2.2.2   photomultiplier tube

The photomultiplier tubes used in the ID, product name Hamamatsu R3600, have photo-cathode with a diameter of 50 cm (20 inch). This 20 inch PMT was originally developed by Hamamatsu Photonics K.K. in cooperation with the Kamiokande collaborators [41]. Later, the dynode structure and the bleeder circuit were modified for Super-Kamiokande to improve timing response and photon collection efficiency [42]. A schematic view of the PMT is shown in Figure 2.4 and the specifications are summarized in Table 2.1.

The photo-cathode of the PMT is coated by bi-alkali (Sb-K-Cs) owing to the high spectral sensitivity to Cherenkov light and the low thermionic emission. The quantum efficiency is 22 % in the peak at 360-400 nm. The dynode structure and the bleeder circuit are optimized to achieve high collection efficiency, fast timing response and good energy resolution. The averaged value of the collection efficiency at the first dynode is 70 %, which is uniform within a difference of $\pm 7$ % everywhere on the photocathode. The gain of the ID PMTs is $10^7$ at a supply high voltage from 1500 V to 2000 V. Figure 2.5 shows the charge distribution for the single photoelectron signal in which a clear 1 p.e. peak can be seen. The transit time spread of the single photoelectron signal is about 2.2 nsec. The average dark noise rate at the 0.25 p.e.s threshold used in SK-I was about 3 kHz.

The magnetic field over 100 mG affects photoelectron trajectories in the PMT and makes the timing resolution worse, while geomagnetic field at the detector site is about 450 mG. To compensate for the magnetic field, 26 sets of horizontal and vertical Helmholtz coils are arranged around the tank. As the result, the magnetic field inside the detector is reduced to about 50 mG.

On November 12th, 2001 while refilling the SK tank after completing the maintenance work, one ID PMT on the bottom of the tank imploded, which triggered a cascade of implosions. About 60 % of the ID and OD PMTs were destroyed. To avoid a chain reaction of implosion, all of the inner PMTs are instrumented with acrylic covers from SK-II period. A clear 12 mm thick UV-transparent acrylic dome is put over the photo-cathode area of each PMT and the side of the PMT is protected by the Fiber-Reinforced-Plastic(FRP) shield with holes, which let water flow into the case freely as shown in Figure 2.6. The transparency of the acrylic cover for photons with normal incidence in water is more than 96 % above 350 nm of wavelength and the effect of the PMT case is small.

1,885 8-inch PMTs, Hamamatsu R1408, are used in the OD. The photocathode of the OD PMT is fitted with 60 cm × 60 cm × 1.3 cm wavelength shifter plate. The wavelength shifter increases the light collection efficiency by 60 %. The timing resolution at single photoelectron is degraded to about 15 nsec from 13 nsec with the plate. However, since the OD is used as a
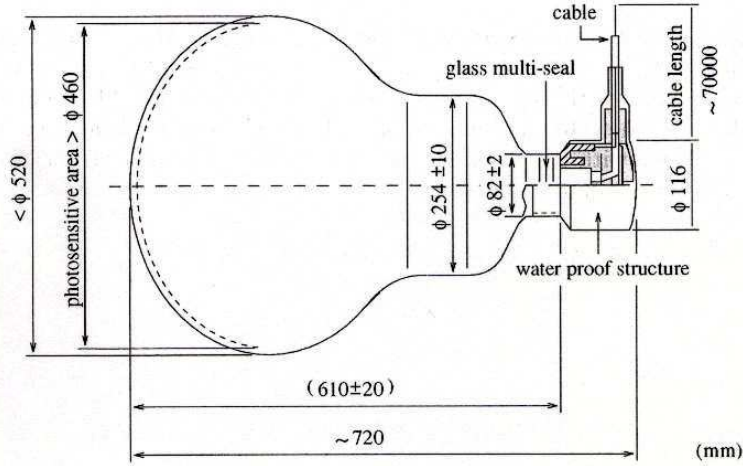
Figure 2.4: A schematic view of a 20-inch PMT.

| | |
|---|---|
| Shape | Hemispherical |
| Photocathode area | 50 cm diameter |
| Window material | Pyrex glass ($4 \sim 5\,\mathrm{mm}$) |
| Photocathode material | Bialkali (Sb-K-Cs) |
| Quantum efficiency | 22 % at $\lambda = 390\,\mathrm{nm}$ |
| Dynodes | 11 stage Venetian blind type |
| Gain | $10^7$ at $\sim 2000\,\mathrm{V}$ |
| Dark current | $200\,\mathrm{nA}$ at $10^7$ gain |
| Dark pulse rate | $3\,\mathrm{kHz}$ at $10^7$ gain |
| Cathode non-uniformity | $< 10\,\%$ |
| Anode non-uniformity | $< 40\,\%$ |
| Transit time | $90\,\mathrm{nsec}$ at $10^7$ gain |
| Transit time spread | $2.2\,\mathrm{nsec}$ ($1\,\sigma$) for 1 p.e. equivalent signals |
| Weight | $13\,\mathrm{kg}$ |
| Pressure tolerance | $6\,\mathrm{kg/cm^2}$ water proof |

Table 2.1: Specifications of 20-inch PMT.
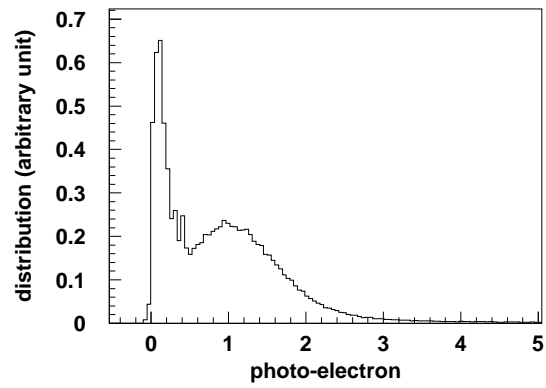
Figure 2.5: Single photoelectron distribution of a typical 20-inch PMT.



Figure 2.6: PMT case attached to the inner PMT in SK-II period and later
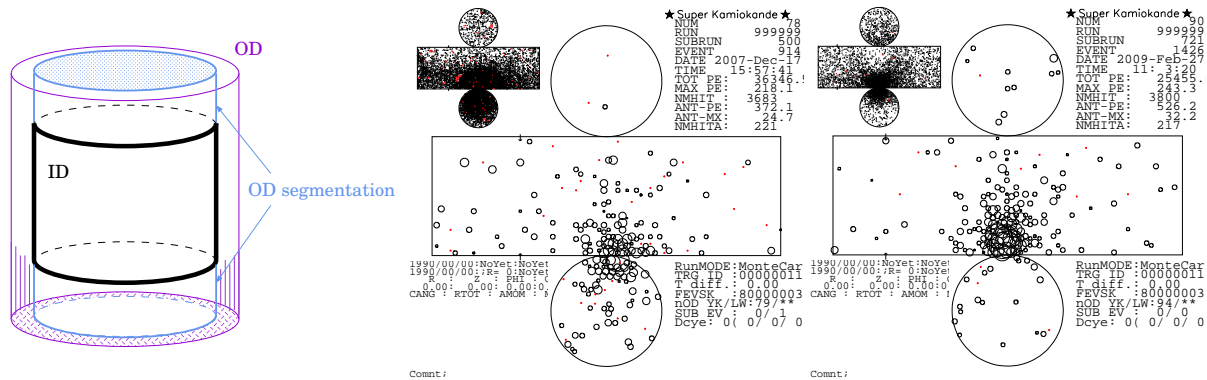
Figure 2.7: A schematic view of the OD segmentation (left). OD regions are separated by tyvec sheet. The OD visual displays of the partially contained event are shown for SK-II (middle), without segmentation, and SK-III (right), with segmentation.

veto counter, rather than a particle tracker, the extra photons are of important while the poor timing resolution is of little consequence.

### 2.2.3  OD segmentation

The separations between top/bottom and barrel region of OD part were installed with tyvek sheet in SK-III period. A schematic view of the segmentation is shown in Figure 2.7. This OD segmentation aims to distinguish the particles (mostly muons) as produced in the tank and going out around the edge of the tank from the corner clipping cosmic ray muons, since the former typically generates the signal in only one of the OD regions (top, side or bottom) while the later typically generates the signal in two OD regions.

The right two panels in Figure 2.7 show examples of the OD visual display for the simulated particle which produces in the tank and goes out around the bottom edge of the tank. The left display and the right display are in case of SK-II detector configuration (without OD segmentation) and SK-III detector configuration (with OD segmentation), respectively. Due to the segmentation, OD signals for SK-III are seen in the side region of the detector and clearly separated from signals in the bottom region, while that for SK-II is not. This feature helps to identify the particle as a clipping muon or not. The OD segmentation is taken advantaged at the event selection process for partially contained events, will be described in Section 5.2.

## 2.3  Water Purification and Air Purification System

The water for the Super-Kamiokande experiment is produced from abundant spring water in the mine. The water in the tank is continuously circulated through the water purification system to keep the high attenuation length. It is also an important purpose of this system to remove the radioactive materials, especially radon (Rn), which is a background source for the solar neutrino observation in the MeV energy range. The water is constantly circulated through the purification system with flow rate of about 35 ton/hour.

It is also essential to have clean air in the detector and the experimental area to minimize the radon level in the detector water.
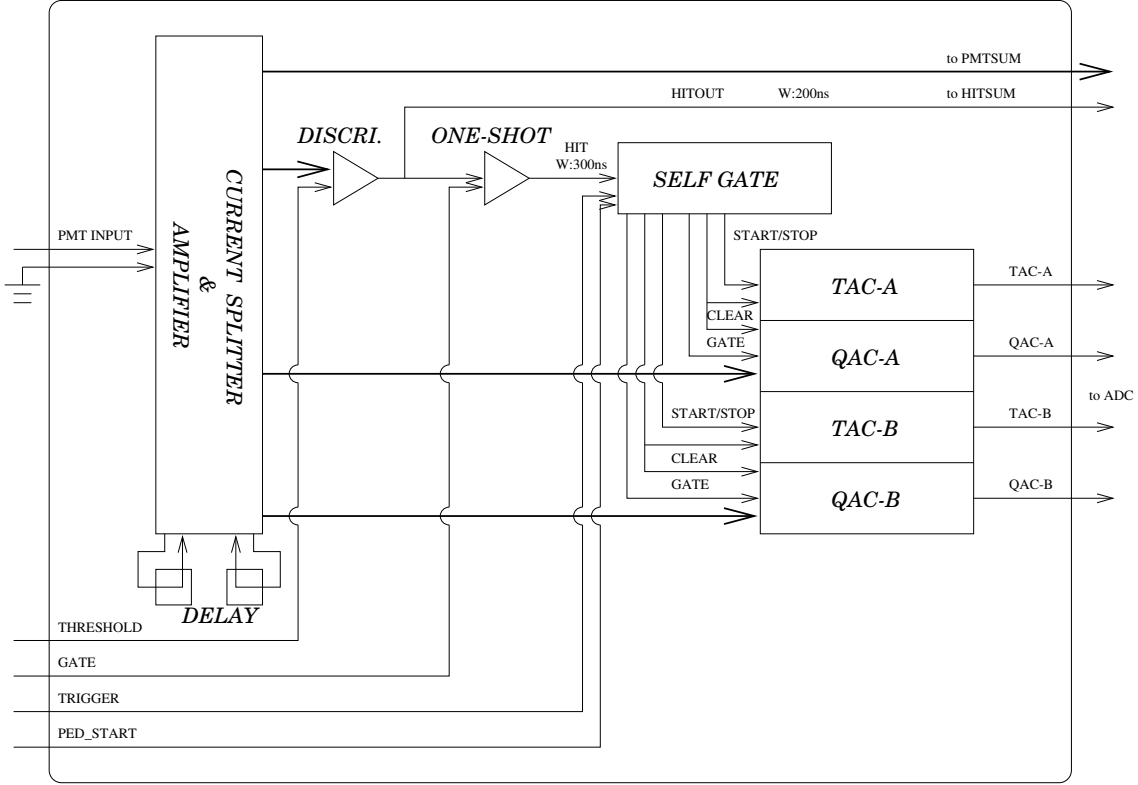
Figure 2.8: A block diagram of analog input part of ATM.

To keep the minimum radon level inside the detector, radon-free air is produced by the air purification system in the mine and is continuously pumped into the space above the water surface inside the tank at a positive pressure to prevent radon in the SK dorm air from entering the detector and dissolving into the purified water [43]. The radon concentration of the radon-free air is less than $3\,\mathrm{mBq/m^3}$. The air purification system consists of compressors, a buffer tank, driers, and the filters. The air flow rate is about $18\,\mathrm{m^3/hour}$.

## 2.4  Electronics and Data Acquisition System

ID PMT signals are processed by custom built electronics modules called ATM (Analog-Timing-Module) of the TKO standard (TRISTAN KEK Online) [44, 45]. The ATM module records the integrated charge and the arrival timing information of each PMT signal.

Figure 2.8 shows the block diagram of the analog input part of the ATM module. Each PMT input channel of ATM has two switching pairs of QAC (Charge to Analog Converter) and TAC (Time to Analog Converter) to minimize the electronics dead time in the data taking for two successive events, such as a muon followed by its decay electron. Each PMT signal sent to ATM is amplified 100 times, and then divided into four signals. One of them is sent to the discriminator. When the pulse height of the PMT signal exceeds the threshold level, which is set to 0.25 p.e.s , a 400 nsec gate signal for QAC and a start signal for TAC are generated. At

21

the same time, rectangular signal called HITSUM(200 ns width and 15 mV pulse hight) is sent to a global trigger module. Other two branches of the split PMT signal are fed to QAC. When a global trigger is issued, a stop signal is sent to TAC and the information in QAC and TAC is digitized by ADC. The digitized charge and timing information is stored in internal FIFO memory in ATM. when a global trigger is not issued within $1.3\,\mu$sec, all the information in QAC and TAC is cleared. ATM has 450 pC dynamic range with a resolution of 0.2 pC, and $1.3\,\mu$sec dynamic range with a resolution of 0.4 nsec. The remaining one signal becomes an output signal of ATM called PMTSUM. Figure 2.9 shows a schematic view of the ID data acquisition system. Signals from 12 PMTs are fed to an ATM board to be processed. There are in total 946 ATM boards installed in 48 TKO crates. The digitized data in ATM FIFO memory are sent to VME memory modules called SMP (Super Memory Partner) every 16 events. 48 SMP are installed in 8 VME crates, and one SMP module handles the data of 20 ATMs. The data in SMP memories are read out by 8 slave computers and sent to the online host computer.

Figure 2.10 shows a schematic view of the OD data acquisition system [46]. The paddle cards distribute high voltage from the main frame to the OD PMTs. A coaxial cable is used to supply the high voltage to an OD PMT and to send a signal from the PMT. These cards also pick off the PMT signals through a high voltage capacitor. Signals from the OD PMTs are sent to QTC (Charge to Time Converter) modules. A QTC module converts the PMT signal to a rectangular pulse whose width is proportional to the input charge. At the same time, a rectangular HITSUM signal is generated by QTC and sent to a global trigger module. The threshold of QTC modules is set to 0.25 p.e.. When a global trigger is received, the leading edge and the width of the rectangular pulse are converted to the timing and charge information by a LeCroy 1877 multi-hit TDC module. The dynamic range is set to $16\,\mu$sec which starts from $10\,\mu$sec before the global trigger timing.

## 2.4.1  Trigger

Figure 2.11 shows a overview of the ID trigger scheme. An ATM module generates a rectangular HITSUM signal with 15 mV in pulse height and 200 nsec in width if an ID PMT signal exceeds the threshold. These signals are analog-summed over all PMTs to generate an ID-HITSUM signal. The pulse height of the ID-HITSUM signal is proportional to the number of hit PMTs within 200 nsec time window. There are three types of trigger signals derived from the ID-HITSUM signal. In SK-I, the high energy (HE) trigger is generated when the pulse hight of ID-HITSUM signal exceeds a threshold of $-340$ mV, which corresponds to 31 hits within a 200 nsec time window. The threshold for the low energy (LE) trigger is set to $-320$ mV, which corresponds to 29 hits. This is equivalent to a signal expected from a 5.7 MeV electron assuming 50 % of trigger efficiency. The trigger rates for HE and LE triggers are $\sim 5$ Hz and $\sim 11$ Hz, respectively. The super low energy (SLE) trigger was implemented in May 1997 in order to lower the solar neutrino analysis threshold. The threshold level for the SLE trigger was lowered gradually with the increasing trigger CPU power. The threshold is set to $-186$ mV in July 2000, which is equivalent to 4.6 MeV electron. The trigger rate is $\sim 1$ kHz. In SK-II and SK-III, the same trigger scheme with the proper thresholds for each period are used. Trigger conditions in each period are summarized in Table 2.2.

The OD trigger is generated by a similar procedure. When an OD PMT signal exceeds a threshold, a QTC module generates a rectangular pulse with 20 mV in height and 200 nsec in width. These signals are also analog-summed to generate an OD-HITSUM signal. The threshold
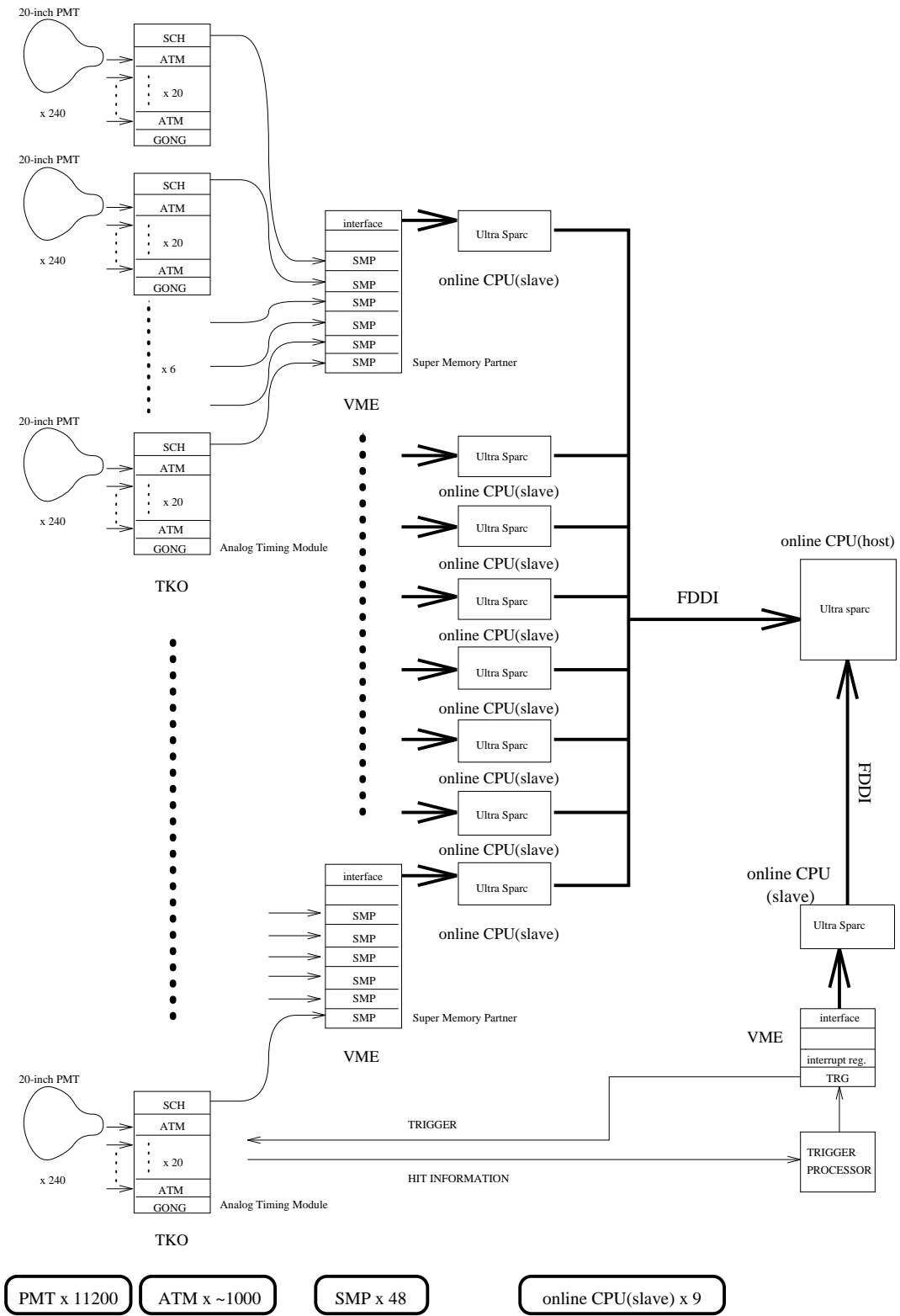
Figure 2.9: A schematic view of the inner detector data acquisition system.
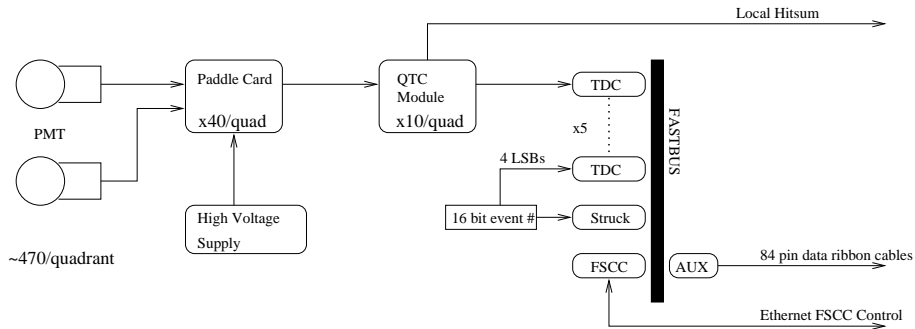
Figure 2.10: A schematic view of the outer detector data acquisition system.

|  | SK-I | SK-II | SK-III |
| --- | --- | --- | --- |
| period | Apr.1996 - Jul.2001 | Oct.2002 - Oct.2005 | Jun.2006 - Sep.2008 |
| number of ID PMTs | 11,146 | 5,182* | 11,129* |
| photocathod coverage | 40 % | 20 % | 40 % |
| HE trigger threshold | -340mV | -180mV | -320mV |
| LE trigger threshold | -320mV | -152mV | -302mV |
| SLE trigger threshold | -186mV | -110mV | -186mV |
| other features |  |  | OD segmentation |

Table 2.2: Summary of characteristic for each SK period. * All inner PMTs are instrumented with acrylic covers.

for the OD trigger is set to 19 hits within a 200 nsec time window.

These four types of trigger signals (HE, LE, SLE and OD) are fed to a hardware trigger module called TRG. The TRG module generates a global trigger signal when any one of the trigger signals is issued.

The specifications in each detector period are summarized in Table 2.2.
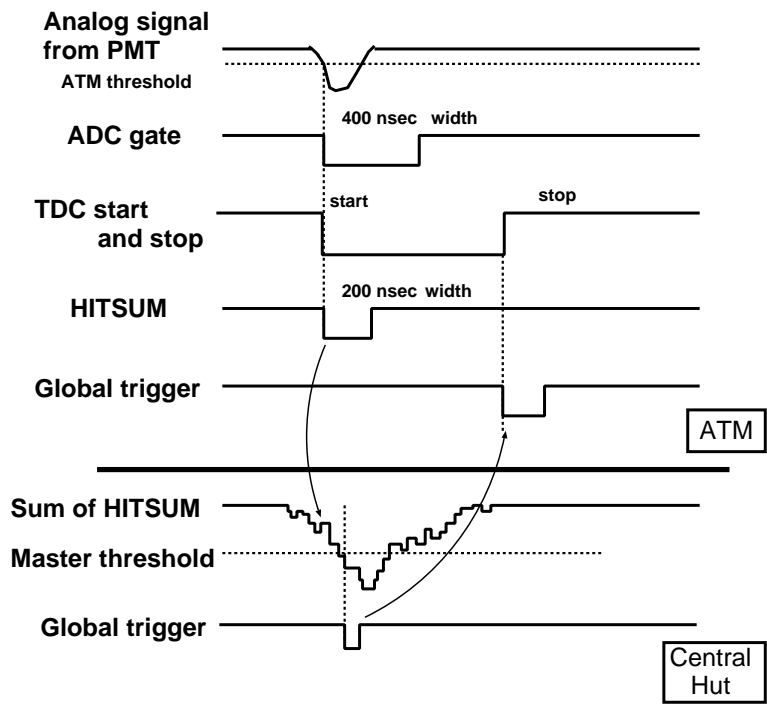
Figure 2.11: An overview of the ID trigger scheme.

# Chapter 3

# Simulation of Atmospheric Neutrino

## 3.1 Overview

Atmospheric neutrino events in Super-Kamiokande are simulated by a Monte Carlo method. Monte Carlo simulation is made of three constituents : neutrino flux, neutrino interactions and particle tracking in the detector. From products of neutrino flux and cross-sections, expected events observed in the detector are calculated during a certain period. The produced particles have the information such as their vertex, direction, momentum and so on. Using such vector information, the detector simulation simulates the particle, Cherenkov photon emission, the photon propagation and the response of detector hardware. In this way, the simulation events, which are the same structure as a real observed data, are constructed. It is often called Monte Carlo events in this thesis.

This chapter describes the neutrino flux model, NEUT library which is the simulator of kinematics of neutrino interaction and the detector simulation.

## 3.2 Atmospheric Neutrino Flux

Nowadays, there are several atmospheric neutrino flux models calculated by M. Honda *et al.* [47, 48, 22] (Honda flux), G. Battistoni *et al.* [49] (Fluka flux) and G. Barr *et al.* [50] (Bartol flux). In this analysis, the Honda flux is adopted as a default model, and the differences from the other two flux models are considered as systematic uncertainties in the flux calculation which will be discussed in Section 6.5.1. The Volkova flux [51] is adopted to simulate the event which has the energy above 10 TeV, because the Honda flux model supports the energy range up to 10 TeV.

The primary cosmic ray flux model which is an input of the neutrino flux calculation is determined by the experimental measurements. Current status of the measurements of cosmic ray proton flux is shown in Figure 3.1 together with the model used in the Honda flux calculation. The primary cosmic ray spectrum has been precisely measured by BESS and AMS experiments up to 100 GeV [52, 53]. The cosmic ray flux changes depending on the turbulence of the solar wind, which is higher when the solar activities are high (solar maximum) than when the solar activities are low (solar minimum). The difference of the cosmic ray flux at solar maximum and solar minimum is more than a factor of two for 1 GeV cosmic rays, while it decrease to $\sim 10\%$ for 10 GeV.
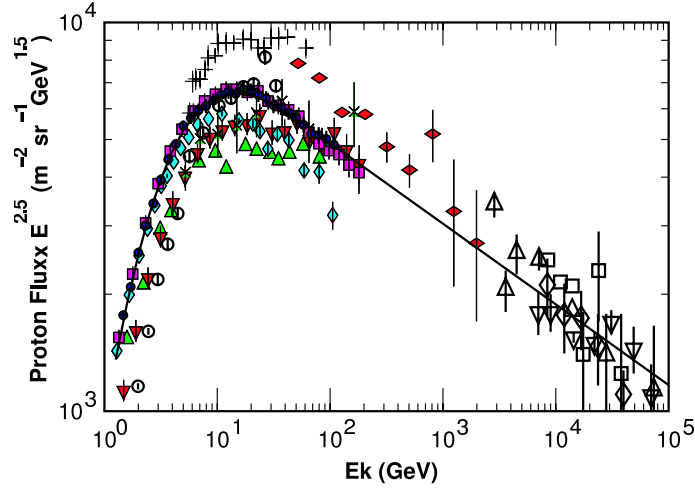
Figure 3.1: The primary cosmic ray proton flux for the model used in Honda flux calculation (line) and the observation results (points). The observation data are taken from Webber [54] (crosses), LEAP [55] (upward triangles), MASS1 [56] (open circles), CAPRICE [57] (vertical diamonds), IMAX [58] (downward triangles), BESS98 [52] (circles), AMS [53] (squares), Ryan [59] (horizontal diamonds), JACEE [60] (downward open triangles), Ivanenko [61] (upward open triangles), Kawamura [62] (open squares) and Runjob [63] (open diamonds).
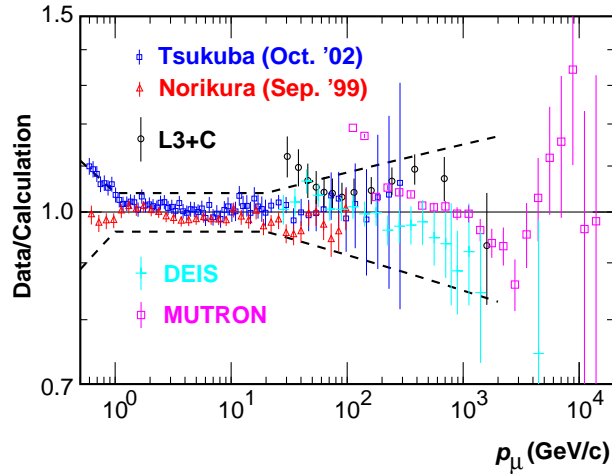


Figure 3.2: Secondary cosmic ray muon fluxes normalized by the calculation [70]. Data are observed at Tsukuba(open box) and Norikura(open triangle) with the BESS detector [71, 72], and at CERN(open circle) with the L3 detector [69]. For reference, DEIS [73] and MUTRON [74] are plotted. Dashed lines indicate the sum of errors in data and calculation. This figure is taken from [70].

In the atmosphere, primary cosmic ray protons and nuclei interact with air nuclei. Through the hadronic interactions, secondary particles, mostly pions and some kaons, are generated. In the Honda flux the US Standard Atmosphere model [64] is employed for the density structure of the atmosphere and the structure gives the zenith angle dependence of the atmospheric neutrinos. Geomagnetic filed effects are calculated based on the IGRF2005 model [65]. In the hadronic interactions of the cosmic rays with air nuclei, the two theoretical models, NUCRIN [66] simulation for the primary cosmic ray energies $< 5\,\mathrm{GeV}$ and DPMJET-III [67] for $> 5\,\mathrm{GeV}$ have been employed. Generated mesons decay into muons and neutrinos. The flux of this cosmic ray muons have been measured by several experiments such as BESS [68] and L3+C [69]. DPMJET-III employed in the Honda flux is modified based on the measurements by BESS and L3+C. Figure 3.2 shows the ratio of cosmic ray muon spectrum after the modification, and results in the hadronic interaction model agreeing with the measurement within $\lesssim 10\%$ in the $1\sim100\,\mathrm{GeV}$ muon energy range.

In the calculation of neutrino flux, interactions and propagation of particles are treated in a 3-dimensional way, considering the curvature of charged particles in geomagnetic field. The features of the 3-dimensional calculation comparing to the 1-dimensional one are an enhancement of neutrino flux for near-horizontal direction and lower production height of neutrinos in the atmosphere which is also prominent for near-horizontal direction. The first feature is explained by a difference of the effective area, generates horizontally incoming neutrinos, between 3-dimensional and 1-dimensional ways as illustrated in Figure 3.3. This effect is important for low energy neutrinos ($< 1\,\mathrm{GeV}$), in which transverse momentum of the secondary particles in hadronic interactions and the bending of muons in the geomagnetic field are considerable. Figure 3.4 shows the calculated zenith angle distributions of the neutrino flux for four different neutrino energy ranges and for the three models. The horizontal enhancement in the left panel is mostly due to the 3-dimensional effect described in Figure 3.3, while the enhancement in the higher energy regions is mostly due to muons reaching to the ground before decaying near vertical.

The calculated energy spectrum of atmospheric neutrinos at the Super-Kamiokande site are shown in Figure 3.5 for the Honda flux, Fluka flux and Bartol flux, in which the flux of $\nu_e + \overline{\nu}_e$ to $\nu_\mu + \overline{\nu}_\mu$ is averaged over all of the direction. The flavor ratio is about 2 in the energy region up to a few GeV, and it becomes larger than 2 as the neutrino energy increases because more cosmic ray muons reach the ground before decaying. The flavor ratio depends on the zenith angle of incoming neutrinos as shown in Figure 3.6.
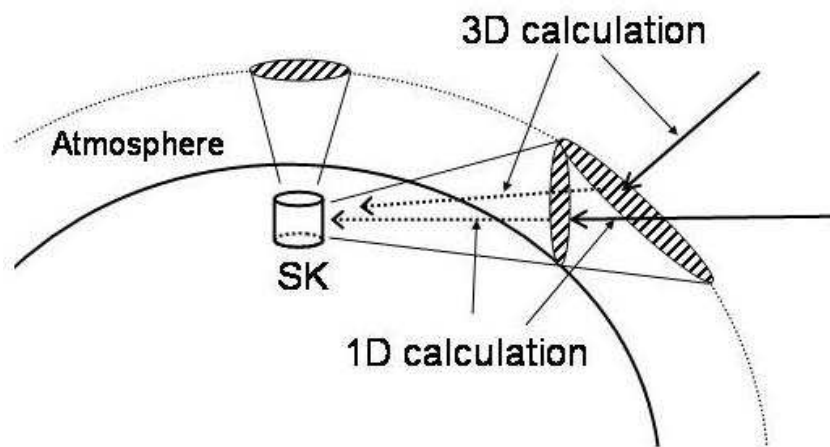
Figure 3.3: A schematic view of the effective areas of primary cosmic rays interacting with air nuclei for 1-dimensional and 3-dimensional calculations. Arrows written by solid lines show the primary cosmic rays and dotted lines show the neutrinos. The 3-dimensional calculation gives larger areas for near-horizontal direction.
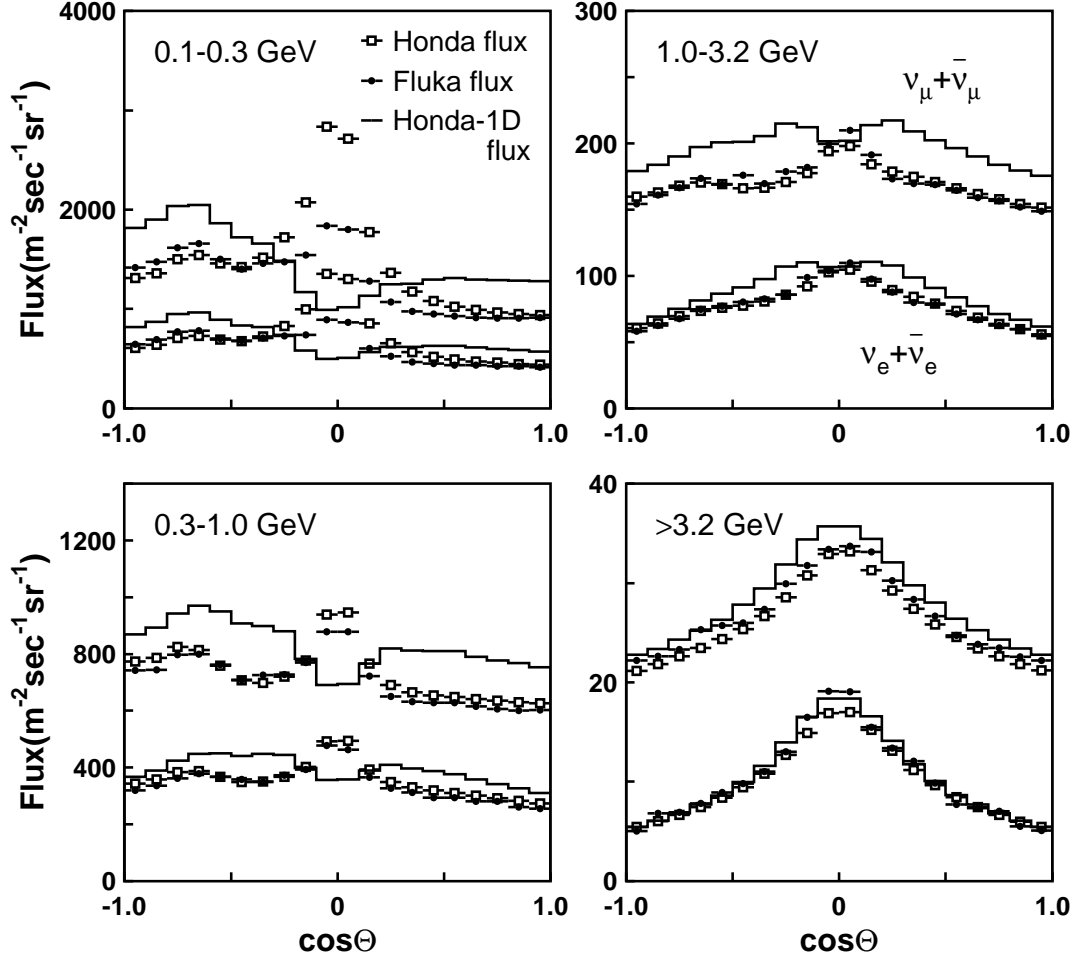
Figure 3.4: Zenith angle dependence of the atmospheric neutrino flux for four energy regions. Boxes show the Honda flux, dots show the Fluka flux and solid lines show the Honda-1D flux. The higher and lower plots in each panel show for $\nu_\mu + \overline{\nu}_\mu$ and $\nu_e + \overline{\nu}_e$, respectively. An enhancement of the neutrino flux is seen for near-horizontal directions at energies below 1 GeV in 3-dimensional calculations of the Honda flux and the Fluka flux, while no enhancement is seen in the Honda-1D flux.
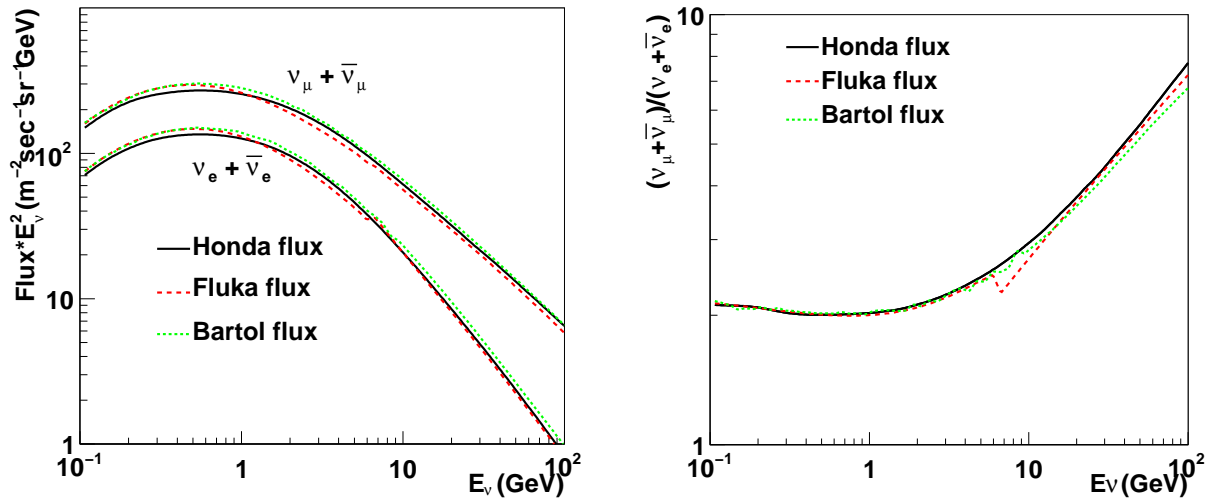
Figure 3.5: Predictions of the direction averaged atmospheric neutrino flux (Left) and the flavor ratio (Right). Solid curves show the Honda flux, dashed curves show the Fluka flux and dotted curves show the Bartol flux.
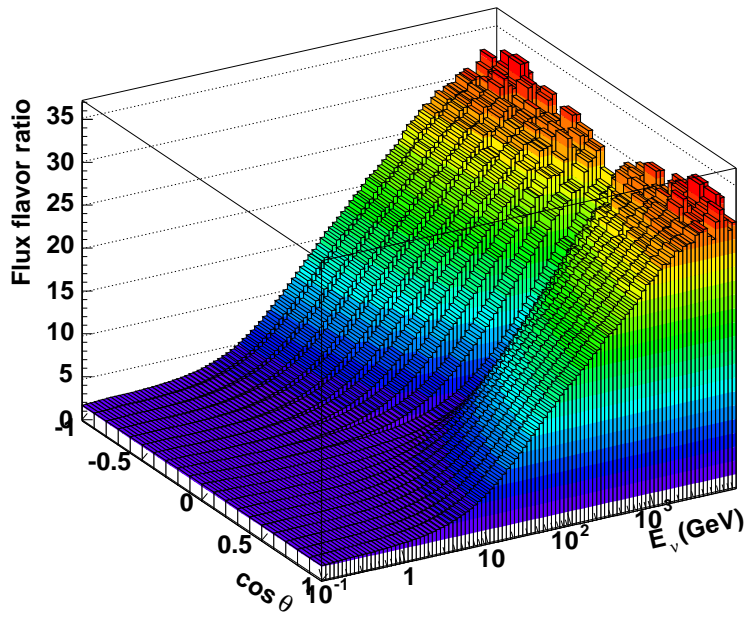


Figure 3.6: Flavor ratio $(\nu_\mu + \overline{\nu}_\mu)/(\nu_e + \overline{\nu}_e)$ as a function of neutrino energy and zenith angle. Calculation is based on the Honda flux.

## 3.3    Neutrino Interaction

Atmospheric neutrinos interact with nucleons and electrons in water or the rock around the detector. In the Monte Carlo simulation for this atmospheric neutrino analysis, the neutrino events are generated through the simulation of the neutrino interaction with the nuclei of water and the rock. The generation volumes are inside the ID detector, the region of OD detector and the rock around the Super-Kamiokande which are assumed to spread spherically up to 4km from the detector to cover all observable events.

For the simulation of neutrino interaction, a simulation program library NEUT [76, 77] is used. In the NEUT simulator, the following charged current (CC) and neutral current (NC) interactions are considered :

CC/NC (quasi-)elastic scattering     $\nu + N \to l + N'$

CC/NC single meson production     $\nu + N \to l + N' + meson$

CC/NC deep inelastic interaction     $\nu + N \to l + N' + hadrons$

CC/NC coherent pion production     $\nu + {}^{16}O \to l + {}^{16}O + \pi$

where $N$ and $N'$ are nucleons (proton or neutron) and $l$ is a lepton. Those interactions are explained briefly in the following sections.

### 3.3.1    Elastic and Quasi-Elastic Scattering

The charged quasi-elastic scattering for free protons (i.e. hydrogen atom) is, treated in this simulator, described by Llewellyn-Smith [78]. For the free nucleon, The differential cross section is :

$$\frac{d\sigma^{\bar{\nu}}}{dq^2} = \frac{M^2 G_F^2 \cos^2 \theta_c}{8\pi E_\nu^2} \left[ A(q^2) + B(q^2)\frac{s-u}{M^2} + C(q^2)\frac{(s-u)^2}{M^4} \right] \tag{3.1}$$

where $E_\nu$ is the neutrino energy, and $s$ and $u$ are Mandelstam variables [78]. The factors $A$, $B$ and $C$ are given as :

$$
\begin{aligned}
A(q^2) &= \frac{m^2 - q^2}{4M^2}\left[\left(4 - \frac{q^2}{M^2}\right)|F_A|^2 - \left(4 + \frac{q^2}{M^2}\right)|F_V^1|^2 \right. \\
&\quad - \frac{q^2}{M^2}|\xi F_V^2|^2\left(1 + \frac{q^2}{4M^2}\right) - \frac{4q^2 F_V^1 \xi F_V^2}{M^2} \\
&\quad \left. - \frac{m^2}{M^2}\left((F_V^1 + \xi F_V^2)^2 + |F_A|^2\right)\right] \tag{3.2} \\
B(q^2) &= \frac{q^2}{M^2}\left(F_A(F_V^1 + \xi F_V^2)\right) \tag{3.3} \\
C(q^2) &= \frac{1}{4}\left(|F_A|^2 + |F_V^1|^2 - \frac{q^2}{4M^2}|\xi F_V^2|^2\right) \tag{3.4}
\end{aligned}
$$

where $m$ is the lepton mass, $\xi$ is defined by means of anomalous magnetic moment $\mu_p - \mu_n = 3.71$. The vector form factors, $F_V^1(q^2)$ and $F_V^2(q^2)$, and axial vector form factor, $F_A(q^2)$ are determined

experimentally and given by :

$$F_V^1(q^2) \quad = \quad \left(1 - \frac{q^2}{4M^2}\right)^{-1} \left[G_E(q^2) - \frac{q^2}{4M^2}G_M(q^2)\right] \tag{3.5}$$

$$\xi F_V^2(q^2) \quad = \quad \left(1 - \frac{q^2}{4M^2}\right)^{-1} \left[G_E(q^2) - G_M(q^2)\right] \tag{3.6}$$

$$F_A(q^2) \quad = \quad -1.232 \left(1 - \frac{q^2}{M_A^2}\right)^{-2} \tag{3.7}$$

$$G_E(q^2) \quad = \quad (1+\xi)^{-1}G_M(q^2) = \left(1 - \frac{q^2}{M_V^2}\right)^{-2} \tag{3.8}$$

where $G_E$ and $G_M$ are the electric and magnetic form factor, $M_V$ and $M_A$ are the vector and axial vector masses.

For the scattering off bound nucleons in $^{16}$O, nuclear effects such as the Fermi motion of the nucleons or the Pauli exclusion principle are taken into account as described by the Smith and Moniz [82] model. Since nucleons are fermions, the outgoing momentum of the nucleons in the interactions is required to be larger than the Fermi surface momentum to allow quasi-elastic scattering to occur. In this simulator, the Fermi surface momentum is assumed to be 225 MeV/c.

Taking into account the experimental results from K2K and MiniBooNe [79, 80, 81], $M_V$ and $M_A$ are set to be 0.84 GeV and 1.21 GeV respectively in the NEUT simulation. Same $M_A$ value is also used for single-meson productions. $M_A$ value affects the cross-section because it is a function of $Q^2$ values. For larger $M_A$ values, interactions with higher $Q^2$ values (and therefore larger scattering angles) are enhanced. In this neutrino oscillation analysis, the uncertainty of $M_A$ value is considered (see Section 6.5.2) and it is estimated to be 10 % by the total uncertaintiy adopted to the K2K and MiniBooNE results.

Various theoretical models have been developed to account for nuclear effects in the neutrino interactions at intermediate energies besides the Smith and Moniz model, for example, Nieves *et al.* [83], and Nakamura *et al.* [84] and so on. These models are used for estimation the systematic uncertainties of the neutrino interaction and nuclear effects (see Section 6.5.2).

Figure 3.7 shows the cross section of the quasi-elastic scattering for the experimental data and the calculation from the NEUT.

The cross sections for neutral current elastic scatterings are estimated from the following relations [85, 86] :

$$\sigma(\nu p \to \nu p) \quad = \quad 0.153 \times \sigma(\nu n \to e^- p) \tag{3.9}$$

$$\sigma(\bar{\nu} p \to \bar{\nu} p) \quad = \quad 0.218 \times \sigma(\bar{\nu} p \to e^+ n) \tag{3.10}$$

$$\sigma(\nu n \to \nu n) \quad = \quad 1.5 \times \sigma(\nu p \to \nu p) \tag{3.11}$$

$$\sigma(\bar{\nu} n \to \bar{\nu} n) \quad = \quad 1.0 \times \sigma(\bar{\nu} p \to \bar{\nu} p). \tag{3.12}$$

### 3.3.2 Single Meson Production

Rein and Sehgal's model [93] is used to simulate the resonance production of single $\pi$, $\eta$ and $K$ productions. This method assumes one meson is generated by the decay of the intermediate
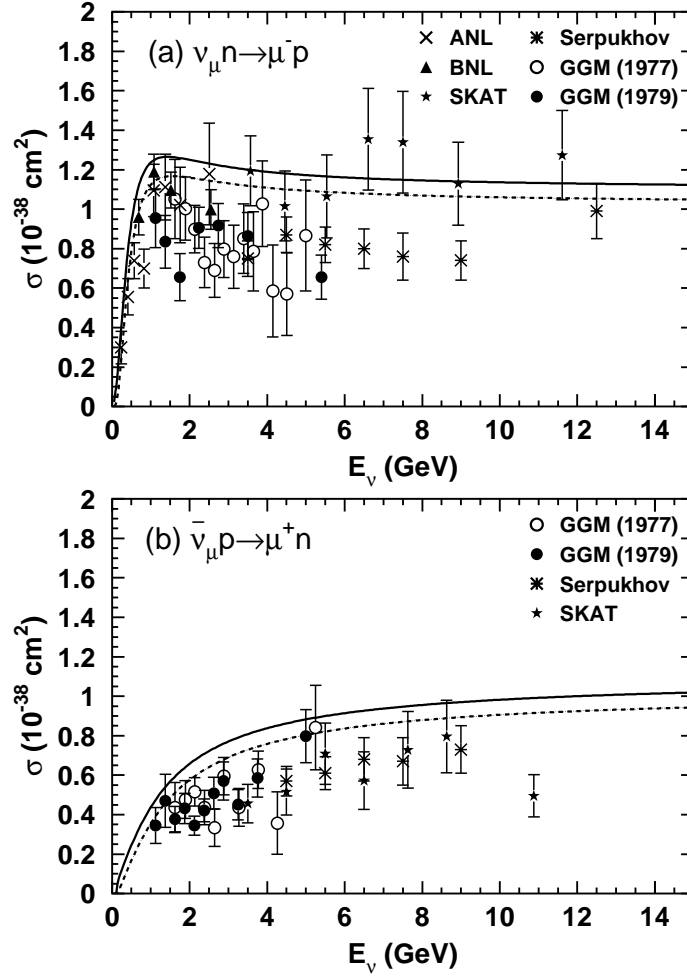
Figure 3.7: Charged current quasi-elastic interaction cross sections of (a) $\nu_\mu$ and (b) $\overline{\nu}_\mu$ with the experimental data from ANL [87], Gargamelle [88, 89], BNL [90], Serpukhov [91] and SKAT [92]. The solid line indicates for the scattering off a free proton. The dashed line indicates for the scattering off bound nucleons in $^{16}$O.
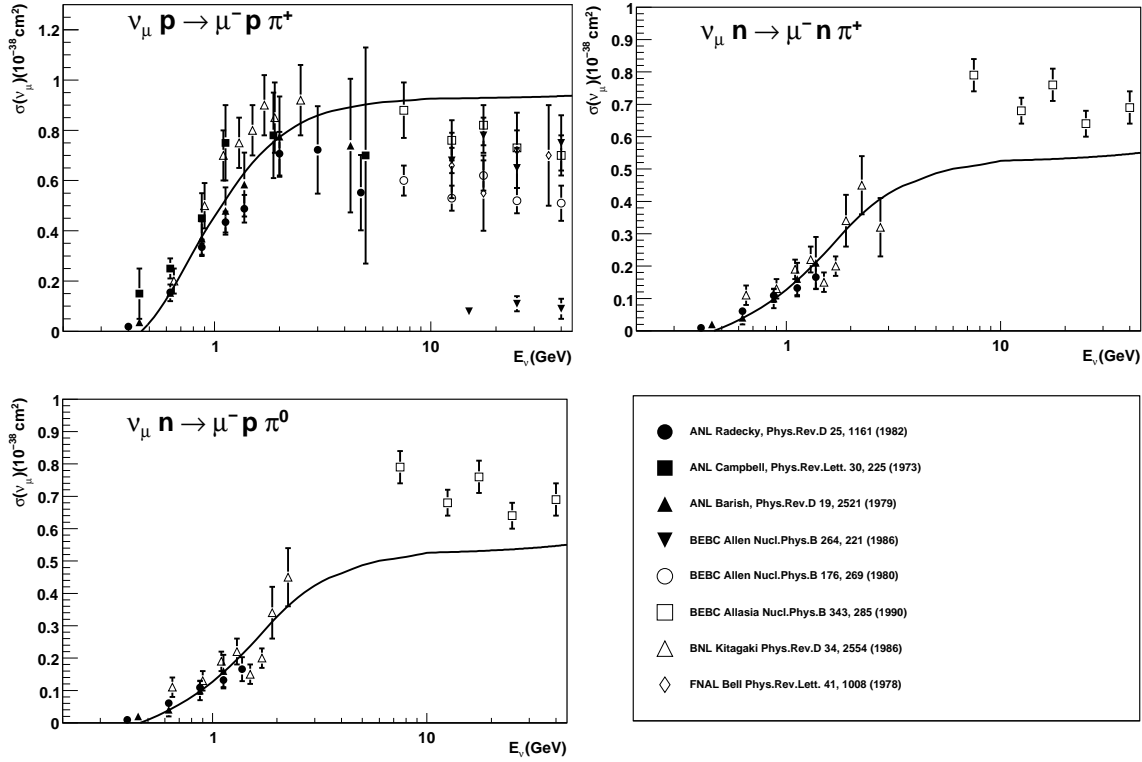
Figure 3.8: Cross sections for $\nu_\mu$ charged current single pion productions. Solid lines are the NEUT calculations. Points show the experimental data as shown in the bottom right panel.

resonances :

$$\nu + N \to l + N^* \quad \text{(resonance production)}$$
$$N^* \to N' + \text{meson} \quad \text{(resonance decay)}$$

(3.13)

where $N$ and $N'$ are nucleons and $N^*$ is a baryon resonance. In this simulator, the invariant mass $W$ of the intermediate baryon resonances is restricted less than $2\,\mathrm{GeV/c^2}$. For $W$ larger than $2\,\mathrm{GeV}$, the interactions are simulated as a part of deep inelastic scattering as described in the next section.

To determine the angular distribution of a pion in the final state, Rein's method [94] is used for the $P_{33}(1232)$ resonance. For the other resonances, the directional distribution of the generated pion is set to be isotropic in the resonance rest frame. The angular distribution of $\pi^+$ has been measured for $\nu_\mu\ p \to \mu^-\ p\ \pi^+$ [95] and the results agree well with the NEUT's prediction.

The Pauli exclusion principle in the decay of the baryon resonance is also considered by requiring the momentum of the nucleon to be greater than the Fermi surface momentum.

A baryon resonance in a nucleus is known to be absorbed without producing mesons occasionally [96]. The NEUT simulation considers such phenomena, and 20% of the resonance events do not have the meson and only the lepton and nucleon are generated.

Figures 3.8, 3.9 and 3.10 show the cross sections of single meson production for the charged current $\nu_\mu$, the charged current $\bar{\nu}_\mu$, and neutral current, respectively, for the calculations from the NEUT and the experimental data.

35
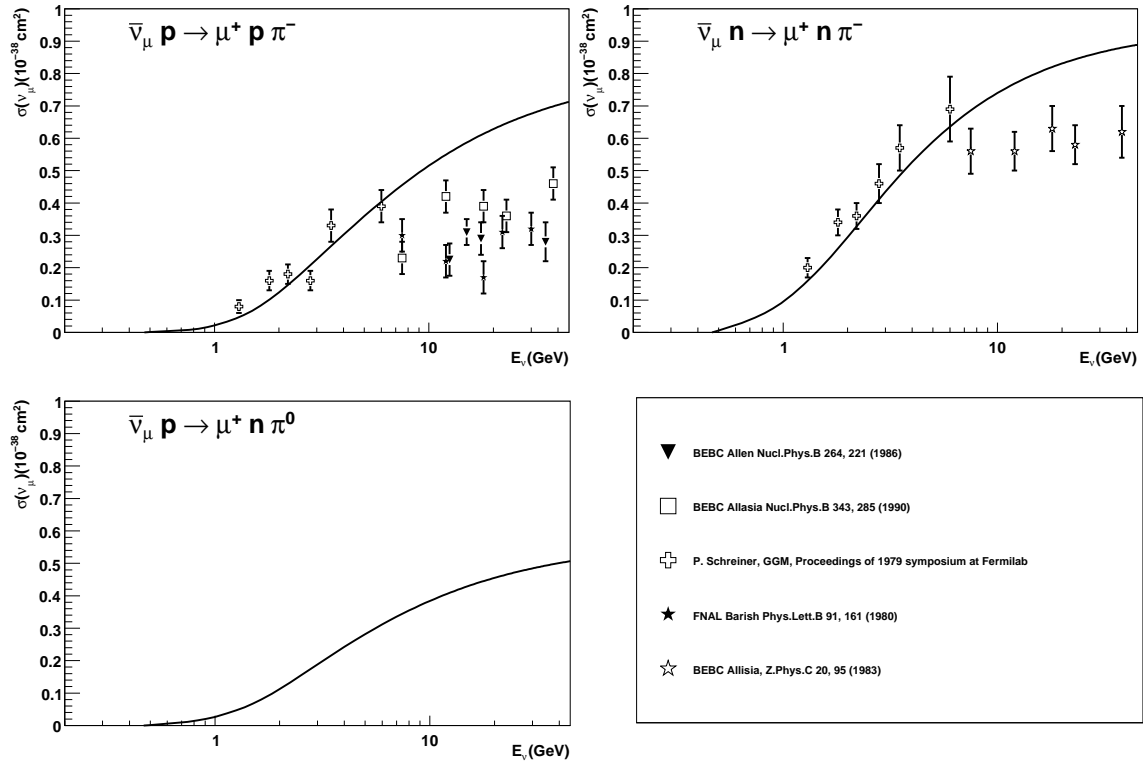
Figure 3.9: Cross sections for $\overline{\nu}_\mu$ charged current single pion productions. Solid lines are the NEUT calculations. Points show the experimental data as shown in the bottom right panel.
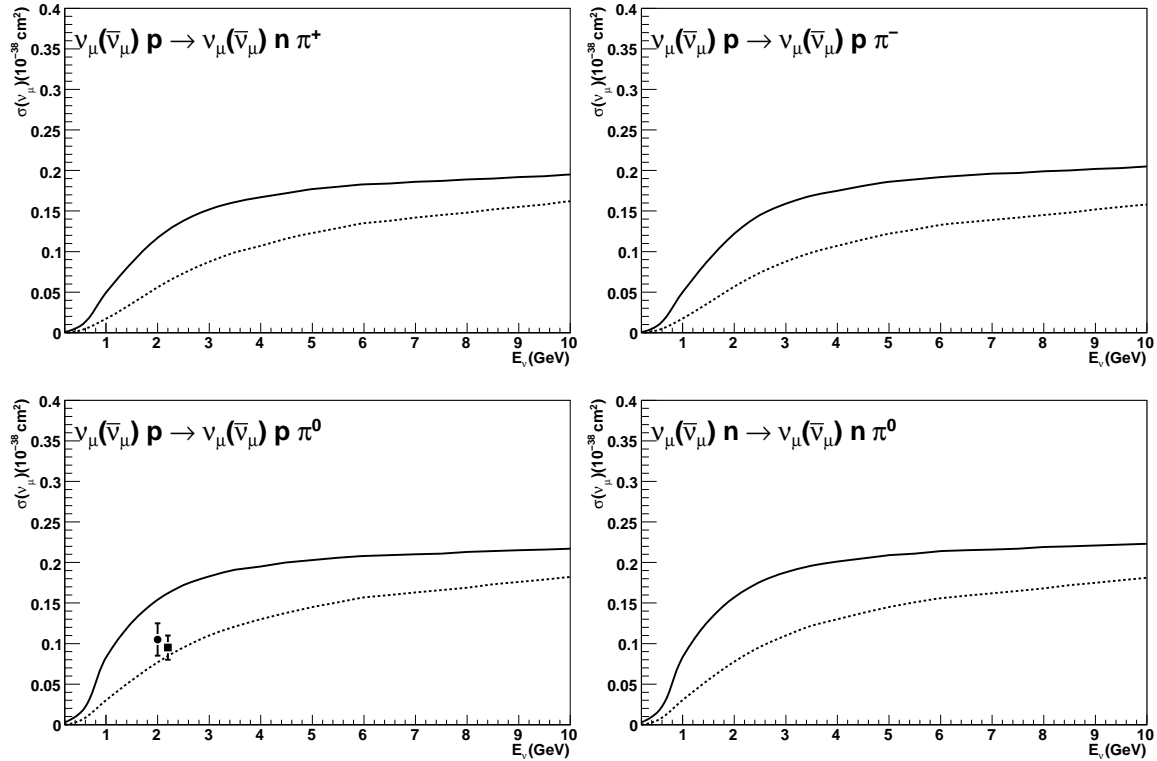
Figure 3.10: Cross sections for neutral current single pion productions. Solid (dashed) lines are the NEUT calculations for $\nu_\mu$ $(\overline{\nu}_\mu)$. Points show the experimental data taken from [97] (dot) and [98] (box).

### 3.3.3 Deep Inelastic Scattering

The cross section of charged current deep inelastic scattering is calculated by [138] in the range of the invariant mass $W > 1.3\,\mathrm{GeV}/c^2$ :

$$\frac{d^2\sigma^{\nu,\bar{\nu}}}{dxdy} = \frac{G_F^2 M_N E_\nu}{\pi}\left((1 - y + \frac{y^2}{2} + C_1)F_2(x, q^2) \pm y(1 - \frac{y}{2} + C_2)xF_3(x, q^2)\right)$$

$$C_1 = \frac{yM_l^2}{4M_N E_\nu x} - \frac{xyM_N}{2E_\nu} - \frac{m_l^2}{4E_\nu^2} - \frac{m_l^2}{2M_N E_\nu x}$$

$$C_2 = -\frac{m_l^2}{4M_N E_\nu x} \tag{3.14}$$

where $x = -q^2/(2M(E_\nu - E_l))$ and $y = (E_\nu - E_l)/E_\nu$ are Bjorken scaling parameters, $M_N$ is the nucleon mass, $m_l$ is the outgoing lepton mass, $E_\nu$ and $E_l$ are the energy of incoming neutrino and outgoing lepton in the laboratory frame, respectively. The nucleon structure functions $F_2$ and $xF_3$ are taken from the Parton distribution function(PDF) of GRV98 [99]. The correction function given by A. Bodek and U. K. Yang [100] are adopted to use the PDF in lower $Q^2$ region.

In the NEUT simulation, the cross section of deep inelastic scattering induced by the neutral current interactions are assumed to have the relations which are estimated from experimental results [101, 102].

Since the range of $W$,$1.3 < W < 2.0$ GeV/c$^2$, overlaps with that in single pion production, $n_\pi \geq 2$ is required in this $W$ region. So the kinematics of the hadronic system are simulated by two different methods for those two range of invariant mass. In the region of $1.3 < W < 2.0$ GeV/c$^2$, only pions are considered as outgoing mesons. The mean multiplicity of pions is estimated from the result of Fermilab 15-foot hydrogen bubble chamber experiment [103]. The number of pions in each event is determined by using the KNO (Koba-Nielsen-Olsen) scaling. The forward-backward asymmetry of pion multiplicity in the hadronic center of mass system is included using the results from BEBC experiment [104].

In the region of $W > 2.0\,\mathrm{GeV}/c^2$, the kinematics of the hadronic system are calculated by PHYTIA/JETSET [105]. This package treats not only $\pi$ but also $K, \eta, \rho$ and so on.

Cross section of the CC $\nu_\mu$ and $\overline{\nu}_\mu$ DIS interactions are shown in Figure 3.11.

### 3.3.4 Coherent Pion Production

The coherent pion production is a neutrino interaction with a oxygen nucleus, which remains intact, and one pion with the same charge as the incoming weak current is produced. Since very small momentum is transferred to the oxygen nucleus, the angular distributions of the outgoing leptons and pions are peaked in the forward direction. The Rein and Sehgal [106] model is adopted to simulate the interactions.

The measurement results by the K2K-SciBar detector set the upper limit of the cross section of CC coherent pion production [107]. This upper limit is significantly lower than the predicted cross section by the Rein and Sehgal model. Therefore the Rein and Sehgal [108], which is modified to take into account the non-vanishing lepton masses in CC interactions, is used in the NEUT simulator. In case of $\nu_\mu$, the cross section is suppressed about 25% at 1.3 GeV due to the interference of the axial vector and pseudoscalar (pion-exchange) amplitudes by this modification.
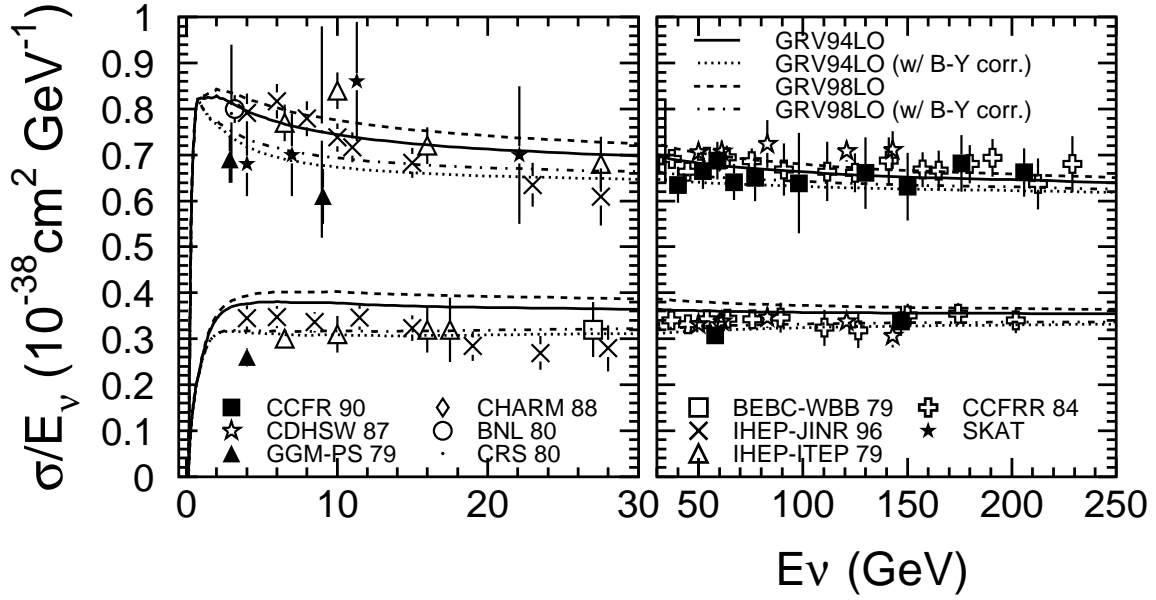
Figure 3.11: Cross sections for DIS charged current $\nu_\mu$ (upper lines and points) and $\overline{\nu}_\mu$ (lower lines and points) interactions. The NEUT treats GRV98 with Bodek-Yang correction as shown in the dashed-dotted lines. Each points indicate the experimental results as shown in the bottom on the figures.

### 3.3.5 Nuclear Effects

The secondary interactions of mesons and baryons or hadrons, produced in neutrino interactions, with nucleons inside the $^{16}$O nuclei is also simulated in the NEUT. All of the mesons produced within the $^{16}$O nuclei are tracked from their production points to their exiting points or points absorbed in the nuclei. This is simulated for $\pi$, $K$ and $\eta$ by using a cascade model.

Since the cross section of the pion production for neutrinos is large in $E_\nu > 1\,\mathrm{GeV}$ and the pion-nucleon interaction cross section is also large in this energy region, the interactions of pions are important. The NEUT considers several pion interactions in $^{16}$O nuclei: inelastic scattering, charge exchange and absorption. The initial pion production point in the nucleus, where neutrino-nucleon interactions occur, is determined by the Wood-Saxon density distribution [109]. The interaction mode of pions is determined by the calculated mean free path for each interaction, which is modeled by L. Salcedo *et al.* [110]. The mean free path of pions depends on their momentum and positions in the nucleus. In the calculation of pion inelastic scattering interaction, the Fermi motion of the nucleus and the Pauli exclusion principle are considered. If inelastic scattering or charge exchange occurs, the angular and momentum distributions of the outgoing pions are determined by using the results of a phase shift analysis from $\pi$ - $N$ scattering experiments [111].

The pion interaction simulation is compared with the experimental data for the following three interactions : $\pi$ - $^{12}$C scattering, $\pi$ -$^{16}$O scattering, and pion photo-production ($\gamma + ^{12}$C $\rightarrow \pi^- + X$) [112, 113]. Figure 3.12 is shown for the $\pi$ - $^{16}$C scattering.

For kaons interactions, the elastic scattering and charge exchange interactions are considered using the results from the cross sections measured by the $K^\pm$-$N$ scattering experiments [114,
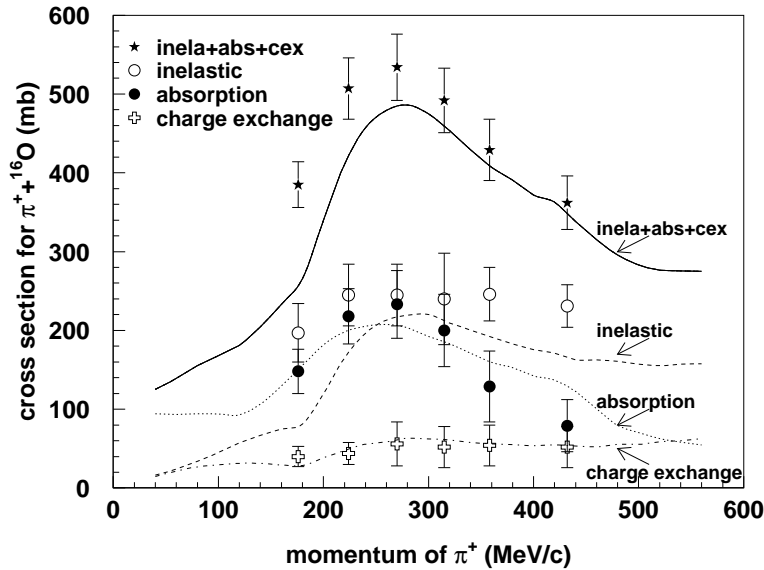
Figure 3.12: The cross sections of $\pi^+$-$^{16}$O scattering as a function of $\pi^+$ momentum. The lines are the cross sections calculated by the NEUT for each interaction mode, and the experimental data points are taking from [113].

115, 116]. For $\eta$ mesons interactions, the absorption $(\eta N \to N^* \to \pi(\pi)N)$ is considered [117].

In the NEUT simulation, the nucleon re-scattering inside the oxygen nucleus is also considered using the cascade model and the measurements by Bertini *et al.* [118]. The pion production caused by the decay of produced deltas is also taken into account as the isobar production model by Lindenbaum *et al.* [119].

## 3.4    Detector Simulation

The produced particles in neutrino interactions are incorporated in a detector simulation code, which simulates (1) the tracks of particles, (2) the generation and propagation of Cherenkov photons in water, and (3) the PMT response and the readout electronics.

### (1) Particle Tracking

The detector simulation has been developed based on the GEANT3 package [120]. Table 3.1 lists various processes which are considered in our simulation program. The hadronic interactions in water are simulated using the CALOR package [121]. This package is known to reproduce the pion interactions well including low energy region ($\sim 1 \, \text{GeV}/c$). For still lower energy region ($p_\pi \leq 500 \, \text{MeV}/c$), a custom program [122] based on experimental data from $\pi-^{16}$O scattering [123] and $\pi - p$ scattering [124] is used in our simulation code.

| $\gamma$ | $(e^+, e^-)$ pair production |
|---------|------------------------------|
|         | Compton scattering |
|         | Photoelectric effect |
| $e^\pm$ | Multiple scattering |
|         | Ionization and $\delta$-rays production |
|         | Bremsstrahlung |
|         | Annihilation of positron |
|         | Generation of Cherenkov radiation |
| $\mu^\pm$ | Decay in flight |
|         | Multiple scattering |
|         | Ionization and $\delta$-rays production |
|         | Bremsstrahlung |
|         | Direct $(e^+, e^-)$ pair production |
|         | Nuclear interaction |
|         | Generation of Cherenkov radiation |
| Hadrons | Decay in flight |
|         | Multiple scattering |
|         | Ionization and $\delta$-rays production |
|         | Hadronic interactions |
|         | Generation of Cherenkov radiation |

Table 3.1: List of the processes considered in simulator.

## (2) Cherenkov photon tracking in water

We take into account the dispersion of the refractive index. The group velocity

$$v_g = \frac{c}{n(\lambda) - \lambda \frac{\partial n(\lambda)}{\partial \lambda}} \qquad (3.15)$$

where $c$ is light velocity in vacuum, $\lambda$ is light wavelength, is used for the light velocity in the water. And the generated Cherenkov light is simulated to be scattered and absorbed in water. The water transparency as a function of wavelength is determined as follows: in case of short wavelength, we employed the relation $C \propto \lambda^{-4}$ where $C$ is the scattering coefficient and $\lambda$ is wavelength. In case of long wavelength, we use the data taken from [125]. The absolute water transparency is determined to be consistent with the direct measurement of the detector (Section 4.1.4).

## (3) Response of the PMT

Charge and timing response of PMTs is considered in the simulator. The detected charge value of each hit PMTs is simulated by the random number distributed as the measured one photon distribution as shown in Figure 2.5. And the timing distribution is dependent on that charge, so the relation between timing and charge is measured using the laser calibration (section 4.1.3). The timing of each PMT is a random variable distributed as Gaussian with one sigma as shown in Figure 4.5.

# Chapter 4

# Calibration

## 4.1 Detector Calibration

Understanding and keeping high quality of the detector performance is important for an accurate observation. There are several calibrations for detector charge and timing information in the Super-Kamiokande detector. Water transparency is also checked continuously in the detector.

### 4.1.1 Relative Gain Calibration

The high voltage value of each PMT is set to provide approximately uniform gain for all PMTs in the detector. The uniformity of the PMT gain is important to determine the momentum without systematic difference depending on its vertex position or direction.

Figure 4.1 shows a schematic view of the relative gain calibration system. Light generated by a Xe lamp is passed through an ultraviolet filter and neutral density filter and is injected into a scintillator ball. The diffused light from the scintillator ball is emitted uniformly. The other outputs from the Xe lamp are used to monitor the intensity of the Xe light and to make a calibration trigger.

The high voltage value of each PMT is adjusted to give the same gain with the others. The relative gain $G_i$ of the i-th PMT is obtained by :

$$G_i = \frac{Q_i}{Q_0 f(\theta)} \cdot l_i^2 \cdot \exp\left(\frac{l_i}{L}\right) \tag{4.1}$$

where $Q_i$ is the charge detected by the $i$-th PMT, $l_i$ is the distance from the light source to the PMT, $f(\theta)$ is the PMT acceptance as a function of the photon incidence angle $\theta$, $L$ is the attenuation length of water and $Q_0$ is the normalization factor. This measurement is performed for several positions of the scintillator ball, changing the voltage. After adjusting high voltage values, the relative gain spread is about $7\%$ for SK-I as shown in Figure 4.2. For SK-II and III, the relative gain calibration method is improved by using standard PMTs whose gain are adjusted within few $\%$ for each other in advance. Since the position dependence of the light intensity from the Xe lamp can be reduced by the standard PMTs, the relative gain uncertainty can be adjusted to $2\%$ for SK-II and III.
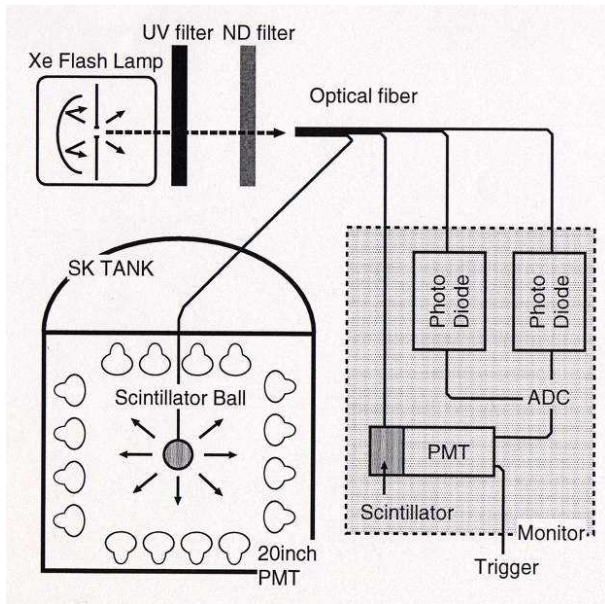
Figure 4.1: A schematic view of the relative gain measurement system using a Xe lamp.
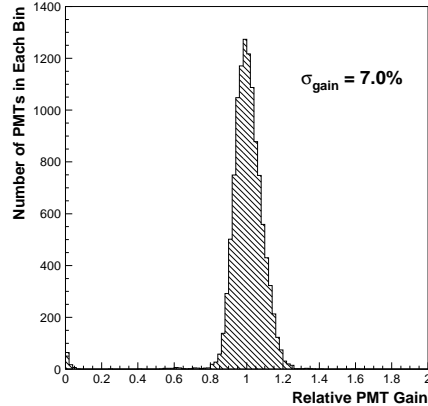


Figure 4.2: The relative gain distribution of all the ID PMTs, measured in 1996.

### 4.1.2 Absolute Gain Calibration

The absolute gain calibration is necessary to convert the charge detected by each PMT in pico Coulomb (pC) into the number of photoelectrons. The absolute gain is determined using the charge distribution of single photoelectron signals.

The low energy $\gamma$-ray generated from neutron capture on Nickel nucleus is used as a calibration source to measure the single photoelectron distributions. The schematic view of the Nickel calibration source is shown in Figure 4.3. Neutrons produced by spontaneous fission of $^{252}$Cf are captured on surrounding Ni wires in polyethylene vessel, and low energy ($6 \sim 9\,$MeV) $\gamma$-rays are generated simultaneously. The number of hit PMT is about $50 \sim 80$ in total, so that the number of p.e. detected by each PMT is at most one. The charge distribution of a typical PMT is also shown in Figure 4.3. The sharp peak near zero is caused by electrons that are emitted from the photocathode but miss the first dynode, and the peak around $2\,$pC corresponds to that of single photoelectrons. The mean value of this 1 p.e. charge distribution is used as a constant to convert the PMT charge from pico Coulomb to the number of p.e.s.. The constants of $2.044\,$pC/p.e, $2.297\,$pC/p.e and $2.243\,$pC/p.e are used for SK-I, SK-II and SK-III, respectively.

### 4.1.3 Relative Timing Calibration

The relative timing calibration is important for the vertex position reconstruction. The timing response of the PMT depends on not only the length of the signal cable but also the detected charge because of the slewing effect of discriminator. The large signal tends to exceed the threshold earlier than the small one.

$N_2$ laser is used in this calibration. Figure 4.4 shows the schematic view of the relative

44
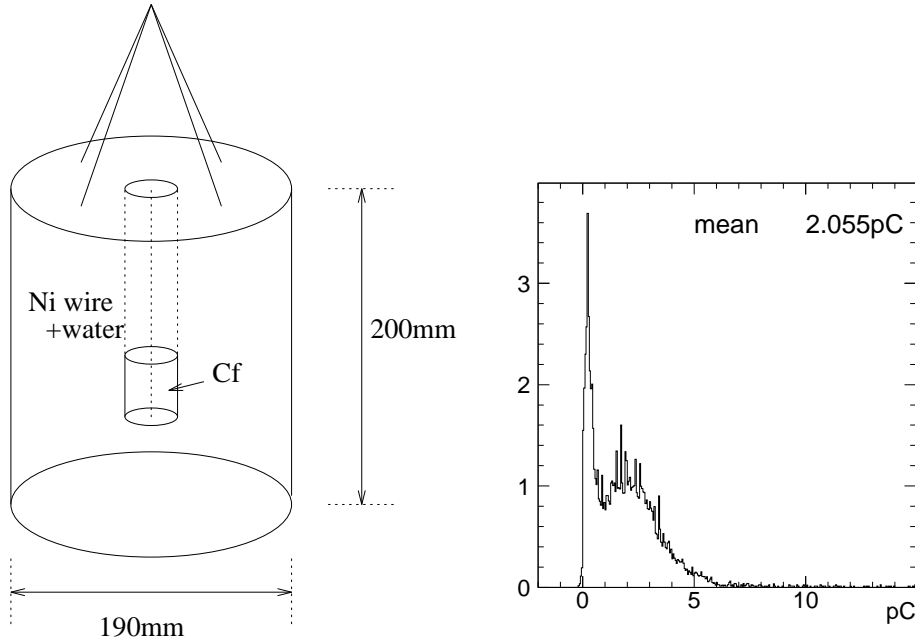
Figure 4.3: Schematic view of an Nickel calibration source (left) and charge distribution of a typical ID PMT (right).

timing calibration system. $N_2$ laser generator emits intense light with 337 nm wavelength within a time width of 0.4 nsec and this laser light is split into two. One of them is used to monitor the light intensity and make event trigger. The other is injected into a diffuser ball in the ID via an optical fiber. For injected light into the detector, the wavelength of the laser light is converted to 398 nm from 337 nm by a dye laser module, since this wavelength is most sensitive to PMTs. The PMT timing response is measured with various light intensity from 1 p.e. to a few hundreds of p.e. using an adjustable attenuation filter. The results are shown as a scatter plot of the timing and the charge called TQ-map in Figure 4.5. Each dot corresponds one measurement, and the open circles are the average timing with respect to charge for a PMT. The TQ-map is made for all ID PMTs and used to correct the timing information.

### 4.1.4 Light scattering measurement using a laser

The understanding a status of detector water transparency is important to determine the number of photons which arrive to PMTs through water in the detector. Water transparency represents the combined effect from absorption and scattering of the light intensity. So the light attenuation length in water can be described as $L = (\alpha_{abs} + \alpha_{scat.sym} + \alpha_{scat.asym})^{-1}$, where $\alpha_{abs}$, $\alpha_{scat.sym}$ and $\alpha_{scat.asym}$ are the absorption, symmetric scattering and asymmetric scattering coefficient respectively. These coefficients are separately measured using a $N_2$ laser. Figure 4.6 shows a schematic view of the measurement system. Each laser, wavelength of 337, 371(365 for SK-III), 400 and 420 nm, fires every 6 seconds during normal data taking. The light from the laser is injected into the ID via an optical fiber. There are several points of the light injection into the ID on the top, bottom and barrel of the tank. A typical event by the laser

45
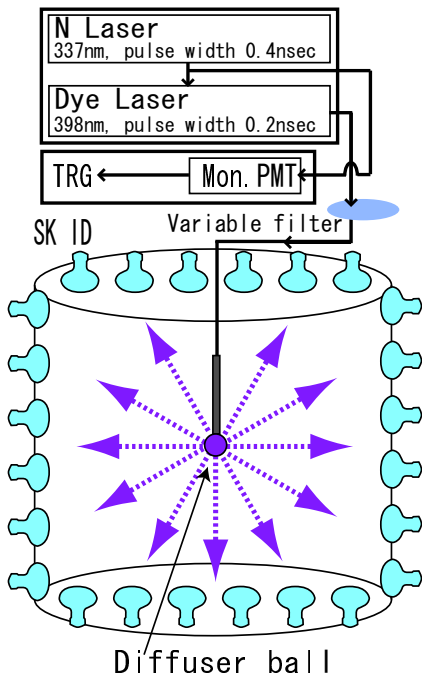
Figure 4.4: A schematic view of the timing measurement system using a laser.
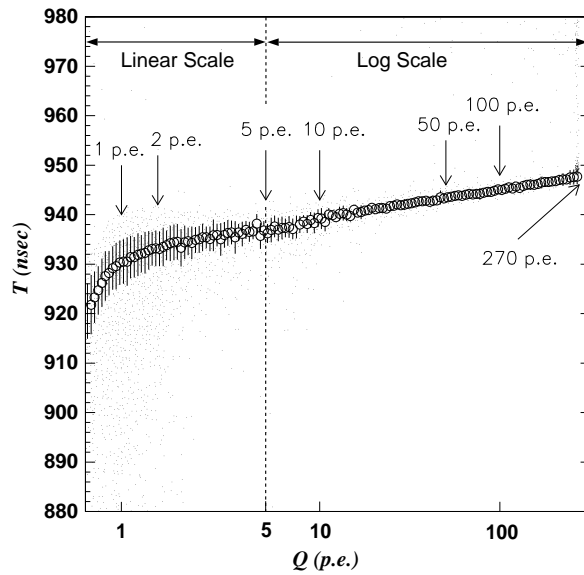


Figure 4.5: TQ-map, a measured two-dimensional plot of timing vs. charge distribution.
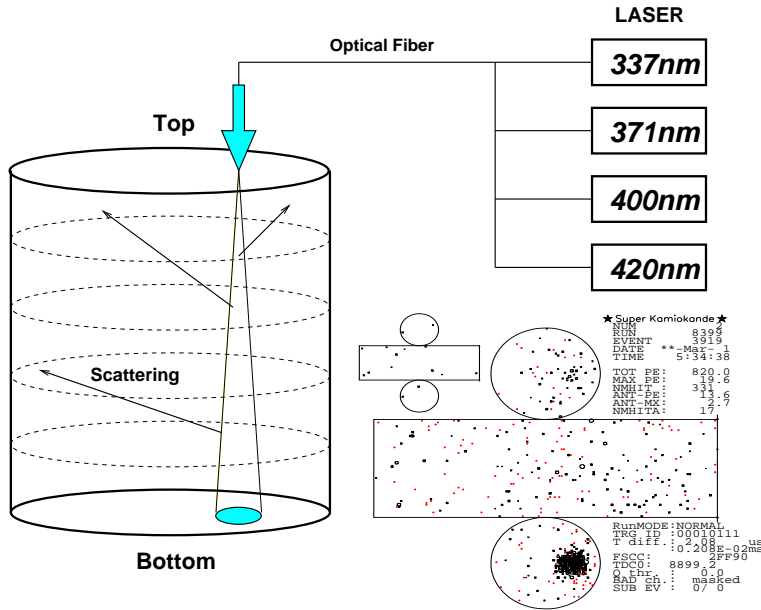
Figure 4.6: A schematic view of the scattering and absorption parameter measurement using laser systems, and a typical laser event.

light from the top is also shown in Figure 4.6. The PMT hits are clustered due to the direct (unscattered) photons.

In this calibration, the detector is separated into 6 regions, top and 5 in barrel, as shown in Figure 4.6. The total charge of hit bottom PMTs is used for the normalization of the light intensity. Figure 4.7 shows the PMT hit timing distributions in each region for data and Monte Carlo simulation. These PMT hits on the top and barrel wall are due to the photons scattered in water, or the photons reflected by surfaces of bottom PMTs or black sheets. The first peaks and slopes are characterized by the absorption and scattering coefficients and the second peaks around 1100 nsec are due to the photons reflected by the PMTs or black sheets. For the Monte Carlo simulation, the absorption and scattering coefficients are adjusted so that the PMT hit time distributions are in agreement with data. The attenuation length in water is calculated using the measured absorption and scattering coefficients.

The attenuation coefficients ($L^{-1}$) obtained by this method are plotted in Figure 4.8 with a star symbol. The lines shows a model used in the Monte Carlo simulation, which are determined by fitting the measurements from this method.

### 4.1.5 Water transparency measurement using cosmic ray muons

Water transparency is also measured by using Cherenkov light from cosmic ray muons passing through the detector. Since the energy deposit of such a energetic muon is almost constant (about $2\,\text{MeV/cm}$), cosmic ray muons can be used as a calibration source.

Only vertical downward muons are selected for this measurement. The muon track is reconstructed by connecting the entrance and the exit points in the ID. Under the assumption that the light detected by each PMT is not scattered, the detected charge (photoelectrons) is

47
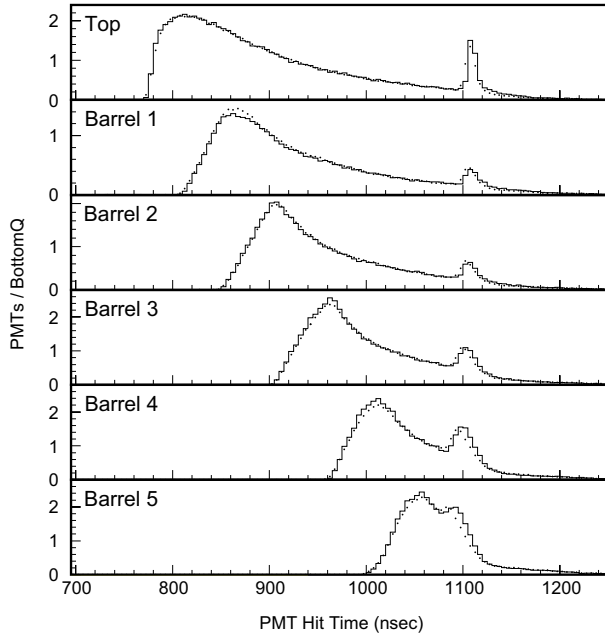
Figure 4.7: PMT hit time distributions of 337 nm-laser events in each detector region for the data (dots) and the Monte Carlo events which is tuned by the scattering and absorption parameters (histograms).
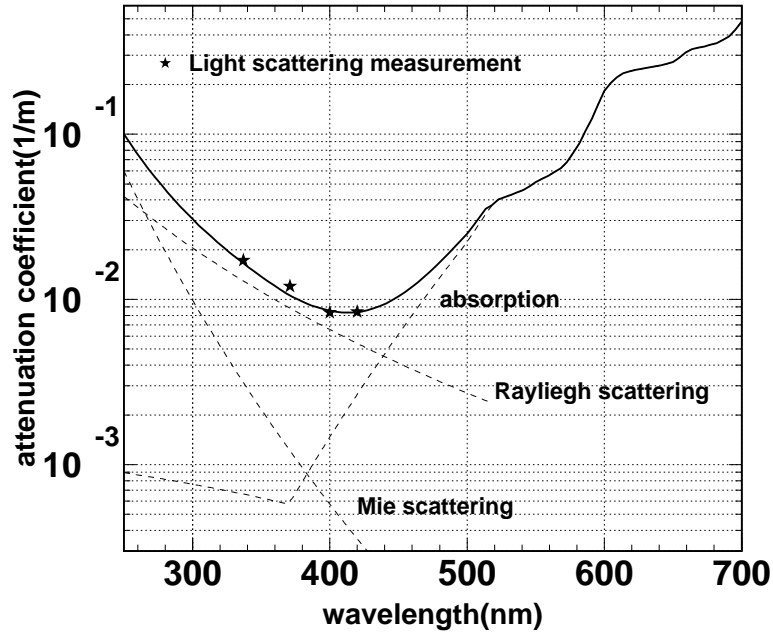


Figure 4.8: Wavelength dependence of attenuation coefficients ($L_{\mathrm{atten}}^{-1}$) obtained by the light scattering measurement (points) together with a model in the detector simulation.
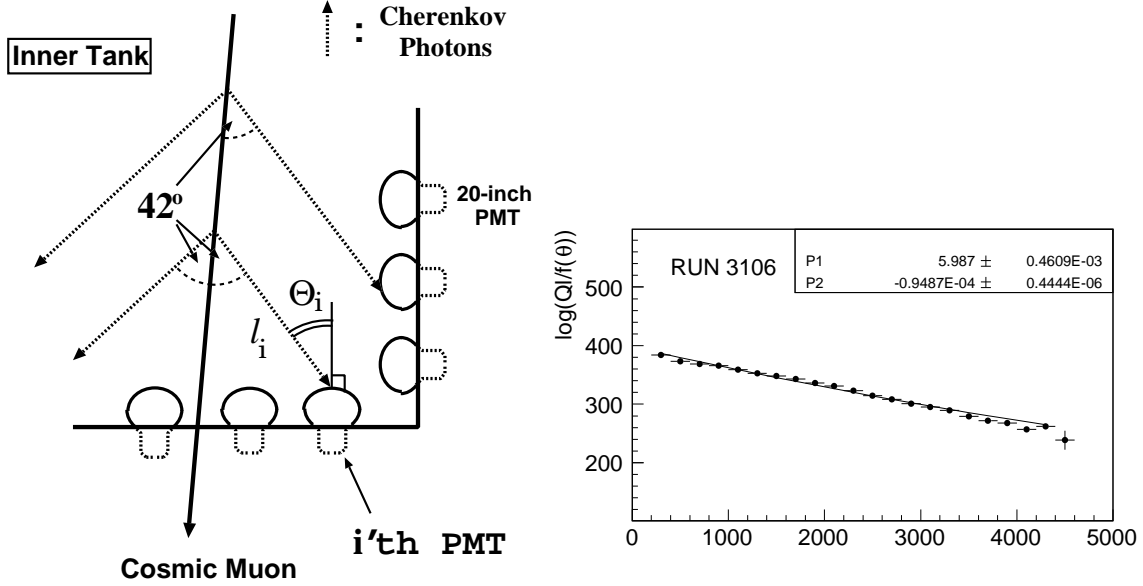
Figure 4.9: (Left) Schematic view of the attenuation length measurement using vertically pene-
trating cosmic ray muons. Arrows from muon track show the trajectories of Cherenkov photons
and $l_i$ shows the flight length of the Cherenkov photons detected by the $i$-th PMT. (Right)
Effective observed charge $(\log(Ql/f(\theta)))$ for through-going muons as a function of the photon
path length $(l)$ where $Q$ is the detected charge and $f(\theta)$ is the PMT acceptance.

expressed by :

$$Q = Q_0 \cdot \frac{f(\theta)}{l} \cdot \exp\left(-\frac{l}{L}\right) \tag{4.2}$$

where $Q_0$ is a constant, $f(\theta)$ is the PMT acceptance, $l$ is the photon path length and $L$ is the
attenuation length. The left panel on Figure 4.9 shows the schematic view of the measure-
ment. The right panel on Figure 4.9 shows $\log(Q \cdot l / f(\theta))$ as a function $l$ in a typical run. The
attenuation length is estimated to be 95 m for this data set.

Since the cosmic ray muons are measured during the normal data taking, continuous check
of the water transparency is possible. Figure 4.10 shows the time variation of the attenuation
length of water in entire period from SK-I to III. This time variation is reflected in the calculation
of a particle momentum (see Section 5.4.5).
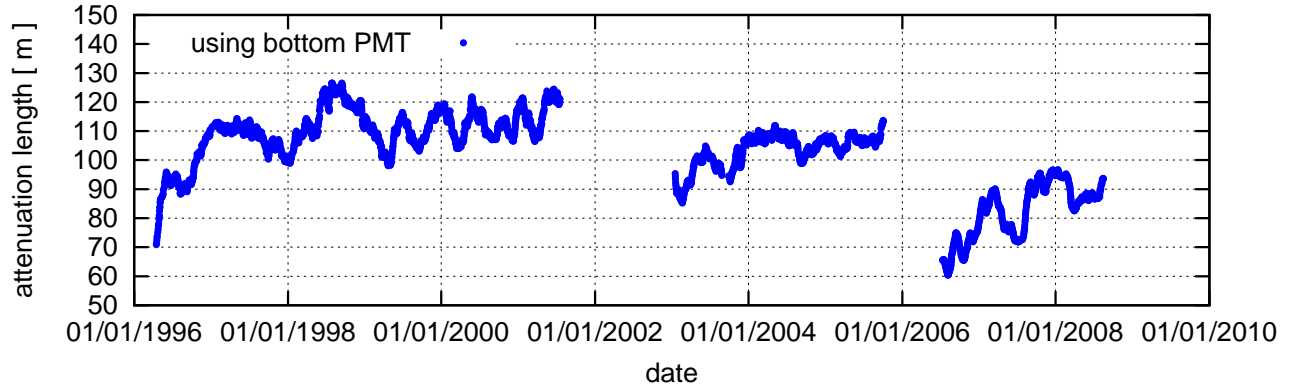
Figure 4.10: Time variation of water attenuation length.

## 4.2 Energy Calibration

The momentum of a particle is determined based on the charge information of PMTs (see Section 5.4.5). The accuracy of the energy scale is essential for the atmospheric neutrino analysis. For the energy scale calibration in momentum range from a few tens of MeV/c to about 10 GeV/c, four independent calibration sources are used:

- Track range of high energy stopping muon ($1 \sim 10$ GeV/c)

- Cherenkov angle of low energy stopping muon ($200 \sim 500$ MeV/c)

- Invariant mass of $\pi^0$'s produced by neutrino interactions ($\sim 130$ MeV/c)

- Momentum of decay electron ($\sim 50$ MeV/c)

The accuracy of the absolute energy scale is checked by comparing observed data with the prediction data from the Monte Carlo simulation for each calibration source. Including the time variation check of energy scale, the uncertainty on the energy scale is estimated (Section 4.2.6). The detector uniformity of energy scale is also checked (Section 4.2.7).

### 4.2.1 High energy stopping muons

The momentum for high energy muons can be determined by its track length which is approximately proportional to the momentum. The stopping cosmic ray muon track can be estimated by the distance from the entrance position into the detector to the vertex position of the subsequent decay electron. The resolutions for both stopping muon and decay electron vertexes are better than 50 cm. The selections for the stopping muon events are follows:

(1) The entrance point is on the top wall of the detector.

(2) The direction is downward ($\cos\theta > 0.94$).

(3) One decay electron event is detected.

(4) The reconstructed range of muon track L is $7 < L < 30$ m.

50

Criteria (1)(2) require the straight down-going muon event entered at the OD top of the detector. The left side panels in Figure 4.11 shows the averaged value of the ratio the momentum to track range (momentum/range) as a function of the track range. The momentum loss per cm is about $2.3\,\mathrm{MeV}/c$. The ratio MC to data of the averaged value of momentum/range is shown in the right side panels of Figure 4.11. They agree within $0.7\,\%$, $1.1\,\%$ and $2.0\,\%$ for SK-I, SK-II and SK-III, respectively.

### 4.2.2 Low energy stopping muons

The Cherenkov angle of charged particles is expressed as follows:

$$\cos\theta_C = \frac{1}{n\beta} = \frac{1}{n}\sqrt{1 + \frac{m^2}{p^2}} \tag{4.3}$$

where $\theta_C$, $n$, $\beta$, $m$ and $p$ are the Cherenkov angle, the refraction index of water, $v/c$, mass and momentum. The Cherenkov angle depends on momentum when the momentum is comparable to the mass. Thus, for low energy stopping muons ($< 400\,\mathrm{MeV/c}$), their momentum can be estimated by the Cherenkov angle based on above equation. The selections for low energy stopping muon events are follows:

(1) The entrance point is on the top wall of the detector.

(2) The direction is downward ($\cos\theta > 0.9$).

(3) One decay electron event is detected.

(4) The total number of p.e.s in the ID is less than $1500\,\mathrm{p.e.s}$ ($750\,\mathrm{p.e.s}$ for SK-II)

Criterion (4) selects low momentum muon event with momentum of $< 380\,\mathrm{MeV/c}$. The upper left panel on Figure 4.12 shows the reconstructed momentum $\mathrm{P}_{p.e.}$ distribution. The upper right panel shows the reconstructed opening angle $\theta_C$ distribution. The scattered plots of $\mathrm{P}_{p.e.}$ and opening angle $\theta_C$ is shown in the lower two panels for data and MC. The momentum dependence on the opening angle is seen in both figures. Figure 4.13 shows the averaged $\mathrm{P}_{p.e.}/\mathrm{P}_\theta$ ($\mathrm{P}_\theta$ is estimated momentum by $\theta_C$) and the ratio MC to data of it as a function of $\mathrm{P}_\theta$. They agree within $0.7\,\%$, $1.3\,\%$ and $2.1\,\%$ for SK-I, SK-II and SK-III, respectively.

### 4.2.3 Neutrino induced $\pi^0$ events

$\pi^0$ events are produced by the interactions of the atmospheric neutrinos in the detector. Since a $\pi^0$ decays immediately into two $\gamma$-rays, the invariant mass of $\pi^0$ can be calculated by using reconstructed momentum of two $\gamma$-rays, $P_{\gamma 1}$ and $P_{\gamma 2}$ as follows:

$$M_{\pi^0} = \sqrt{2P_{\gamma 1}P_{\gamma 2}(1 - \cos\theta)} \tag{4.4}$$

where $\theta$ is the opening angle between two $\gamma$-rays. The NC single $\pi^0$ events are selected from the atmospheric neutrino sample by the following criteria :

(1) Two Cherenkov rings are recognized and both of them are identified as electron-like.

(2) Electrons from muon decay is not detected.

51
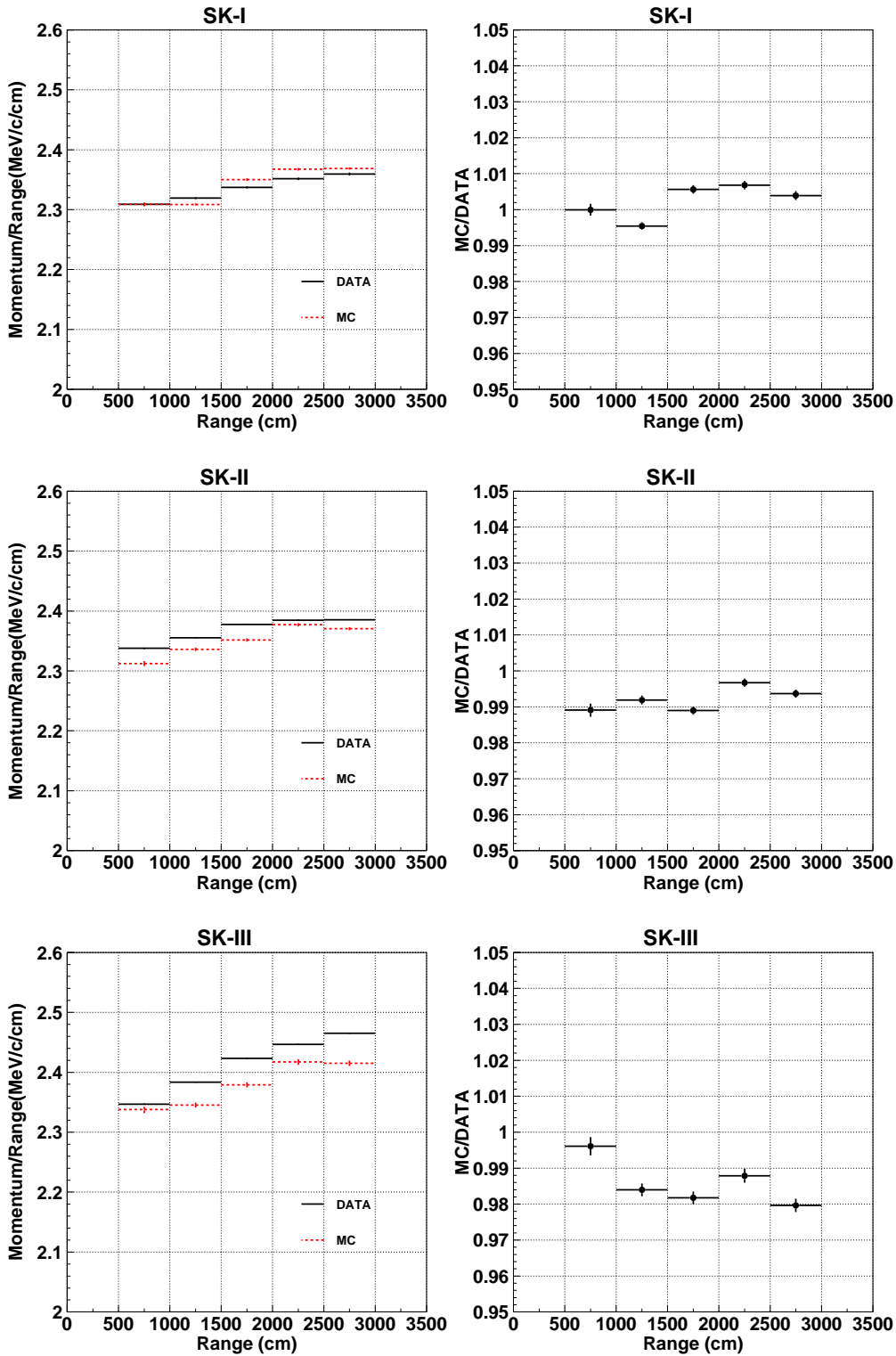
Figure 4.11: Left side panels show the range v.s. the averaged momentum/range of stopping muon events for the data (solid line) and the Monte Carlo events (dashed line), for each SK-I (upper), SK-II (middle) and SK-III (lower). Right side panels show the ratio the Monte Carlo events to the data of the averaged momentum/range in each left panel.
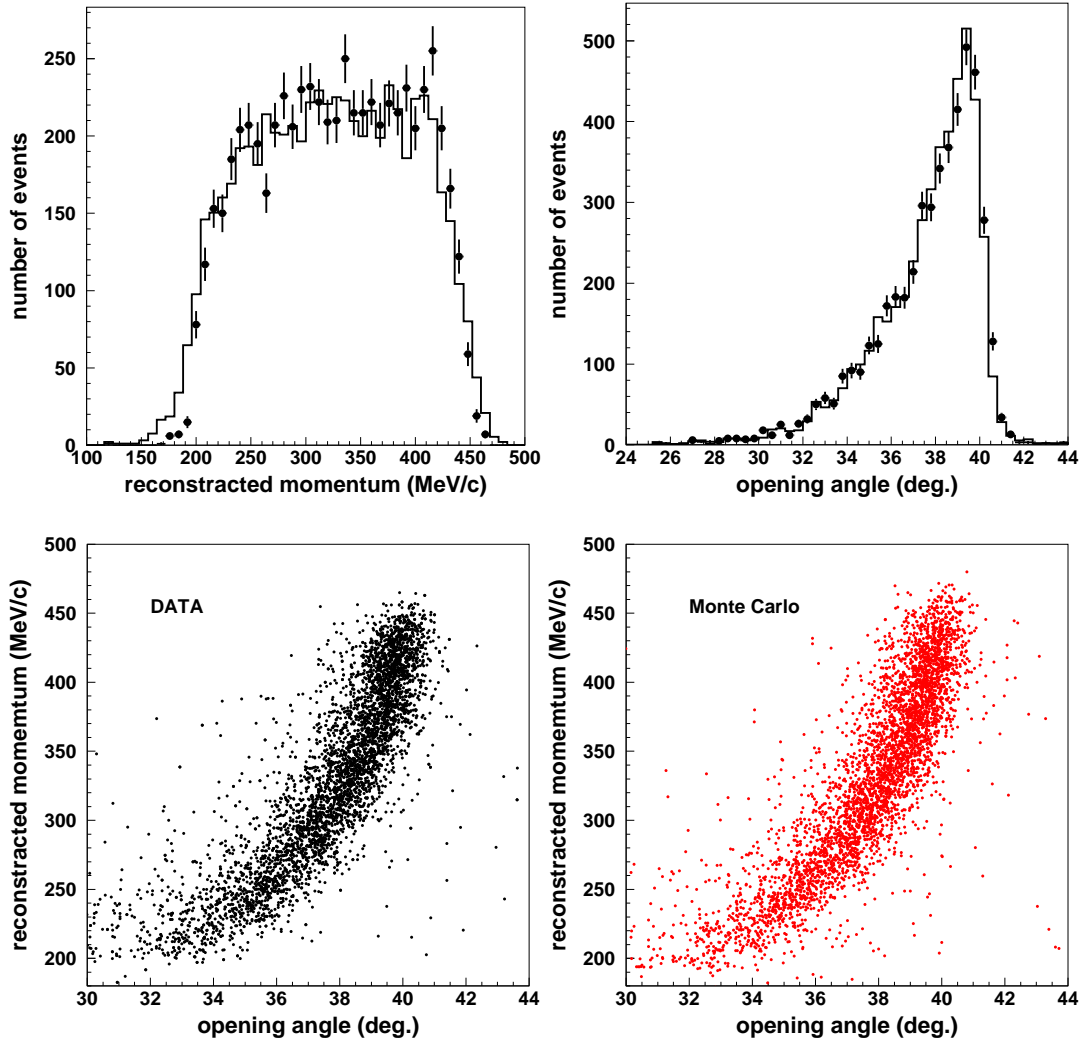
Figure 4.12: Upper left panel shows the reconstructed momentum distribution $P_{p.e.}$ for the data (circle and error) and the Monte Carlo simulation (histogram). Upper right panel shows the reconstructed opening angle distribution. Lower two panels show the correlation between the reconstructed Cherenkov opening angle $\theta_C$ and the reconstructed momentum $P_{p.e.}$ for data (left) and the Monte Carlo simulation (right). All distributions come from sample for SK-II.
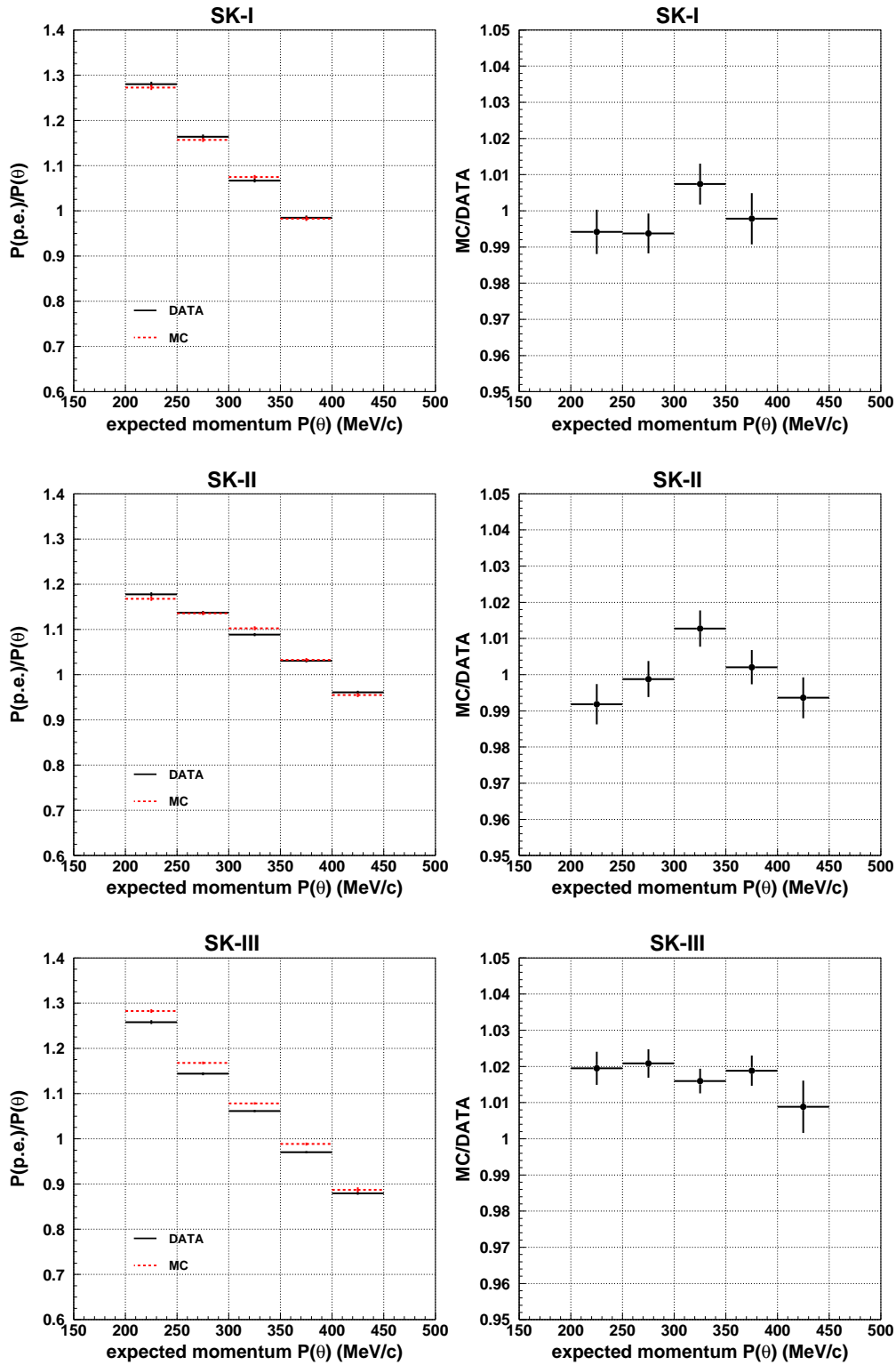
Figure 4.13: Left side panels show the averaged ratio of the momentum derived from the charge to that from the opening angle ($P_{p.e.}/P_\theta$) as a function of the momentum $P_\theta$ for the data (solid line) and the Monte Carlo events (dashed line), for each SK-I (upper), SK-II (middle) and SK-III (lower). Right side panels show the ratio MC events to the data of $P_{p.e.}/P_\theta$ in each left panel.

(3) The vertex position is reconstructed within the fiducial volume (more than 2 m away from the ID wall).

Criterion (2) rejects the contamination of $\pi^+\pi^0$ or $\mu^\pm\pi^0$ events. Figure 4.14 shows the invariant mass distribution of $\pi^0$ events compared with the prediction from the Monte Carlo simulation. The peak positions of data spectrum agree with MC within 0.7 %, 1.3 % and 0.3 % for SK-I, SK-II and SK-III, respectively.

### 4.2.4  Decay electrons

A large number of electron events is produced in the detector by the decay of stopping cosmic ray muons. The decay electron's energy spectrum is well understood and spreads around 50 MeV. The selection criteria for decay electrons are as follows:

(1) The time interval from a stopping muon event is $2.0\,\mu$sec to $8.0\,\mu$sec.

(2) The number of hit PMT in a 50 nsec time window is larger than 60 (30 for SK-II).

(3) The goodness of the vertex fit is greater than $0.5$.

(4) The vertex position is reconstructed within the fiducial volume (more than 2 m away from the ID wall).

Criterion (1) is for the efficient timing for electron tagging. Criterion (2) rejects $\sim$6 MeV $\gamma$-rays from $\mu^-$ capture on the nucleon. In the simulation, measured $\mu^+/\mu^-$ ratio of 1.37 [130] and the effect of $\mu^-$ capture by oxygen nuclei are considered. We use the vertex fitter which has been developed for the low energy neutrino observations such as solar and supernova neutrinos [131]. Figure 4.15 shows the overlaid momentum spectra of decay electrons for the data and MC. The mean values of data spectrum agree with MC within 0.6 %, 1.6 % and 0.8 % for SK-I, SK-II and SK-III, respectively.

### 4.2.5  Time variation of energy scale

The stability of the energy scale is also confirmed by the stopping muons and the decay electrons. In the reconstruction process, the particle momentum is corrected by the water transparency to consider the time variation of it (see Section 5.4.5). In addition, the correction to consider the time variation of trigger rate which affects the output charge of the electronics is also used. Figure 4.16 show the time variation of the mean value of momentum/range for the stopping muons, and the mean value of momentum for the decay electrons. The maximum RMS of the variation among these calibration sources is given as 0.88 %, 0.55 % and 1.79 % for SK-I, SK-II and SK-III, respectively. Since water quality is worse and not stable in SK-III (ref. Figure 4.10), the stability of the energy scale is thought to be worse than the other SK run periods.

### 4.2.6  Summary of the energy scale calibration

The absolute energy scale is checked by various methods for the momentum range from a few tens of MeV/$c$ to about 10 GeV/$c$. Figure 4.17 summarizes these absolute energy calibrations. The uncertainty of the absolute energy scale is estimated to be less than 0.74 %, 1.60 % and
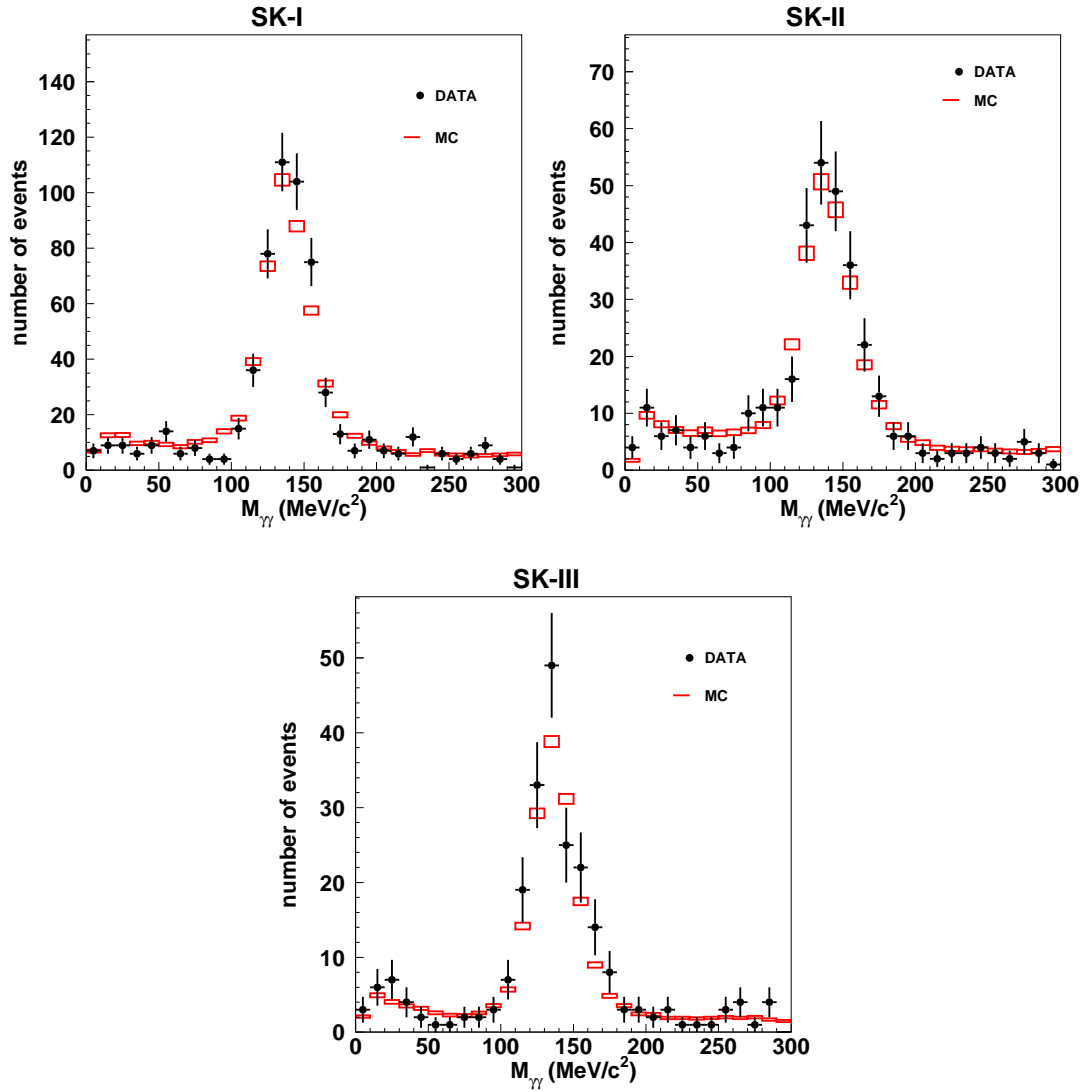
Figure 4.14: Invariant mass distribution of neutrino induced $\pi^0$ events of the observed data (dot) and the atmospheric neutrino Monte Carlo events (boxes) for SK-I (upper left), SK-II (upper right) and SK-III (lower). The peak position is fitted by a Gaussian distribution. Monte Carlo events are normalized by the livetime of the observed data.
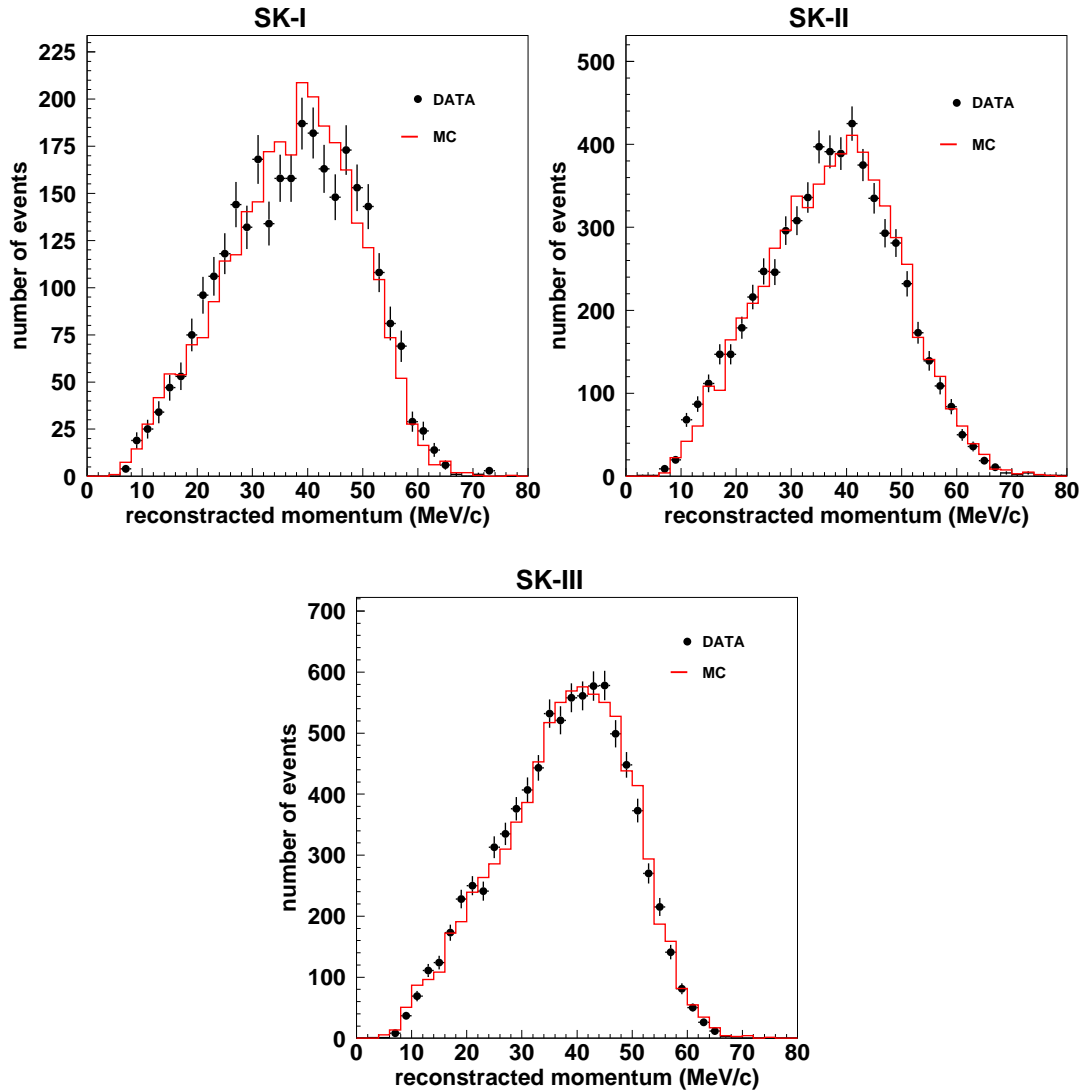
Figure 4.15: The momentum distribution of decay electrons of the data (dot) and the Monte Carlo (line) for SK-I (upper left), SK-II (upper right) and SK-III (lower). Monte Carlo events are normalized by the number of observed data events.
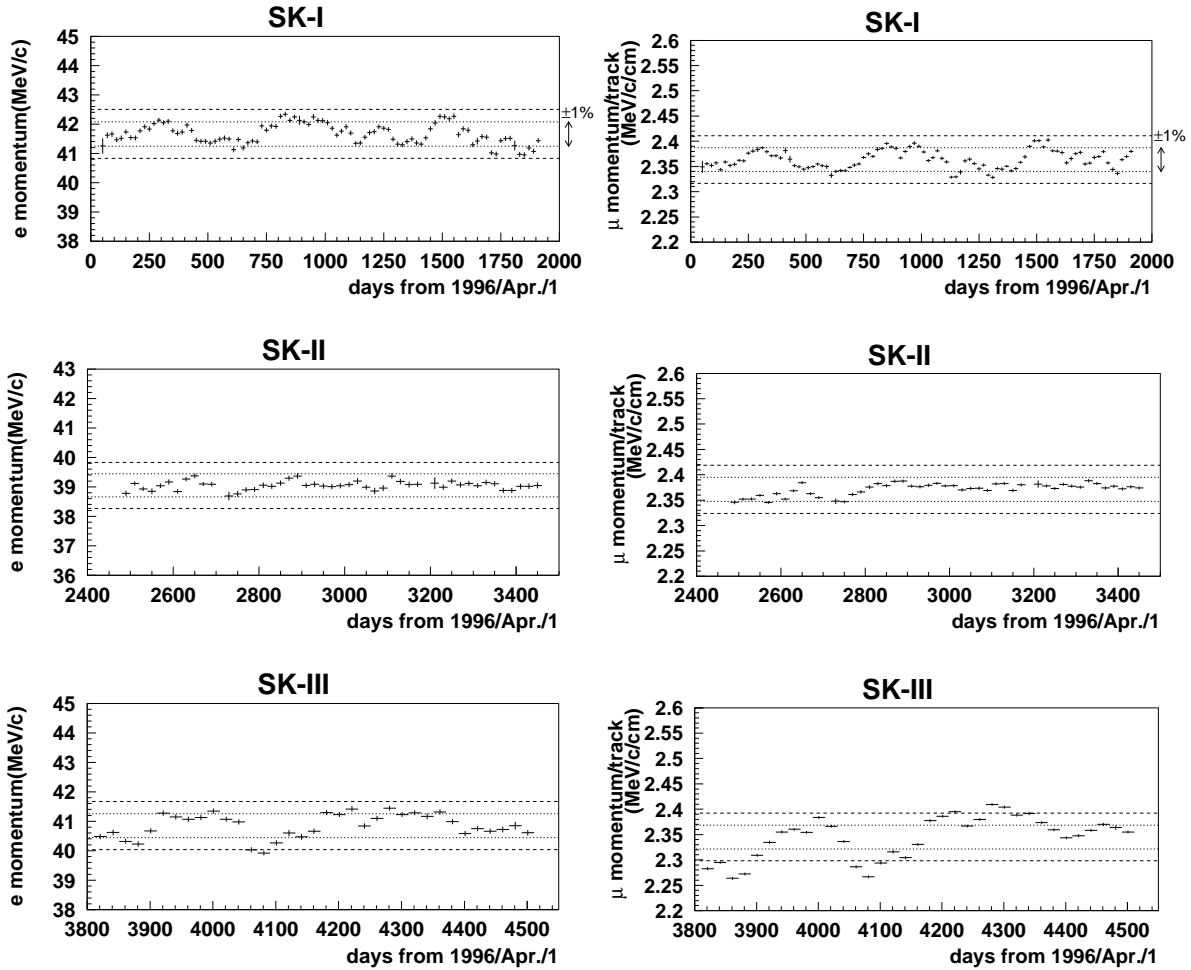
Figure 4.16: The time variation of the reconstructed momentum of the decay electrons (left) and the averaged momentum/range of stopping muons (right) as a function of elapse days for each SK run period. Dotted (dashed) lines show $\pm 1\ \%(\pm 2\ \%)$ from mean value in each SK run period.

2.08 % for SK-I, SK-II and SK-III, respectively. To consider the time variation of the energy scale, the RMS of the variation is combined to the energy scale uncertainty. In summary, 1.1 %, 1.7 % and 2.7 % are estimated as the energy scale uncertainties for SK-I, SK-II and SK-III, respectively.

### 4.2.7 Uniformity of Energy Scale

The uniformity of the detector is measured using the decay electrons from the cosmic ray muons. They are good calibration sources to check the detector uniformity because the vertex is distributed uniformly in the fiducial volume and the momentum distribution is almost uniform in all directions. To take into account the muon polarization, only electrons whose direction is perpendicular to the parent muon direction are used. This condition is $-0.25 < \cos \Theta_{e \leftrightarrow \mu} < 0.25$, where $\cos \Theta_{e \leftrightarrow \mu}$ is the opening angle between the electron and muon directions. Figure 4.18 shows the averaged momentum of decay electrons for the Monte Carlo events normalized by that for data as a function of the zenith angle of the electrons. From this figure, the detector gains are uniform within $\pm 0.6 \%$, $\pm 0.6 \%$ and $\pm 1.3 \%$ for SK-I, SK-II and SK-III, respectively.
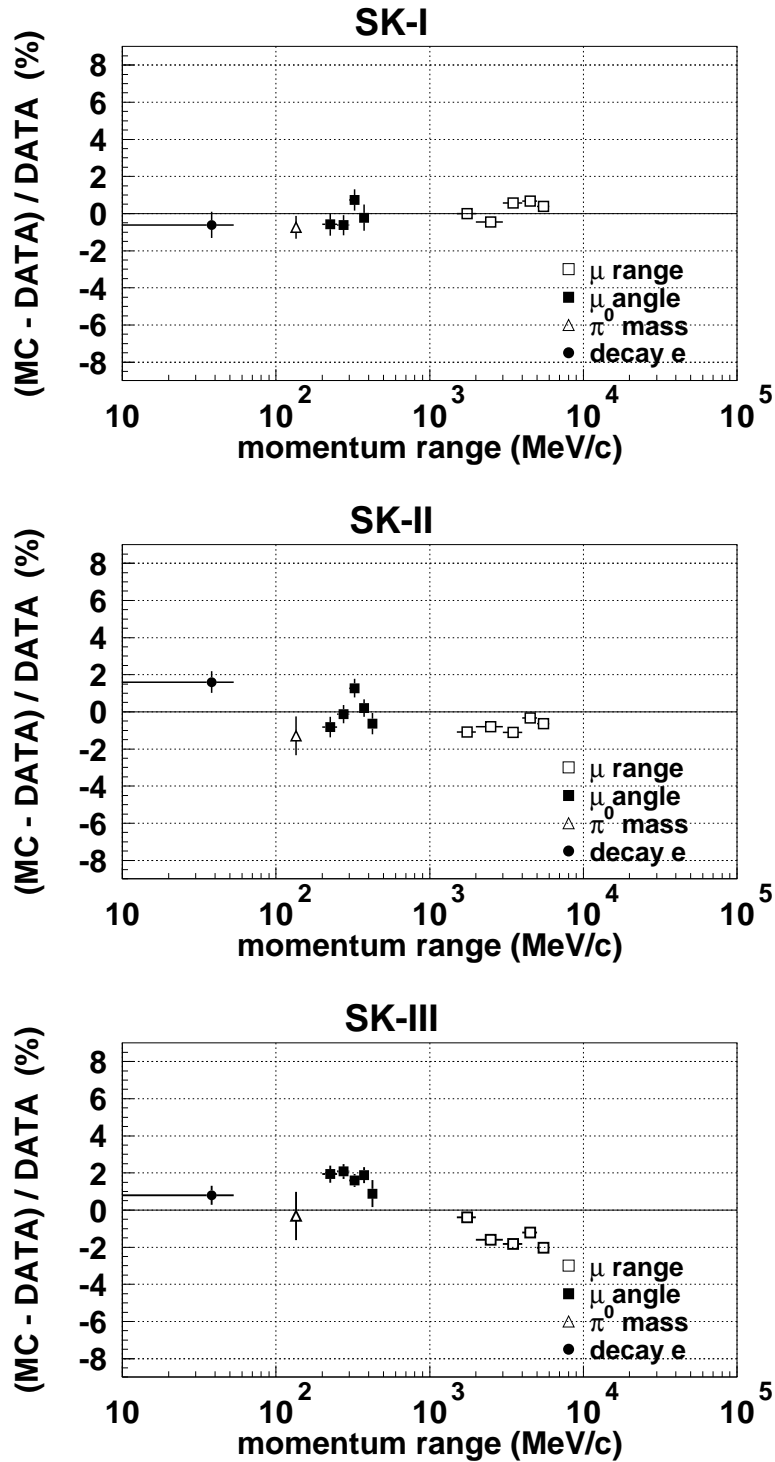
Figure 4.17: The summary of the absolute energy scale calibration for each SK run period. The horizontal axis shows the momentum range and the vertical axis shows the deviation of the data from the Monte Carlo predictions.
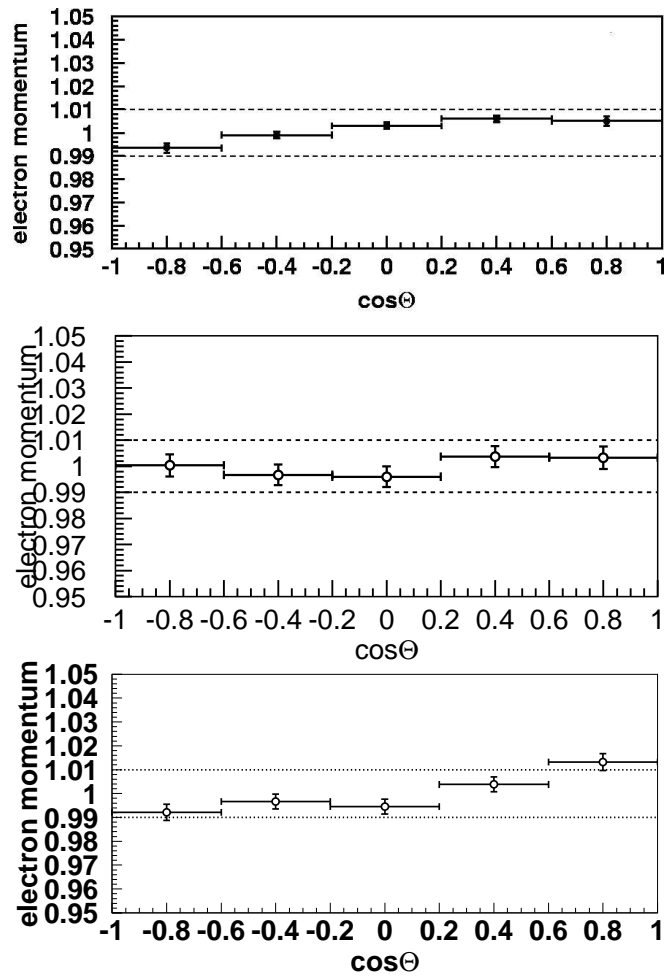
Figure 4.18: The uniformity of the detector gain as a function of zenith angle for each SK period. The vertical axes are the ratio MC to data of the averaged momentum of decay electron events.

# Chapter 5

# Data Selection

The Super-Kamiokande detector collects about $10^6$ HE and LE trigger events per day. But most of the events are background events such as cosmic rays and gamma rays from radioactivities. An efficient selection is required to select neutrino events in such a large amount of the data.

The atmospheric neutrino events observed in Super-Kamiokande are categorized to 3 types: fully contained (FC), partially contained (PC) and upward-going muon (UPMU). For FC and PC event types, the neutrino interacts in the fiducial volume of the detector (2m away from the ID wall). If all of the energy of induced lepton is deposited inside the ID, the event is classified into FC. If high energy muon lepton exits the ID and deposits its energy in the OD region, the event is classified into PC. UPMU events are the high energy muons produced by the neutrino interactions with the rock surrounding the detector. Since these events cannot be distinguished from the cosmic rays traveling in the downward direction, only muons traveling in upward direction through the detector are selected. They are separated into two categories: those that come to rest in the detector (upward stopping muons), and those that traverse the entire detector volume (upward through-going muons). Figure 5.1 shows the scheme of these event types. These neutrino mean energy is distributed $\sim$ 1GeV for FC, $\sim$ 10 GeV for PC and stopping UPMU, and $\sim$ 100GeV for through-going UPMU as shown in Figure 5.2. The procedures to select the neutrino events are performed separately to each event type.

The event selection consists of reduction and reconstruction processes. The reduction pro-



Fully contained     Partially contained     Upward stopping muon     Upward through-going muon
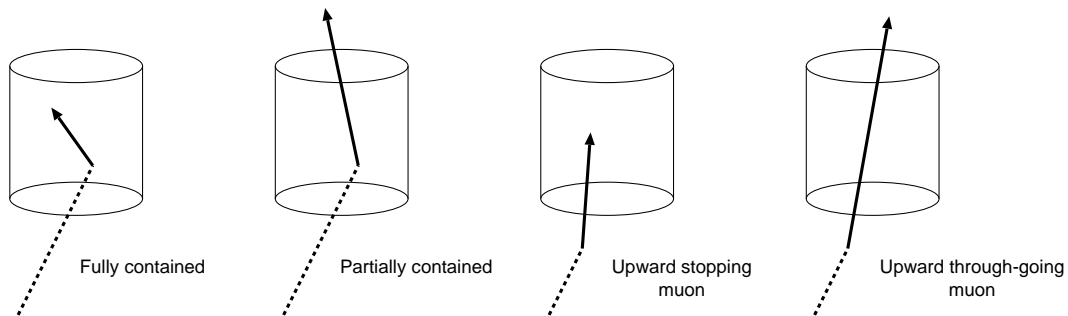
Figure 5.1: Schematic view of observed atmospheric neutrino in Super-Kamiokande
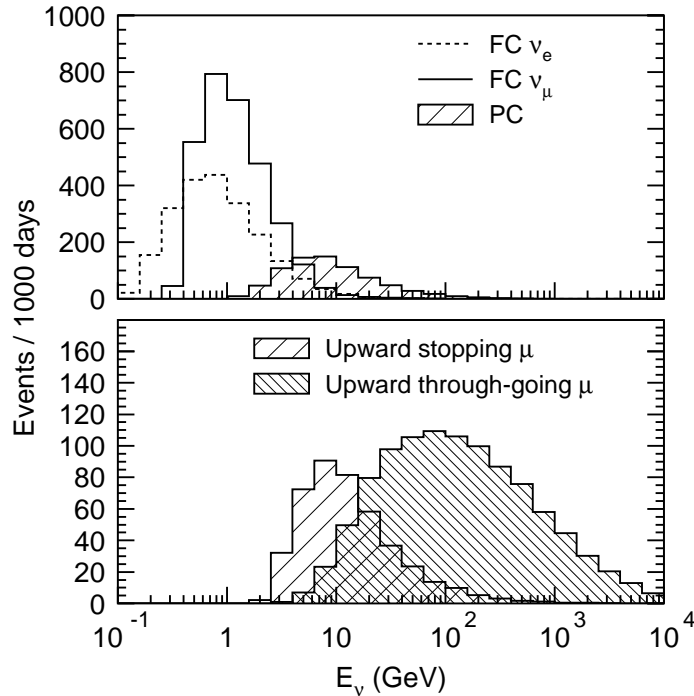
Figure 5.2: The expected neutrino spectra for each event category

cess is to search neutrino events by removing background events in the collected data. The background events observed in Super-Kamiokande are categorized to:

- Cosmic ray through-going muons which pass through the detector

- Cosmic ray stopping muons which enter and stop inside the detector

- Cosmic ray corner clipping muon which graze the corner of the detector

- Flasher event which is accidentally happened when a PMT emit light by internal corona discharge

- Low energy event such as gamma-ray from radioactivities.

These background events are removed dramatically by the reduction processes. After the reduction, various quantities, such as the vertex position, are reconstructed for each neutrino event.

In this chapter, the reduction methods for each event type FC, PC and UPMU are described. (Since the author was most deeply involved in the SK-III data reduction and the analysis, various distributions from SK-III are mainly shown.) The reconstruction methods and their performance are also described.

When the distributions of Monte Carlo events compare with the data in the reduction sections, MC sample is assumed to be not oscillated unless specified in the caption. In the reconstruction sections, the distributions of MC sample are assumed to be 2-flavor mixing with $(\sin^2 2\theta, \Delta m^2) = (1.00, 2.5 \times 10^{-3}\,\text{eV}^2)$.

## 5.1 Reduction for Fully Contained Events

Firstly, FC events are distinguished from PC events using the number of OD hit PMTs in the highest charge cluster (will be described in Section 5.1.6). Here describes the data reduction procedure consisting of five steps for FC. Note that since the number of ID PMTs for SK-II is about half of that for SK-I and III, the SK-II selection criteria relating to the number of hit and observed charge of ID PMTs are different from that of SK-I and III.

### 5.1.1 First Reduction

An event passes the 1st reduction if it fulfills the following all criteria :

(1)  $PE_{total}$ should be $> 200$ p.e.s (100 p.e.s for SK-II).
     $PE_{total}$ is the number of total p.e.s observed by the ID PMTs.

and

(2)  $NHITA_{800}$ should be $\leq 50$ or OD trigger is off.
     $NHITA_{800}$ is the number of hit OD PMTs in a fixed 800 nsec time window from 500 nsec to 1300 nsec before and after the trigger timing.

Criterion (1) rejects the low energy background events due to radio activities. The 200 p.e.s (100 p.e.s for SK-II) corresponds to 22 MeV/$c$ of electron momentum. Since the events which have visible energy below 30 MeV are not used in the analysis (see in Section 5.1.6), this cut is safe. Criterion (2) removes the cosmic ray muon events. The FC 1st reduction reduces the data size from $10^6$ events/day to $\sim 3000$ events/day.

### 5.1.2 Second Reduction

In the second reduction, low energy events and cosmic ray muons are rejected. The selection criteria are follows :

(1)  $NHITA_{800}$ should be $\leq 25$     if $PE_{tot} < 100,000$ p.e.s (50,000 p.e.s for SK-II)
     or OD trigger is off.

and

(2)  $PE_{max}/PE_{300}$ should be $< 0.5$.
     $PE_{max}$ is the maximum number of p.e.s observed by an ID PMT. $PE_{300}$ is the maximum number of total p.e.s observed by the ID PMTs in a sliding 300 nsec time window.

Criterion (1) is to reject cosmic ray muons by a tighter threshold than the 1st reduction. Figure 5.3 show the $NHITA_{800}$ distributions for the data, FC atmospheric neutrino Monte Carlo events whose vertices 2m away from the ID wall, and the FC final sample events. Criterion (2) removes the low energy events and electrical noise events, which have one larger hit signal from a single PMT. Figure 5.4 shows the $PE_{max}/PE_{300}$ distributions.

The event rate is $\sim 200$ events/day after the FC 2nd reduction.
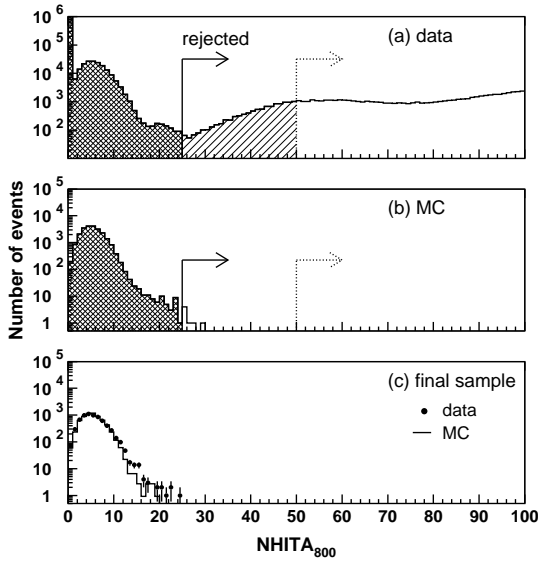
Figure 5.3: (FC 2nd reduction) $NHITA_{800}$ distributions for SK-II. (a) shows the observed data after FC 1st reduction. (b) shows FC Monte Carlo events after FC 1st reduction. (c) shows the final samples for the data and the the Monte Carlo events. The number of the Monte Carlo events in (c) is normalized to that of the data. The selection criteria are shown by arrows. Dashed line is cut criteria in FC 1st reduction. Solid line is cut criteria in FC 2st reduction.
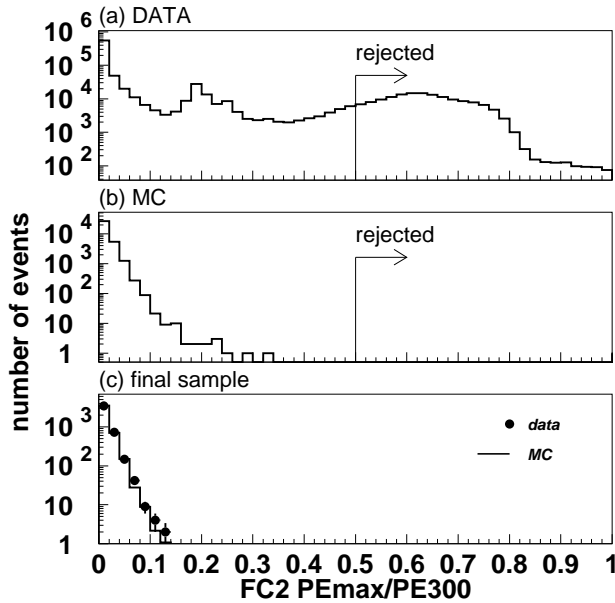


Figure 5.4: (FC 2nd reduction) $PE_{max}/PE_{300}$ distributions for SK-III. (a) shows the data after the FC 1st reduction. (b) shows FC Monte Carlo events after the FC 1st reduction. (c) shows the final samples for the data and the the Monte Carlo events. The number of the Monte Carlo events in (c) is normalized to that of the data. The selection criteria are shown by arrows.

### 5.1.3 Third Reduction

Remaining background events, mostly noise events and cosmic ray muons which have a small number of OD hits, are rejected by following cuts.

**Through-going muon cut**

The through-going muons are very energetic and deposit a lot of charge in the ID. To eliminate these events, a through-going muon fitter is applied if there are more than 1000 PMTs, each detecting more than 230 p.e.s.. This fitter finds the point where the through-going muon enters into the ID by using earliest hit PMT with some neighboring hit PMTs. The exit point where the through-going muon goes out the ID is defined the center of the saturated ID PMTs. The goodness of through-going muon fit is defined as :

$$ goodness \quad = \quad \frac{1}{\sum_i \dfrac{1}{\sigma_i^2}} \times \sum_i \frac{1}{\sigma_i^2} \exp\left( - \frac{(t_i - T_i)^2}{2(1.5 \times \sigma_i)^2} \right) \tag{5.1} $$

where $t_i$ and $\sigma_i$ are the observed hit time of the $i$-th PMT and its resolution, and $T_i$ is the hit time expected from the entering time of muon and its track. Using a goodness-of-fit, the cut criteria are following:

(1)    goodness of through-going muon fit > 0.75

and

(2)    $NHITA_{in} \geq 10$    or    $NHITA_{out} \geq 10$
NHIT is the number of ID hits. $NHITA_{in}$ ($NHITA_{out}$) is the number of hit OD PMTs located within 8 m from the entrance (exit) point in a fixed 800 nsec time window.

Events that satisfy all those criteria are rejected. Figure 5.5 show the scatter plots of $NHITA_{in}$ and $NHITA_{out}$ satisfying criterion (1) for the data after the 2nd reduction, the FC atmospheric neutrino Monte Carlo events and the FC final samples.

**Stopping muon cut**

For rejection of stopping muons, a stopping muon fitter is applied to find the entrance point by the similar way as the through-going muon fit. The goodness is defined as equation (5.1). The events fulfilling the following criteria are removed as stopping muons:

(1)    $NHITA_{in} \geq 10$    if  goodness of stopping muon fit $\geq 0$
$NHITA_{in}$ is the number of hit OD PMTs located within 8 m from the entrance point in a fixed 800 nsec time window.

or $NHITA_{in} \geq 5$  if  goodness of stopping muon fit > 0.5    (for SK-I)

The direction of muon is reconstructed to maximize the total number of p.e.s inside the cone with a half opening angle 42°. For SK-I, the additional criteria is included. Figure 5.6 shows $NHITA_{in}$ distributions for the data after the 2nd reduction, the FC atmospheric neutrino Monte Carlo events and the FC final events.
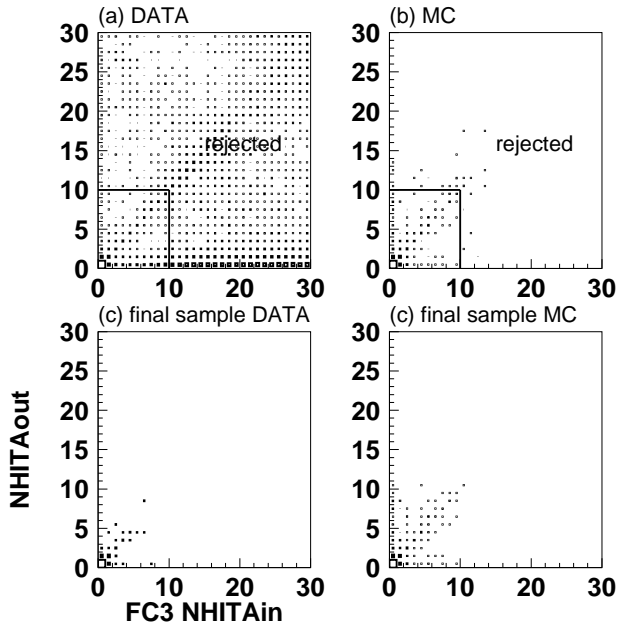
Figure 5.5: (FC 3rd reduction) Scatter plot of the number of hit OD PMTs within 8 m of the entrance point $NHITA_{in}$ (x-axis) and the exit point $NHITA_{out}$ (y-axis) for SK-III. (a) shows the data after the FC 2nd reduction. (b) shows FC Monte Carlo events after the FC 2nd reduction. (c) shows the final samples for the data and the the Monte Carlo events. The selection criteria are shown by arrows.
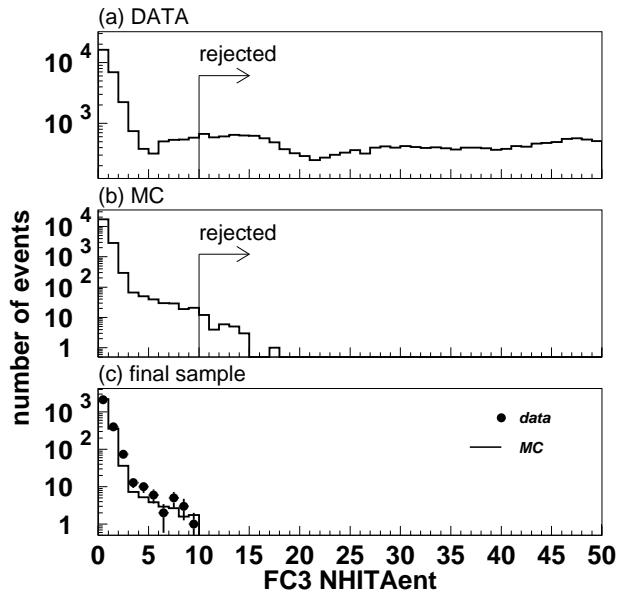


Figure 5.6: (FC 3rd reduction) Number of hit OD PMTs near the entrance point of muons $NHITA_{in}$ for SK-III. (a) shows the data after the FC 2nd reduction. (b) shows FC Monte Carlo events after the FC 2nd reduction. (c) shows the final samples for the data and the the Monte Carlo events. The number of the Monte Carlo events in (c) is normalized to that of the data. The selection criteria are shown by lines.
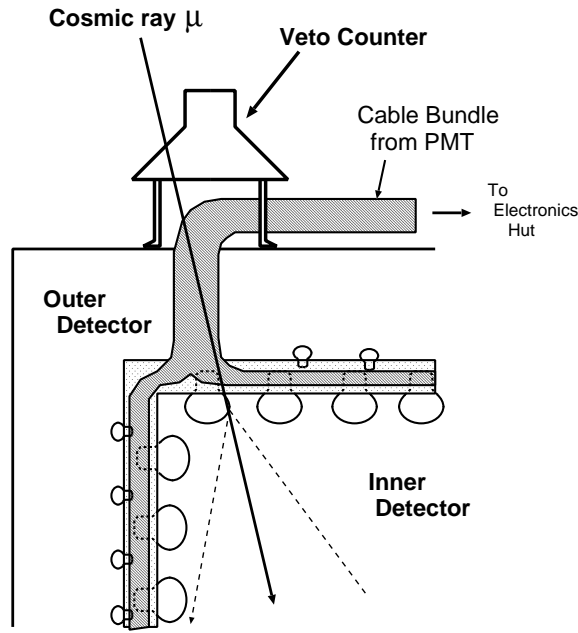
Figure 5.7: A schematic view of a cable-hole muon and a veto counter.

## Cable hole muons

On top of the detector tank, there are twelve cable holes to take the signal and HV supply cables out. Four holes of those are covering the OD PMTs as shown in Figure 5.7. When cosmic ray muons enter into the ID region through these holes, this event could be detected as contained neutrino events because of no OD signal. In order to avoid such mis-identification, veto counters ($2\,\mathrm{m} \times 2.5\,\mathrm{m}$ plastic scintillation counters) were installed in April, 1997. The rejection criteria using the veto counters of the cable hole muons are :

(1)    One veto counter hit

and

(2)    $L_{veto} < 4\,\mathrm{m}$
       $L_{veto}$ is the distance from the cable hole to the the reconstructed vertex.

## Flasher event cut

Flasher events usually have a broad hit timing distribution compared with that of the neutrino events. By using this feature, following criteria are applied.
For SK-I :

(1)    $NMIN_{100} \geq 15$
       or
       $NMIN_{100} \geq 10$        if    the number of hit ID PMTs $\leq 800$
       $NMIN_{100}$ is the minimum number of hit ID PMTs in a sliding 100 nsec time
       window from $+300$ nsec to $+800$ nsec after the trigger.
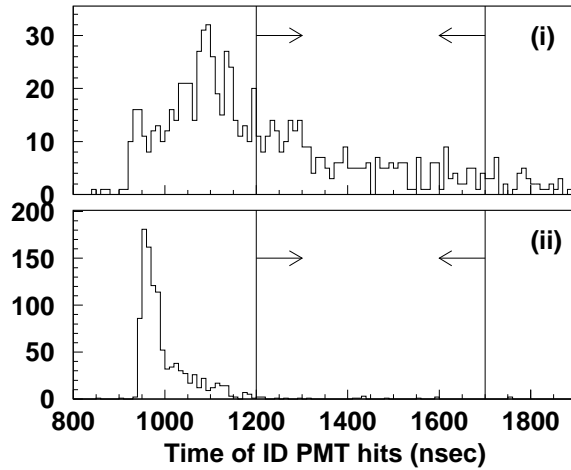
Figure 5.8: (FC 3rd reduction) The timing distribution of (i) a typical flashing PMT event and (ii) a typical FC neutrino event. The arrows show the time window for counting $NMIN_{100}$.

For SK-II and SK-III :

(1)     $NMIN_{100} \geq 20$

Figure 5.8 shows the timing distribution of (i) a typical flashing PMT event and (ii) a typical FC neutrino event and the time window for $NMIN_{100}$ is shown by arrows. Figure 5.9 shows $NMIN_{100}$ distributions for the data after the 2nd reduction, the FC atmospheric neutrino Monte Carlo events and the FC final events.

**Accidental coincidence events cut**

The accidental coincidence occurs when a low energy event forms the trigger and a cosmic ray muon event follows in a single trigger gate. These events are not rejected in the former reduction because of the absence of the OD activities on the trigger timing and the large number of total p.e.s in the ID due to the muons. The accidental coincidence events are removed by the following cuts :

(1)     $NHITA_{off} \geq 20$
        $NHITA_{off}$ is the number of hit OD PMTs in a fixed 500 nsec off-timing window
        from +400 nsec to +900 nsec after the trigger timing.

    and

(2)     $PE_{off} > 5000$ p.e.s   (2500 p.e.s for SK-II)
        $PE_{off}$ is the number of p.e.s observed by ID PMTs in a fixed 500 nsec off-timing
        window from +400 nsec to +900 nsec.

**Low energy events cut**

This is the rejection for the remaining low energy events such as the decay of radio isotopes and the electrical noise. Events satisfying the following criteria are removed :

(1)     $NHIT_{50} < 50$ (25 for SK-II)
        $NHIT_{50}$ is the number of hit ID PMTs in a sliding 50 nsec time window.

69
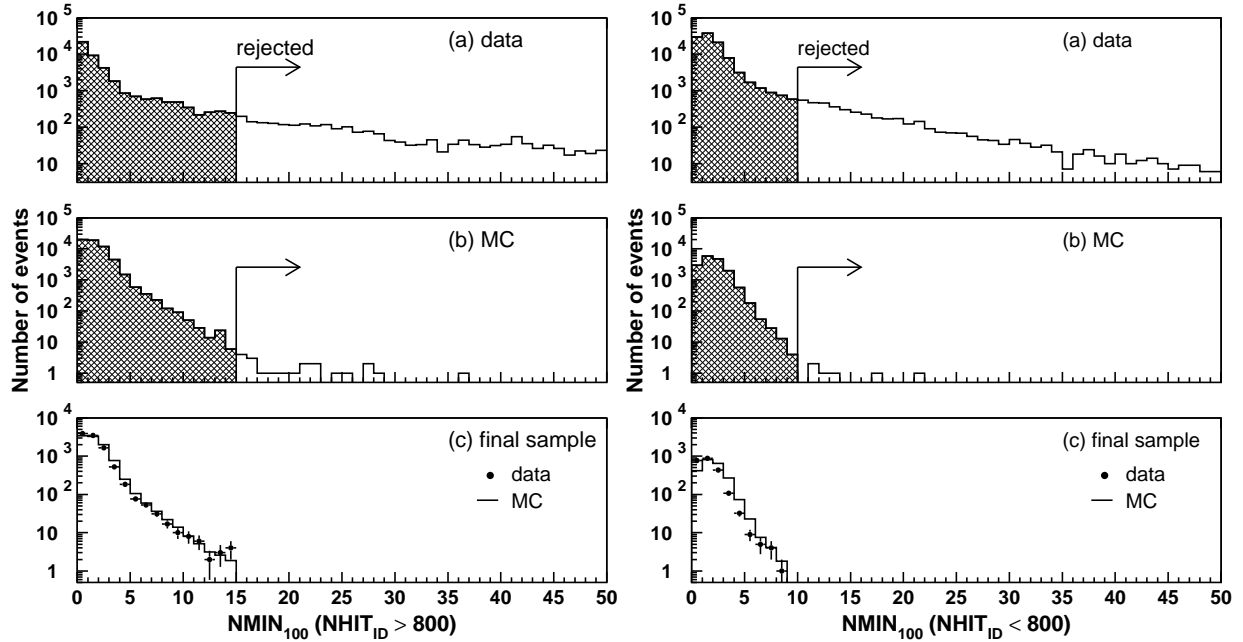
Figure 5.9: (FC 3rd reduction) $NMIN_{100}$ distributions for the events with more than 800 hit PMTs in ID (left) and less than 800 hit PMTs (right) for SK-I. (a) shows the data after the FC 2nd reduction. (b) shows FC Monte Carlo events after the FC 2nd reduction. (c) shows the final samples for the data and the the Monte Carlo events. The number of the Monte Carlo events in (c) is normalized to that of the data. The selection criteria are shown by arrows.

where $NHIT_{50}$ is counted after subtracting the time of flight (TOF) of each observed photon assuming all photons are generated at a same point. The vertex is determined as the position at which the timing residual distribution is peaked. $NHIT_{50}$=50 corresponds to visible energy of 9 MeV. It is enough low to keep efficiency for contained neutrino events which is $E_{vis} >30$ MeV.

After the FC third reduction, the event rate is $\sim 45$ events/day.

### 5.1.4 Fourth Reduction

In the fourth reduction, an intelligent pattern matching algorithm is used to remove the remaining flasher events. Flasher events usually repeat with similar hit patterns in the detector. These repeated events are not likely to be caused by neutrinos.

The algorithm of the pattern matching is as follows :

(1) Divide the ID wall into 1450 patches of $2\,m \times 2\,m$ square.

(2) Compute the correlation factor $r$ by comparing the total charge in each patch of two events, A and B. The correlation is defined as :

$$r = \frac{1}{N} \sum_i \frac{\left(Q_i^A - \langle Q^A \rangle\right) \times \left(Q_i^B - \langle Q^B \rangle\right)}{\sigma_A \times \sigma_B} \tag{5.2}$$

where $N$ is the number of the patches, and $\langle Q^{A(B)} \rangle$ and $\sigma_{A(B)}$ are the averaged charge and its standard deviation for event A and B, respectively.

(3) Calculate the distance $(DIST_{max})$ between the PMTs with the maximum pulse heights in the two compared events

(4) If $DIST_{max} < 75\,cm$, an offset value is added to $r$ :r=r+0.15.

(5) If r exceeds the threshold$(r_{th})$, events A and B are recognized as matched events. $r_{th}$ is defined as :

$$r > r_{th} = 0.168 \times \log_{10}((PE_{tot}^A + PE_{tot}^B)/2.) + 0.130, \tag{5.3}$$

where $PE_{tot}$ is the total number of p.e.s observed in the ID.

(6) Repeat the above calculation over 10,000 events around the target event and count the number of matched events.

(7) Remove the events with large correlation factor $r$, or large number of matched events.

The event rate after the fourth reduction is $\sim 18$ events/day.

### 5.1.5 Fifth reduction

In the 5th reduction, the final rejection is applied by the several criteria specialized for each background source.
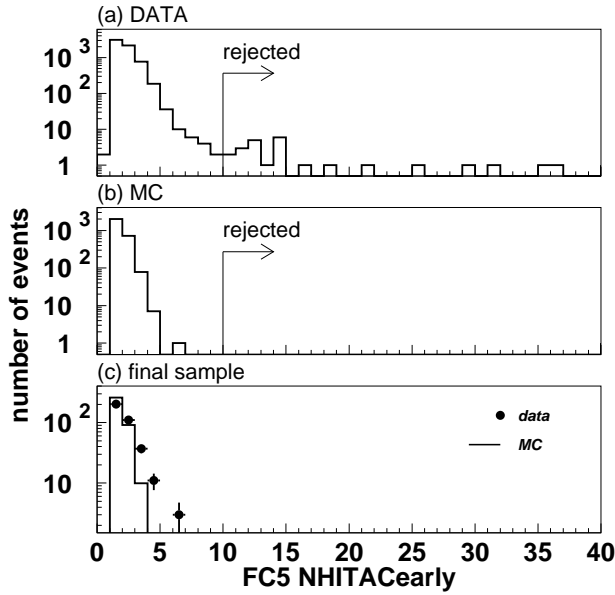
Figure 5.10: (FC 5th reduction) $NHITAC_{early}$ distribution satisfying criteria $PE_{tot} < 1000$ p.e.s and $DIST_{clust} > 500$ cm for SK-III. (a) shows the data after the FC 4th reduction. (b) shows FC Monte Carlo events after the FC 4th reduction. (c) shows the final samples for the data and the the Monte Carlo events. The number of the Monte Carlo events in (c) is normalized to that of the data. The selection criteria are shown by arrows.

## Invisible muon cut

If a cosmic ray muon has momentum less than the Cherenkov threshold and the subsequent decay electron is observed, this event could be mis-identified as neutrino event. Such event is characterized by a low energy signal from decay electron in the ID and a signal in the OD before the trigger timing. An event fulfilling the following cut criteria are rejected as invisible muons :

(1)     $PE_{tot} < 1000$ p.e.s    (500 p.e.s for SK-II)
        $PE_{tot}$ is the total number of p.e.s observed in the ID.

and

(2)     $NHITAC_{early} + NHITAC_{500} \geq 10$         if   $DIST_{clust} < 500$ cm
        $NHITAC_{early}$                    $> 9$         otherwise

$NHITAC_{early}$ is the maximum number of hit PMTs in the OD hit cluster in a sliding 200 nsec time window from $-8800$ nsec to $-100$ nsec.
$NHITAC_{500}$ is the number of hit PMTs in the OD hit cluster in a fixed 500 nsec time window from $-100$ nsec to $+400$ nsec.
$DIST_{clust}$ is a distance between two OD hit clusters, which are used for the $NHITAC_{early}$ and the $NHITAC_{500}$.

Figure 5.10 shows the $NHITAC_{early}$ distribution, satisfying criteria (1) and $DIST_{clust} > 500$ cm, for the data after the FC 4th reduction, Monte Carlo events and the final samples.

## Coincidence muon cut

The remaining accidental coincidence muon events which are not rejected in the Forth reduction (Accidental coincidence events cut) are removed by following criteria :

72
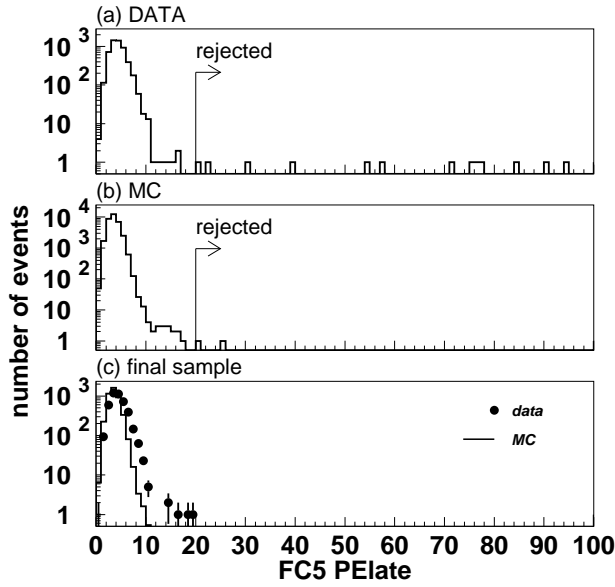
Figure 5.11: (FC 5th reduction) $PE_{late}$ distribution for SK-III. (a) shows the data after the FC 4th reduction. (b) shows FC Monte Carlo events after the FC 4th reduction. (c) shows the final samples for the data and the the Monte Carlo events. The number of the Monte Carlo events in (c) is normalized to that of the data. The selection criteria are shown by arrows.

(1)     $PE_{500} < 300$ p.e.s   (150 p.e.s for SK-II)
        $PE_{500}$ is the total number of p.e.s observed in the ID in a fixed 500 nsec time window from $-100$ nsec to $+400$ nsec.

and

(2)     $PE_{late} \geq 20$ p.e.s
        $PE_{late}$ is the maximum number of hit OD PMTs in a 200 nsec sliding time window from $+400$ nsec to $+1600$ nsec.

Figure 5.11 shows the $PE_{late}$ distribution satisfying the criterion (1) for the data after the FC 4th reduction, Monte Carlo events and the final samples.

**Long-tail flasher cut**

This is a stricter version of the flasher cut in the FC 3rd reduction stage. Events satisfying the following criterion are removed as flasher events :

(1)     $NMIN_{100} \geq 6$          if the goodness of Point-fit $< 0.4$
        $NMIN_{100}$ is the minimum number of the hit ID PMTs in a sliding 100 nsec time window from $+300$ nsec to $+800$ nsec.

For SK-II and SK-III, additional cuts are applied :

(2)     $NMIN_{100} \leq 5$          if the goodness of Point-fit $< 0.3$

The Point-fit will be explained in Section 5.4.1.

After the fifth reduction, the FC event rate is $\sim 16$ events/day.
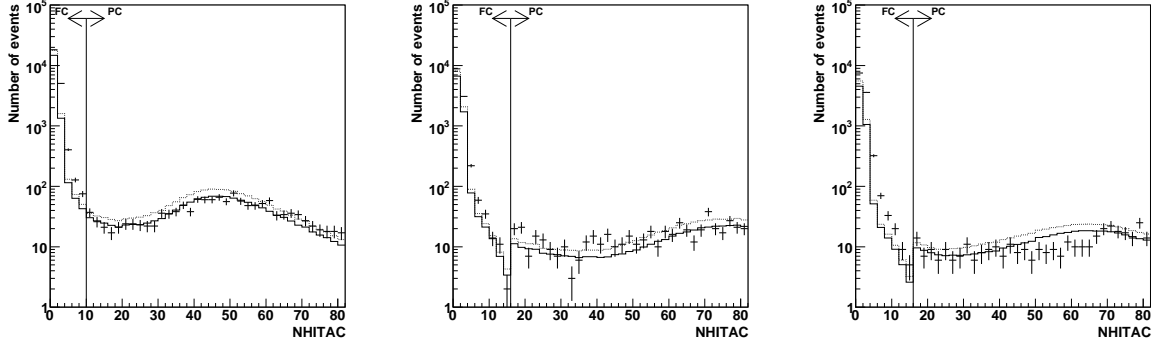
Figure 5.12: NHITAC distributions for FC and PC final samples for SK-I (left), SK-II (middle) and SK-III(right). The points show the observed data, and histograms show the atmospheric neutrino Monte Carlo events assuming no oscillation (dashed lines) and $\nu_\mu \leftrightarrow \nu_\tau$ 2-flavor oscillation with $(\sin^2 2\theta, \Delta m^2) = (1.00, 2.5 \times 10^{-3}\,\mathrm{eV}^2)$ (solid lines).

### 5.1.6   FC Reduction Summary

Finally, the fully contained neutrino events are selected by following criteria :

· Vertex of neutrino interactions is inside the fiducial volume (2 m from the ID PMT surface).

· The number of hit PMTs in the highest charge OD cluster (NHITAC) is less than 16 (10 for SK-I).

· Visible energy ($E_{vis}$) is greater than 30 MeV.

Figure 5.12 shows the NHITAC distribution for FC and PC final sample for each SK run period. The detection efficiencies in each reduction step are estimated by the atmospheric neutrino Monte Carlo events as shown in Table 5.1. The number of events in the final sample and the event rate are also summarized in Table 5.1. The event rate is consistent with constant for each SK run period.

The background events contaminated in the final FC sample are mainly cosmic ray muons and flasher events. These background events are largely rejected by a fiducial volume cut, the reconstructed vertex position > 2m from the ID PMT surface. In addition, background events are checked by eye-scan using a visual display. Since flasher events could be a background source for e-like sample, and cosmic ray muons events could be a background source for $\mu$-like sample, the contaminations of the backgrounds for each sample are estimated as shown in Table 5.2.

The uncertainty of FC reduction efficiency is estimated by comparing the distributions of each cut variables of data and Monte Carlo. The uncertainties are estimated to be 0.2%, 0.2% and 0.8% for SK-I, SK-II and SK-III, respectively.

## 5.2   Reduction for Partially Contained Events

PC events have OD activities while FC events do not, thus PC reduction processes are different from those of FC. Since OD segmentation was installed in SK-III period (see Section 2.2.3),

| FC | SK-I | SK-II | SK-III |
|---|---|---|---|
| reduction step | selection efficiency (%) | | |
| 1st | 99.95 | 99.92 | 100.0 |
| 2nd | 99.94 | 99.89 | 99.97 |
| 3rd | 99.85 | 99.71 | 99.79 |
| 4th | 99.17 | 99.39 | 98.62 |
| 5th | 99.15 | 99.32 | 98.55 |
| 5th(FV) | 97.59 | 99.17 | 98.55 |
| | number of events | | |
| Monte Carlo | 13461.3 | 7222.5 | 4753.6 |
| DATA | 12232 | 6584 | 4356 |
| (event rate[/day]) | (8.21±0.07) | (8.24±0.10) | (8.41±0.12) |

Table 5.1: The selection efficiencies and number of events for FC sample are summarized for each SK period. The selection efficiencies are for events whose real vertex is in the fiducial volume, the number of outer detector hits fewer than 16(10 for SK-I) and the visible energy larger than 30 MeV. In the last line with FV, events with the fitted vertex in fiducial volume are selected. Numbers of events for MC are normalized without oscillation to real data livetime, 1489.2, 798.6 and 518.1 days for SK-I, SK-II and SK-III, respectively.

| | SK-I | | SK-II | | SK-III | |
|---|---|---|---|---|---|---|
| BG | cosmic ray | flasher | cosmic ray | flasher | cosmic ray | flasher |
| sub-GeV | 0.1% | 0.5% | 0.1% | 0.2% | 0.1% | 0.1% |
| multi-GeV | 0.1% | 0.3% | 0.1% | 0.3% | 0.2% | 0.4% |

Table 5.2: Estimated contamination for each background event. Sub-GeV is events with $E_{vis} <$1.3GeV ,and Multi-GeV is events with $E_{vis} >$1.3GeV.

the reduction process is substantially modified to adjust to it for SK-III. Here describes the data reduction procedure consisting of 5 steps for PC.

### 5.2.1 First Reduction

For SK-I and -II, the 1st reduction rejects the through-going cosmic ray muons and low energy events. An event satisfying all of the following criteria is selected.
For SK-I:

(1)     $PE_{tot}$ should be $\geq 1000$ p.e.s
$PE_{tot}$ is the number of p.e.s observed in the ID.

and

(2)     TWIDA should be $\leq 260$ nsec.
TWIDA is the width of the hit timing distribution in the OD PMTs.

and

(3)     NCLSTA should be $\leq 1$.
NCLSTA is the number of the hit clusters in the OD.

For SK-II:

(1)     $PE_{tot}$ should be $\geq 500$ p.e.s

and

(2)     TWIDA should be $\leq 170$ nsec.

Exiting particles in the PC sample, mostly muons, must have at least 2 m track length in the ID, which corresponds to the momentum loss of 500 MeV/$c$ for muons. In criterion (1), $PE_{tot}$ should be larger than 1000 p.e.s (500 p.e.s for SK-II), which corresponds to 310 MeV/c for muons. The criteria (2) rejects through-going muons which have a broad hit timing distribution and two hit clusters around the entrance and exit point in the OD. Since the reflected photon in the OD is increased and the quantum efficiency of OD PMTs is increased in SK-II, TWIDA cut criterion is tuned for SK-II.

For SK-III, the efficient reduction for the through-going muons is performed taking advantage of the OD segmentation. An event fulfilling following all criteria are selected :

(1)     $PE_{tot}$ should be $\geq 1000$ p.e.s

and

(2)     $NHITA_{top} < 10$     or     $NHITA_{bottom} < 10$
$NHITA_{top}(NHITA_{bottom})$ is the number of OD hits in top(bottom) region.

and

(3)     $NHITA_{endcap} < 25$     or     $NHITA_{side} < 70$
$NHITA_{endcap}(NHITA_{side})$ is the number of OD hits in top and bottom (side) region.
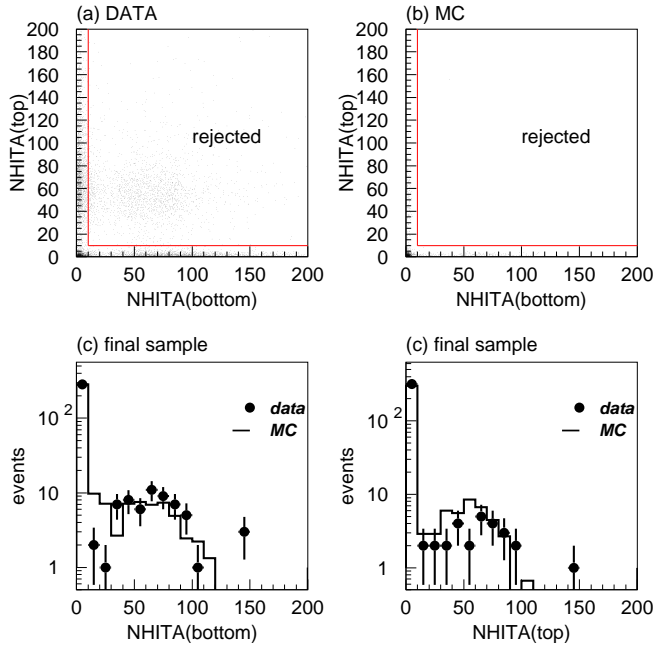
Figure 5.13: (PC 1st reduction) The scatter plots of $NHITA_{top}$ and $NHITA_{bottom}$. (a) shows the raw data. (b) shows PC Monte Carlo events with the vertex in the fiducial volume. (c) shows the 1-dimensional plot of each $NHITA_{top}$ and $NHITA_{bottom}$ for final samples. The number of the Monte Carlo events in (c) is normalized to that of the data. The selection criteria are shown by lines.

and

(4)     $ODR_{mean} < 2100\,cm$     if OD hits $< 20$ in 500 nsec time window
        $ODR_{mean}$ is the average distance between all hit pairs:
        $ODR_{mean} = \frac{1}{N_{pair}} \sum_{i=1}^{N-1} \sum_{j=i+1}^{N} |\vec{x_i} - \vec{x_j}|$ .

The criteria (2) rejects through-going muons which passes both top and bottom regions. Figure 5.13 shows the scatter plots of $NHITA_{top}$ and $NHITA_{bottom}$ for the observed data, PC atmospheric neutrino Monte Carlo events, and the distributions of each variable for the final sample. The criteria (3) rejects corner clipping muons. Figure 5.14 shows the scatter plots and distributions for $NHITA_{endcap}$ and $NHITA_{side}$. In the criteria (4), the $ODR_{mean}$ value for the through-going muons is expected lager than that of PC events. Figure 5.15 shows the scatter plots for $ODR_{mean}$ and the number of OD hits and the distribution of $ODR_{mean}$.

The 1st reduction reduces the number of events to $\sim 2 \times 10^4$ event/day.

## 5.2.2   Second Reduction

In the second reduction, a clustering algorithm of OD hit is used to reject the through-going muons and the stopping muons. The OD (ID) walls are divided into $11 \times 11$ ($21 \times 21$) patches and the charge observed in each patch is counted. The clusters are formed by looking for the charge gradient to the neighboring patches. The algorithm is illustrated in Figure 5.16. Events satisfying the following all criteria remain after the PC 2nd reduction. For both SK-I and -II,

(1)     NCLSTA2 should be $\leq 1$
        NCLSTA2 is the number of the OD hit clusters including more than 6 hit
        PMTs.

and, for SK-I :
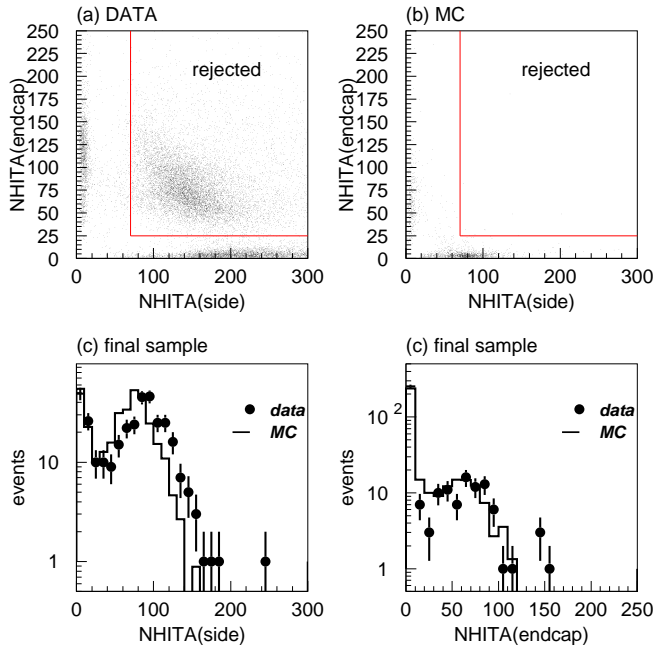
Figure 5.14: (PC 1st reduction) The scatter plots of NHITA$_{endcap}$ and NHITA$_{side}$. (a) shows the raw data. (b) shows PC Monte Carlo events with the vertex in the fiducial volume. (c) shows the 1-dimensional plot of each NHITA$_{endcap}$ and NHITA$_{side}$ for final samples. The number of the Monte Carlo events in (c) is normalized to that of the data. The selection criteria are shown by lines.
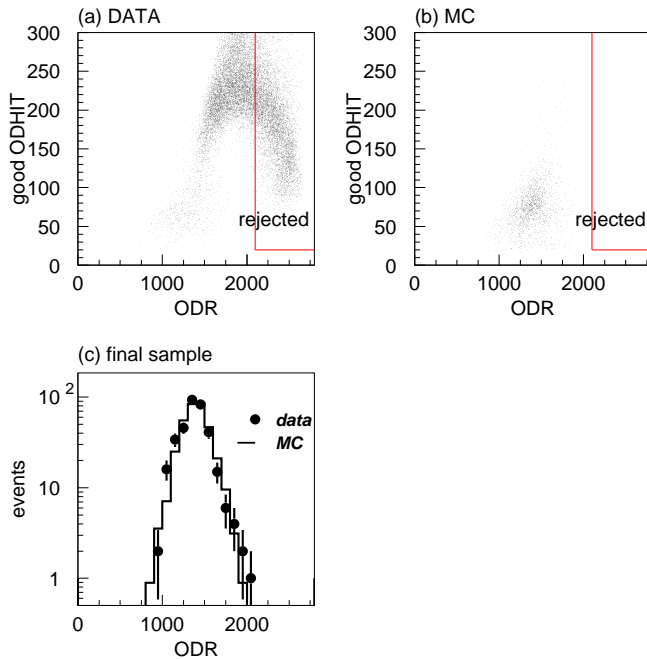


Figure 5.15: (PC 1st reduction) The scatter plots of the number of good OD hits and ODR$_{mean}$. (a) shows the raw data. (b) shows PC Monte Carlo events with the vertex in the fiducial volume. (c) shows the 1-dimensional plot of ODR$_{mean}$ for final samples. The number of the Monte Carlo events in (c) is normalized to that of the data. The selection criteria are shown by lines.

78
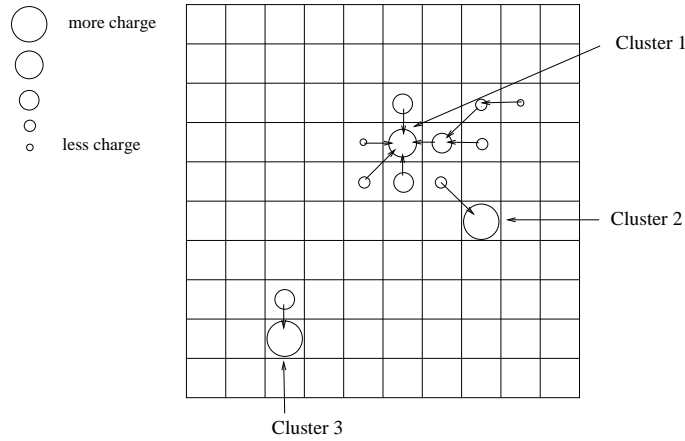
Figure 5.16: A schematic view of the algorithm to find hit clusters in the PC 2nd reduction. The circles represent the charge observed in each patch. The size of the circle is proportional to the number of p.e.s. The arrows represent the vector charge gradient, which point to the highest charge among the neighboring patches.

(2)    NCLSTA2(2) should be $\leq 1$
NCLSTA2(2) is the number of the 2nd OD hit clusters including more than 6 hit PMTs.

and

(3)    $NHITAC_{min}$ should be $< 7$
$NHITAC_{min}$ is the minimum number of hit PMTs among top (or bottom) and side regions in the OD hit cluster.

and

(4)    $PE_{200}$ should be $> 1000$ p.e.s    if   NCLSTA2 $= 1$
$PE_{200}$ is the number of the observed p.e.s within $200$ cm from the highest charge PMT in the ID hit cluster closest to the OD hit cluster.

for SK-II :

(2)    NCLSTA2(2) should be $\leq 1$
NCLSTA2(2) is the number of the 2nd OD hit clusters including more than 10 hit PMTs.

and

(3)    $NHITA_{endcap} < 20$ or $NHITA_{endcap} < MAX(NHITA_{side})$
$MAX(NHITA_{side})$ is defined as :
$MAX(NHITA_{side} = \exp(5.8\text{-}0.023\times NHITA_{side})$    if $NHITA_{side} < 75$
$MAX(NHITA_{side} = \exp(4.675\text{-}0.008\times NHITA_{side})$    if $NHITA_{side} \geq 75$
$NHITA_{endcap}$ is the number of OD hit PMTs in the top and bottom region.
$NHITA_{side}$ is the number of hit OD PMTs in the side region.

(a) DATA

(b) MC

(c) final sample

number of events

PC2 NCLSTA2
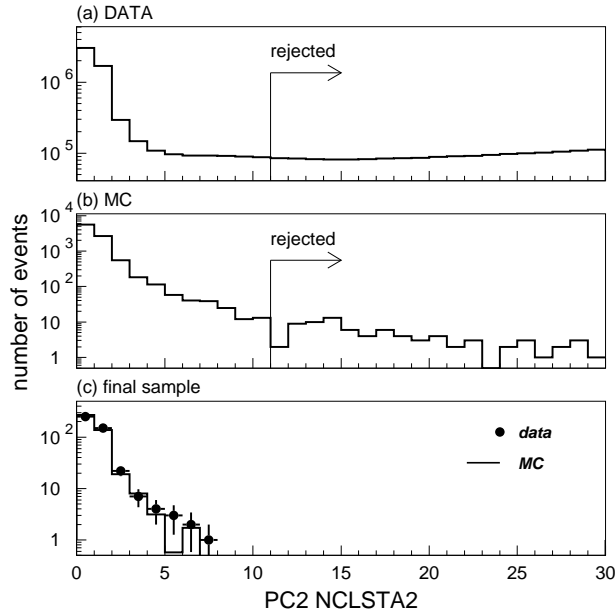
Figure 5.17: (PC 2nd reduction) The number OD hit PMTs in the 2nd OD hit cluster. (a) shows the data after the PC 1st reduction. (b) shows PC Monte Carlo events after the PC 1st reduction. (c) shows the final samples for the data and the the Monte Carlo events. The number of the Monte Carlo events in (c) is normalized to that of the data. The selection criteria are shown by arrows.

(4)     $NHITAC2 < 12 + 0.085 \times PE_{200}$
NHITAC2 is the number of the OD hit PMTs in the 2nd cluster.

Criteria (3) rejects corner clipping muons, which left the hit PMTs in both top (or bottom). Criteria (4) rejects stopping muons by using ID hit cluster located behind the OD hit cluster.

For SK-III, since 1st reduction using the OD segmentation is very efficient, the 2nd reduction consists of only criteria (2) and (3) of SK-II. Figure 5.17 shows the number OD hit PMTs in the 2nd OD hit cluster for the data after 1st reduction, PC Monte Carlo events and the final samples. The criteria (3) is more strict cut of criteria (3) in the 1st reduction. Figure 5.18 shows the scatter plots of $NHITA_{endcap}$ and $NHITA_{side}$ for the data after 1st reduction, PC Monte Carlo events and the final samples.

The event rate after the PC 2nd reduction is $\sim 8000$ events/day.

## 5.2.3   Third Reduction

The flasher events are rejected by the same way as that in the FC 3rd reduction, in which the broad timing distribution of the flasher events is used for the cut. Events which satisfy the following criteria are rejected as the flasher event:

(1)     $NMIN_{100} > 14$
or
$NMIN_{100} > 9$        if   the number of hit ID PMTs < 800
$NMIN_{100}$ is the minimum number of hit ID PMTs in a sliding 100 nsec time window from +300 nsec to +800 nsec.

The stopping muon events are removed by the number of the hit OD PMTs near the entrance position. To find the entrance position, vertex and direction are fitted by the point-fit

80
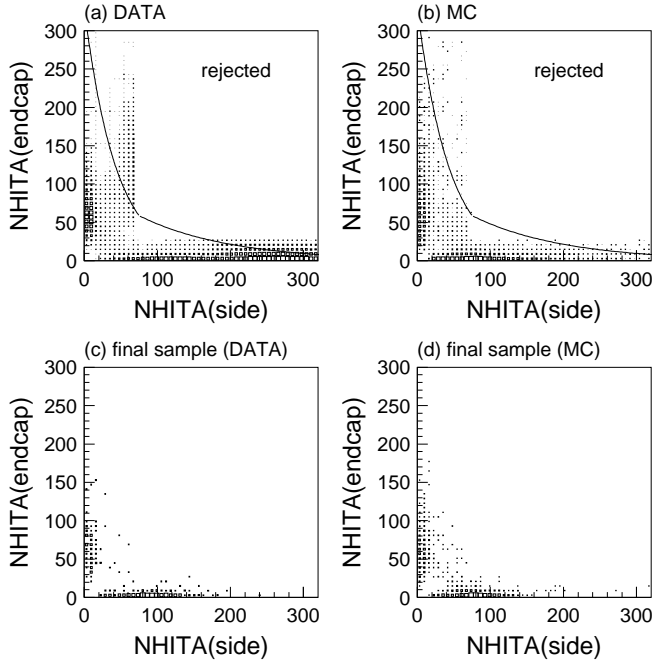
Figure 5.18: (PC 2nd reduction) Scatter plots of NHITA$_{endcap}$ and NHITA$_{side}$. (a) shows the data after the PC 1st reduction. (b) shows PC Monte Carlo events after the PC 1st reduction. (c) and (d) show the final samples for the data and the Monte Carlo events. The size of the boxes shows the number of the events in each bin. The cut criteria are shown by the lines.

(see Section 5.4.1). The entrance position is estimated by a backward extrapolation from the reconstructed vertex. Events satisfying the following criteria are rejected as stopping muons for SK-I and SK-II :

(2)     NHITA$_{in}$ > 10
NHITA$_{in}$ is the number of hit OD PMTs located within 8 m from the entrance point in a fixed 500 nsec time window.

For SK-III, this cut is not used but this cut variable is used in the 5th reduction.

The event rate after the PC 3rd reduction is ∼100 events/day.

### 5.2.4   Fourth Reduction

In the 4th reduction, the selection criteria are completely modified for SK-III. Here describes two versions of the 4th reduction. The event rate after the PC 4th reduction is ∼150 events/day.

< For SK-I and SK-II >

The 4th reduction rejects cosmic ray muons which have the relatively small OD activities. The two types of event reconstruction tools are used in this reduction stage, the Point-fit and a though going muon fit. The through going muon fit determines the entrance point as the position of the earliest hit cluster in the ID. For the PC events, the entrance point can not be correctly determined by the through-going muon fit because they are generated inside the ID, and the goodness tends to be worse compared with the through-going muon events. On the other hand, the vertex position and the direction can be reasonably well estimated by the Point-fit for both the PC events and the cosmic ray muons. An event fulfilling following all criteria are selected:

(1)     $\vec{d}_{\text{pfit}} \cdot \vec{d}_{\text{PMT}}$ should be $> -0.8$
$\vec{d}_{\text{pfit}}$ is the reconstructed direction by Point-fit, and $\vec{d}_{\text{PMT}}$ is the direction from the reconstructed vertex to the earliest saturated PMT.

and

(2)     DCORN should be $> 150\,\text{cm}$
DCORN is the distance from the reconstructed vertex by the Point-fit to the nearest fringe of the ID.

and

(3)     TLMU should be $> 30\,\text{m}$      if   goodness of through-going muon fit $> 0.85$
TLMU is the track length of a muon estimated from the entrance and the exit points by the through going muon fit.

The criterion (1) rejects the cosmic ray stopping muons which have the entrance point in opposite direction to the reconstructed direction by Point-fit. The second criterion aims to reject corner clipping muons. Through-going muons which have a long track length are rejected by the cut criterion (3).

< For SK-III >

The event reconstruction tool is used in this reduction stage. This fitter classifies each event as either, stopping muon, through-going muons, multiple muons or corner clipping muons. 97% of background events are categorized as stopping or through-going muons, whereas 96% PC events categorized as the other muons types. The 5 selections based on the fitter results are follows:

(1)     $\text{angle}_{\text{muon}} < 90^o$
$\text{angle}_{\text{muon}}$ is the angle between the fitted direction and the vector between the Point-fit vertex and the center of the highest charge OD cluster.

(2)     $\text{dotprod}_{\text{muon}} > \text{-0.8}$
$\text{dotprod}_{\text{muon}}$ is similar variable to $\text{angle}_{\text{muon}}$ but using the earliest saturated ID PMT instead of the center of the highest charge OD cluster.

(3)     $\text{length}_{\text{muon}} < 1750$ cm
$\text{length}_{\text{muon}}$ is the length of the fitted muon track. Very long track length hints toward cosmic ray muons.

(4)     $\text{goodness}_{\text{muon}} < 0.52$
$\text{goodness}_{\text{muon}}$ is the goodness from muon fitter.

(5)     $\text{corner}_{\text{muon}} \geq 300$ cm
this is the distance between fitted entrance point and the corner of the tank.

If an event is classified as through-going muon, it should pass 4 of above 5 criteria to be selected. If an event is classified as stopping muon, it should pass 4 of above 5 criteria including $\text{dotprod}_{\text{muon}}$ pass necessarily. Then the stopping muon needs to pass the criteria $\text{goodness}_{\text{muon}} <$
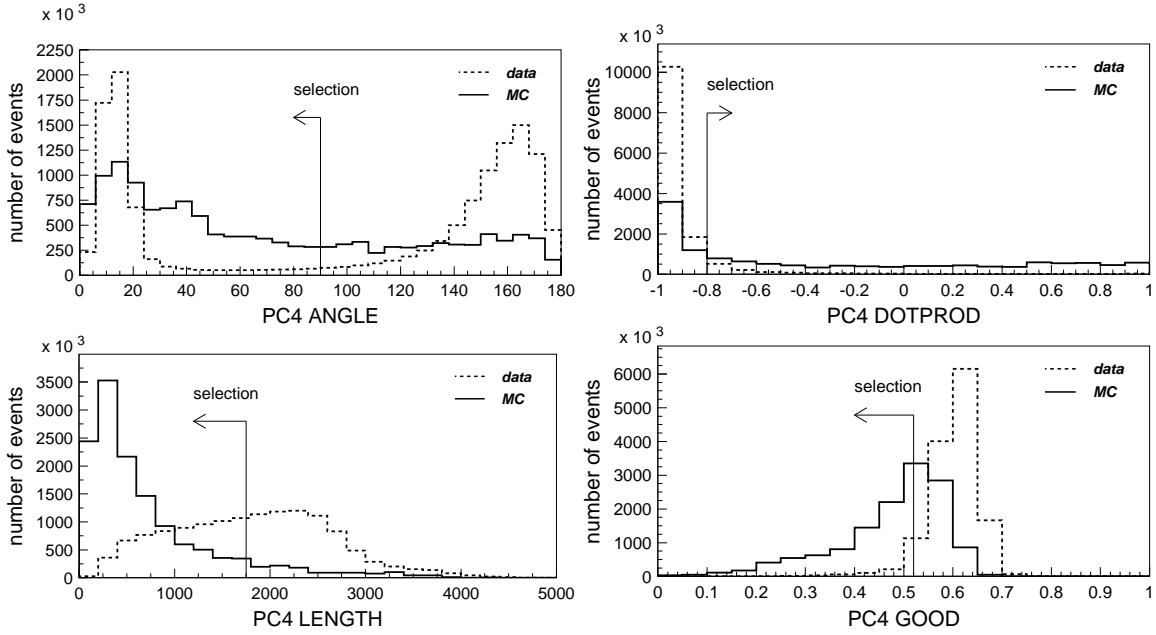
Figure 5.19: (PC 4th reduction) The distributions of variables in 4th reduction for the data (dashed line) and PC MC events (solid line) which are classified as through-going muons or stopping muons after the 3rd reduction. The distributions, angle$_{muon}$, dotprod$_{muon}$, length$_{muon}$ and goodness$_{muon}$ are shown in from the left top panel to the right bottom panel. The number of the Monte Carlo events are normalized to that of the data. The selection criteria are shown by arrows.

0.5 or ehit$_{muon}$ < 10; ehit$_{muon}$ is the number of OD hits located within 8 m from the fitted entrance point in a fixed 500 nsec time window. For events classified as the other types, they have only to pass 2 of above 5 criteria. Figures 5.19 shows the distributions for each cut variable in criteria (1)∼(4) for the data and MC events which are classified as the through-going muon or the stopping muon by the fitter. Figures 5.20 shows the same distributions for the final samples which are classified as the other muon types by the fitter from the final sample.

Finally, events satisfying the following criteria are removed as the low energy background events:

(1)    $PE_{tot} < 2900$ p.e.s
       $PE_{tot}$ is the total number of p.e.s observed in the ID.

The requirement of total photoelectrons > ∼3000 p.e.s, which corresponds to muon momentum of 500 MeV/$c$, is safe for PC events because the exiting muons must have at least momentum of 700 MeV/$c$ to reach the OD.
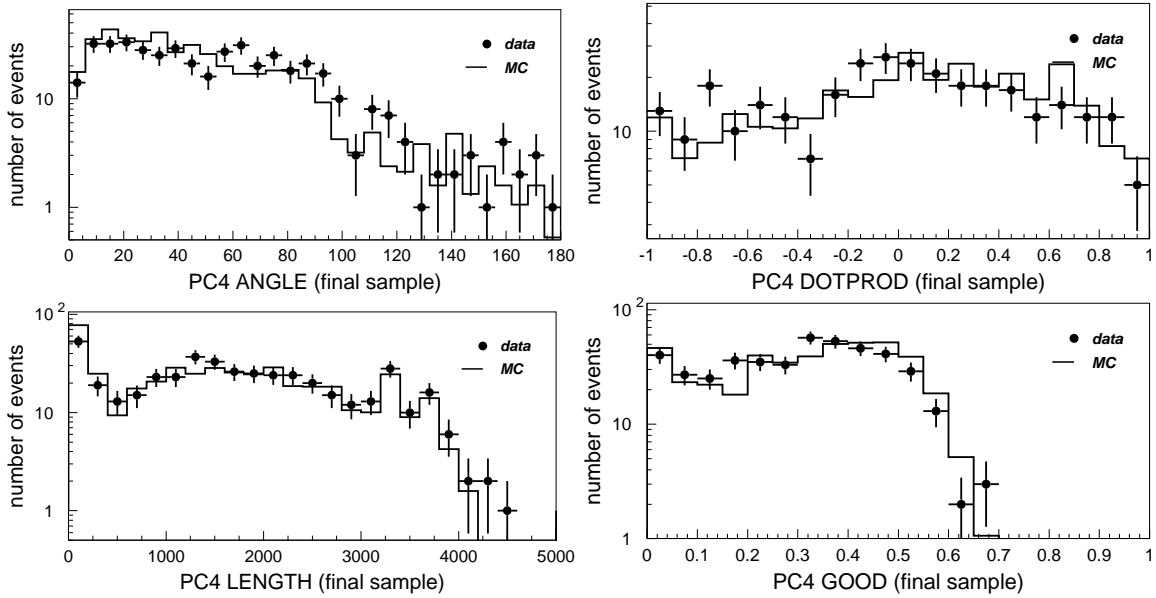
Figure 5.20: (PC 4th reduction) The distributions of variables in 4th reduction for the final samples, data events (dot) and the PC MC events (line) which are classified as multiple muons or corner clipping muons. The distributions, $angle_{muon}$, $dotprod_{muon}$, $length_{muon}$ and $goodness_{muon}$ are shown in from the left top panel to the right bottom panel. The number of the Monte Carlo events is normalized to that of the data.

### 5.2.5 Fifth Reduction

The 5th reduction is the final rejection of the remaining background events. This is done by some elaborate criteria specialized for each background source. In this stage, the SK-III reduction criteria are different from the other SK period. So here also describes two versions of 5th reductions.

< For SK-I and SK-II >

**Low energy event cut**

Events satisfying the following criteria are removed as the remaining low energy background events :

(1)     $PE_{tot} < 3000\,p.e.s$ (1500 for SK-II)
         $PE_{tot}$ is the total number of p.e.s observed in the ID.

**Through-going muon cut A**

The remaining through-going muons are removed by investigating the existence of two OD hit clusters and the existence of hit OD PMTs near the entrance and the exit points. The first cut uses the OD hit cluster information obtained by the algorithm in the PC 2nd reduction. Events satisfying the following criteria are removed as through-going muons :

(1)     $\mathrm{DIST}_{\mathrm{clust}} > 20\,\mathrm{m}$
       $\mathrm{DIST}_{\mathrm{clust}}$ is the distance between the highest charge OD hit cluster and the second highest one.

and

(2)     $\mathrm{PEAC}_{\mathrm{2nd}} \geq 10\,\mathrm{p.e.s}$
       $\mathrm{PEAC}_{\mathrm{2nd}}$ is the number of p.e.s detected in the second highest charge OD hit cluster.

and

(3)     $\mathrm{NCLSTA5} \geq 2$
       NCLST5 is the number of OD hit clusters which contain more than 9 hit PMTs.

In criterion (3), the same clustering algorithm as that in the PC 2nd reduction with different parameters is used. The OD wall is divided into $6 \times 6$ instead of $11 \times 11$ in the PC 5th reduction to avoid the boundary effect of the patches.

The event passed above two cuts is reconstructed its vertex and so on. The reconstruction methods will be described in Section 5.4. After applying the reconstruction, the final background rejections are performed in follows.

**Through-going muon cut B**

Some cosmic ray muons enters from the edge on top, passes along the ID wall and exits from the edge of the bottom. These through-going muon events tend to pass through the former reduction criteria because the light collection efficiency around the edge of the OD is not good and the event reconstruction is not so accurate for these events. To reject these events, the number of hit OD PMTs and the observed p.e.s in 8 m radius spheres centered at the top and the bottom edges or fringes are used. Events satisfying the following criteria are rejected as through-going muons :

(1)     $\mathrm{NHITA}_{\mathrm{top}} \geq 7 \quad$ and $\quad \mathrm{NHITA}_{\mathrm{bottom}} \geq 7$
       $\mathrm{NHITA}_{\mathrm{top}}$ ($\mathrm{NHITA}_{\mathrm{bottom}}$) is the maximum number of hit OD PMTs in a 8 m radius sphere centered at the top (bottom) edge.

and

(2)     $\mathrm{PEA}_{\mathrm{top}} \geq 10\,\mathrm{p.e.s} \quad$ and $\quad \mathrm{PEA}_{\mathrm{bottom}} \geq 10\,\mathrm{p.e.s}$
       $\mathrm{PEA}_{\mathrm{top}}$ ($\mathrm{PEA}_{\mathrm{bottom}}$) is the number of p.e.s in OD detected in the same sphere as that for the $\mathrm{NHITA}_{\mathrm{top}}$ ($\mathrm{NHITA}_{\mathrm{bottom}}$)

and

(3)     $0.75 < \mathrm{TDIFFA} \times c/40\,\mathrm{m} < 1.5$
       TDIFFA is a time interval between the averaged hit timing in the top and the bottom spheres.

**Through-going muon cut C**

The remaining through-going muons are removed by the number of hit OD PMTs near the entrance and the exit points. The vertex position and the ring direction are reconstructed by a precise fit (MS-fit) using the Cherenkov ring pattern (see Section 5.4.4). The entrance and the exit points on the detector wall are estimated by an extrapolation. The cut criteria are follows :

(1)    $\mathrm{NHITA_{in}} \geq 5$    and    $\mathrm{NHITA_{out}} \geq 5$
       $\mathrm{NHITA_{in}}$ ($\mathrm{NHITA_{out}}$) is the number of hit OD PMTs within $8\,\mathrm{m}$ from the entrance (exit) point.

and

(2)    $0.75 < \mathrm{TDIFFA} \times c/\mathrm{TRACK} < 1.5$
       TRACK is distance between the entrance and exit point estimated using the vertex position and the ring direction reconstructed by MS-fit.

**Stopping muon cut A**

The number of hit OD PMTs near the entrance position is counted. The entrance position of the stopping muons are estimated by reconstructing the vertex position and direction using MS-fit and back extrapolating to the wall. Events satisfying the following criteria are rejected as stopping muons :

(1)    $\mathrm{NHITA_{in}} \geq 10$
       $\mathrm{NHITA_{in}}$ is the number of OD hit PMTs within $8\,\mathrm{m}$ from the reconstructed entrance.

**Stopping muon cut B**

The opening angles between the OD hit cluster and the ring estimated by two different fitters, TDC-fit (see Section 5.4.1) and MS-fit are compared. In case of the stopping muon event, the opening angle is expected to be large, while it is small for th PC event. The cut criterion is the following :

(1)    $\Theta_{\mathrm{TDC\text{-}fit}} > 90°$    or    $\Theta_{\mathrm{MS\text{-}fit}} > 90°$

       $\Theta_{\mathrm{TDC\text{-}fit}}$ ($\Theta_{\mathrm{MS\text{-}fit}}$) is the opening angle between the direction to the OD hit cluster and the ring direction reconstructed by TDC-fit (MS-fit).

**Stopping muon cut C**

The charge inside a 42° cone in the ID is used. The vertex and direction are determined by stopping muon fit, which estimate the entrance as the position of the earliest hit cluster in the ID. The entrance position can not be reconstructed correctly for the PC events since the vertex of the PC events are not on the wall. Events satisfying the following criteria are rejected as stopping muons :

(1)    goodness of stopping muon fit > 0

and

(2)      $PE_{cone}/PE_{tot} \geq 0.6$
PE$_{cone}$ is the number of p.e.s observed by ID PMTs located inside a 42° cone.
PE$_{tot}$ is the total number of p.e.s observed in the ID.

and

(3)      NHITA$_{in}$ > 6
NHITA$_{in}$ is the number of hit OD PMTs within 8 m from the entrance position.

**Cable hole muon cut**

The veto scintillation counters are placed over the four cable holes on top of the detector. The simple condition that only requiring veto counter hit is inapplicable for the PC event selection.

(1)      One veto counter hit.

and

(2)      $\vec{d}_{ring} \cdot \vec{d}_{veto\text{-}vertex} > -0.8$
$\vec{d}_{ring}$ is the reconstructed ring direction by TDC-fit, and $\vec{d}_{vertex\text{-}veto}$ is the direction from the hit veto counter to the reconstructed vertex.

**Corner clipping muon cut A**

The corner clipping muon events have a small hit cluster in the ID, then the vertexes are occasionally mis-reconstructed inside the ID. As a result, the track length from the vertex to the exit point reconstructed by MS-fit is large, while the track length which is estimated by the visible energy using the energy loss of muons $\sim 2\,MeV/cm$ is small. The cut criterion for rejecting corner clipping events is the following :

(1)      $E_{vis}/2\,(MeV/cm) < TRACK - 1500$      if TRACK > 15 m
$E_{vis}/2$ is the estimated track length by the visible energy and TRACK is the track length from the vertex to the exit point estimated from the vertex point and the direction by MS-fit.

< For SK-III >

PC reduction for SK-III is modified to keep efficiency as SK-I and II. In this reduction, there are two types of cut, Hard cut and Soft cut. PC events are required to pass all Hard cuts. And, the events may fail Soft cuts just once.
The Hard cuts are:

(1)      Through-going muon cut A

(2)      Through-going muon cut B

(3)      Stopping muon cut B

(4)      Cable hole muon cut

Figure 5.21: (PC 5th reduction) The distribution of DCORN for SK-III. (a) shows the data after the PC 4th reduction. (b) shows PC Monte Carlo events after the PC 4th reduction. (c) shows the final samples for the data and the the Monte Carlo events. The number of the Monte Carlo events in (c) is normalized to that of the data. The selection criteria are shown by arrows.

(5)     Corner clipping muon cut B

Criteria (1), (2), (3) and (4) have already described in above reductions for SK-I and II.

**Corner clipping muon cut B**

This criterion aims to reject corner clipping muons.

(1)     DCORN should be $> 150\,\mathrm{cm}$
DCORN is the distance from the reconstructed vertex by the Point-fit to the nearest fringe of the ID.

Figure 5.21 shows the DCORN distributions for the data, PC atmospheric neutrino Monte Carlo events, and the PC final sample events.

The Soft cuts are:

(1)     Through-going muon cut C

(2)     Through-going muon cut D

(3)     Stopping muon cut A

(4)     Stopping muon cut C

(5)     Stopping muon cut D

(6)     Stopping muon cut E

(7)     Corner clipping muon cut A

(8)     Decay electron cut

Criteria (1), (3), (4) and (7) have been already described in above reductions for SK-I and II.

88
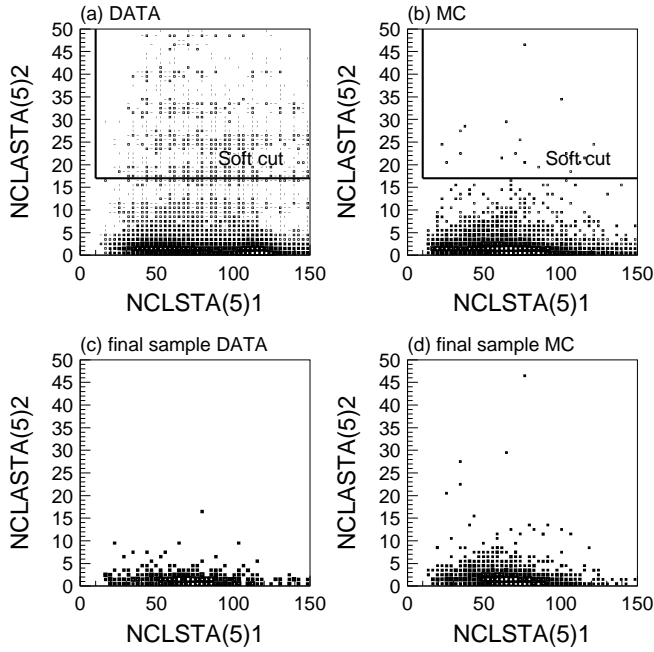
Figure 5.22: (PC 5th reduction) The scatter plots of NCLSTA5(1) and NCLSTA5(2) for SK-III. (a) shows the data after the PC 4th reduction. (b) shows PC Monte Carlo events after the PC 4th reduction. (c) and (d) show the final samples for the data and the the Monte Carlo events, respectively. The Soft cut criteria are shown by lines.

**Through-going muon cut D**

The remaining through-going muons are removed by the number of hit OD PMTs in 1st and 2nd highest charge clusters. The cut criterion is following :

(1)     $NCLSTA5(1) \geq 10$    and    $NCLSTA5(2) \geq 17$
NCLSTA5(1) (NCLSTA5(2)) is the number of hit OD PMTs in 1st(2nd) highest charge cluster.

Figure 5.22 shows the scatter plots of NCLSTA5(1) and NCLSTA5(2) for the data, PC atmospheric neutrino Monte Carlo events, and the PC final sample events.

**Stopping muon cut D**

The stopping muon rejection is performed using the number of OD hits within 8 m of the reconstructed entry point ($NHITA_{in}$) as found in 3rd reduction. In the 3rd reduction, the reconstructed entry point is based on Point-fit. If the entry points between by Point-fit and by MS-fit are not disagreed, this stopping muon rejection is applied.

(1)     $NHITA_{in} > 6$     if $|\overrightarrow{P}_{point} - \overrightarrow{P}_{MS}| < 1500cm$
$NHITA_{in}$ is the number of hit OD PMTs within 8 m from the entrance position.
$\overrightarrow{P}_{point}$ ($\overrightarrow{P}_{MS}$) is the vertex position by the Point-fit (MS-fit).

**Stopping muon cut E**

The same criterion of $angle_{muon}$ in 4th reduction is applied since the cut was looser for the events which were classified as stopping or though-going muons.
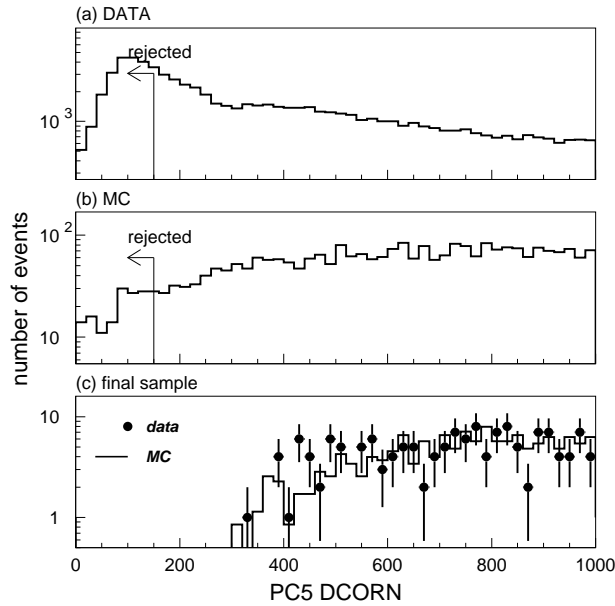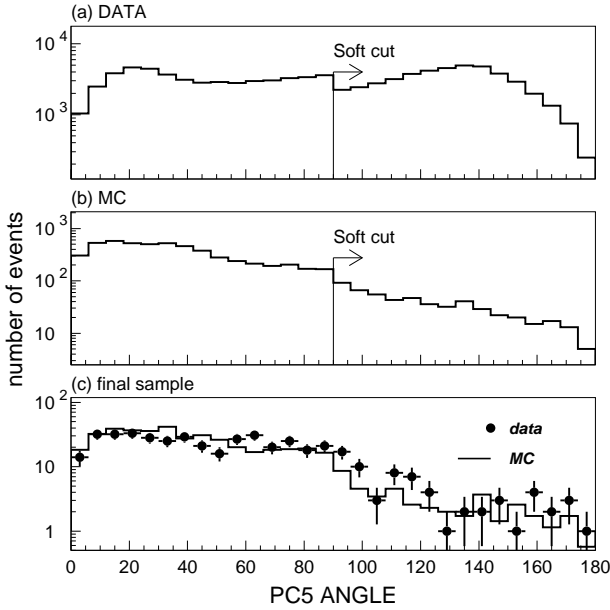
Figure 5.23: (PC 5th reduction) The distribution of angle$_{\text{muon}}$ for SK-III. (a) shows the data after the PC 4th reduction. (b) shows PC Monte Carlo events after the PC 4th reduction. (c) shows the final samples for the data and the the Monte Carlo events. The number of the Monte Carlo events in (c) is normalized to that of the data. The Soft cut criteria are shown by arrows.

(1)     angle$_{\text{muon}}$ < 90°
        angle$_{\text{muon}}$ is the angle between the fitted direction and the vector between the
        pfit vertex and the center of the highest charge OD cluster.

Figure 5.23 shows the angle$_{\text{muon}}$ distributions for the data, PC atmospheric neutrino Monte Carlo events, and the PC final sample events.

**Decay electron cut**

High energy neutrinos mostly interact with nucleons in water via DIS interaction. and produce hadrons including charged pions. Those pions decay into muons which in turn decay into electrons. These electrons can be tagged by the method described in Section 5.4.6. If high energy cosmic ray muon decays in the detector, no decay electron can be observed due to the decay in flight. Therefore no decay electron event with high energy, $E_{vis} > 25\,\text{GeV}$, are rejected as the cosmic ray muon.

## 5.2.6   PC Reduction Summary

Finally, the partially contained neutrino events are selected by following criteria :

· Vertex of neutrino interactions is inside the fiducial volume (2 m from the ID PMT surface).

· The number of hit PMTs in the highest charge OD cluster (NHITAC) is larger than 15 (9 for SK-I).

· Visible energy ($E_{vis}$) is greater than 350 MeV
  ( The total observed charge of ID is > 3000 p.e.s (1500 p.e.s for SK-II) )

The detection efficiency in each reduction step is estimated by the atmospheric neutrino Monte Carlo events as shown in Table 5.3. The detection efficiency for final events is estimated to

| PC | SK-I | SK-II | SK-III |
|---|---|---|---|
| reduction step | selection efficiency (%) | | |
| 1st | 98.98 | 98.58 | 99.08 |
| 2nd | 96.74 | 93.43 | 98.50 |
| 3rd | 95.69 | 92.32 | 98.49 |
| 4th | 89.86 | 84.60 | 97.79 |
| 5th | 88.66 | 82.63 | 96.54 |
| 5th(FV) | 80.98 | 74.80 | 88.64 |
| | number of events | | |
| Monte Carlo | 1185.5 | 589.6 | 437.7 |
| DATA | 896 | 430 | 343 |
| (event rate[/day]) | (0.60±0.02) | (0.54±0.03) | (0.66±0.04) |

Table 5.3: Selection efficiencies and number of events for PC sample are summarized for each SK period. The selection efficiencies are for events whose real vertex is in the fiducial volume, the number of outer detector hits more than 15(9 for SK-I) and the total observed charge larger than 3000p.e.s (1500p.e.s for SK-II). In the last line with FV, events with the fitted vertex in fiducial volume are selected. Numbers of events for MC are normalized without oscillation to the livetime for the data, 1489.2, 798.6 and 518.1 days for SK-I, SK-II and SK-III, respectively.

be 81.0 %, 74.8 % and 88.6 % for SK-I, SK-II and SK-III, respectively. The number of selected events for each SK period are shown in Table 5.3.

The background events in final PC sample mainly come from cosmic ray muons. These background events are checked by eye-scan. Few background events contaminate PC final sample but the most of background events are rejected by the fiducial volume cut. The contaminations due to the background events is also estimated by extrapolating the distribution of background events outside the fiducial volume. Figure 5.24 shows the number of background events outside the fiducial volume for SK-II. Background events in the fiducial volume may lead to contamination as shown by the fitted exponential curve in this figure. As the results of eye-scan check and the extrapolation estimation, the number of background events is expected to be 3 events for SK-II. Table 5.4 summarizes the estimated contaminations due to background events for each SK run period.

Uncertainties of the PC reduction efficiencies are estimated by the difference of cut variables between data and Monte Carlo. The uncertainties are estimated to be 2.4%, 4.8% and 0.5% for SK-I, SK-II and SK-III, respectively. The smaller uncertainty is obtained for SK-III due to the improvement of the reduction efficiency and also better matching between data and MC distributions for cut variables by introducing new cuts or modification of the existing cuts.

### 5.2.7 PC OD stop/through separation

The events stopping in the outer detector region contain in the PC sample. Such events can be accurately reconstructed their energies rather than events going out through the OD. Thus
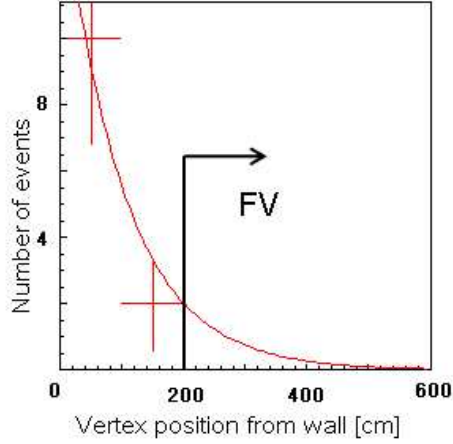
Figure 5.24: The number of background events outside of fiducial volume as a function of the reconstructed vertex position from the ID surface. The line shows the fitted exponential curve.

|  | SK-I | SK-II | SK-III |
|---|---|---|---|
| cosmic ray BG | 0.2% | 0.7% | 1.8% |

Table 5.4: Estimated contamination of cosmic ray muons for PC sample.

PC sample is further separated to two categories, OD stopping and OD through-going, by the energy deposit in OD region. The selection criteria for the OD stopping event are follows :

- The maximum number of p.e.s observed in the OD in a sliding 500 nsec time window from $-400$ nsec to $+600$ nsec ($PE_{anti}$) is less than $PE_{exp}/1.5$
  ($PE_{exp}$ is the expected number of p.e.s in the OD from the potential track length in the OD).

- The most energetic ring or the second one should be identified as $\mu$-like.

Figure 5.25 shows the $PE_{anti}/PE_{exp}$ distributions of the data and PC Monte Carlo events which exit from ID barrel region to OD region.

## 5.3 Reduction for Upward-going Muon Events

The reduction for the upward-going muon (UPMU) events are briefly described in following sections.

### 5.3.1 Charge cut

In the first reduction, the low energy events and extremely high energy events are rejected :

(1)    $PE_{tot}$ should be $> 6000$ p.e.s (3000 p.e.s for SK-II)

and

(2)    $PE_{tot}$ should be $< 1,750,000$ p.e.s (800,000 p.e.s for SK-II)
    $PE_{tot}$ is the total number of p.e.s observed in the ID.
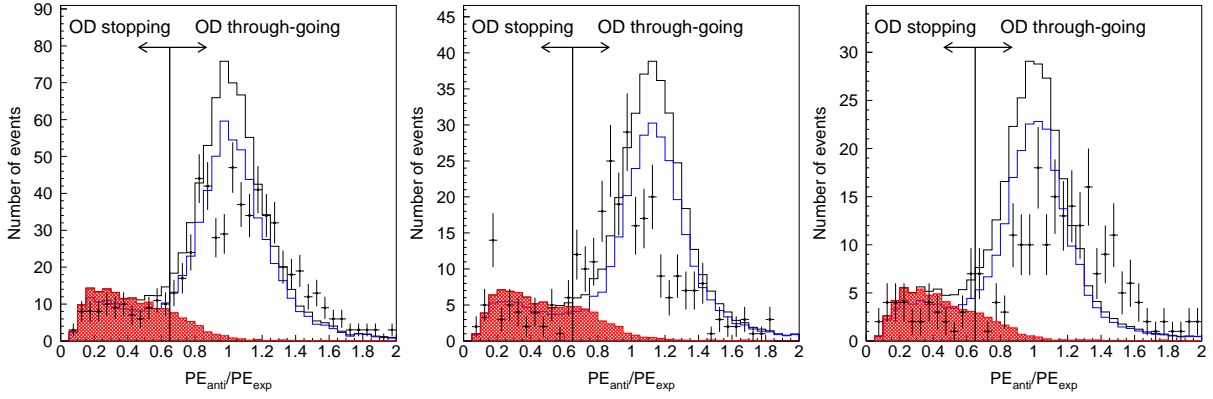
Figure 5.25: The distributions of $PE_{anti}/PE_{exp}$ for the PC stop/through separation for the events exiting from ID barrel region to the OD. The left, middle and right panels show for SK-I, SK-II and SK-III, respectively. The points show the data, and histograms show the PC atmospheric neutrino Monte Carlo events assuming no oscillation (black lines) and $\nu_\mu \leftrightarrow \nu_\tau$ 2-flavor oscillation with $(\sin^2 2\theta, \Delta m^2) = (1.00, 2.5 \times 10^{-3} \, \mathrm{eV}^2)$ (blue lines). Filled histograms are the true number of the OD stopping MC events without the oscillation. The selection criteria are shown by arrows.

$PE_{tot}=6000$ p.e.s corresponds to muon momentum of $1 \, \mathrm{GeV/c}$ and to track length of $3.5 \, \mathrm{m}$. The requirement for final sample is track length longer than $7 \, \mathrm{m}$ so this criterion is safe. At very high ID charge corresponding to $\sim 1{,}750{,}000$ p.e.s, the ID electronics is saturated and the muon fitters cannot work.

### 5.3.2 Zenith angle cut

In order to reject the downward-going muon cosmic ray muons, seven different fitters specialized to fit stopping muons, through-going muon events and muon events with Bremsstrahlung are used. The algorithm of the zenith angle cut is as following :

(1) Apply a muon fitter.

(2) If the event is classified as upward and the goodness of fit is above the threshold, the event is saved.

(3) If the event is classified as downward and the goodness of fit is above the threshold, the event is rejected.

(4) If the event is classified as horizontal with the goodness of fit above the threshold, or if the goodness of fit is below the threshold, the judgment is suspended.

(5) Go to (1) and apply the next muon fitter.

This sequence continues until the event has passed through all the fitters or has been classified. If no fitter gives a goodness above the threshold, the event is rejected, while if at least one fitter classifies the event as horizontal, the event is saved. Detailed description about the seven muon fitters and the definition of the goodness can be found in [127].

All events from the output of the upward-going muon reduction are passed through the precise fitter which is described in section 5.4.4. The fitter results are used to select upward-going events by the criterion that zenith angle is $\cos\Theta < 0$.

### 5.3.3 Scanning

In order to eliminate the remaining misfitted backgrounds events, the selected events are scanned by physicists using a visual display. The upward-going muon events are selected one by one. All events are checked by two independent scanners not to miss neutrino events. The efficiency of scanning is estimated to be almost 100 %. About a half of the events remaining after all the automated reduction steps are rejected by this final scan. We note that the scanners only check that the reconstructed vertex and direction is not largely wrong.

### 5.3.4 UPMU Reduction Summary

The final selection criteria for UPMU stopping events are :

- fitter classification is stopping event

- the fitted momentum $\geq 1.6$ GeV/c (corresponding to track length = 7 m)

- the number of hit OD PMTs within 8 m from the exit point (NHITEX) < 10 (16 for SK-II).

The selection criteria for UPMU through-going events are :

- fitter classification is through-going event

- the distance from the ID entrance point to the ID exit point $\geq 7$ m

- the number of hit OD PMTs within 8 m from the exit point (NHITEX) $\geq 10$ (16 for SK-II).

Figure 5.26 shows the distributions of NHITEX. The detection efficiency for the final events is estimated to be 98.0% (99.4%) for SK-I Stopping muons (Through-going muons), 97.0% (98.1%) for SK-II Stopping muons (Through-going muons), 98.2% (99.4%) for SK-III Stopping muons (Through-going muons). The number of events in the final sample are summarized in Table 5.5. The final sample is made by subtracting the expected background events. The background estimation method is described in the next section.

### 5.3.5 Background estimation for Upward-going muon

The background events are mostly cosmic-ray muons, which are reconstructed as upward-going due to multiple Coulomb scattering of the muons or to the slight mis-reconstruction of near horizontally going muons. Therefore, they are mostly distributed in the most horizontal bin $(-0.1 < \cos\theta < 0)$. The contaminations of the backgrounds are estimated by extrapolating the distribution of downward events in $0 < \cos\theta$. Figure 5.27 shows the zenith versus azimuth directions for the upward going muon sample. Clusters of cosmic ray downward muons are seen in the regions zenith angle $\cos\Theta > 0$ (downward) and azimuth angle around $\phi = 120°$, $180°$ and $270°$. These clusters are caused by the thin rock covered over the detector. When

94
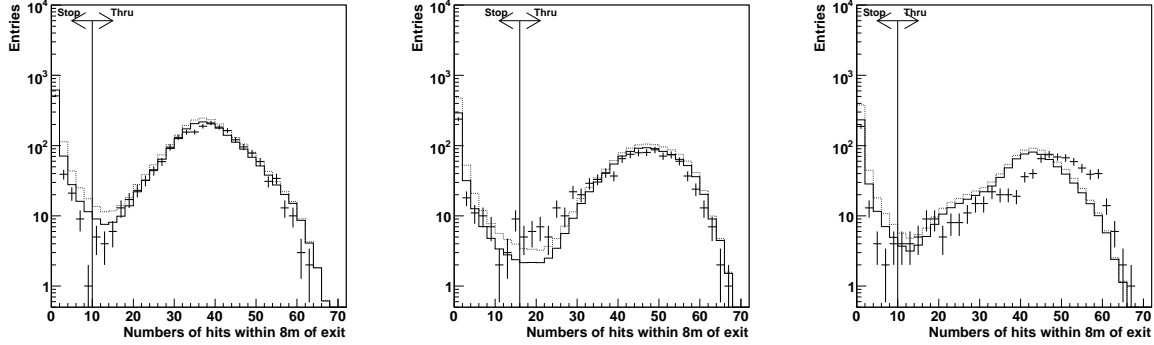
Figure 5.26: The distributions of NHITEX for the UPMU stop/through separation for SK-I (left), SK-II (middle) and SK-III (right). The points show the observed data, and histograms show the PC atmospheric neutrino Monte Carlo events assuming no oscillation (dashed lines) and $\nu_\mu \leftrightarrow \nu_\tau$ 2-flavor oscillation with $(\sin^2 2\theta, \Delta m^2) = (1.00, 2.5 \times 10^{-3}\,\text{eV}^2)$ (solid lines). The selection criteria are shown by arrows.

| UPMU | SK-I | | SK-II | | SK-III | |
|---|---|---|---|---|---|---|
| | stopping | through | stopping | through | stopping | through |
| final sample (MC) | 701.7 | 1850.7 | 355.2 | 915.4 | 273.8 | 715.6 |
| final sample (data) | 465 | 1879 | 223 | 871 | 210 | 735 |
| BG subtracted | 432 | 1848.6 | 210 | 833.4 | 193 | 722.9 |
| event rate (/day) | 0.26±0.01 | 1.12±0.03 | 0.25±0.02 | 1.01±0.30 | 0.03±0.02 | 1.14±0.04 |

Table 5.5: Number of events for UPMU data sample are summarized for each SK period. For the BG subtraction, see the text. Numbers of MC events and event rate are calculated by normalization of the livetime, 1645.9, 827.7 and 635.6 days for SK-I, SK-II and SK-III, respectively.

95

| | SK-I | | SK-II | | SK-III | |
|---|---|---|---|---|---|---|
| | BG event | sys. error | BG event | sys. error | BG event | sys. error |
| stopping $\mu$ | 1.97% | 16% | 1.59% | 21% | 2.69% | 20% |
| through $\mu$ (non-shower) | 1.01% | 11% | 2.02% | 15% | 0.65% | 19% |
| through $\mu$ (shower) | 0.81% | 18% | 2.53% | 14% | 1.26% | 24% |

Table 5.6: The fraction of the estimated number of background events, contamination of horizontal muon to UPMU sample, in the zenith angle $-0.1 < \cos\theta < 0$. These numbers are normalized by the livetime, 1645.9, 827.7 and 635.6 days for SK-I, SK-II and SK-III, respectively. The uncertainties for each estimated number of background events are also shown.

the contamination of the background events is estimated, the upward going muon samples are divided into two azimuth angle regions. Figure 5.28 shows the azimuth angle distributions for upward going muon samples, in which region (2) shows the thinner mountain direction, which is defined as $60° < \phi < 310°$ and region (1) shows the thicker mountain direction.

Figure 5.29 shows the zenith angle distributions for upward-going muon samples, in which region (1) and (2) are normalized by the coverage of the azimuth angle. While the zenith angle distributions are almost flat for upward going events ($\cos\Theta < 0$), the number of events in the region (2) exponentially increase with the cosine of zenith angle for downward-going ($\cos\Theta > 0$). The contaminations of the cosmic ray muons into the upward-going direction are estimated by an extrapolation from the downward direction in the region (2) with ($exponential + constant$) function. In Figure 5.29, there are the best-fitted curves as the function which is defined as $f(\cos\theta) = p0 + \exp(p1 + p2(\cos\theta))$. In the fitting, $p0$ is fixed to the value determined by the average of region (1) events. The contaminations of background events are estimated by $N_{bg} = \int_{\cos\theta_x}^{0} (\exp(p1 + p2(\cos\theta)))$. The numbers of fraction of background events in the range of $-0.1 < \cos\Theta < 0$ are summarized in Table 5.6. The uncertainties of these estimated numbers of background events are evaluated by the maximum change on the number of background events when fit parameters ($p0, p1$ and p2) shift to increase or decrease the background events within that parameter's allowed regions. Table 5.6 also summarizes the systematic uncertainties for each sample.

### 5.3.6 Upward through-going showering muon

Among the upward through-going muon events, some of them are accompanied with an electromagnetic shower. The showering muons are observed as the high energy muons which lose energy through radiative processes such as bremsstrahlung, $e^+$ $e^-$ pair production and photo-nuclear interaction. Thus, the energy of the parent neutrino is approximately 1 TeV. Therefore, the upward through-going muons is further separated into showering muon sample and non-showering sample. Figure 5.30 shows the energy spectrum of the primary neutrino for those UPMU samples.

The showering muons selection uses $\chi^2$ test based on the observed charge and the expected charge of the non-showering muons [127]. The difference between the corrected observed charge and the expected charge of non-showering muon is set as $\Delta(Q)$. The selection of the showering muon criteria are follows :
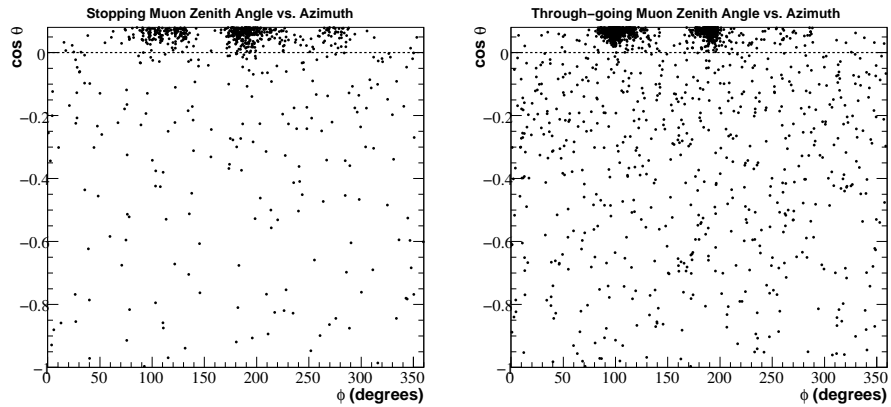
Figure 5.27: The scatter plots of the zenith versus azimuth directions for stopping muon (left) and through-going muons (right) samples for SK-III.
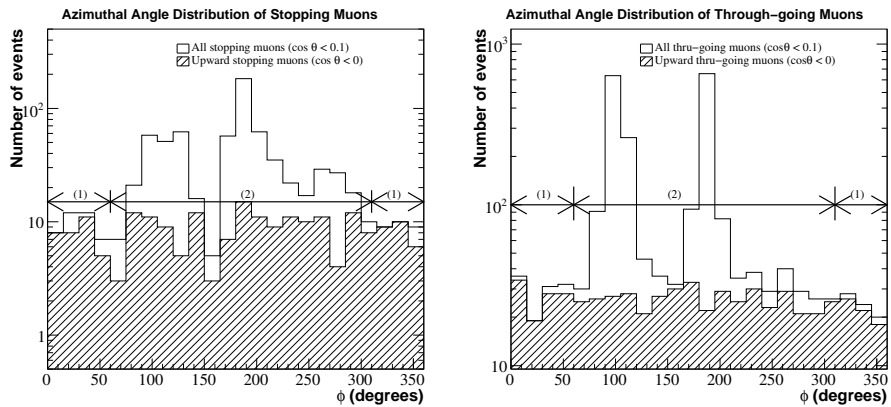


Figure 5.28: The azimuth angle distributions for stopping muon (left) and through-going muons (right) samples for SK-III. Region (1) is the thicker-mountain direction. Region (2) is the thinner-mountain direction. White histograms show the events of downward-going muons, while the hatched histogram is upward-going muons.
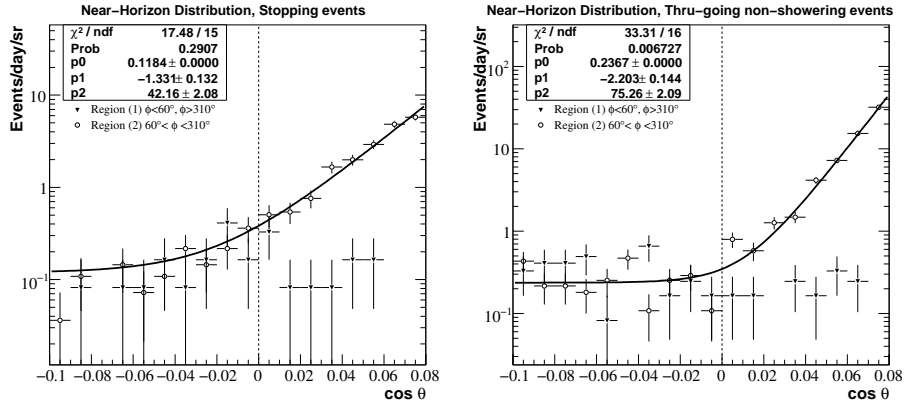
Figure 5.29: The zenith angle distributions for stopping muon (left) and through-going muons (right) samples for SK-III in both regions (1) and (2). The solid curves are fitted functions to estimate the background contaminations.
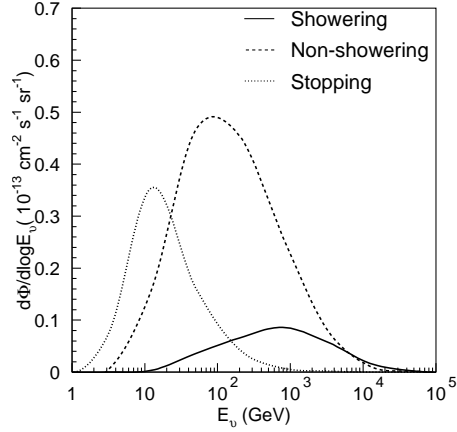


Figure 5.30: The energy spectrum of primary neutrino for upward stopping (dotted line), non-showering (dashed line) and showering (solid line) muon events.

- The difference between the corrected charge and the expected charge for non-showering muon $(\Delta(Q) = <Q> - q_l) > 0.5$ when $\chi^2$ variable for showering selection $\geq 50$.

- $\Delta(Q) > 4.5 - 0.08\chi^2$ when $\chi^2 < 50$.

Figure 5.31 shows the scatter plot of $\Delta(Q)$ and $\chi^2$, and $\Delta(Q)$ distributions for the data and MC events which are classified as through-going muon.
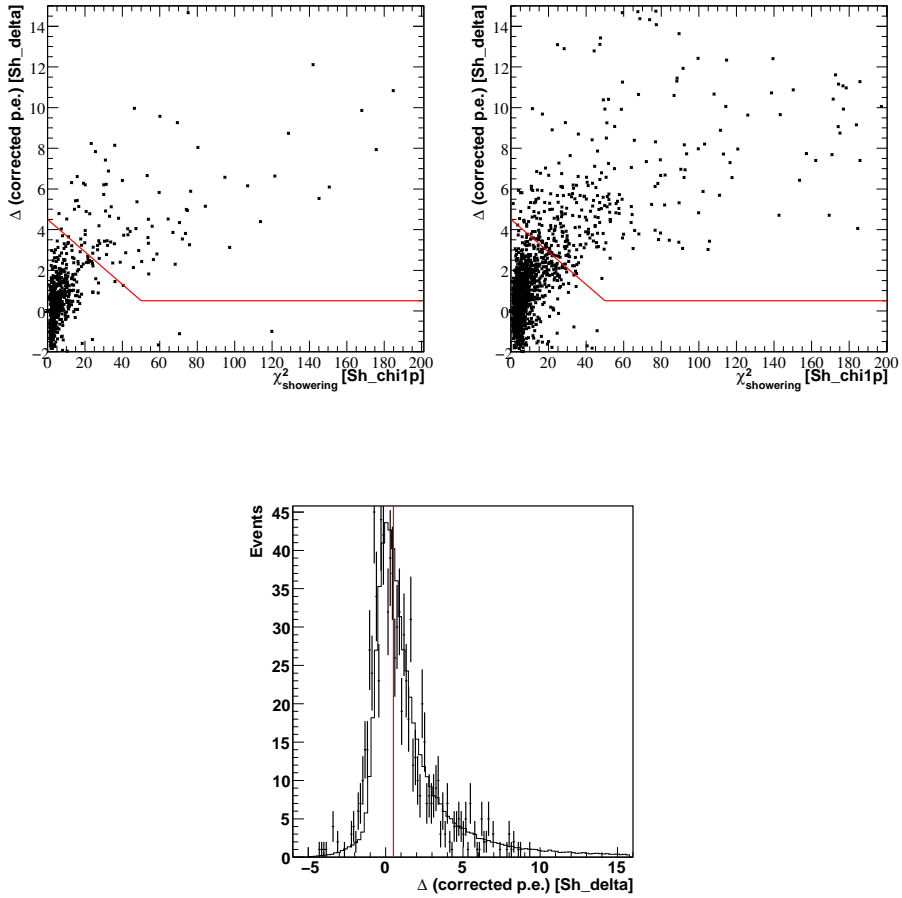
Figure 5.31: The distributions for the UPMU showering separation for SK-III. The scatter plot of $\Delta(Q)$ and $\chi^2$ of UPMU through-going events for the data (left) and MC (middle). $\Delta(Q)$ distributions are shown in right panel with the data (point) and MC events (histogram) The selection criteria are shown by red lines.

## 5.4    Event Reconstruction

Selected neutrino events are reconstructed to get their neutrino flavor type, directions momentum and so on. For FC and PC events, the reconstruction process consists of following steps :

(1) Vertex Fitting

The vertex position is determined as the point where the timing residual distribution of hit PMTs has the sharpest peak. The direction and the outer edge of the dominant ring is estimated.

(2) Ring Counting

The other possible rings are searched for using the vertex position and the direction of the dominant ring. The ring candidates are tested whether they are true rings or not by a likelihood method, then the number of rings is determined.

(3) Particle Identification

Each ring is classified into two types, a showering type $(e^{\pm}, \gamma)$ to be called as e-like and non-showering type $(\mu^{\pm}, \pi^{\pm})$ to be called as $\mu$-like, based on a likelihood method using the Cherenkov ring pattern and the Cherenkov opening angle.

(4) Precise Vertex Fitting (MS-fit)
(only for single-ring event)

More precise vertex position is determined using the Cherenkov ring pattern assuming the obtained particle type.

(5) Momentum Determination

The momentum of each ring is determined by the detected charge inside a Cherenkov cone. The conversion from the charge to the momentum is based on a Monte Carlo simulation and the detector calibration.

(6) Decay Electron Search

Decay electrons produced by the primary events are searched.

(7) Ring Number Correction
(only for FC multi-ring events)

Rings which have fitted by mistake are discarded using precise reconstructed information.

(8) $\pi^0$ Fitting
(only for FC single-ring e-like events)

Candidates $\pi^0$ events are searched for among the events which are recognized as single-ring e-like by the above reconstruction processes.

UPMU events are also reconstructed by using some of these processes. Since PC and UPMU events are basically treated as single-ring and $\mu$-like events, information such as PID and the number of rings for these events are not used in the analysis.

In following sections, the reconstruction methods are described briefly. Detailed explanation of the reconstruction can also be found in [128]. The distributions and the numbers of Monte Carlo events found in following sections are assumed to have undergone 2-flavor oscillation with $(\sin^2 2\theta,\ \Delta m^2) = (1.00,\ 2.5 \times 10^{-3}\,\text{eV}^2)$.

## 5.4.1 Vertex fitting

The vertex position is reconstructed using the timing information of hit PMTs in three steps.

In the first step, a simple fit, called Point-fit is applied. A vertex is roughly estimated under an assumption that all photons are emitted at the same time from a point source. Subtracting the time of flight from a tested vertex a distribution of residual PMT hit times is constructed. The point which gives maximal goodness-of-fit, defined as a Gaussian fit to this distribution, is taken as the vertex of the event.

In the second step, the direction and the outer edge of the dominant ring is measured. A pair of direction and opening angle is tested by a parameter defined as:

$$Q(\theta_{\text{edge}}) = \frac{\displaystyle\int_0^{\theta_{\text{edge}}} \text{PE}(\theta)d\theta}{\sin\theta_{\text{edge}}} \times \left( \left.\frac{d\text{PE}(\theta)}{d\theta}\right|_{\theta=\theta_{\text{edge}}} \right)^2 \times \exp\left( -\frac{(\theta_{\text{edge}} - \theta_{\text{exp}})^2}{2\sigma_\theta^2} \right) \qquad (5.4)$$

where $\theta_{exp}$ and $\sigma_\theta$ are the Cherenkov opening angle expected from the charge within the Cherenkov corn and its resolution, respectively. $\text{PE}(\theta)$ is the angular distribution of the observed charge as a function of the opening angle $\theta$. Varying the direction around that given by Point-fit, the direction and the ring edge which maximize $Q(\theta_{edge})$ are estimated.

In the final step, more precise vertex position is determined, which is called TDC-fit. Unlike Point-fit, photons are assumed to be generated along the particle's track. Then the time residual for PMTs inside of the Cherenkov ring is calculated considering this effect. For the photons outside the ring, the time residual is still computed assuming all photons originated at the vertex and the goodness-of-fit is defined including the effect of scattering photons. Then the precise vertex is determined as the position to maximize the goodness parameter.

The vertex position thus determined is used for multi-Cherenkov-ring events. Figure 5.37 and Table 5.9 show the estimated vertex position resolutions for multi-ring events. For single ring events, a more precise fitter is used, see Section 5.4.4.

## 5.4.2 Ring counting

After an initial Cherenkov ring is detected and the vertex is determined, other ring candidates are searched for by a Hough transform method [132]. Figure 5.32 illustrates the method to find other possible rings, in witch a spherical coordinate centered on the vertex position is considered. The shaded circle in this figure represents the Cherenkov ring image. The dashed line circles centered on the hit PMTs are drawn with 42° half angle. The direction of the Cherenkov ring is identified as a intersection point of those dashed line circles. The second ring candidate is searched for choosing possible ring directions based on this method, and likelihood technique is used to determine if the candidate ring is consistent with a ring. If the second ring
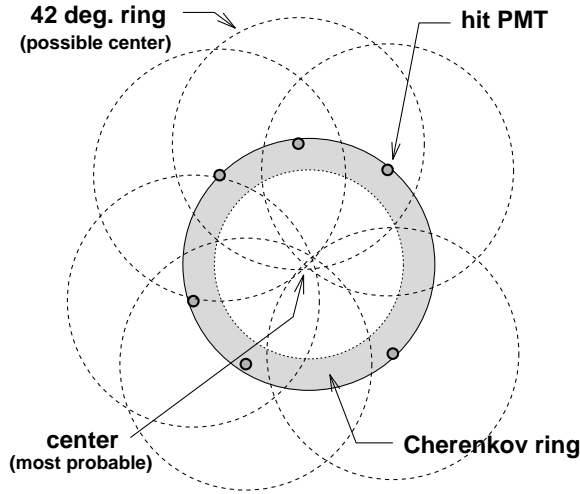
Figure 5.32: A basic idea of finding ring candidates is shown. By drawing rings around the hit PMT with Cherenkov opening angle of 42 ° from the vertex, the center of the actual Cherenkov ring can be identified.

| | SK-I | | SK-II | | SK-III | |
|---|---|---|---|---|---|---|
| | sub-GeV | multi-GeV | sub-GeV | multi-GeV | sub-GeV | multi-GeV |
| CCQE $\nu_e$ | 97.1 % | 94.5 % | 95.7 % | 93.6 % | 97.3 % | 95.6 % |
| CCQE $\nu_\mu$ | 97.2 % | 95.9 % | 97.2 % | 96.8 % | 97.2 % | 95.8 % |

Table 5.7: The efficiencies to select CCQE events as single-ring for each SK period. Sub-GeV and Multi-GeV represent with $E_{vis} < 1.33$ GeV and $E_{vis} > 1.33$ GeV, respectively.

is determined to be existing, the same procedure is repeated to find other possible rings up to 5 rings. Figure 5.33 show the likelihood distributions between single-ring and multi-ring for both the data and Monte Carlo. The cut threshold is 0 to separated single-ring events from multi-ring events. The efficiencies to select CCQE events as single-ring are summarized in Table 5.7.

The distributions have slight difference between the data and MC. This difference is taken as a source of systematic uncertainty in the event selection.

### 5.4.3 Particle Identification

The detected Cherenkov rings are identified as e-like or $\mu$-like by Particle Identification (PID). Figure 5.34 shows the event display of electron and muon neutrino MC events. An electron (and a gamma-ray) produces diffused ring pattern since electrons produce the electromagnetic shower and low energy electrons suffer multiple scattering whereas muon (and charged pion) produces shaper ring edges. In addition, the Cherenkov rings from muons or charged pions can have smaller Cherenkov angles if they are not highly relativistic ($\beta = v/c < 1$). These differences are taken into account to classify the event into 2 types by the PID algorithm.

Figures 5.35 and 5.36 show the PID likelihood distribution for FC single-ring sample and
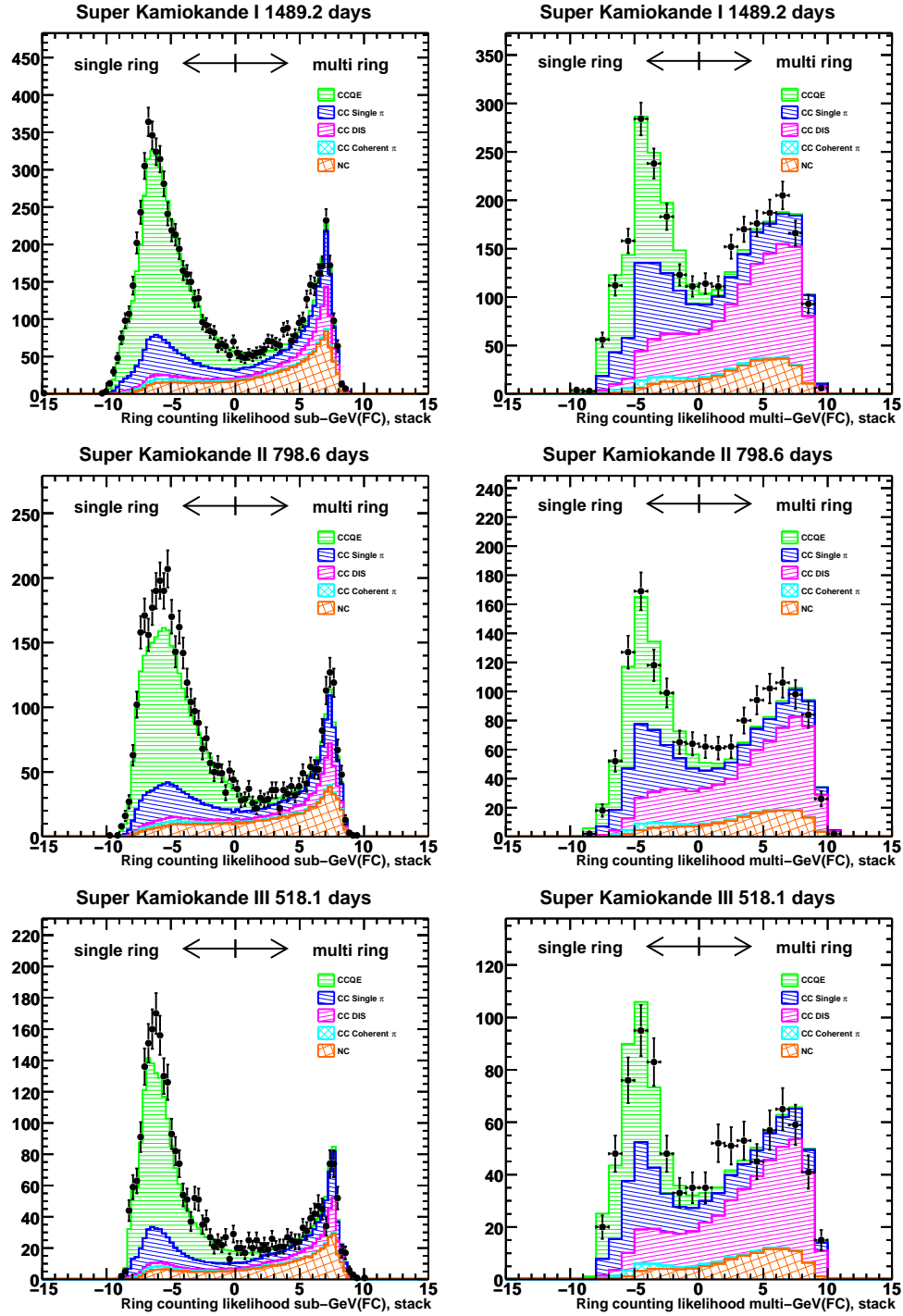
Figure 5.33: The ring counting likelihood distribution for SK-I (upper), SK-II (middle) and SK-III (lower). The left (right) side plots are in case of FC Sub-GeV (Multi-GeV) sample. Dots (solid lines) are the data (the MC events). The MC histograms assume the 2-flavor oscillation $(\sin^2 2\theta, \Delta m^2) = (1.00, 2.5 \times 10^{-3} \, \text{eV}^2)$. Hatched green histograms show the CCQE interactions.
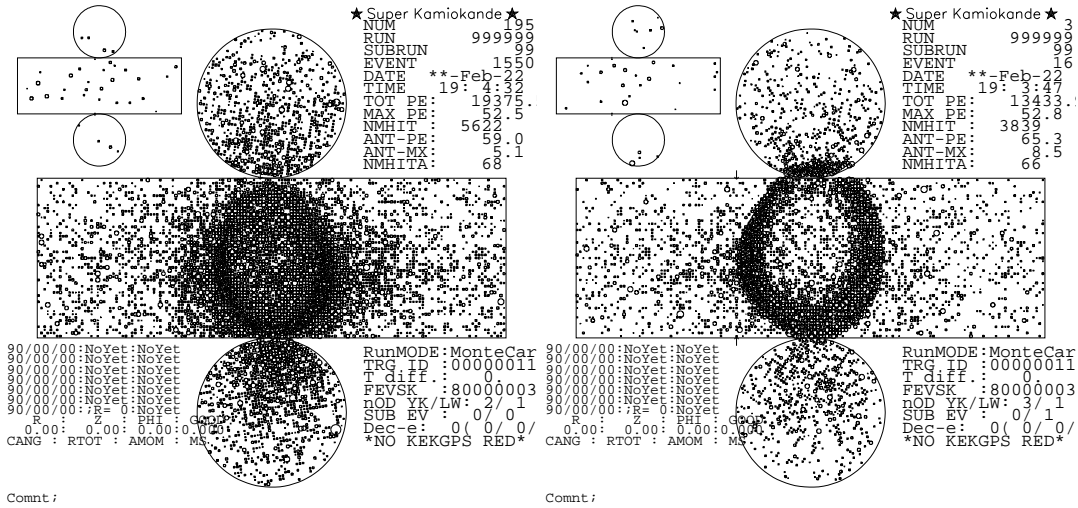
Figure 5.34: Event display of single-ring electron (left) and single-ring muon (right) neutrino MC event.

| | SK-I | SK-II | SK-III |
|---|---|---|---|
| $\nu_e$ mis-identified as $\nu_\mu$ | 1.0 % | 1.2 % | 1.5 % |
| $\nu_\mu$ mis-identified as $\nu_e$ | 0.7 % | 0.8 % | 0.5 % |

Table 5.8: The misidentification probabilities of PID for Sub-GeV 1-ring CCQE events for each SK run period.

multi-ring sample, respectively. The separation of particle type for multi-ring events is not as good as that for a single-ring event due to overlapping of Cherenkov photons from multiple Cherenkov rings. The misidentification probabilities for single-ring events are summarized in Table 5.8.

The distributions have slight difference between the data and MC. This difference is taken as a source of systematic uncertainty in event selection.

### 5.4.4 Precise Vertex Fitting

The FC/PC single-ring events are re-fitted to optimize their vertex position and direction using expected light pattern such as e-like or $\mu$-like. This fitter is called MS-fit. UPMU events are also fitted by MS-fit with the assumption that the particle is a muon and the vertex is at the inner detector surface.

The performance of fitting, MS-fit for single-ring events and TDC-fit for multi-ring events, is represented by the resolution which is estimated using atmospheric neutrino Monte Carlo sample. Figure 5.37 shows the distance between the true vertex and the reconstructed vertex for various single-ring samples. Figures 5.38 and 5.39 show the angular difference between the true direction and the reconstructed direction. The estimated resolutions including those for multi-ring events are summarized in Table 5.9.
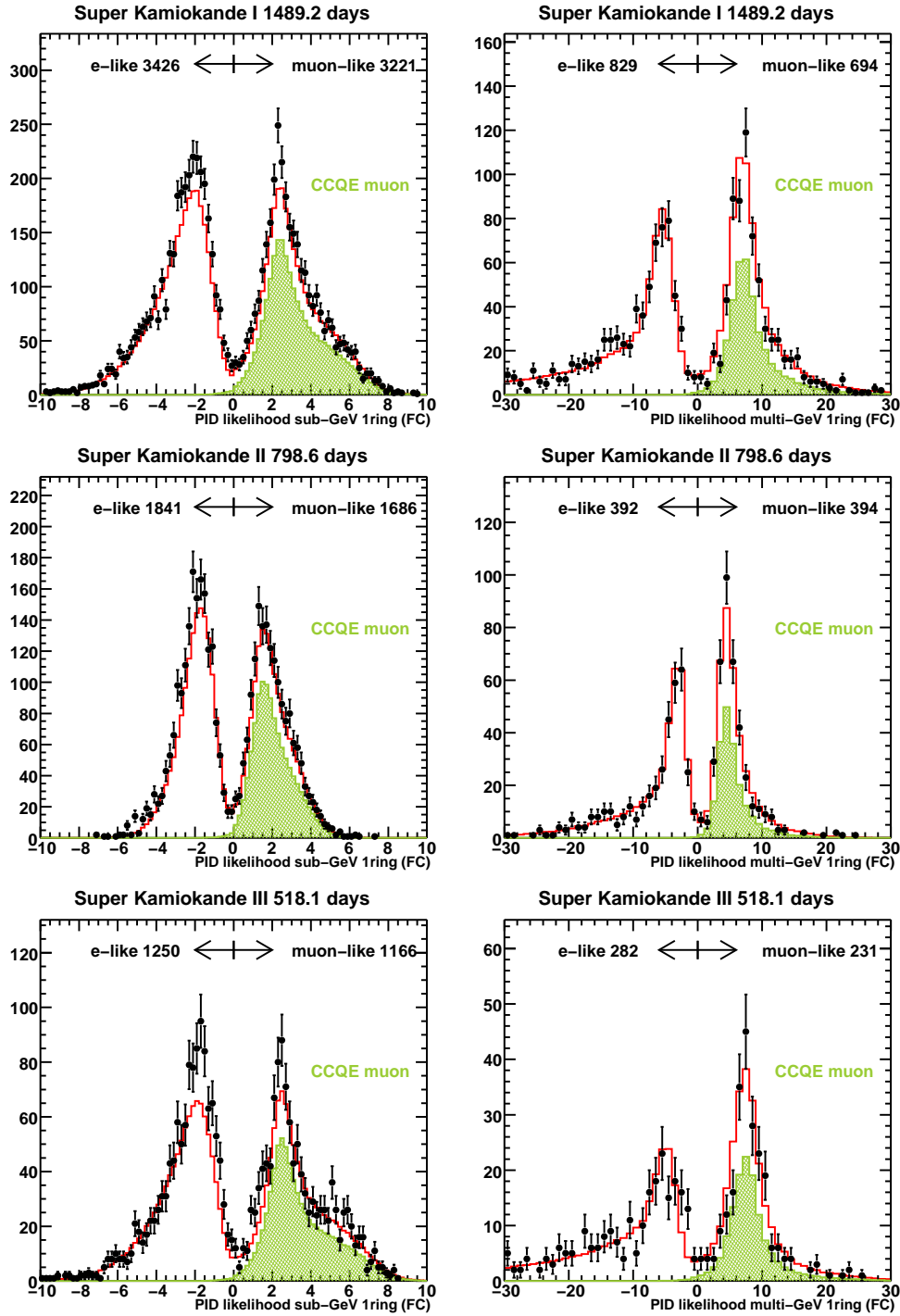
Figure 5.35: The PID likelihood distribution for FC 1-ring sample for SK-I (upper), SK-II (middle) and SK-III (lower). The left (right) side plots are in case of FC Sub-GeV (Multi-GeV) 1-ring sample. Dots (solid lines) are the data (the MC events). The MC histograms assume the 2-flavor oscillation $(\sin^2 2\theta, \Delta m^2) = (1.00, 2.5 \times 10^{-3}\,\text{eV}^2)$. Hatched histograms show the CCQE $\nu_\mu$ events.
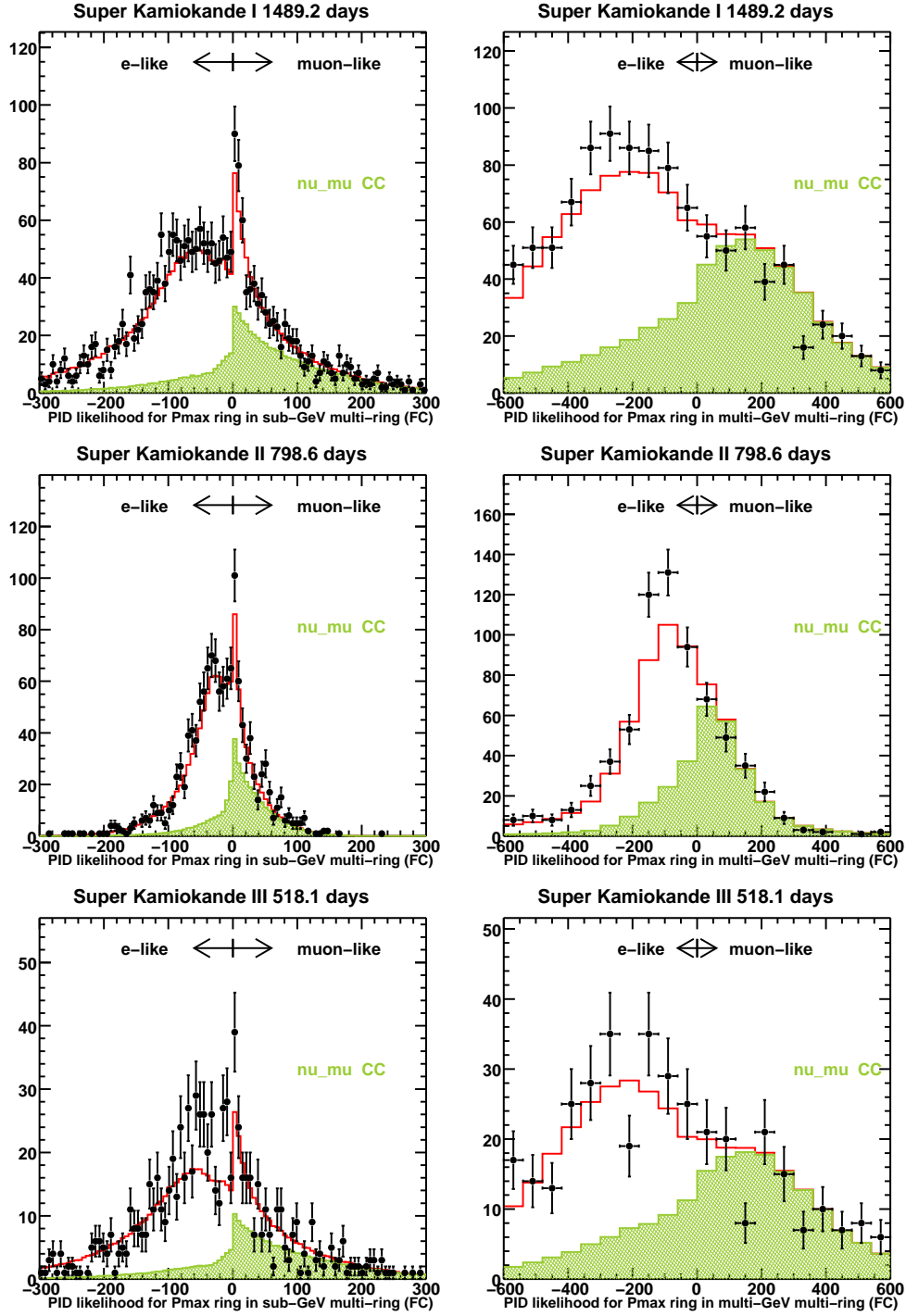
Figure 5.36: The PID likelihood distribution for FC multi-ring sample for SK-I (upper), SK-II (middle) and SK-III (lower). The left (right) side plots are in case of FC Sub-GeV (Multi-GeV) multi-ring sample. Dots (solid lines) are the data (the MC events). The MC histograms assume the 2-flavor oscillation $(\sin^2 2\theta, \Delta m^2) = (1.00, 2.5 \times 10^{-3}\,\mathrm{eV}^2)$. Hatched histograms show the CC $\nu_\mu$ events.
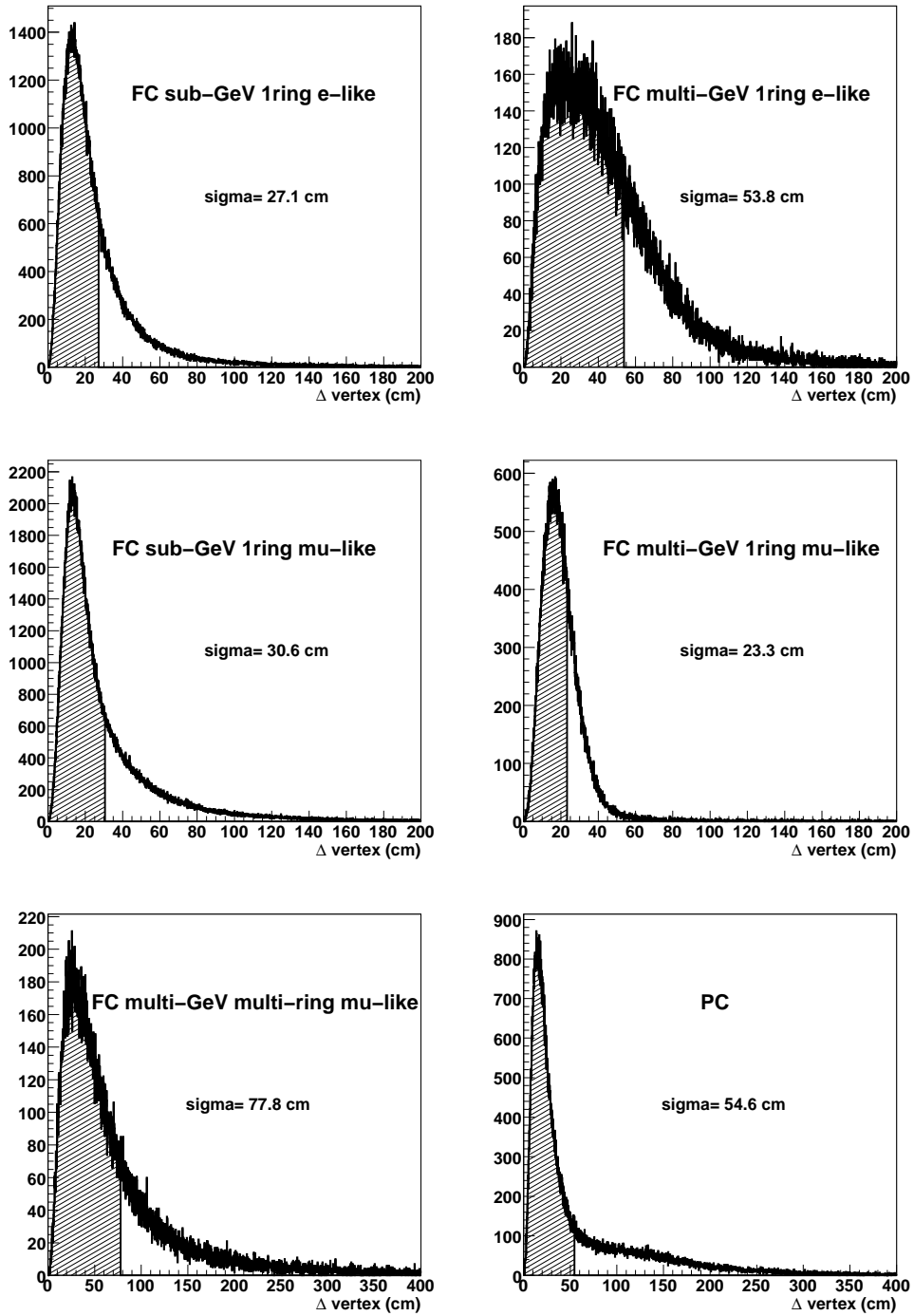
Figure 5.37: Distance between the true vertex and the reconstructed of FC and PC Monte Carlo sample for SK-III. Hatched region is where 68% of all events are indecated.

107
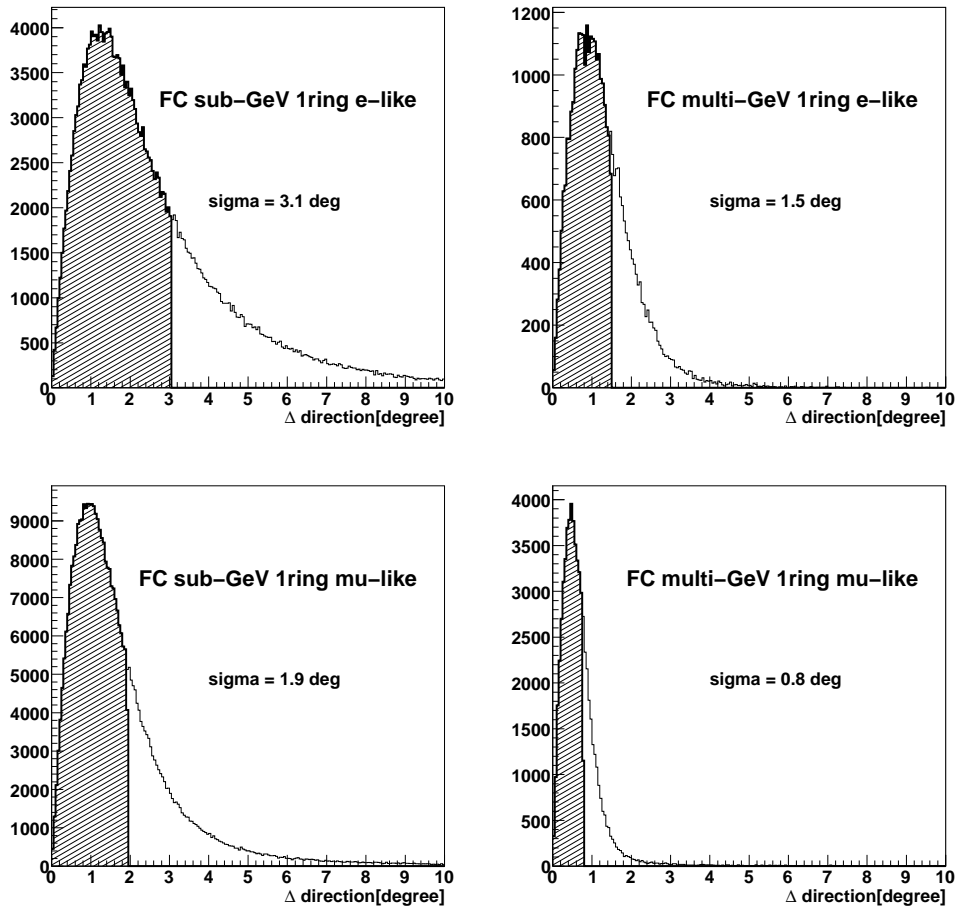
Figure 5.38: Angular difference between the true direction and the reconstructed direction of FC Monte Carlo sample for SK-III. Hatched region is where 68% of all events are indecated.
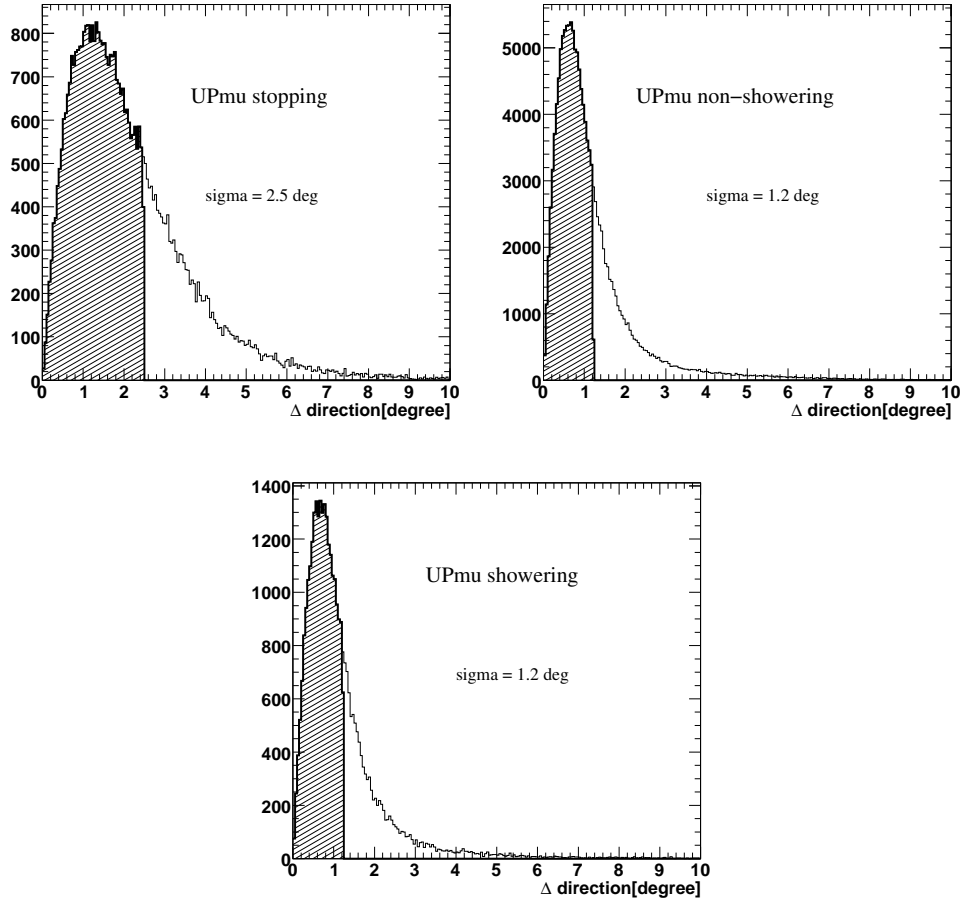
Figure 5.39: Angular resolution of UPMU Monte Carlo sample for SK-III. Hatched region is where 68% of all events are indecated.

| Vertex resolution (cm) | | | |
|---|---|---|---|
| | SK-I | SK-II | SK-III |
| FC Sub-GeV | | | |
| single-ring | | | |
|    $e$-like | 27 | 31 | 27 |
|    $\mu$-like | 26 | 31 | 31 |
| FC Multi-GeV | | | |
| single-ring | | | |
|    $e$-like | 49 | 47 | 54 |
|    $\mu$-like | 24 | 27 | 23 |
| multi-ring | | | |
|    $\mu$-like | 67 | 75 | 78 |
| PC | 56 | 64 | 55 |

| Angular resolution (degree) | | | |
|---|---|---|---|
| | SK-I | SK-II | SK-III |
| FC Sub-GeV | | | |
| single-ring | | | |
|    $e$-like | 3.1 | 3.2 | 3.1 |
|    $\mu$-like | 1.9 | 2.2 | 1.9 |
| FC Multi-GeV | | | |
| single-ring | | | |
|    $e$-like | 1.5 | 1.5 | 1.5 |
|    $\mu$-like | 0.8 | 0.9 | 0.8 |
| PC | 1.0 | 1.2 | 0.9 |
| UPMU stop | 2.5 | 2.5 | 2.5 |
| UPMU through non-showering | 1.2 | 1.6 | 1.2 |
| UPMU through showering | 1.3 | 2.3 | 1.2 |

Table 5.9: Vertex and angular resolutions for each event category and each SK period are summarized.

### 5.4.5 Momentum reconstruction

The momentum reconstruction for each particle is estimated by the observed p.e.s inside a Cherenkov cone with the half opening angle of $70^o$. In order to determine the momentum for individual rings, the observed p.e.s in hit PMTs are separated to the contribution from each ring. The separation of the observed p.e.s is carried out based on the expected p.e. distribution from each ring as a function of the opening angle $\theta$, assuming a uniformity in azimuthal angle $\phi$. The observed p.e.s in the $i$-th PMT from the $n$-th ring are estimated as :

$$q_{i,n}^{\mathrm{obs}} = q_i^{\mathrm{obs}} \times \frac{q_{i,n}^{\mathrm{exp}}}{\sum_{n'} q_{i,n'}^{\mathrm{exp}}} \tag{5.5}$$

where $q_{i,n}^{\mathrm{obs}}$ is the fractional p.e.s from the $n$-th ring in the $i$-th PMT, $q_i^{\mathrm{obs}}$ is the observed p.e.s in the $i$-th PMT and $q_{i,n}^{\mathrm{exp}}$ is the expected p.e.s.

To calculate the total number of p.e.s inside the $70°$ cone, the number of p.e.s in each PMT is corrected considering the light attenuation in the water and the acceptance of the PMT as follows :

$$RTOT_n = \frac{G_{\mathrm{MC}}}{G_{\mathrm{data}}} \left[ \alpha \times \sum_{\substack{\theta_{i,n}<70° \\ -50\mathrm{nsec}<t_i<250\mathrm{nsec}}} \left( q_{i,n}^{\mathrm{obs}} \times \exp\left(\frac{r_i}{L}\right) \times \frac{\cos\Theta_i}{f(\Theta_i)} \right) - \sum_{\theta_{i,n}<70°} S_i \right] \tag{5.6}$$

where

| | | |
|---|---|---|
| $\alpha$ | : | normalization factor |
| $G_{\mathrm{data}}, G_{\mathrm{MC}}$ | : | relative PMT gain parameter for the data and the Monte Carlo simulation |
| $\theta_{i,n}$ | : | opening angle between the $n$-th ring direction and the $i$-th PMT direction |
| $t_i$ | : | photon time-of-flight subtracted hit timing of the $i$-th PMT position |
| $L$ | : | light attenuation length in water |
| $r_i$ | : | distance from the vertex position to the $i$-th PMT |
| $f(\Theta_i)$ | : | correction function for the PMT acceptance as a function of the photon incidence angle $\Theta_i$ |
| $S_i$ | : | expected p.e.s for the $i$-th PMT from scattered photons |

The summation is restricted inside the time window from -50 nsec to +250 nsec around the peak of the photon time-of-flight subtracted hit timing distribution to reject the effect from muon decay electrons. The attenuation length in water $L$ is measured continuously using cosmic ray through-going muons (Section 4.1.5). Figure 5.40 shows the momentum resolution for electrons and muons estimated from the Monte Carlo simulation as a function of the true momentum for each SK geometry. The resolution is defined as $1\sigma$ width of the Gaussian fit.

The absolute energy scale is calibrated using the four independent calibration sources as described in Section 4.2.
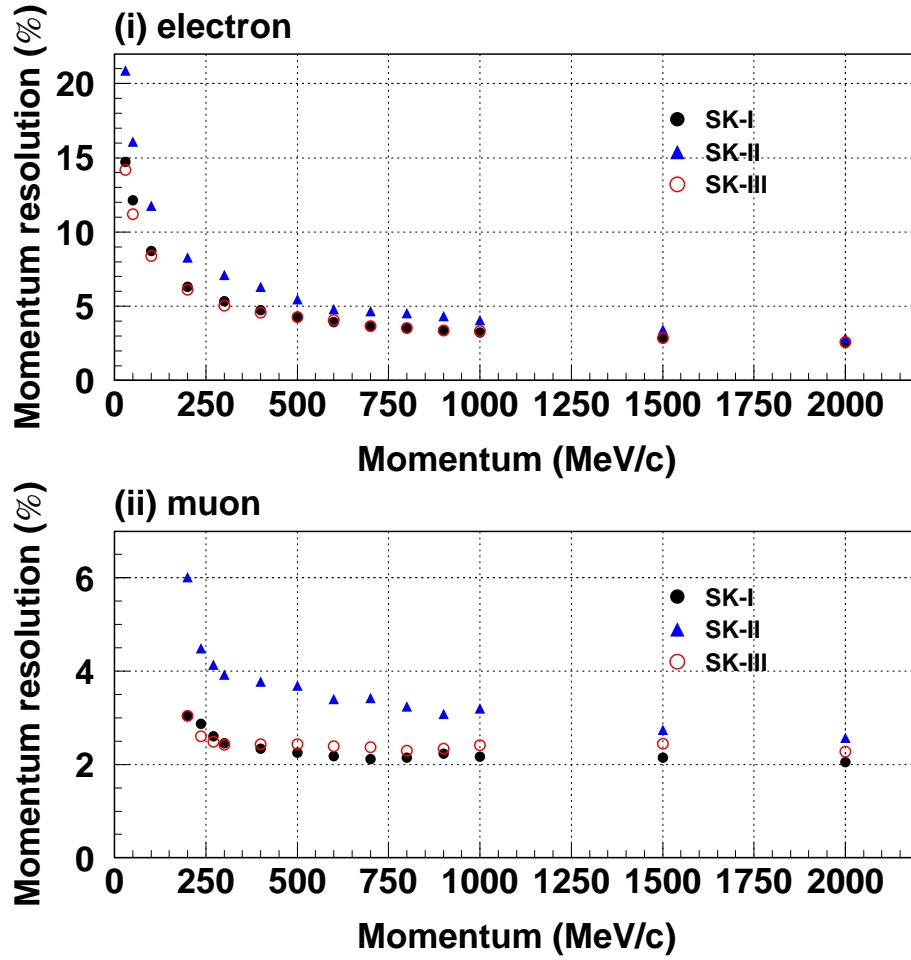
Figure 5.40: Momentum resolutions for electron (top) and muon (bottom) estimated by the Monte Carlo simulation as a function of the true momentum.

### 5.4.6 Decay Electron Search

Electrons may be produced from the decay of muons which stopped in the detector. Also $\pi^+$ produced by a neutrino interaction may decay into $\mu^+$, then to $e^+$. Therefore, for example, if a muon decay is observed for single-ring e-like event, the event is likely to be a CC-nonQE $\nu_e$ event that produced $\pi^+$ along with an electron. Thus the information from the decay-electrons is useful to estimate the type of neutrino interactions. Decay electrons are observed in a later independent time window (900 nsec) from that of the primary event or in a same time window of the primary event. If the decay occurs around 900 nsec, the electron event may be observed separately in the primary trigger and subsequent event trigger.

The detection efficiency of decay electron is 80 % for $\mu^+$ and 63 % for $\mu^-$, since approximately 20 % of $\mu^-$ is captured on $^{16}$O nuclei [129].

### 5.4.7 $\pi^0$ reconstruction

$\pi^0$ reconstruction is applied to only single-ring e-like events. In the FC sub-GeV single-ring e-like event sample, the contamination of NC events is estimated to be about 9 %. These NC are mostly originated from NC single $\pi^0$ production. $\pi^0$ immediately decays two gamma-rays and produces two e-like Cherenkov rings. If one of these two rings was not detected due to too low energy or overlapping rings, the event can be identified to single-ring e-like. To find these $\pi^0$ events, the $\pi^0$ fitter reconstructs the second gamma-ray on the assumption of the existence of two Cherenkov rings by comparing the observed photoelectron distribution with the expected photoelectron distribution of two gamma-rays. Then the likelihood technique is used to determine the best-fit configuration of two gamma-rays. The results from $\pi^0$ reconstruction are used in the analysis sample as described in Section 6.2.1.

# Chapter 6

# Neutrino Oscillation Analysis

## 6.1 Overview

Neutrino oscillation is examined using the information of detected neutrino momenta and directions. The observed data are compared against the MC expectation using a $\chi^2$ method. In this chapter, data samples for this analysis and the expected effects from the full oscillation on that samples are explained. The analysis method together with detail systematics and results are described.

## 6.2 Data Set

For this analysis, all data samples, FC, PC and UPMU, are used. In order to separate CCQE, CC non-QE and NC events from the 1-ring sample, FC sub-GeV 1-ring samples are further separated to sub-samples by using information such as the number of decay electrons. Additionally, in order to use the high energy electron sample in the analysis, Multi-GeV multi-ring e-like sample which contains inelastic interaction events mostly is selected by the likelihood method. These additional selection methods are described in the following sections.

### 6.2.1 Selection for Sub-GeV sample

The FC sub-GeV single-ring e-like sample contains background events which are mainly NC $\pi^0$ events producing two gamma-rays. If one of the two $\gamma$ rays is missed by the event reconstruction, the NC $\pi^0$ event is identified as single-ring e-like since the electromagnetic shower from the $\gamma$ gives a light pattern similar to that of an electron. To reduce this type of background a specialized $\pi^0$ fitter is used [136]. This fitter enforces a second ring on the 1-ring data event and then predicts a light pattern that would result from $\gamma$ rays propagating through the tank with the vertex of the fitted ring and with the best fit direction. The left five panels in Figure 6.1 show the invariant mass distributions from this $\pi^0$ fitter for CCQE and NC events in the FC sub-GeV single-ring e-like Monte Carlo in five energy regions. NC events tend to form a peak close to the $\pi^0$ mass while CCQE events do not. For events with electron momentum below 250 MeV/c, a cut at 100 MeV/c$^2$ is used to create a $\pi^0$-like sample. However, this cut is not sufficient for events in higher momenta. Thus a likelihood selection is additionally used incorporating three variables: the fraction of the event's reconstructed momentum carried by the second ring, the $\pi^0$ invariant mass distribution, and the difference of two likelihood variables which result from

a $\pi^0$-fit and electron-fit. The distribution of these variables is also shown in Figure 6.1 for each energy region. The $\pi^0$-like selection likelihood functions are defined as:

$$\mathcal{L}_{\pi^0} = \sum_{i=1}^{3} \log(\Gamma_i^S(x_i)) - \log(\Gamma_i^B(x_i)), \tag{6.1}$$

where $\Gamma_i^S(x_i)$ ($\Gamma_i^B(x_i)$) represents the CCQE (NC) events' probability distribution function (PDF) for the $i^{th}$ variable with observable $x_i$. After separating the $\pi^0$-like sample, the remaining $e$-like events are divided into two categories, 0-decay which has no decay electrons and 1-decay which has one or more decay electrons. Since $\nu_e$ CCQE events are not expected to produce decay electrons, there is a high fraction of CCQE interactions in the 0-decay sample.

For the FC sub-GeV single-ring $\mu$-like sample, there are three categories using the number of decay electrons: 0-decay, 1-decay, and 2-decay (2 and more), corresponding to the number of decay electrons reconstructed in the event. Since these CCQE events produce a muon they are expected to have one decay electron. The fraction of CCQE events is increased in 1-decay $\mu$-like samples.

Details of the event composition by interaction mode after these event selections are shown in Table 6.1.

### 6.2.2 Selection for Multi-GeV multi-ring e-like sample

In order to make a $\nu_e$-enriched Multi-GeV multi-ring e-like sample, an additional selection is applied based on the likelihood method. Four variables are used in the selection for each five energy region, PID likelihood, momentum fraction of the most energetic ring, number of decay electrons, and distance between the neutrino vertex and any muon decay electrons. The distribution of these variables is shown in Figure 6.2 for each energy region. The likelihood functions for the Multi-GeV Multi-ring e-like selection are defined as,

$$\mathcal{L}_{MME} = \sum_{i=1}^{4} \log(\Gamma_i^S(x_i)) - \log(\Gamma_i^B(x_i)), \tag{6.2}$$

where $\Gamma_i^S(x_i)$ ($\Gamma_i^B(x_i)$) represents the CC$\nu_e$ (NC+CC$\nu_\mu$; background) events' PDF for the $i^{th}$ variable with observable $x_i$. Details of the event composition by interaction mode after this selection are shown in Table 6.2. The likelihood selection increases CC events and decreases background events significantly.

### 6.2.3 Data set for the analysis

In summary, data sets for the analysis are specified as follows :

- FC samples

  (1) FC sub-GeV single-ring e-like samples
     * single-ring which is identified as e-like
     * $p_e > 100 \, \mathrm{MeV}/c$
     * $\mathrm{E}_{vis} < 1.33 \, \mathrm{GeV}$

115
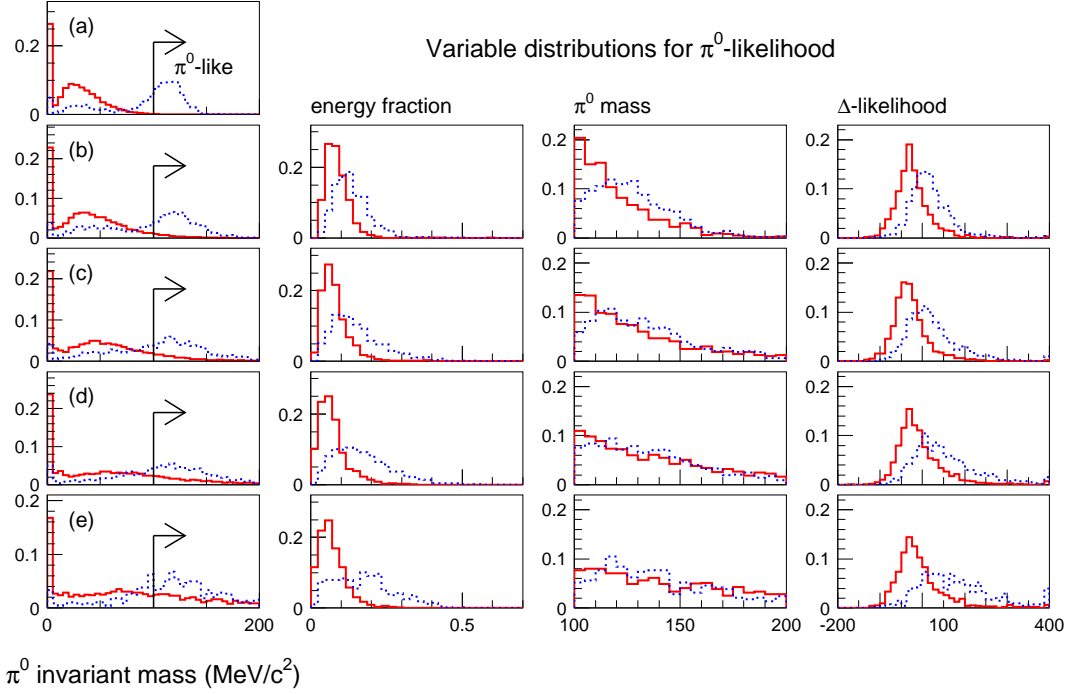
Figure 6.1: The distributions used in the $\pi^0$ selection for five momentum regions: (a)$P_e <$ 250 MeV/c, (b)250 MeV/c $\le P_e <$ 400 MeV/c, (c)400 MeV/c $\le P_e <$ 630 MeV/c, (d)630 MeV/c $\le P_e <$ 1000 MeV/c and (e)1000 MeV/c $\le P_e$. Solid (dashed) lines represent CCQE (NC) events in the FC sub-GeV single-ring $e$-like Monte Carlo in SK-I. Events with $\pi^0$ mass above 100 MeV/c$^2$ are selected as $\pi^0$-like. To separate $\pi^0$-like and electron-like more efficiently, an additional likelihood selection is applied for events with momentum above 250 MeV/c. The distributions of the three likelihood variables are shown: the fraction of energy carried by the second fitted ring ($E_2/(E_1 + E_2)$), the $\pi^0$ mass and $\Delta$-likelihood (described in the text). All distributions have been normalized to unit area.

|  |  | FC sub-GeV single-ring $e$-like | | | FC sub-GeV |
|  |  | 0-decay | 1-decay | $\pi^0$-like | single-ring $e$-like |
| MC events | | 2663.2 | 210.9 | 191.8 | 2996.4 |
|  | Q.E. | 77.7 % | 3.8 % | 10.6 % | 70.6 % |
| CC | single meson | 12.4 % | 50.3 % | 7.0 % | 15.2 % |
| $\nu_e + \bar{\nu}_e$ | multi $\pi$ | 1.0 % | 9.7 % | 1.8 % | 1.7 % |
|  | coherent $\pi$ | 1.3 % | 8.5 % | 0.5 % | 1.7 % |
| CC $\nu_\mu + \bar{\nu}_\mu$ | | 0.6 % | 15.2 % | 7.0 % | 2.0 % |
| NC | | 6.8 % | 11.2 % | 72.0 % | 8.7 % |
|  |  | FC sub-GeV single-ring $\mu$-like | | | FC sub-GeV |
|  |  | 0-decay | 1-decay | 2-decay | single-ring $\mu$-like |
| MC events | | 1412.4 | 2745.4 | 164.3 | 4297.8 |
|  | Q.E. | 71.3 % | 78.5 % | 5.8 % | 74.7 % |
| CC | single meson | 12.9 % | 15.5 % | 65.7 % | 16.7 % |
| $\nu_\mu + \bar{\nu}_\mu$ | multi $\pi$ | 1.1 % | 1.5 % | 14.9 % | 1.9 % |
|  | coherent $\pi$ | 0.8 % | 1.5 % | 8.6 % | 1.6 % |
| CC $\nu_e + \bar{\nu}_e$ | | 1.8 % | <0.1 % | <0.1 % | 0.7 % |
| NC | | 11.8 % | 2.6 % | 3.3 % | 4.3 % |

Table 6.1: The number of FC Sub-GeV events and their fractional composition by neutrino interaction mode for the SK-I MC scaled to 1489 days without oscillations. The upper (lower) table shows the $e$-like ($\mu$-like) sample. The most right side of the table shows the result before separation into sub-samples. After separation the CCQE purity is increased and the NC backgrounds are reduced in the 0-decay $e$-like and 1-decay $\mu$-like sub-samples.

|  | CC $\nu_e + \bar{\nu}_e$ | | CC $\nu_\mu + \bar{\nu}_\mu$ | | NC | | Total | |
|  | No $\mathcal{L}$ | $\mathcal{L}$ | No $\mathcal{L}$ | $\mathcal{L}$ | No $\mathcal{L}$ | $\mathcal{L}$ | No $\mathcal{L}$ | $\mathcal{L}$ |
|  | 472.1 | 331.0 | 201.7 | 39.2 | 218.1 | 74.4 | 891.9 | 444.6 |
| Percentage (%) | 53.0 | 74.5 | 22.6 | 8.8 | 24.5 | 16.7 | 100.0 | 100.0 |

Table 6.2: The expected number of events for each interaction component of the Multi-GeV multi-ring $e$-like sample before (No $\mathcal{L}$) and after ($\mathcal{L}$) likelihood selection for the SK-I MC scaled to 1489 days. Two-flavor neutrino oscillations $\nu_\mu \leftrightarrow \nu_\tau$ are assumed with full-mixing ($\Delta m^2 = 2.1 \times 10^{-3}$ eV$^2$, $\sin^2 2\theta = 1.0$).
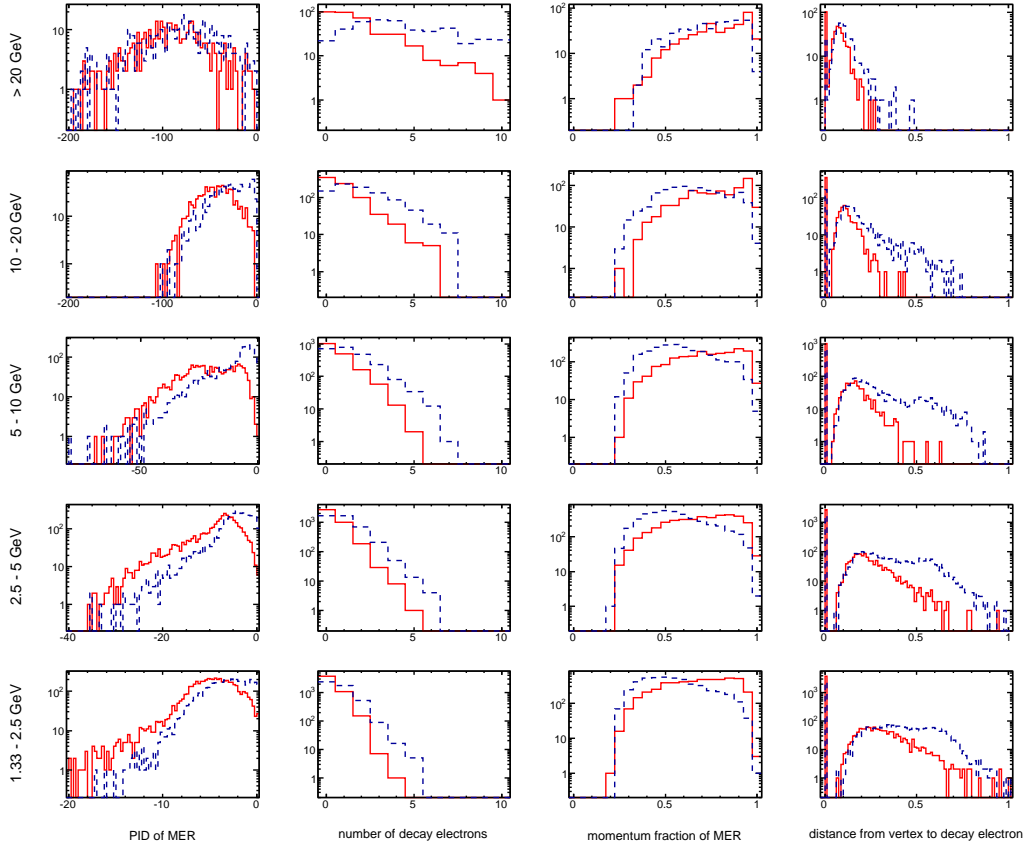
Figure 6.2: Variables used in the likelihood definition to create the SK-I multi-GeV multi-ring $e$-like sample. The energy bins correspond to the energy of the most energetic ring. Signal events (CC $\nu_e + \bar{\nu}_e$) are shown the solid lines and background events (CC $\nu_\mu + \bar{\nu}_\mu$ and NC) are shown the dashed lines.

(1-a) 0-decay electron sample
  · without any decay electrons
(2-b) 1-decay electron sample
  · with one decay electrons
(3-c) $\pi^0$-like sample
  · fitted as $\pi^0$-like by $\pi^0$-fitter and $\pi^0$-likelihood

(2) FC sub-GeV single-ring $\mu$-like samples
  * single-ring which is identified as $\mu$-like
  * $p_\mu > 200\,\mathrm{MeV}/c$
  * $\mathrm{E}_{vis} < 1.33\,\mathrm{GeV}$

(2-a) 0-decay electron sample
  · without any decay electrons
(2-b) 1-decay electron sample
  · with one decay electrons
(2-c) 2-decay electron sample
  · with two or more decay electrons

(3) FC Multi-GeV single-ring e-like sample
  * single-ring which is identified as e-like
  * $\mathrm{E}_{vis} > 1.33\,\mathrm{GeV}$

(4) FC Multi-GeV single-ring $\mu$-like sample
  * single-ring which is identified as $\mu$-like
  * $\mathrm{E}_{vis} > 1.33\,\mathrm{GeV}$

(5) FC Multi-GeV multi-ring e-like sample
  (described in Section 6.2.2)
  * The most energetic ring is identified as e-like and $\mathrm{E}_{vis} > 1.33\,\mathrm{GeV}$
  * Events that satisfy the Multi-GeV, multi-ring e-like likelihood cut

(6) FC Sub- and Multi-GeV multi-ring $\mu$-like sample
  * The most energetic ring is identified as $\mu$-like and the momentum $p_\mu > 600\,\mathrm{MeV}/c$ and $\mathrm{E}_{vis} > 600\,\mathrm{MeV}$

(7) FC 2-ring $\pi^0$-like sample
  (described in Section 4.2.3)
  * Two rings are recognized and both of them are identified as e-like
  * without any decay electrons

• PC samples

(8) PC OD stopping sample
  (described in Section 5.2.7)

119

* The maximum number of p.e.s observed in the OD in a sliding 500 nsec time window from $-400$ nsec to $+600$ nsec ($PE_{anti}$) is less than $PE_{exp}/1.5$ (see Section 5.2)
* The most energetic ring or the second one should be identified as $\mu$-like

(9) PC OD through-going sample

* (rest of the events after stopping selection)

- UPMU samples

(10) Upward stopping muon sample

* Classified as stopping event by the fitter
* The number of hit OD PMTs within 8 m from the exit point (NHITEX) < 10 for SK-I and -III (16 for SK-II)
* The fitted momentum $\geq$ 1.6 GeV/c

(11) Upward through-going muon sample

* Classified as through-going event by the fitter
* The number of hit OD PMTs within 8 m from the exit point (NHITEX) $\geq$ 10 for SK-I and -III (16 for SK-II)
* The distance from the entrance point to the exit point $\geq$ 7 m

(11-a) showering muon sample

(described in Section 5.3.6)

· The difference between the average corrected charge and the expected charge for non-showering muon ($\Delta(Q) = < Q > - q_l$) > 0.5 when $\chi^2$ valuable for showering selection $\geq$ 50.

· $\Delta(Q) > 4.5 - 0.08\chi^2$ when $\chi^2 < 50$.

(11-b) non-showering muon sample

· (rest of the events after showering selection)

In this analysis, FC, PC and UPMU data during SK-I (1489.2 days for FC and PC, 1645.9 days for UPMU), SK-II (798.6 days for FC and PC, 827.7 days for UPMU) and SK-III (518.1 days for FC and PC, 635.6 days for UPMU) period are used. The live time is determined by the requirement of the good detector condition. Since the reconstruction of long path length muon for UPMU events is less affected by the detector condition, the live time is longer than that of FC and PC. The amount of simulated MC atmospheric neutrino events are equivalent to an exposure of 500 years for each SK run period.

Table 6.3 summarizes the number of events in each categorized sample for the data and MC events.

## 6.3 Oscillation effect

As discussed in Section 1.3, the electron neutrino oscillation is observable by the sub-dominant oscillation effects. Figure 6.3 shows the expected flux ratio at the detector site for each electron and muon neutrino as a functions of the zenith angle and momentum. The expected

| | SK-I | | SK-II | | SK-III | |
|---|---|---|---|---|---|---|
| | Data | MC (osc.) | Data | MC (osc.) | Data | MC (osc.) |
| **FC Sub-GeV** | | | | | | |
| single-ring | | | | | | |
| $e$-like | | | | | | |
| 0-decay | 2984 | 2655.9 (2652.4) | 1605 | 1405.8 (1403.4) | 1098 | 935.7 (934.7) |
| 1-decay | 275 | 204.4 (194.3) | 155 | 113.5 (107.1) | 106 | 69.6 (66.7) |
| $\pi^0$-like | 167 | 159.1 (155.2) | 81 | 81.3 (79.1) | 46 | 45.6 (44.4) |
| $\mu$-like | | | | | | |
| 0-decay | 1036 | 1385.6 (973.0) | 563 | 765.9 (537.2) | 346 | 497.5 (350.4) |
| 1-decay | 2035 | 2760.6 (1846.8) | 1043 | 1429.4 (957.3) | 759 | 999.8 (668.3) |
| 2-decay | 150 | 163.7 (114.6) | 80 | 82.8 (57.7) | 61 | 58.5 (41.0) |
| 2-ring $\pi^0$-like | 497 | 460.0 (456.1) | 267 | 237.3 (235.1) | 178 | 157.8 (156.5) |
| **FC Multi-GeV** | | | | | | |
| single-ring | | | | | | |
| $e$-like | 829 | 777.8 (777.7) | 392 | 409.9 (411.1) | 282 | 279.3 (278.4) |
| $\mu$-like | 694 | 1027.4 (744.4) | 394 | 550.2 (399.0) | 231 | 352.8 (255.7) |
| multi-ring | | | | | | |
| $e$-like | 433 | 457.9 (458.9) | 260 | 252.3 (251.9) | 149 | 159.2 (159.1) |
| $\mu$-like | 617 | 882.4 (660.9) | 361 | 459.6 (344.1) | 226 | 313.8 (234.4) |
| **PC** | | | | | | |
| OD stopping | 163 | 222.7 (167.3) | 116 | 105.8 (80.9) | 63 | 75.1 (55.7) |
| OD through-going | 735 | 965.4 (755.0) | 314 | 482.5 (374.7) | 280 | 334.9 (262.8) |
| **Upward-going muon** | | | | | | |
| stopping | 435.9 | 701.7 (419.4) | 207.6 | 355.2 (212.5) | 193.7 | 273.8 (163.5) |
| non-showering | 1577.4 | 1548.0 (1343.9) | 725.3 | 767.6 (668.7) | 612.9 | 599.4 (520.0) |
| showering | 271.6 | 302.7 (292.2) | 108.1 | 147.8 (143.6) | 110 | 116.2 (112.3) |

Table 6.3: Summary of the number of neutrino events for the data and MC events. The number of MC events is normalized by the livetime of the data, and the number of oscillated MC events is shown in (osc.) assuming 2-flavor full-mixing at $(\Delta m^2_{23} = 2.1 \times 10^{-3} \text{ eV}^2, \sin^2\theta_{23} = 0.5)$.
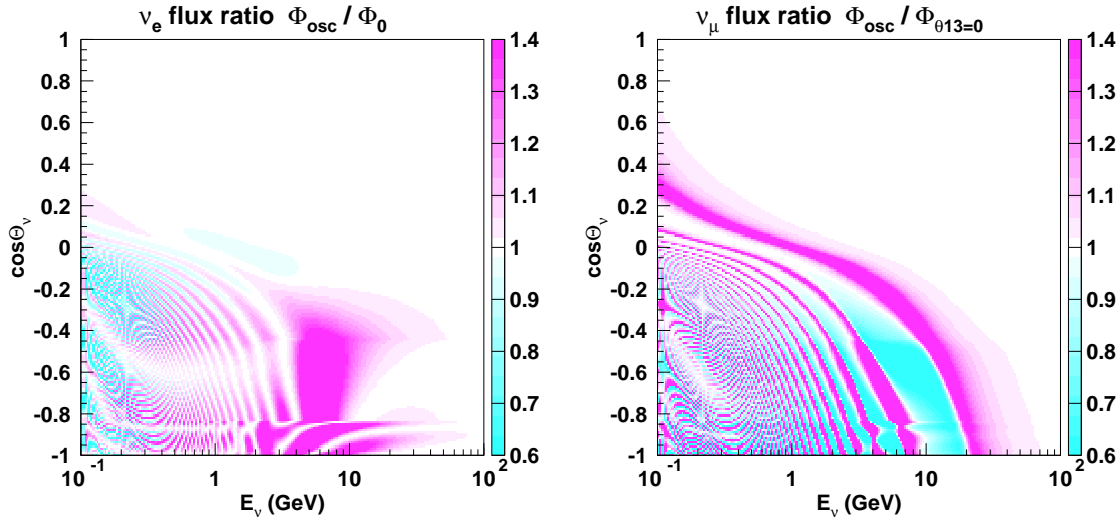
Figure 6.3: The flux change of electron neutrino events (left) and muon neutrino events (right) for oscillations with the parameters $(\Delta m_{12}, \Delta m_{23}, \sin^2\theta_{12}, \sin^2\theta_{23}, \sin^2\theta_{13}, \delta_{cp}) = (7.7 \times 10^{-5}, 2.1 \times 10^{-3}, 0.30, 0.60, 0.04, 180°)$. The plots are shown relative to null oscillation for the electron neutrino, and no $\nu_e$ oscillation $(\sin^2\theta_{13} = 0)$ for the muon neutrino. The intensity scale of the plots is restricted to $\pm 40\%$.

events are calculated by using both disappearance and appearance oscillation probabilities. Figure 6.3 show the expected events assuming full oscillations, $(\Delta m_{12}, \Delta m_{23}, \sin^2\theta_{12}, \sin^2\theta_{23}, \sin^2\theta_{13}, \delta_{cp}) = (7.7 \times 10^{-5}, 2.1 \times 10^{-3}, 0.30, 0.50, 0.04, 0°)$, which are normalized to the non-oscillated events and the events after 2-flavor full mixing $(\Delta m_{23} = 2.1 \times 10^{-3}, \sin^2\theta_{23} = 0.50)$ for the electron neutrino and for the muon neutrino, respectively. For the electron neutrino, the oscillation effect due to $\theta_{13}$ is dominant from a few GeV to 10 GeV. In Multi-GeV region, resonance enhancement of $\nu_\mu \to \nu_e$ $(\bar{\nu}_\mu \to \bar{\nu}_e)$ oscillation due to non-zero $\theta_{13}$ is expected for normal hierarchy (inverted hierarchy) case, while there is no enhancement for inverted hierarchy (normal hierarchy) case. According to the solar neutrino oscillation parameters (LMA-MSW), the electron neutrino flux change should be seen in Sub-GeV energy region. The muon neutrino flux shows alternating bands of event excess and deficit. Since the energy reconstruction is not perfect, it is difficult to see such flux changes. However, the wide regions of excess and deficit are appeared in Multi-GeV region due to the electron neutrino oscillation. Thus, the muon neutrino events could be somewhat useful to detect the sub-dominant oscillation effects.

The CP phase changes the sub-dominant effects intricately. Figures 6.4 and 6.5 show the zenith angle distributions for sub-GeV 1-ring e-like 0-decay sample (will be discussed in Section 6.2.1) and multi-GeV 1-ring e-like sample. Each plot is described relative to non-oscillation events. Each colored line indicates the different CP phase value. If $\theta_{13}$ is zero, there is no difference in the sub-dominant effect among the CP phase values. When $\theta_{13}$ is not zero, the small difference appears due to the CP phase.

Since the enhancement only occurs for neutrinos or anti-neutrinos depending on the hierarchy, and since the absolute cross section and $d\sigma/dy$ (where $y = (E_\nu - E_{lepton})/E_\nu$) are different between neutrinos and anti-neutrinos, the excess for single and multi-ring multi-GeV
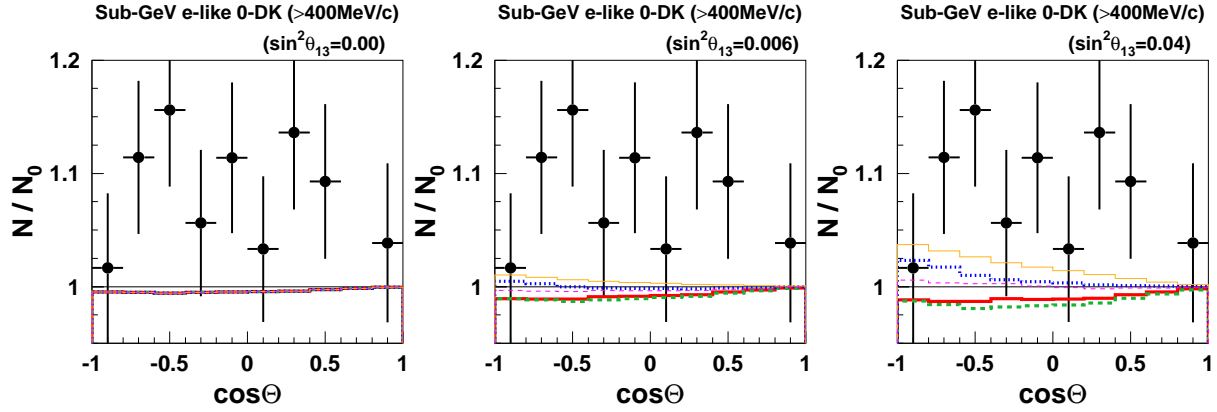
Figure 6.4: Zenith angle distributions for Sub-GeV 1-ring e-like 0-decay ( $> 400 MeV/c$ ) sample with the data (dots) and the expected MC events (lines) assuming the oscillation parameters $(\Delta m_{12}, \Delta m_{23}, \sin^2 \theta_{12}, \sin^2 \theta_{23}) = (7.7 \times 10^{-7}, 2.1 \times 10^{-3}, 0.30, 0.55)$ in normal hierarchy case. The left, middle and right panels show the case of $\sin^2 \theta_{13} = 0.0$, 0.006 and 0.04, respectively. Each line indicates the different CP phase value as described in Fig. 6.6. All plots are normalized by the number of events without the oscillations.
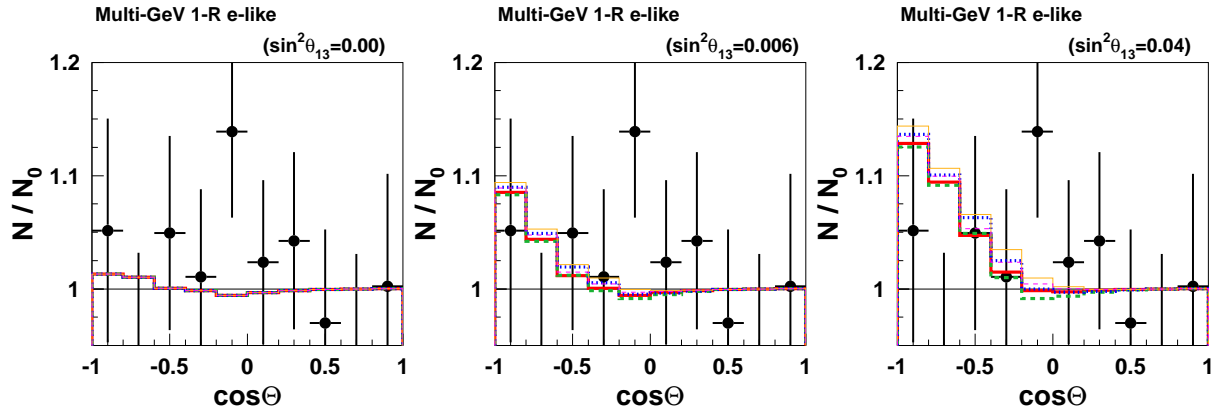


Figure 6.5: Zenith angle distributions for Multi-GeV 1-ring e-like sample with the data (dots) and the expected MC events (lines) assuming the oscillation parameters $(\Delta m_{12}, \Delta m_{23}, \sin^2 \theta_{12}, \sin^2 \theta_{23}) = (7.7 \times 10^{-3}, 2.1 \times 10^{-3}, 0.30, 0.55)$ in normal hierarchy case. The left, middle and right panels show the case of $\sin^2 \theta_{13} = 0.0$, 0.006 and 0.04, respectively. Each line indicates the different CP phase value as described in Fig. 6.6. All plots are normalized by the number of events without the oscillations.

e-like events depends on the hierarchy. About multi-ring Multi-GeV e-like sample will be more discuss in Section 6.2.2. Figure 6.6 shows the same zenith angle distributions for single and multi-ring Multi-GeV e-like samples in each mass hierarchy case as Fig. 6.5. It is seen that an electron excess for the inverted hierarchy case is suppressed compared with that for the normal hierarchy case. Due to the difference in the number of excess events between normal and inverted hierarchy, mass hierarchy can be examined.

Note, in this analysis a algebraically computation for the neutrino oscillation probabilities described in [144] is used. The Earth density is measured by the seismic velocity observation. The density described in [135] is used in this analysis.

## 6.4    Analysis Method

To examine the neutrino oscillation parameters, the data are compared against the MC expectation using a pulled $\chi^2$ method based on a Poisson probability distribution:

$$
\begin{aligned}
\chi^2 &\equiv 2\sum_i \left( N_i^{\mathrm{exp}}(1 + \sum_j f_j^i \cdot \epsilon_j) - N_i^{\mathrm{obs}} \right) + N_i^{\mathrm{obs}} \ln \left( \frac{N_i^{\mathrm{obs}}}{N_i^{\mathrm{exp}}(1 + \sum_j f_j^i \cdot \epsilon_j)} \right) \\
&+ \sum_j \left( \frac{\epsilon_j}{\sigma_j^{sys}} \right)^2,
\end{aligned}
\tag{6.3}
$$

where $N_i^{\mathrm{obs}}$ is the number of observed events in the $i$-th bin and $N_i^{\mathrm{exp}}$ is the expected number of events in the $i$-th bin from MC simulation. In the fitting process, $N_i^{\mathrm{exp}}$ is recalculated to account for neutrino oscillations and systematic errors, represented by 123 error parameters $\epsilon_j$ ($j$ : the systematic error index). These $\epsilon_j$ are varied to minimize $\chi^2$ for each choice of oscillation parameter sets. $f_j^i$ is the fractional change in the predicted MC events in $i$-th bin due to $1\sigma$ change of $j$-th systematic error. The $1\sigma$ value of a systematic error is labeled as $\sigma_j^{sys}$. Detail explanation about systematic errors is given in next section.

At the minimum $\chi^2$ location for each choice of oscillation parameters, each of the parameters $\epsilon_j$ is estimated according to $\partial \chi^2 / \partial \epsilon_j = 0$. So the minimization of $\chi^2$ in the equation (6.3) is equivalent to solving the following equations for every $\epsilon_j$ [140]:

$$
\sum_{j=1} \left( \frac{1}{(\sigma_j^{sys})^2} \delta_{jk} + \sum_{i=1} N_i^{\mathrm{obs}} f_j^i f_k^i \right) \epsilon_j = \sum_{i=1} \left( \left( 1 + (\sum_{j=1} f_j^i \epsilon_j)^2 - ... \right) N_i^{\mathrm{obs}} - N_i^{\mathrm{exp}} \right) f_k^i. \tag{6.4}
$$

Since these equations have nonlinear terms of $\epsilon_j$, an approximate solution by an iteration method is obtained.

To ensure a proper function in equation (6.3) the binning is defined so that there are 6 expected MC events for each bin after scaling to the SK-I live time. The binning is defined by the zenith angle and momentum information as shown in Figure 6.7. All sub-GeV samples are divided into 5 momentum bins. Furthermore, e-like 0-decay sample and $\mu$-like 0- and 1-decay samples are divided into 10 zenith angle bins. All multi-GeV samples including PC and UPMU are divided into 10 zenith angle bins. Their momentum bin divisions are set to each sample properly as shown in Figure 6.7. The number of bins is 420 for each SK-I, SK-II and SK-III. Since there is the low statistics data in the later SK run periods, it is expected to have
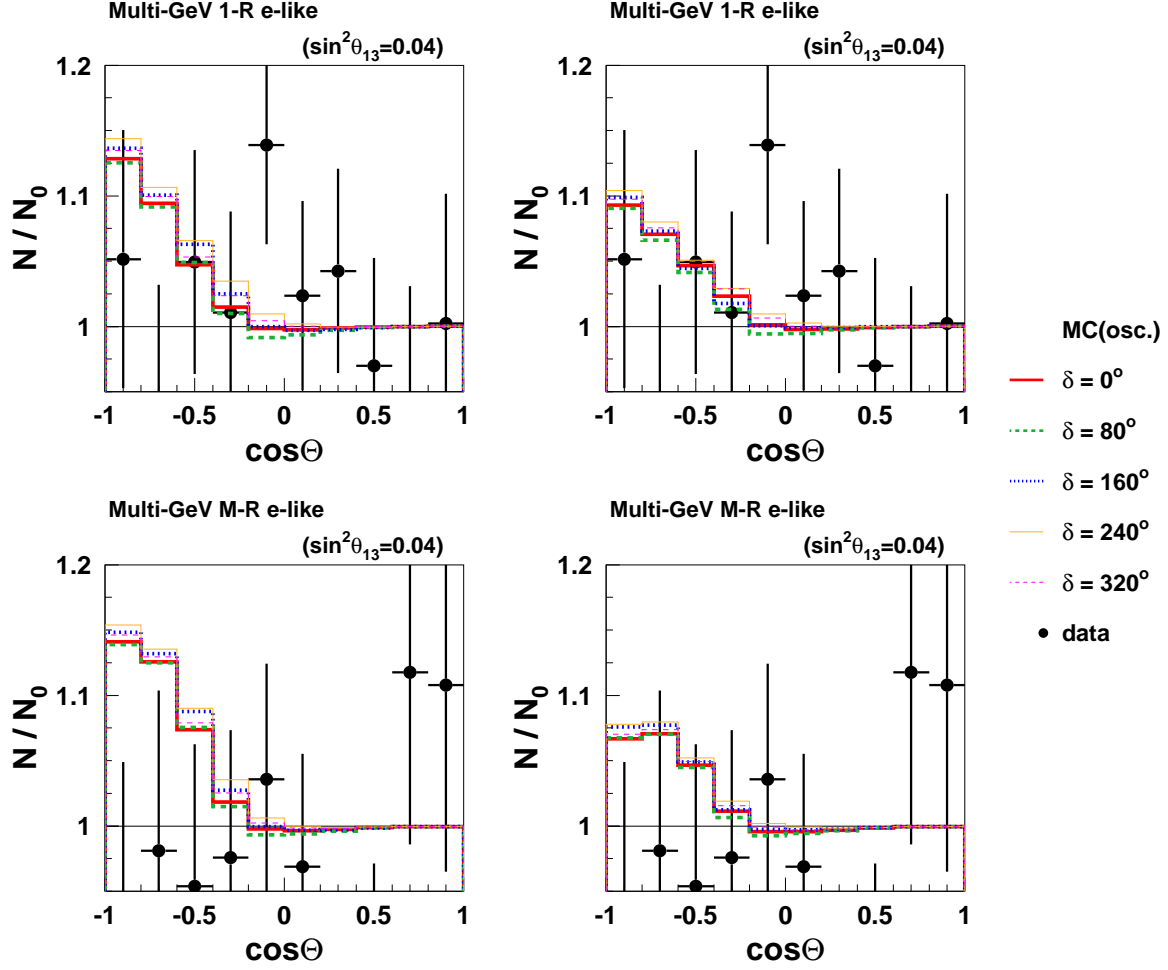
Figure 6.6: Zenith angle distributions for Multi-GeV 1-ring e-like sample (upper) and Multi-GeV multi-ring e-like sample (lower) in case of normal (left) and inverted (right) hierarchy cases. The points show the data and lines show the expected MC events assuming the oscillation parameters $(\Delta m_{12}, \Delta m_{23}, \sin^2 \theta_{12}, \sin^2 \theta_{23}, \sin^2 \theta_{13}) = (7.7 \times 10^{-3}, 2.1 \times 10^{-3}, 0.30, 0.55, 0.04)$. Each line indicates the different CP phase value as shown in the right side of the figures. All plots are normalized by the number of events without the oscillations.
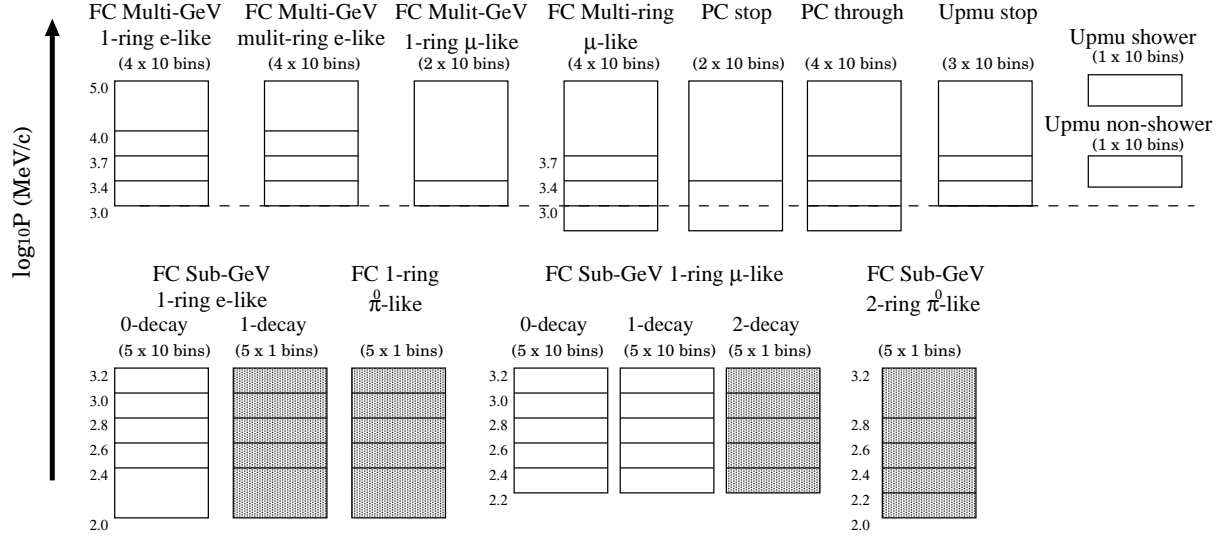
Figure 6.7: The definition of the binning for the neutrino oscillation analysis : 310 bins for the FC samples, 60 for the PC samples, 50 for the UPMU samples. The bins shown in white boxes are divided into 10 bins equally spaced between $\cos\Theta = -1$ and $\cos\Theta = +1$ for FC and PC, $\cos\Theta = -1$ and $\cos\Theta = 0$ for UPMU. The FC single-ring e-like 1-decay, $\pi^0$-like, the $\mu$-like 2-decay samples and 2-ring $\pi^0$ sample are not divided by the zenith angle bins.

instabilities in the $\chi^2$ value. To avoid this problem, SK-II and SK-III bins are merged with those of SK-I after evaluating the systematic error parameters by Eq. (6.4) :

$$
\begin{aligned}
N_i^{\mathrm{obs}} &\rightarrow \sum_n N_{i,SKn}^{\mathrm{obs}} \\
N_i^{\mathrm{exp}}\left(1 + \sum_j f_j^i \cdot \epsilon_j\right) &\rightarrow \sum_n N_{i,SKn}^{\mathrm{exp}}\left(1 + \sum_j f_j^i \cdot \epsilon_j\right)
\end{aligned}
$$

Since the systematic error coefficients for each SK-I, II and III are computed in advance, the systematic error effects specific to each SK run period are properly taken into account.

Details of the systematic error terms are described together with the best fit results of the error parameter $\epsilon_j$ in the next section.

## 6.5   Systematic Uncertainties

As discussed in the previous section, 123 systematic error parameters are used in this analysis. Among them, 21 are for the errors related to the neutrino flux model, 18 are for the neutrino interaction, $28 \times 3$ are for the detector response for each SK run period. All the systematic errors are assumed to be uncorrelated.

The best-fit systematic uncertainty parameters $\epsilon_j$ for the fit in normal hierarchy case are summarized together with the estimated $1\sigma$ uncertainty $(\sigma_j^{sys})$ in Tables from 6.4 to 6.10 for each systematic error term. Their summary can be also found in Appendix A.3.
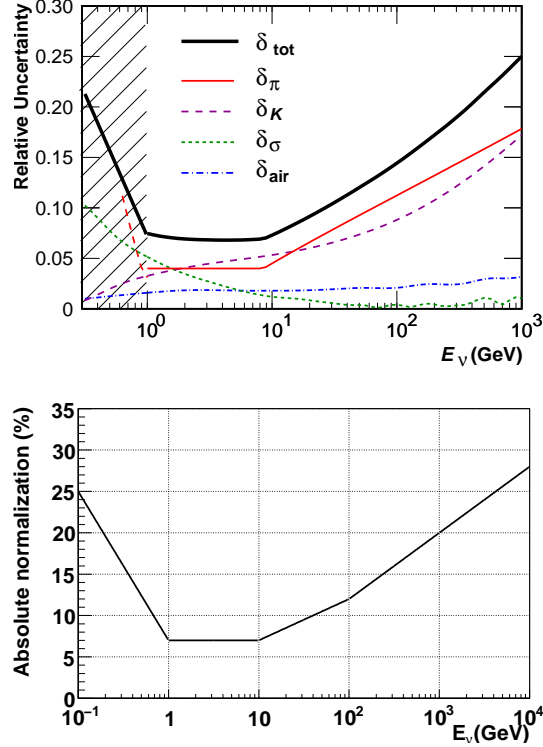
Figure 6.8: The contribution of each error source for atmospheric neutrino flux [22] is shown in the upper panel. In the lower panel, absolute normalization uncertainty due only to $\delta_\pi$ (atmospheric muon data (pion production)) and $\delta_\sigma$ (hadronic interaction model) as a function of neutrino energy is shown.

### 6.5.1  Systematics in neutrino flux

- Absolute normalization
  The uncertainty in the absolute atmospheric neutrino flux is calculated by Honda *et al.* [22], taking into account the atmospheric muon data ($\delta_\pi$, pion production in the hadronic interaction model), Kaon production ($\delta_K$), hadronic interaction cross section ($\delta_\sigma$) and atmospheric density profile ($\delta_{air}$) as shown in the upper panel of Figure 6.8. The sum of dominant uncertainties, $\delta_\pi$ and $\delta_\sigma$, is considered as the absolute normalization uncertainty which is shown in the solid line in the lower panel of Figure 6.8. The uncertainty due to Kaon production is separately included, as discussed later. This systematic uncertainty is divided into two terms for two energy region, $E_\nu < 1$ GeV and $E_\nu > 1$ GeV.

- Flavor ratio
  The systematic uncertainty in the flavor ratio $(\nu_\mu + \overline{\nu}_\mu)/(\nu_e + \overline{\nu}_e)$ of the atmospheric neutrino flux is estimated by comparing of the Honda flux [22] with FLUKA [49] and Bartol [50] flux models. Figure 6.9 shows the flavor ratio normalized by Honda flux model. The uncertainty is estimated 2 % for $E_\nu < 1$ GeV, 3 % for $1 < E_\nu < 10$ GeV, and 5 % for $10 < E_\nu < 30$ GeV. Above 30 GeV, the uncertainty increases along with the function $\log E_\nu$ from 5 % to 30 % up to 1TeV. Due to the difference of error sources in each energy
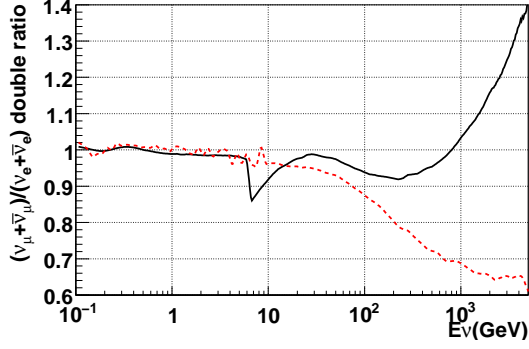
Figure 6.9: The flavor ratio $(\nu_\mu + \overline{\nu}_\mu)/(\nu_e + \overline{\nu}_e)$ of the atmospheric neutrino flux. Vertical axis stands for the double ratio, FLUKA flux/Honda flux(solid) and Bartol flux/Honda flux(dashed). A kink in the FLUKA flux around 8 GeV due to the technical treatment in the original calculation is corrected in the application.
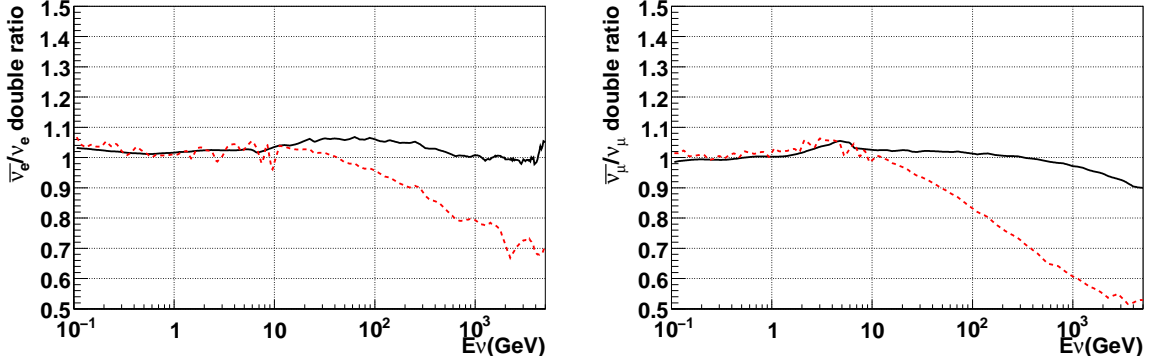


Figure 6.10: Anti-neutrino/neutrino double ratio for $\overline{\nu}_e/\nu_e$ (left panel) and $\overline{\nu}_\mu/\nu_\mu$ (right panel). Double ratio is defined as $(\overline{\nu}/\nu)_{\text{Fluka or Bartol}}/(\overline{\nu}/\nu)_{\text{Honda}}$. Solid(dashed) line indicates the double ratio with the Fluka(Bartol) flux.

region, this uncertainty is divided into three terms, $E_\nu < 1$ GeV, $1 < E_\nu < 10$ GeV, $10 < E_\nu$.

- Anti-neutrino/neutrino ratio
  The systematic uncertainty in the anti-neutrino to neutrino ratio comes from $\pi^+/\pi^-$ and $K^+/K^-$ ratio in hadronic interaction of the flux calculation. The uncertainty is estimated by comparing the three flux models [22, 49, 50]. Figure 6.10 shows anti-neutrino to neutrino ratio normalized by Honda flux model for each $\nu_e$ and $\nu_\mu$ case. In case of $\overline{\nu}_e/\nu_e$, the estimated uncertainty is 5 % in $E_\nu < 1\,\text{GeV}$, 5 % for $1 < E_\nu < 10$ GeV, 8 % for $10 < E_\nu < 100$ GeV, and above that, the error increases with $\log E_\nu$ upto 30 % (1 TeV). In case of $\overline{\nu}_\mu/\nu_\mu$, the estimated uncertainty is 2 % in $E_\nu < 1\,\text{GeV}$, 6 % for $1 < E_\nu < 10$ GeV, 6 % for $10 < E_\nu < 50$ GeV, and above that, the error increases with $\log E_\nu$ upto 60 % (1 TeV).

- Up/down ratio
  The neutrino flux has an up/down asymmetry due to the rigidity cutoff by the geomagnetic field. However, the uncertainty in low energy neutrino flux is not expected to affect the zenith angle distributions substantially, because the up/down asymmetry in low energy is largely smeared by the poor angular correlation in neutrino interactions. The systematic uncertainties of the up/down ratio are estimated by the comparison of the zenith angle distributions using the three flux calculation models for each neutrino sample, which are

summarized in Table 6.4.

- Horizontal/vertical ratio
  The systematic uncertainty of horizontal/vertical ratio is caused mainly by the difference in the 3-dimensional calculation method in each flux calculation model below 3 GeV of neutrino energy. For the neutrinos above 3 GeV, the uncertainty is caused by the difference in the predicted $K/\pi$ ratio in hadronic interactions in the atmosphere. The systematic uncertainties of horizontal/vertical ratio are estimated by the comparison of the zenith angle distributions using the three flux calculation models for each neutrino sample, which are summarized in Table 6.5.

- K/$\pi$ ratio
  Atmospheric neutrinos source is mainly $\pi^+$ or $\pi^-$ in the neutrino energy region below 10 GeV. $K$'s contribute to the neutrino production above a few tens of GeV. The uncertainty of $K/\pi$ ratio production ratio in cosmic ray interactions in atmosphere could be the systematic error. According to the SPY experiment [133], the measurement of the $K/\pi$ ratio is obtained with an accuracy of 3%, where $K$ and $\pi$ momentum ranges from 7 GeV/c to 135 GeV/c. Using the SPY experiment result and the correspondence between hadron momentum and neutrino energy, the uncertainty of $K/\pi$ ratio is estimated to be 5% below $E_\nu$=100GeV and 20% above $E_\nu$=1TeV. The uncertainty is assumed to increase linearly from 5% to 20% between 100GeV and 1TeV.

- Neutrino pass length
  Since the atmospheric neutrino flight length is used in the calculation of the neutrino oscillation probabilities, the uncertainty in the altitude of the neutrinos production hight is needed to be estimated, especially for downward-going and horizontally-going neutrinos. The uncertainty of the neutrino production hight is related to the structure of the atmosphere. The systematic uncertainty is estimated using the flux calculation which is carried out by changing the density structure of atmosphere by 10%. This 10% uncertainty is given by the comparison between US-standard'76 and MSISE90 [134]. Figure 6.11 shows the comparison of the flight length in the different density structures. The difference of the neutrino flux due to the change of the path length is taken into account in the systematic uncertainty.

- Solar activity
  The primary cosmic ray flux is affected by the solar activity, which changes the cosmic ray flux in every 11 year period. $\pm$ 1 year of uncertainty is assigned to the modulation of the solar activity, which corresponds to 20 % uncertainty in the activity for SK-I, 50 % for SK-II and 20 % for SK-III.

- Sample-by-sample normalization
  The energy dependence of the absolute normalization is different for each flux model and the difference can not be explained by a simple spectral index uncertainty as seen in Figure 6.12. From a comparison of the predicted number of events among three flux models [22, 49, 50], 5 % is assigned as the relative normalization uncertainty for FC multi-GeV sample and PC+UPMU-stop sample.

- Matter effect
  The electron density of the Earth affects to the calculation of the neutrino oscillation
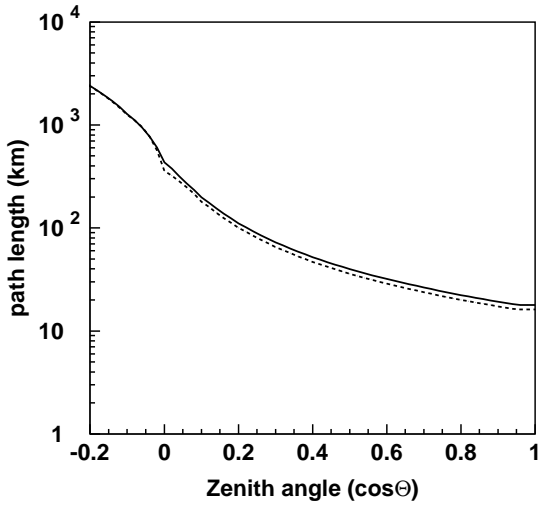
Figure 6.11: Neutrino flight length as a function of zenith angle. Solid curve shows the flight length used in our analysis and dashed curve shows that for the compressed density structure of atmosphere by 10%.
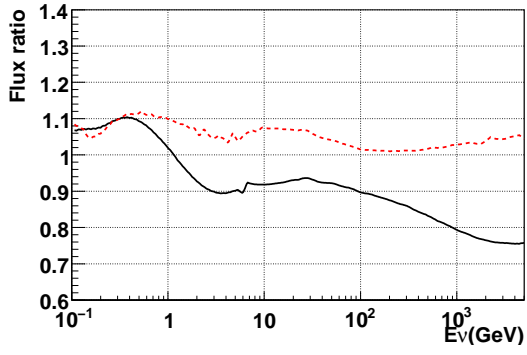


Figure 6.12: The ratio of the calculated neutrino flux in which the fluxes calculated in Bartol (solid line) and FLUKA (dashed line) are normalized by the Honda flux.
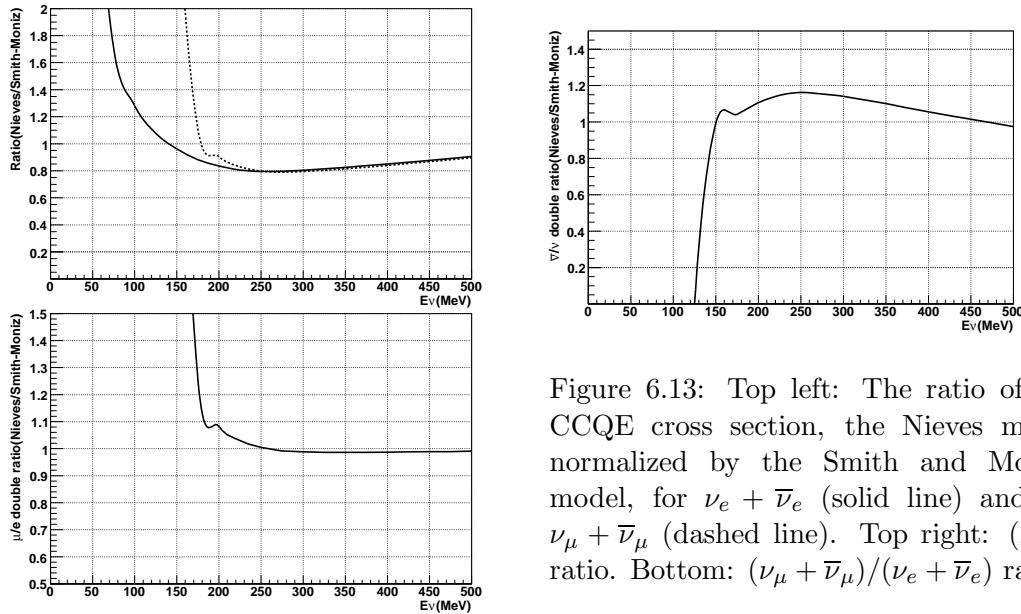
Figure 6.13: Top left: The ratio of the CCQE cross section, the Nieves model normalized by the Smith and Monitz model, for $\nu_e + \overline{\nu}_e$ (solid line) and for $\nu_\mu + \overline{\nu}_\mu$ (dashed line). Top right: $(\overline{\nu}/\nu)$ ratio. Bottom: $(\nu_\mu + \overline{\nu}_\mu)/(\nu_e + \overline{\nu}_e)$ ratio.

probabilities. The density of matter is measured well by [135], but the electron density depends on the chemical composition in the Earth. Since the core region is expected to consist of heavy elements (Fe) mostly, the electron density is less than that of light elements by about 6.8 %. The difference of number of oscillated neutrino events from the reduced electron density is taken into account in the uncertainty of the matter effect.

## 6.5.2 Systematics in neutrino interaction

- CCQE cross-section
  The cross-section of CCQE for the bound nucleon is calculated based on the Smith and Monitz Fermi-gas model. The difference from the Nieves *et al.* model [83] is set to $1\sigma$ uncertainty as the CCQE total cross-section. The uncertainties in the CCQE cross-section of $(\overline{\nu}/\nu)$ ratio and flavor ratio $(\nu_\mu + \overline{\nu}_\mu)/(\nu_e + \overline{\nu}_e)$ are also set by the difference from the Nieves model. Figure 6.13 shows the calculated CCQE cross-section ratio, the Nieves model to the Smith and Monitz model, as a function of the neutrino energy for the total cross-section, the $\overline{\nu}/\nu$ ratio and the flavor ratio.

- $M_A$ in CCQE and single meson production
  For $M_A$ in CCQE and single meson production, the difference of $Q^2$ spectrum between $M_A = 1.2$ and $M_A = 1.1$ is set to the systematic uncertainty in order to take into account 10 % uncertainty of $M_A$ parameter as described in Section 3.3.1.

- Single meson production cross-section
  The uncertainty in the cross-section of the single-meson production is estimated to be 20 % according to the difference between the expectation and experimental data of the $\nu_\mu p \to \mu^- p \pi^+$ observation. The $\nu_\mu n \to \mu^- p \pi^0$ interaction is poorer understood due to few experimental results. So the additional uncertainty is estimated by the comparison

| Systematic error in neutrino flux (1) | | | fit value % | $\sigma$ (%) |
|---|---|---|---|---|
| Flux normalization | $E_\nu < 1\mathrm{GeV}$ | | 37.20 | $25^a$ |
| | $E_\nu > 1\mathrm{GeV}$ | | 9.51 | $15^b$ |
| $\nu_\mu/\nu_e$ | | | | |
| | $E_\nu < 1\mathrm{GeV}$ | | -0.68 | 2 |
| | $1 < E_\nu < 10\mathrm{GeV}$ | | -2.31 | 3 |
| | $E_\nu > 10\mathrm{GeV}$ | | -2.97 | $5^c$ |
| $\bar{\nu}_e/\nu_e$ | | | | |
| | $E_\nu < 1\mathrm{GeV}$ | | 3.43 | 5 |
| | $1 < E_\nu < 10\mathrm{GeV}$ | | 0.73 | 5 |
| | $E_\nu > 10\mathrm{GeV}$ | | -0.76 | $8^d$ |
| $\bar{\nu}_\mu/\nu_\mu$ | | | | |
| | $E_\nu < 10\mathrm{GeV}$ | | -0.17 | 2 |
| | $1 < E_\nu < 10\mathrm{GeV}$ | | -1.25 | 6 |
| | $E_\nu > 10\mathrm{GeV}$ | | -4.38 | $15^e$ |
| Up/down ratio | < 400 MeV | $e$-like 0-decay | -0.05 | 0.1 |
| | | $\mu$-like 0-decay | -0.52 | 1.1 |
| | | $\mu$-like 1-decay | -0.14 | 0.3 |
| | > 400 MeV | $e$-like 0-decay | -0.38 | 0.8 |
| | | $\mu$-like 0-decay | -0.88 | 1.7 |
| | | $\mu$-like 1-decay | -0.24 | 0.5 |
| | Multi-GeV | $e$-like | -0.33 | 0.7 |
| | | $\mu$-like | -0.10 | 0.2 |
| | Multi-ring Sub-GeV | $\mu$-like | -0.10 | 0.2 |
| | Multi-ring Multi-GeV | $e$-like | -0.15 | 0.3 |
| | | $\mu$-like | -0.10 | 0.2 |
| | PC | | -0.10 | 0.2 |

[a]Uncertainty linearly decreases with $\log E_\nu$ from $25\,\%(0.1\,\mathrm{GeV})$ to $7\,\%(1\,\mathrm{GeV})$.

[b]Uncertainty is $7\,\%$ upto $10\,\mathrm{GeV}$, and it linearly increases with $\log E_\nu$ from $7\,\%(10\,\mathrm{GeV})$ to $12\,\%(100\,\mathrm{GeV})$ and then from $12\,\%(100\,\mathrm{GeV})$ to $20\,\%(1\,\mathrm{TeV})$

[c]Uncertainty linearly increases with $\log E_\nu$ from $5\,\%(30\,\mathrm{GeV})$ to $30\,\%(1\,\mathrm{TeV})$.

[d]Uncertainty linearly increases with $\log E_\nu$ from $8\,\%(100\,\mathrm{GeV})$ to $20\,\%(1\,\mathrm{TeV})$.

[e]Uncertainty linearly increases with $\log E_\nu$ from $6\,\%(50\,\mathrm{GeV})$ to $40\,\%(1\,\mathrm{TeV})$.

Table 6.4: Systematic errors in neutrino flux calculation, that are common between all the SK geometries. The second column shows the best fit value of the systematic errors parameter $\epsilon_i$ in percent and the third column shows the estimated $1\sigma$ error size in percent.

| Systematic error in neutrino flux (2) | | | fit value % | $\sigma$ (%) |
|---|---|---|---|---|
| Horizontal/Vertical ratio | < 400 MeV | $e$-like 0-decay | 0.04 | 0.1 |
| | | $\mu$-like 0-decay | 0.11 | 0.3 |
| | | $\mu$-like 1-decay | 0.04 | 0.1 |
| | > 400 MeV | $e$-like 0-decay | 0.52 | 1.4 |
| | | $\mu$-like 0-decay | 0.52 | 1.4 |
| | | $\mu$-like 1-decay | 0.71 | 1.9 |
| | Multi-GeV | $e$-like | 1.19 | 3.2 |
| | | $\mu$-like | 0.86 | 2.3 |
| | Multi-ring Sub-GeV | $\mu$-like | 0.50 | 1.3 |
| | Multi-ring Multi-GeV | $e$-like | 1.04 | 2.8 |
| | | $\mu$-like | 0.56 | 1.5 |
| | PC | | 0.63 | 1.7 |
| K/$\pi$ ratio in flux calculation | | | -9.43 | $10^a$ |
| Neutrino path length | | | -0.71 | 10 |
| Sample-by-sample | FC Multi-GeV | | -5.39 | 5 |
| | PC + Up-stop $\mu$ | | -3.93 | 5 |
| Matter effect | | | -0.002 | $1.0^b$ |
| Solar Activity | SK-I | | -0.11 | 20 |
| | SK-II | | 23.32 | 50 |
| | SK-III | | 2.88 | 20 |

[a]Uncertainty increases linearly from 5% to 20% between 100GeV and 1TeV.
[b]Difference of the electron density in the core region from heavy element case is set to 1.0

Table 6.5: Systematic errors in neutrino flux calculation, that are common between all the SK geometries. The second column shows the best fit value of the systematic errors parameter $\epsilon_i$ in percent and the third column shows the estimated $1\sigma$ error size in percent.
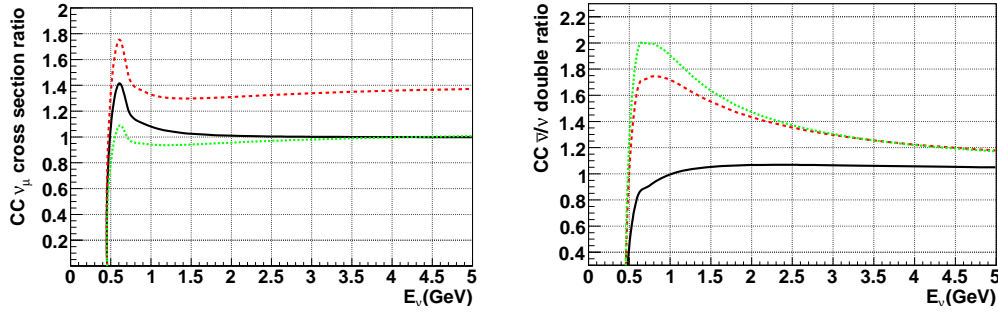
Figure 6.14: the predicted cross-section(left panel) and the $\overline{\nu}/\nu$ ratio(right panel) of the Hernandez model normalized by that of the Rein and Sehgal model for $\nu_\mu p \to \mu^- p \pi^+$(solid line), $\nu_\mu n \to \mu^- p \pi^0$(dashed line) and $\nu_\mu n \to \mu^- p \pi^+$(dotted line).

with the Hernandez [141] model. The cross-section ratio of $\nu_\mu n \to \mu^- p \pi^0$ is shown by the dashed line in the left panel of Figure 6.14. It is considered that $\pi^0$ production interaction has 40 % uncertainty relative to the $\pi^\pm$ emitting interaction. The uncertainty in the single meson production cross-section of the $\bar{\nu}/\nu$ ratio is also set by the difference from the Hernandez model. The right panel of Figure 6.14 shows the $\bar{\nu}/\nu$ ratio of the CC cross-section normalized by the Rein and Sehgal model.

- Deep inelastic scattering cross section
  The calculation of cross-section for DIS agrees with the experimental measurement within 5 %. But, since the uncertainty is larger in the lower energy region ($< 10$ GeV) , the additional error is estimated by the difference from the CKMT model [142].

- $Q^2$ spectrum in deep inelastic scattering
  The uncertainty of the $Q^2$ spectrum is taken into account by the comparison with original GRV98 model. This uncertainty is considered to be separated for W $< 1.3$ GeV/c$^2$ and W $> 1.3$ GeV/c$^2$.

- Coherent pion production cross-section
  The uncertainty is obtained as 50 % by the difference between the Rein and Sehgal model and experimental measurement for NC and CC$\nu_e$ interactions. Since CC$\nu_\mu$ coherent pion production is not measured, 100 % uncertainy is considered.

- NC/CC ratio
  The uncertainty of NC/CC ratio is estimated to be 20 %.

- Nuclear effect in $^{16}O$ nucleus
  The uncertainty in the mean free path of hadrons produced via neutrino interaction in the $^{16}O$ nucleus is estimated to be 30 % by the comparison with experimental data.

- Nuclear effect in $\pi$ spectrum
  The difference in the predicted pion spectrum between two simulator, NEUT [76, 77] and NUANCE [137], is taken to be the systematic uncertainty.

- CC$\nu_\tau$ interaction cross section
  The systematic uncertainty for CC$\nu_\tau$ cross-section is estimated to be 30 % by the comparison with Hagiwara *et al.* model [143].

### 6.5.3 Systematics in event selection and reconstruction

- FC/PC separation
  The FC and PC events are separated by the number of OD hit PMT clusters (NHITAC). The systematic uncertainty is estimated to be 0.6 % for SK-I, 0.5 % for SK-II and 0.9 % for SK-III by the difference between observed data and MC NHITAC distributions (Figure 5.12).

- FC reduction related
  The uncertainty in FC reduction efficiency is estimated to be 0.2 % for SK-I, 0.2 % for SK-II and 0.8 % for SK-III by comparing the distributions of each cut valuable for observed data and MC. The contamination of the background is estimated as described in Section 5.1. Error values are summarized in Table 6.7.

- PC reduction related
  The uncertainty in PC reduction efficiency is estimated to be 2.4 % for SK-I, 4.8 % for SK-II and 0.5 % for SK-III by comparing the distributions of each cut valuables for observed data and MC. The contamination of the background is estimated as described in Section 5.2.

- PC stop/through separation
  PC OD stopping and OD through-going events are separated by the energy deposit in OD region (PE$_{anti}$/PE$_{exp}$). The systematic uncertainty is estimated by the difference between observed data and MC PE$_{anti}$/PE$_{exp}$ distributions (Figure 5.25). The estimation is separately performed for OD bottom, barrel and top region since the OD calibration has the difference depending on the OD position. The error values are summarized in Table 6.7.

- UPMU reduction related
  The uncertainty in UPMU reduction efficiency is estimated by comparing the distributions of each cut valuables for observed data and MC. For stopping muon, the estimated uncertainties are 0.7 % for SK-I, 0.7 % for SK-II and 0.7 % for SK-III. For through-going muon, the estimated uncertainties are 0.5 % for SK-I, 0.5 % for SK-II and 0.5 % for SK-III. These uncertainties for stopping and through-going muons are assumed to be correlated. The stopping muon and through-going muon are separated by the number of hit OD PMTs within 8m from the projected exit point (NHITEX). The separation uncertainty is estimated to be 0.4 % for SK-I, 0.4 % for SK-II and 0.6 % for SK-III by the difference between observed data and MC NHITEX distributions (Figure 5.26). Additional systematic uncertainty for stopping muon from energy cut in the final selection is estimated to be 0.8 % for SK-I, 1.4 % for SK-II and 2.1 % for SK-III. Other additional systematic uncertainty for through-going muon from path length cut in the final selection is estimated to be 1.8 % for SK-I, 2.1 % for SK-II and 1.6 % for SK-III. Finally, the contamination of the background in UPMU sample is estimated as described in Section 5.3. The error values are summarized in Table 6.7.

| Systematic error in neutrino interaction | | | fit value % | $\sigma$ (%) |
|---|---|---|---|---|
| CCQE cross section | | | 0.57 | 1.0[a] |
| CCQE $\bar{\nu}_i/\nu_i$ (i=e,$\mu$) ratio | | | 0.92 | 1.0[a] |
| CCQE $\mu$/e ratio | | | 0.68 | 1.0[a] |
| $M_A$ in CCQE and single meson production | | | 0.59 | 10 |
| Single meson production cross section | | | 9.87 | 20 |
| Single $\pi$ production, $\pi^0/\pi^{\pm}$ ratio | | | -29.21 | 40 |
| Single $\pi$ production, $\bar{\nu}_i/\nu_i$ (i=e,$\mu$) ratio | | | -0.01 | 1.0[b] |
| DIS cross section ($E_\nu < 10$ GeV) | | | 0.05 | 1.0[c] |
| DIS cross section | | | 2.02 | 5 |
| $Q^2$ spectrum in DIS (W < 1.3 GeV/c$^2$) | | | 0.24 | 1.0[d] |
| $Q^2$ spectrum in DIS (W > 1.3 GeV/c$^2$) | | | 0.39 | 1.0[d] |
| Coherent $\pi$ production | | | -30.99 | 100 |
| NC/(CC) | | | 0.40 | 20 |
| Nuclear effect in $^{16}$O nucleus | | | -12.92 | 30 |
| Nuclear effect in pion spectrum | | | 0.85 | 1.0[e] |
| $\nu_\tau$ contamination | | | -5.59 | 30 |
| NC in FC $\mu$-like (hadron simulation) | | | -2.40 | 10 |
| Decay-e tagging ($\pi^+$ interaction)[f]   Sub-GeV 1-ring | $e$-like 0-decay | | -0.2~-0.5 | 0.2~0.5 |
| | $e$-like 1-decay | | 4.0~4.2 | -3.9~-4.1 |
| | $\mu$-like 0-decay | | -0.5~-0.8 | 0.5~0.8 |
| | $\mu$-like 1-decay | | 0.5~0.9 | -0.4~-0.8 |
| | $\mu$-like 2-decay | | 5.2~5.8 | -5.1~-5.7 |

[a]Difference from the Nieves model is set to 1.0.

[b]Difference from the Hernandez model is set to 1.0.

[c]Difference from CKMT parametrization is set to 1.0.

[d]Difference from original GRV98 model is set to 1.0.

[e]Difference between NEUT and NUANCE is set to 1.0.

[f]They are assumed to be identical and full correlated for each SK run period.

Table 6.6: Systematic errors in neutrino interactions, that are common between all the SK geometries. The second column shows the best fit value of the systematic errors parameter $\epsilon_i$ in percent and the third column shows the estimated $1\sigma$ error size in percent.

- UPMU non-showering/showering separation
  The UPMU non-showering and showering events are separated by the difference between the average corrected charge and expected charge for non-showering events ($\Delta(Q)$). The systematic uncertainty is estimated by the comparison of $\Delta(Q)$ distribution (Figure 5.30) for data and MC. The error values are set to be 9 % for SK-I, 13 % for SK-II and 6 % for SK-III.

- Ring separation
  Ring separation is based on the ring-counting algorithm (Section 5.4.2). The uncertainties are estimated by the difference of likelihood distributions between observed data and MC for each sample. The error values are summarized in Tables 6.8, 6.9 and 6.10.

- Particle identification
  The uncertainties in the particle identification are estimated by the difference of PID likelihood distributions (Section 5.4.3) between observed data and MC for each sample. The error values are summarized in Tables 6.8, 6.9 and 6.10.

- Energy calibration
  The energy scale uncertainties are estimated in Section 4.2. The systematic uncertainty for absolute energy scale is set to 1.1 % for SK-I, 1.7 % for SK-II and 2.7 % for SK-III. The uncertainty in the upward/downward symmetry of energy calibration is estimated to be 0.6 % for SK-I, 0.6 % for SK-II and 1.3 % for SK-III.

- Multi-GeV Multi-ring e-like sample selection
  The FC Multi-GeV Multi-ring e-like events are selected as described in Section 6.2.2. The uncertainties in the selection efficiency are estimated by comparing observed data with MC for the likelihood distributions. The MC likelihood distribution is re-scaled to get the best-fit to the data distribution. The maximal change on the number of events after shifted distributions by $\pm 1\sigma$ from the best-fit parameter is taken to the systematic uncertainty. The change on the signal event ($CC\nu_e$) is set to the selection efficiency uncertainty, and the change on the background event (NC and $CC\nu_\mu$) is set to the uncertainty for the contamination of the background in this sample. The estimated systematic uncertainties for the selection efficiencies are 6.4 % for SK-I, 11.1 % for SK-II and 5.3 % for SK-III. The estimated systematic uncertainties for the BG contamination are 35.6 % for SK-I, 22.3 % for SK-II and 38 % for SK-III.

- Single-ring $\pi^0$-like sample selection
  The FC Sub-GeV single-ring $\pi^0$-like events are selected as described in Section 6.2.1. The uncertainties in the selection efficiency are estimated by comparing observed data with MC for the $\pi^0$ mass and likelihood distributions. Since likelihood distribution is different for each momentum bin, the systematic uncertainties are estimated for each momentum region. The uncertainties in the selection efficiency also come from the absolute energy scale uncertainty. The combined uncertainties, from the difference of distribution and the shift of energy scale, are summarized in Tables 6.8, 6.9 and 6.10.

- Two-ring $\pi^0$ selection
  The FC Sub-GeV two-ring $\pi^0$-like events are selected as described in Section 4.2.3. The uncertainty in the selection efficiency comes from the ring-counting and PID. The uncertainty is estimated to be 2 % for SK-I, 2 % for SK-II and 1 % for SK-III.

- Decay electron tagging

  The systematic error in the decay electron detection efficiency is estimated to be 1.5 % using cosmic ray muons [139]. This systematic error is assumed to be identical for each SK run period. In addition, $\pi^+$ decay probability uncertainty is considered for that systematic error. Since $\pi^+$'s are interacted in the water depending on the energy, the differences of the decay probability are 3∼13 % due to the $\pi^+$ momentum. So it affects the uncertainty for decay electron tagging by 0.3∼0.6 % for FC Sub-GeV single-ring e-like 0-decay sample. The error values are summarized in Tables 6.6 for each sub-sample. This systematic error is assumed to be correlated for each sub-sample and it is a common error value for all SK run periods.

| Systematic error in event reduction | | SK-I | | SK-II | | SK-III | |
|---|---|---|---|---|---|---|---|
| | | fit | $\sigma$ | fit | $\sigma$ | fit | $\sigma$ |
| FC/PC separation | | -0.03 | 0.6 | 0.08 | 0.5 | -0.24 | 0.9 |
| FC reduction | | 0.003 | 0.2 | 0.006 | 0.2 | 0.03 | 0.8 |
| PC reduction | | -1.64 | 2.4 | -3.33 | 4.8 | 0.02 | 0.5 |
| Non-$\nu$ BG ( $e$-like ) | Sub-GeV e-like | 0.03 | 0.5 | -0.001 | 0.2 | 0.002 | 0.1 |
| | Multi-GeV e-like | 0.02 | 0.3 | -0.001 | 0.3 | 0.009 | 0.4 |
| Non-$\nu$ BG ( $\mu$-like ) | Sub-GeV $\mu$-like | -0.01 | 0.1 | 0.001 | 0.1 | 0.03 | 0.1 |
| | Multi-GeV $\mu$-like | -0.01 | 0.1 | 0.001 | 0.1 | 0.05 | 0.2 |
| | PC | 0.03 | 0.2 | 0.04 | 0.7 | 0.47 | 1.8 |
| PC-stop/PC-through separation -TOP- | | 13.29 | 14 | -16.00 | 21 | -15.19 | 31 |
| PC-stop/PC-through separation -BARREL- | | -1.57 | 7.5 | -33.62 | 17 | 3.49 | 23 |
| PC-stop/PC-through separation -BOTTOM- | | -5.08 | 11 | -9.88 | 12 | 0.48 | 11 |
| Fiducial volume | | -0.88 | 2 | 0.06 | 2 | 0.53 | 2 |
| Upward-going muon reduction [a] | Stopping | 0.02 | 0.7 | -0.11 | 0.7 | 0.19 | 0.7 |
| | Through-going | 0.02 | 0.5 | -0.08 | 0.5 | 0.14 | 0.5 |
| Upward stopping/through-going $\mu$ separation | | 0.006 | 0.4 | 0.01 | 0.4 | 0.05 | 0.6 |
| Upward through-going $\mu$ showering separation | | 13.28 | 9 | 5.65 | 13 | 8.30 | 6 |
| Energy cut for upward stopping $\mu$ | | -0.006 | 0.8 | -0.07 | 1.4 | 1.02 | 2.1 |
| Path length cut for upward through-going $\mu$ | | 0.27 | 1.8 | -1.13 | 2.1 | 0.55 | 1.6 |
| BG subtraction for upward $\mu$ [b] | Stopping | 5.00 | 16 | -7.38 | 21 | 0.79 | 20 |
| | Non-showering | -6.19 | 11 | 3.47 | 15 | 2.30 | 19 |
| | Showering | -0.47 | 18 | -19.58 | 14 | 23.84 | 24 |

[a]The uncertainties in the upward-going stopping and through-going muons are assumed to be correlated. Therefore there is only one error term in each run period.

[b]The uncertainties in BG subtraction for upward-going muons are only for the most horizontal events which are in the bin of $-0.1 < \cos\theta < 0$.

Table 6.7: Systematic errors in event reduction for each SK run period. The column of "fit" show the best fit values of the systematic errors parameter $\epsilon_i$ in percent and the column of "$\sigma$" show the estimated $1\sigma$ error sizes in percent.

| (SK-I) Systematic error in event reconstruction and selection | | | fit value % | $\sigma(\%)$ |
|---|---|---|---|---|
| Ring separation | < 400 MeV | $e$-like | 1.23 | 2.3 |
| | | $\mu$-like | 0.37 | 0.7 |
| | > 400 MeV | $e$-like | 0.22 | 0.4 |
| | | $\mu$-like | 0.37 | 0.7 |
| | Multi-GeV | $e$-like | 1.98 | 3.7 |
| | | $\mu$-like | 0.91 | 1.7 |
| | Multi-ring sub-GeV | $\mu$-like | -2.41 | -4.5 |
| | Multi-ring multi-GeV | $e$-like | -1.66 | -3.1 |
| | | $\mu$-like | -2.19 | -4.1 |
| PID (single-ring) | Sub-GeV | $e$-like | -0.01 | 0.1 |
| | | $\mu$-like | 0.01 | -0.1 |
| | Multi-GeV | $e$-like | 0.02 | -0.2 |
| | | $\mu$-like | -0.02 | 0.2 |
| PID (multi-ring) | Sub-GeV | $\mu$-like | -0.33 | -3.9 |
| | Multi-GeV | $e$-like | 0.15 | 1.7 |
| | | $\mu$-like | -0.26 | -2.9 |
| Energy calibration | | | 0.10 | 1.1 |
| Up/Down asymmetry energy calibration | | | -0.33 | 0.6 |
| Multi-GeV Single-ring $e$-like non CC$\nu_e$ BG | | | 5.21 | 16.3 |
| Multi-GeV Multi-ring $e$-like non CC$\nu_e$ BG | | | -5.16 | 35.6 |
| Multi-GeV Multi-ring $e$-like selection (likelihood) | | | -1.56 | 6.4 |
| Sub-GeV 1-ring $\pi^0$ selection | $100 < P_e < 250$ MeV/c | | -3.35 | 11.2 |
| | $250 < P_e < 400$ MeV/c | | -3.44 | 11.5 |
| | $400 < P_e < 630$ MeV/c | | -7.01 | 23.4 |
| | $630 < P_e < 1000$ MeV/c | | -5.72 | 19.1 |
| | $1000 < P_e < 1330$ MeV/c | | -3.89 | 13 |
| Sub-GeV 2-ring $\pi^0$ | | | -0.18 | 2 |
| Decay-e tagging ($\mu$ decay) | | | 0.26 | 1.5 |

Table 6.8: Systematic errors in event reconstruction and selection for SK-I. The second column shows the best fit value of the systematic errors parameter $\epsilon_i$ in percent and the third column shows the estimated $1\sigma$ error size in percent.

| (SK-II) Systematic error in event reconstruction and selection | | | fit value % | $\sigma(\%)$ |
|---|---|---|---|---|
| Ring separation | < 400 MeV | $e$-like | -1.53 | 1.3 |
| | | $\mu$-like | -2.70 | 2.3 |
| | > 400 MeV | $e$-like | -2.00 | 1.7 |
| | | $\mu$-like | -0.82 | 0.7 |
| | Multi-GeV | $e$-like | -3.06 | 2.6 |
| | | $\mu$-like | -2.00 | 1.7 |
| | Multi-ring sub-GeV | $\mu$-like | 9.64 | -8.2 |
| | Multi-ring multi-GeV | $e$-like | 2.23 | -1.9 |
| | | $\mu$-like | 0.94 | -0.8 |
| PID (single-ring) | Sub-GeV | $e$-like | 0.06 | 0.5 |
| | | $\mu$-like | -0.05 | -0.4 |
| | Multi-GeV | $e$-like | 0.01 | 0.1 |
| | | $\mu$-like | -0.01 | -0.1 |
| PID (multi-ring) | Sub-GeV | $\mu$-like | 0.44 | 2.2 |
| | Multi-GeV | $e$-like | -0.36 | 1.8 |
| | | $\mu$-like | 0.68 | -3.4 |
| Energy calibration | | | -1.19 | 1.7 |
| Up/Down asymmetry energy calibration | | | -0.18 | 0.6 |
| Multi-GeV Single-ring $e$-like non CC$\nu_e$ BG | | | -5.77 | 23.4 |
| Multi-GeV Multi-ring $e$-like non CC$\nu_e$ BG | | | -1.39 | 22.3 |
| Multi-GeV Multi-ring $e$-like selection (likelihood) | | | 0.24 | 11.1 |
| Sub-GeV 1-ring $\pi^0$ selection | $100 < \mathrm{P}_e <\ 250$ MeV/c | | -3.67 | 7.5 |
| | $250 < \mathrm{P}_e <\ 400$ MeV/c | | -4.35 | 8.9 |
| | $400 < \mathrm{P}_e <\ 630$ MeV/c | | -8.56 | 17.5 |
| | $630 < \mathrm{P}_e < 1000$ MeV/c | | -5.23 | 10.7 |
| | $1000 < \mathrm{P}_e < 1330$ MeV/c | | -5.43 | 11 |
| Sub-GeV 2-ring $\pi^0$ | | | -0.03 | 2 |
| Decay-e tagging ($\mu$ decay) | | | 0.47 | 1.5 |

Table 6.9: Systematic errors in event reconstruction and selection for SK-II. The second column shows the best fit value of the systematic errors parameter $\epsilon_i$ in percent and the third column shows the estimated $1\sigma$ error size in percent.

| (SK-III) Systematic error in event reconstruction and selection | | | fit value % | $\sigma(\%)$ |
|---|---|---|---|---|
| Ring separation | < 400 MeV | $e$-like | 0.10 | 2.3 |
| | | $\mu$-like | 0.03 | 0.7 |
| | > 400 MeV | $e$-like | 0.02 | 0.4 |
| | | $\mu$-like | 0.03 | 0.7 |
| | Multi-GeV | $e$-like | 0.15 | 3.7 |
| | | $\mu$-like | 0.07 | 1.7 |
| | Multi-ring sub-GeV | $\mu$-like | -0.19 | -4.5 |
| | Multi-ring multi-GeV | $e$-like | -0.17 | -3.1 |
| | | $\mu$-like | -0.17 | -4.1 |
| PID (single-ring) | Sub-GeV | $e$-like | 0.002 | 0.1 |
| | | $\mu$-like | -0.002 | -0.1 |
| | Multi-GeV | $e$-like | -0.004 | -0.2 |
| | | $\mu$-like | 0.004 | 0.2 |
| PID (multi-ring) | Sub-GeV | $\mu$-like | -0.29 | -3.9 |
| | Multi-GeV | $e$-like | 0.13 | 1.7 |
| | | $\mu$-like | -0.22 | -2.9 |
| Energy calibration | | | -0.23 | 2.7 |
| Up/Down asymmetry energy calibration | | | 0.007 | 1.3 |
| Multi-GeV Single-ring $e$-like non CC$\nu_e$ BG | | | 3.92 | 41.4 |
| Multi-GeV Multi-ring $e$-like non CC$\nu_e$ BG | | | -19.18 | 38 |
| Multi-GeV Multi-ring $e$-like selection (likelihood) | | | -0.39 | 5.3 |
| Sub-GeV 1-ring $\pi^0$ selection | $100 < P_e < 250$ MeV/c | | -5.09 | 7.7 |
| | $250 < P_e < 400$ MeV/c | | -17.47 | 26.4 |
| | $400 < P_e < 630$ MeV/c | | -8.27 | 12.5 |
| | $630 < P_e < 1000$ MeV/c | | -17.66 | 26.7 |
| | $1000 < P_e < 1330$ MeV/c | | -17.66 | 26.7 |
| Sub-GeV 2-ring $\pi^0$ | | | 0.02 | 1 |
| Decay-e tagging ($\mu$ decay) | | | 1.1 | 1.5 |

Table 6.10: Systematic errors in event reconstruction and selection for SK-III. The second column shows the best fit value of the systematic errors parameter $\epsilon_i$ in percent and the third column shows the estimated $1\sigma$ error size in percent.

## 6.6 Results

In this analysis, the zenith angle and momentum distributions of the various samples are simultaneously fitted with the simulated distributions including all oscillation parameters, two mass differences ($\Delta m_{12}^2$, $\Delta m_{23}^2$), three mixing angles ($\theta_{12}$, $\theta_{23}$, $\theta_{13}$), and CP phase ($\delta_{cp}$). A $\chi^2$ is calculated in the fitting process by four dimensional oscillation parameter spaces of $\Delta m_{23}^2$, $\theta_{23}$, $\theta_{13}$ and $\delta_{cp}$. The parameters $\Delta m_{12}^2$ and $\sin^2 \theta_{12}$ are fixed to the values determined by the solar neutrino analyses ([37, 146, 147, 18, 19, 20]), since they are already well constrained. It is found that changes of these parameters in the allowed region give negligible effect on the fitting (refer Appendix A.1).

The examined oscillation parameter spaces are:

- $(\Delta m_{12}^2, \sin^2 \theta_{12}) = (7.65 \times 10^{-5}, 0.304)$ (fixed)

- $\Delta m_{23}^2 = 10^{-2.875}$ to $10^{-2.450}$ (18 points)

- $\sin^2 \theta_{23} = 0.3$ to $0.7$ (17 points)

- $\sin^2 \theta_{13} = 0.0$ to $0.4$ (65 points)

- $\delta_{cp} = 0°$ to $340°$ (18 points)

for both mass hierarchy cases.

In the normal hierarchy case, the best-fit is obtained at $(\Delta m_{23}^2, \sin^2 \theta_{23}, \sin^2 \theta_{13}, \delta_{cp}) = (2.1 \times 10^{-3}, 0.525, 0.006, 220°)$ with $\chi_{min}^2/\text{dof} = 469.94/416$. In the inverted hierarchy case, the best-fit is obtained at $(\Delta m_{23}^2, \sin^2 \theta_{23}, \sin^2 \theta_{13}, \delta_{cp}) = (2.5 \times 10^{-3}, 0.575, 0.044, 220°)$ with $\chi_{min}^2/\text{dof} = 468.34/416$. Figures 6.15 and 6.16 (6.17 and 6.18) show the best-fit zenith angle distributions together with the distributions of the observed data and null oscillation for the normal (inverted) mass hierarchy case. These distributions were merged from that of each SK run period, and divided into momentum bins as shown in the figures. The distributions divided by SK run period can be found in Appendix A.2. The best-fit oscillations reproduce the observed data well for both the normal and inverted mass hierarchy cases.

Figures 6.19 and 6.20 show the $\chi^2 - \chi_{min}^2$ distributions as a function of oscillation parameter. When finding the minimum $\chi^2$ against one oscillation parameter dimension, the other three parameters are chosen so that the $\chi^2$ is minimized. The 90 % confidence interval is located at $\chi^2 = \chi_{min}^2 + 2.7$. The parameter allowed regions are estimated using linear interpolating and summarized in Table 6.11.

| | Normal hierarchy | Inverted hierarchy |
|---|---|---|
| $\Delta m_{23}^2$ (eV$^2$) 90 % C.L. | $(1.88 < \Delta m_{23}^2 < 2.75) \times 10^{-3}$ | $(1.98 < \Delta m_{23}^2 < 2.81) \times 10^{-3}$ |
| $\sin^2 \theta_{23}$ 90 % C.L. | $0.406 < \sin^2 \theta_{23} < 0.629$ | $0.426 < \sin^2 \theta_{23} < 0.644$ |
| $\sin^2 \theta_{13}$ 90 % C.L. | $\sin^2 \theta_{13} < 0.066$ | $\sin^2 \theta_{13} < 0.122$ |
| $\delta_{cp}$ 90 % C.L. | — | $121.4° < \delta_{cp} < 319.1°$ |

Table 6.11: Results of the allowed regions for each neutrino oscillation parameters at 90 %C.L.. 90 % C.L. regions are defined to be $\chi^2 - \chi_{min}^2 < 2.7$.

Figures 6.21 and 6.22 show the allowed regions drawn in the two dimensions at 68 %, 90 % and 99 % C.L. defined as $\chi^2 - \chi^2_{min} = 2.3$, 4.6 and 9.2, respectively.
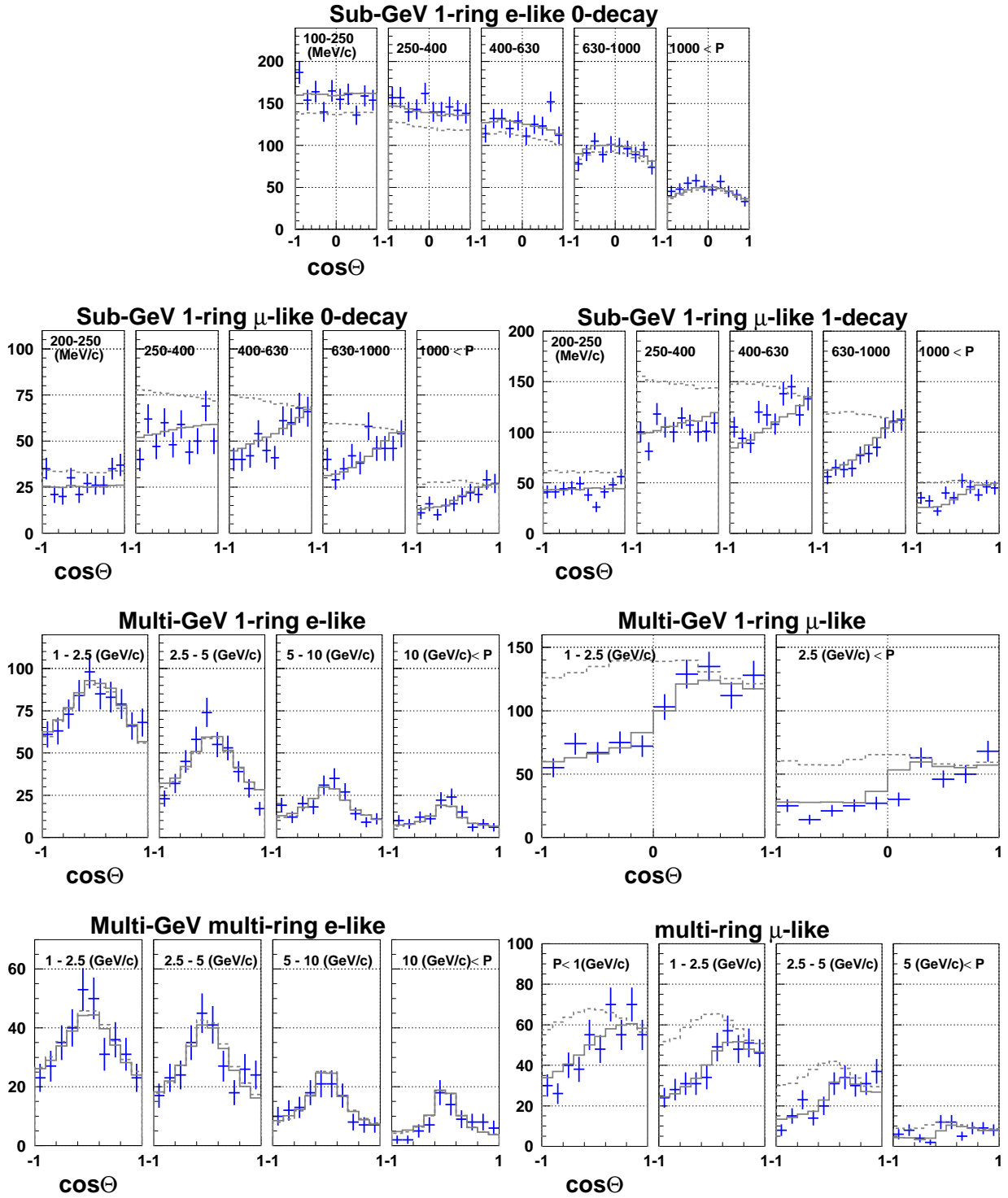
Figure 6.15: SK-I + II + III zenith angle distributions for FC events for data (line with error bar) and MC assuming no oscillation (dashed line) and the best-fit results (solid line). Normal hierarchy is assumed.
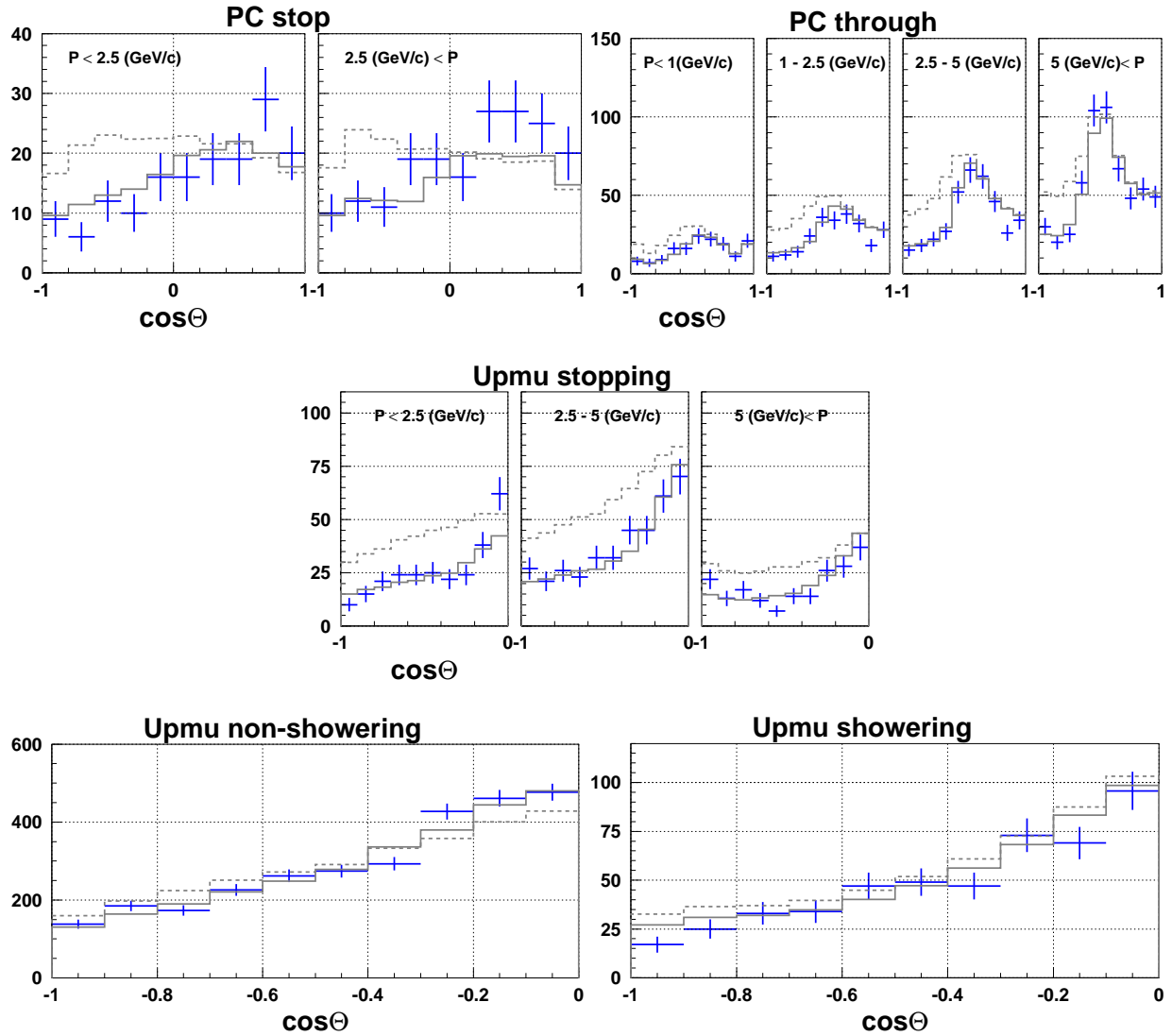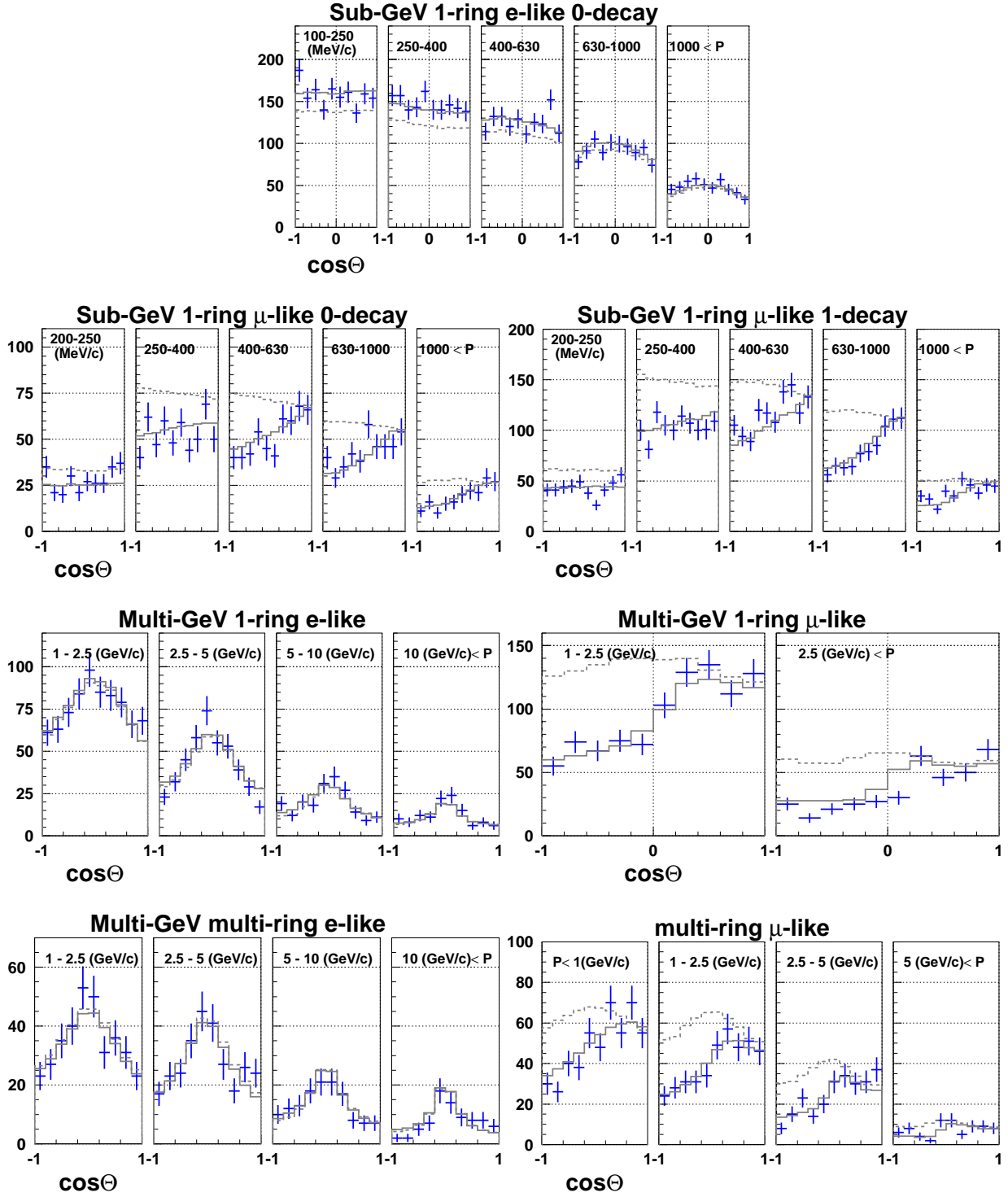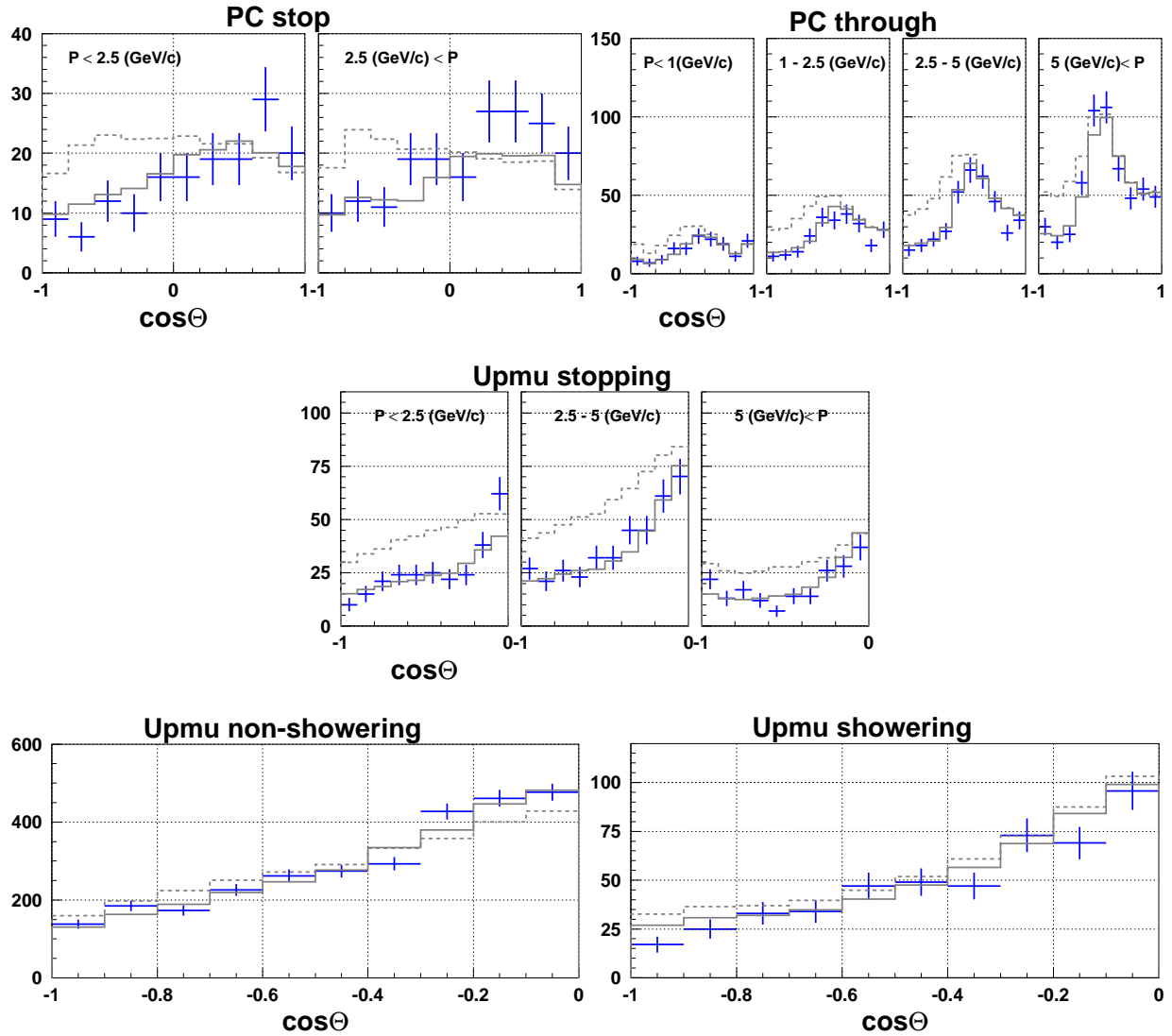
145

Figure 6.16: SK-I + II + III zenith angle distributions for PC and UPMU events for data (line with error bar) and MC assuming no oscillation (dashed line) and the best-fit results (solid line). Normal hierarchy is assumed.

Figure 6.17: SK-I + II + III zenith angle distributions for FC events for data (line with error bar) and MC assuming no oscillation (dashed line) and the best-fit results (solid line). Inverted hierarchy is assumed.

147

Figure 6.18: SK-I + II + III zenith angle distributions for PC and UPMU events for data (line with error bar) and MC assuming no oscillation (dashed line) and the best-fit results (solid line). Inverted hierarchy is assumed.
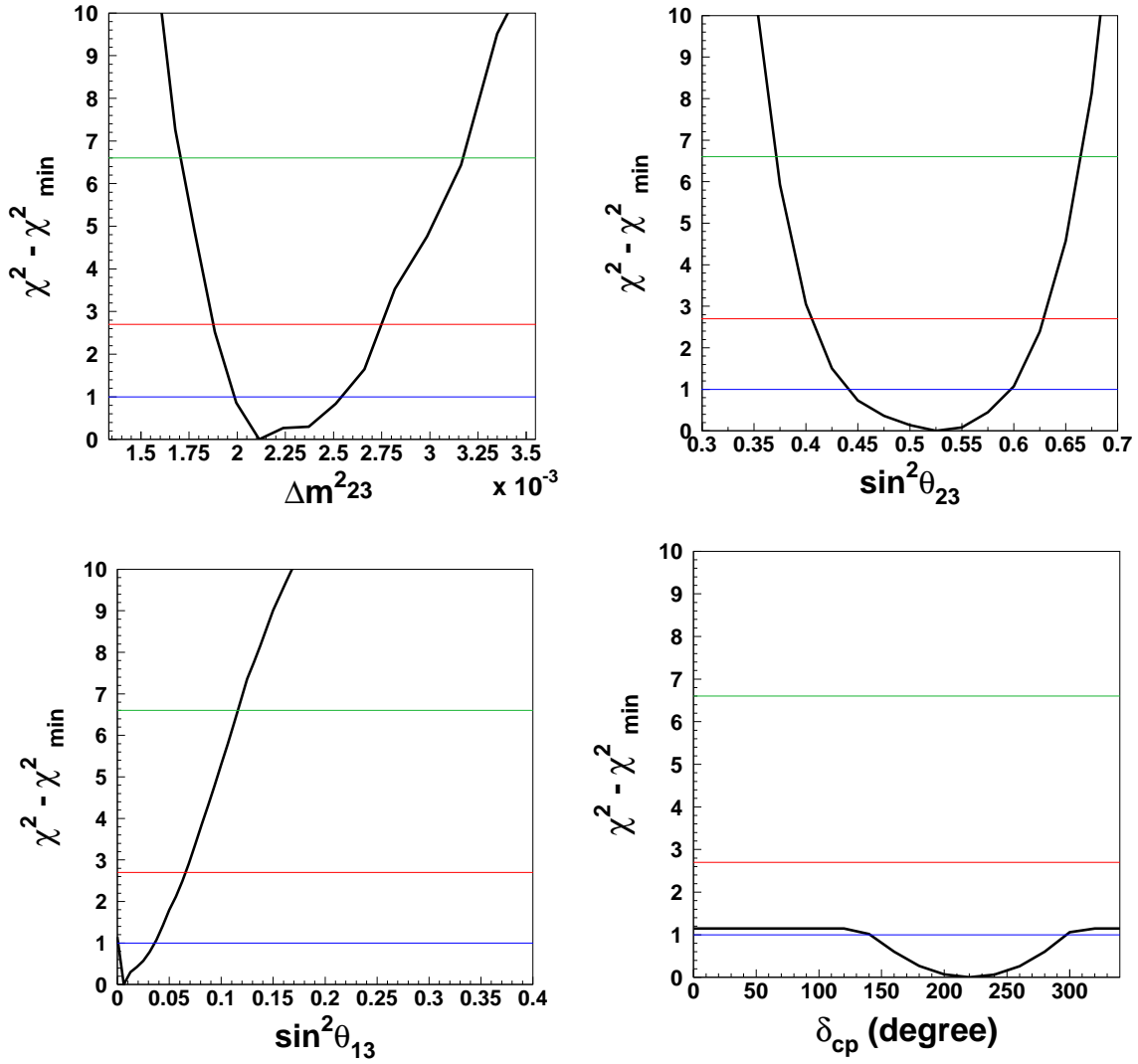
Figure 6.19: The $\Delta\chi^2 = \chi^2 - \chi^2_{min}$ distributions of each $\Delta m^2_{23}$, $\sin^2\theta_{23}$, $\sin^2\theta_{13}$ and $\delta_{cp}$ parameter for the normal mass hierarchy case. The three horizontal lines at $\Delta\chi^2 = 1.0$, 2.7 and 6.6 indicate 68 % C.L., 90 % C.L. and 99 % C.L.
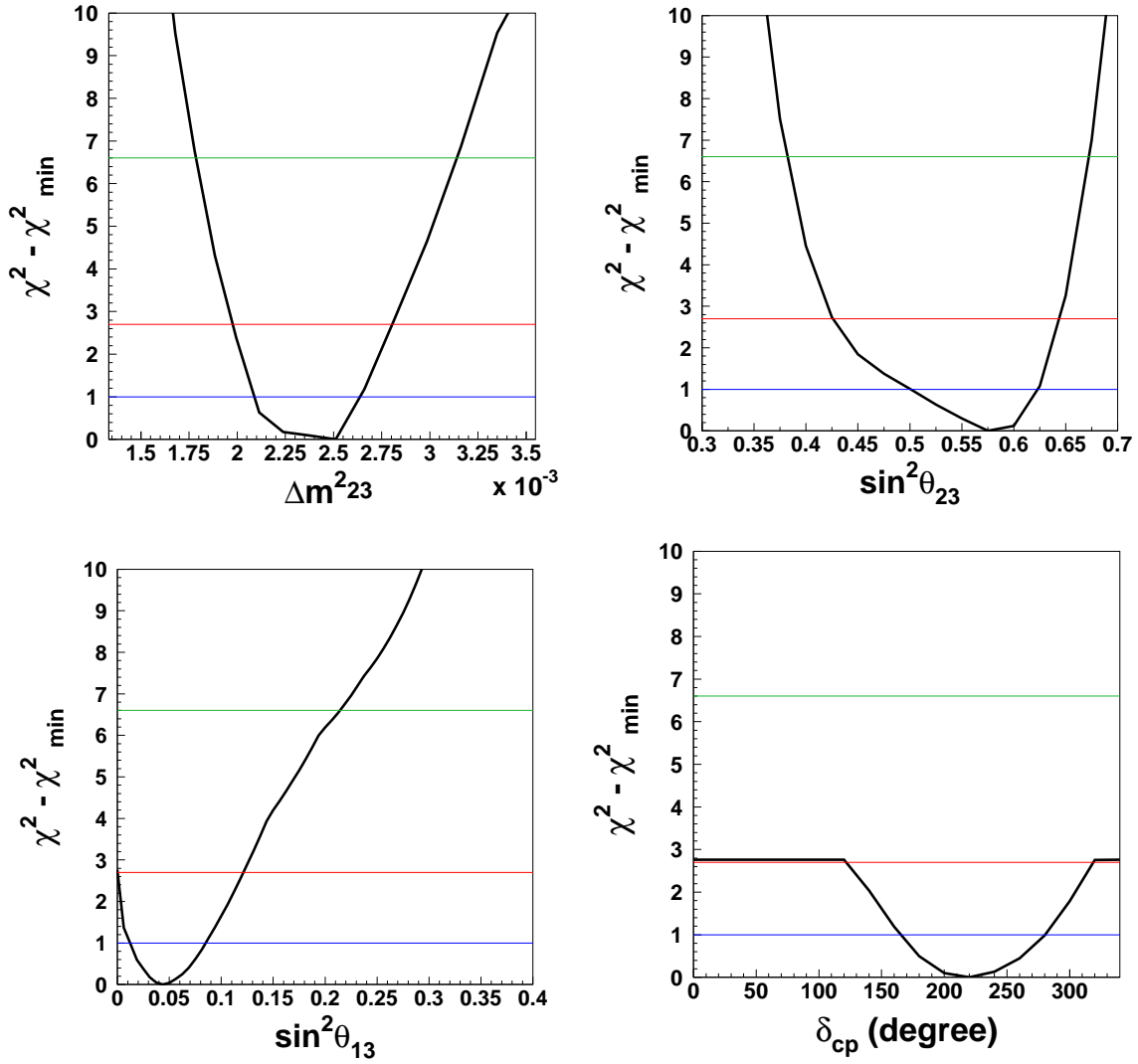
Figure 6.20: The $\Delta\chi^2 = \chi^2 - \chi^2_{min}$ distributions of each $\Delta m^2_{23}$, $\sin^2\theta_{23}$, $\sin^2\theta_{13}$ and $\delta_{cp}$ parameter for the inverted mass hierarchy case. The three horizontal lines at $\Delta\chi^2 = 1.0$, 2.7 and 6.6 indicate 68 % C.L., 90 % C.L. and 99 % C.L.
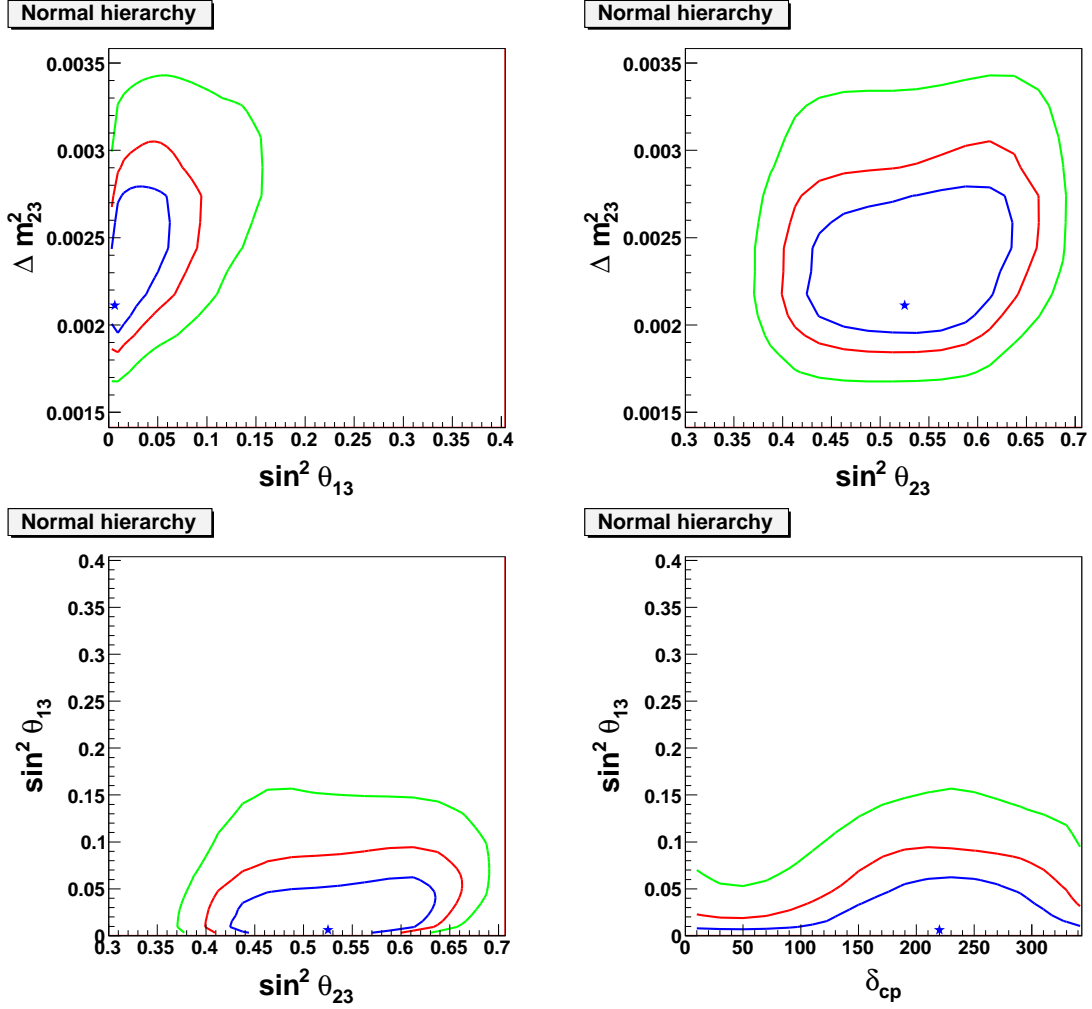
Figure 6.21: Contours for the normal mass hierarchy case. The three lines indicate the allowed regions at 68 % C.L., 90 % C.L. and 99 % C.L. defined as $\Delta\chi^2 = 2.3$, 4.6 and 9.2. The stars show the best-fit parameter point.
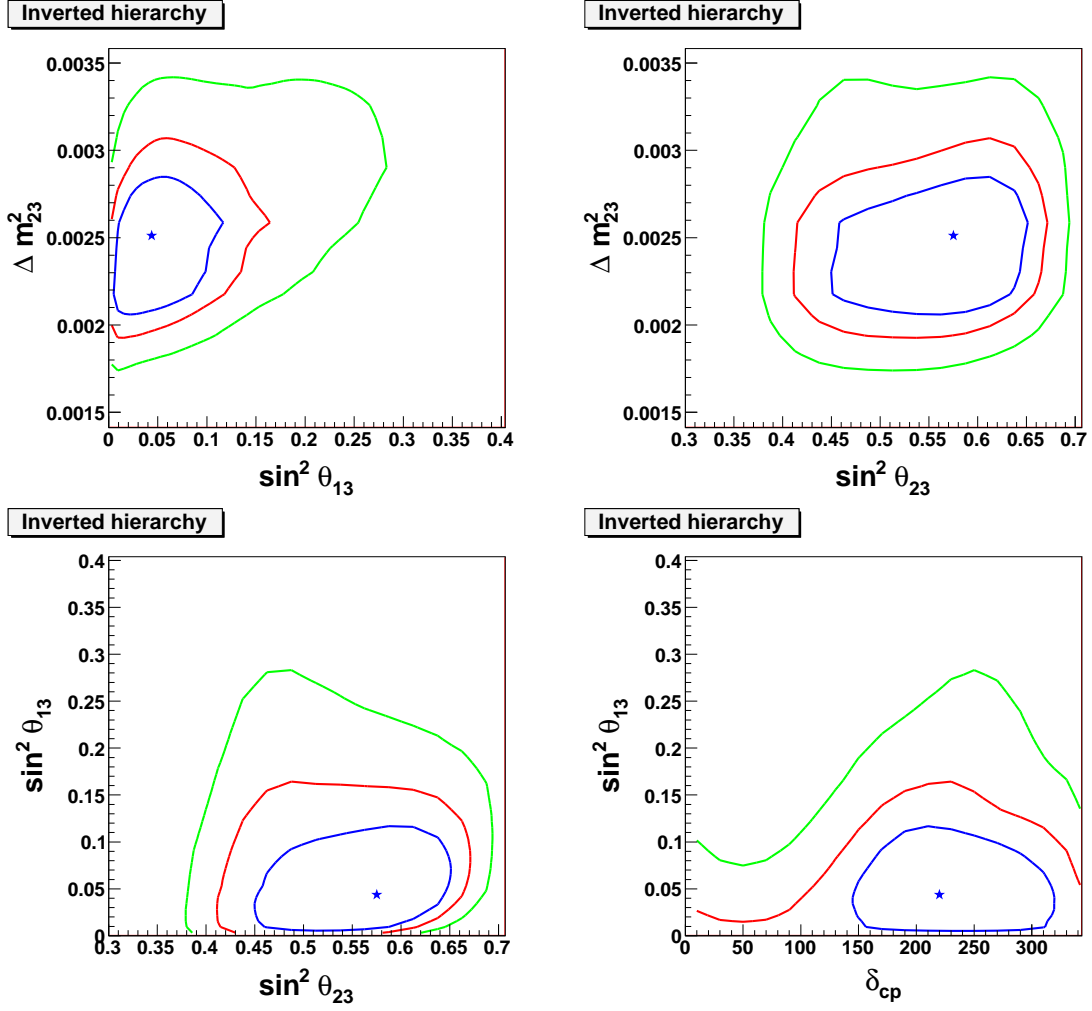
Figure 6.22: Contours for the inverted mass hierarchy case. The three lines indicate the allowed regions at 68 % C.L., 90 % C.L. and 99 % C.L. defined as $\Delta\chi^2 = 2.3$, 4.6 and 9.2. The stars show the best-fit parameter point.

## 6.7 Discussion

The obtained 90 % C.L. limits are compared with the other experiments. The $\Delta m_{23}^2$ and $\sin^2 2\theta_{23}$ parameter allowed regions from 2-flavor analyses, SK zenith and L/E with SK-I to -III data, and MINOS [32], are shown in Figure 6.23, together with the results of this analysis. 90 %C.L. 1-dof allowed regions from global-fit [37] are $(2.22 < \Delta m_{23}^2 < 2.60) \times 10^{-3}$ and $0.401 < \sin^2 \theta_{23} < 0.615$ while this full 3-analysis gave $(1.88 < \Delta m_{23}^2 < 2.75) \times 10^{-3}$ and $0.406 < \sin^2 \theta_{23} < 0.629$ for normal mass hierarchy case. Therefore, this new analysis considering the oscillation scheme without any approximations was confirmed to obtain consistent results with the 2-flavor analyses. Since the change in the oscillation probability from CP phases has small but non-negligible effects on the measured distributions, this analysis gives slightly wider allowed regions compared with the previous 2-flavor analyses. Figure 6.24 shows $\chi^2$ distributions for CP phase values fixed at $0°$, $140°$, $220°$ and $300°$. The $\chi^2$ distribution at $\delta_{cp} \sim 220°$ shows the largest allowed region.

In Figure 6.25, new results of $\Delta m_{23}^2 - \sin^2 \theta_{13}$ parameter allowed regions are overlaid with the past 3-flavor analysis with one-mass-scale-dominant scheme and the excluded region by Chooz experiment [36]. The results are consistent with that of the Chooz experiment. $\sin^2 \theta_{13} < 0.066$ for normal mass hierarchy and $\sin^2 \theta_{13} < 0.122$ for inverted mass hierarchy in 90 %C.L. 1-dof allowed region while global-fit [37] shows $\sin^2 \theta_{13} < 0.035$.

The sensitivity of this experiment on $\theta_{13}$ is studied for the normal hierarchy case. The best-fit point of oscillation parameters with $\sin^2 \theta_{13} = 0.006$ were used as true values. The probability for $\sin^2 \theta_{13} < 0.066$ was calculated by "Toy Monte Carlo" experiments which were determined based on the Poisson distribution. Figure 6.26 shows the histogram of the 90 %C.L. upper limit on $\sin^2 \theta_{13}$ by toy MC calculations. The probability for $\sin^2 \theta_{13} < 0.066$ is estimated to be 38.5 %. This test suggests that the constraint from the real SK data is almost as good as expected.

The best-fit parameter among all oscillation parameter sets in both mass hierarchies is in case of inverted mass hierarchy. The $\chi^2$ distributions of the two cases are overlaid in Figure 6.27. The difference of the minimum $\chi^2$ $(\Delta \chi^2 = \chi_{min}^2(normal) - \chi_{min}^2(inverted))$ is found to be 1.6. The significance is still low to draw a conclusion the mass hierarchy.

As for as CP phase, this is the first time that the SK atmospheric neutrino data gives information. The best-fit value appeared at $\delta_{cp} = 220°$ for both mass hierarchies. For inverted hierarchy case, 90 % C.L. can be barely set as $121.4 < \delta_{cp} < 319.1$, as shown in Figure 6.20. But the $\chi^2$ value is become flat just above the limit so no strong conclusion can be drawn for the CP phase. More statistics is expected to make better sensitivity to the CP phase as shown in Figure 6.28. Meanwhile, a large $\theta_{13}$ is needed to enable the SK analysis to constrain CP phase in the future. The current global-best $\theta_{13}$ value remains consistent to zero, although non-zero $\theta_{13}$ topic has been discussed in many literatures [37, 38]. On the other hand, there is a tension between solar [145, 146, 147, 18, 150] and KamLAND [20] experiments and the preliminary MINOS $\nu_e$ appearance results [149], which may indicate the value of $\sin^2 2\theta_{13}$ could be near the CHOOZ bound [148]. In this analysis, although the significance is still insufficient, the best values are obtained at $\sin^2 \theta_{13} = 0.04$ $(\sin^2 2\theta_{13} = 0.15)$ with $\Delta \chi^2 = 2.76$ from $\sin^2 \theta_{13} = 0.0$ for inverted hierarchy case. At this moment, the uncertainty in $\sin^2 2\theta_{13}$ is still large to draw any conclusion. However, if new T2K [151] and reactor [152, 153] experiments confirm the large $\sin^2 2\theta_{13}$, the present and future results from the atmospheric neutrino analysis could be used to constrain the $\delta_{cp}$ value depending on the actual $\theta_{13}$ value.
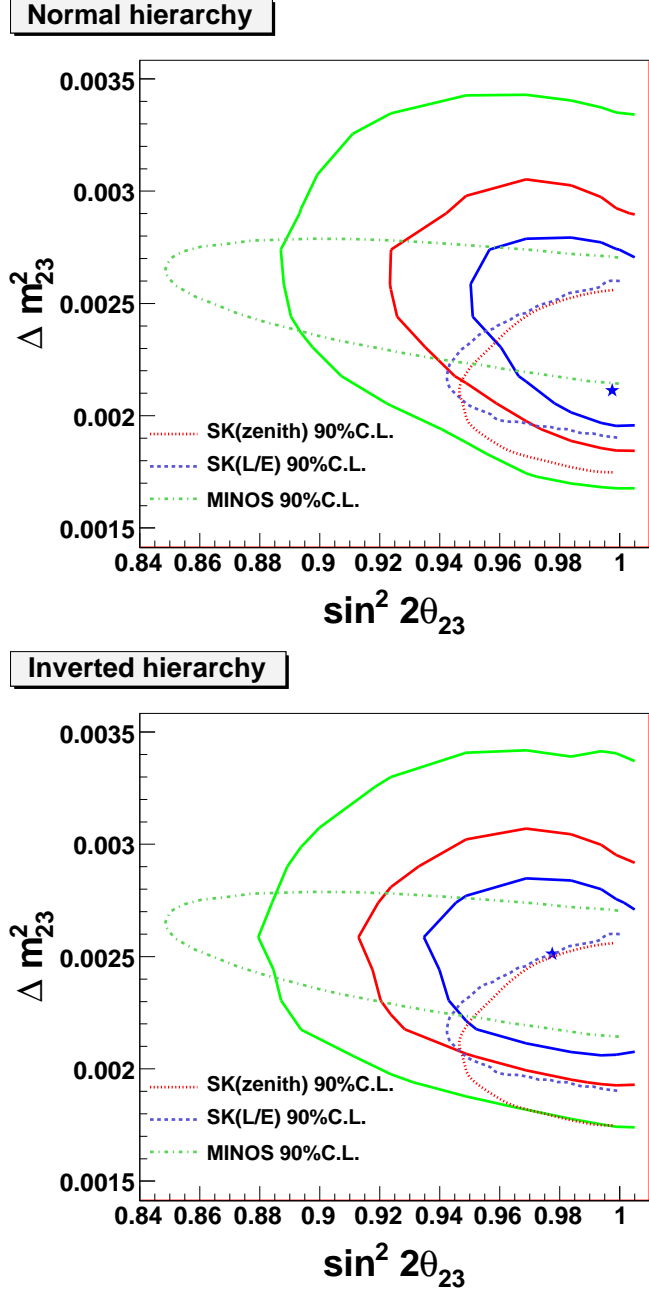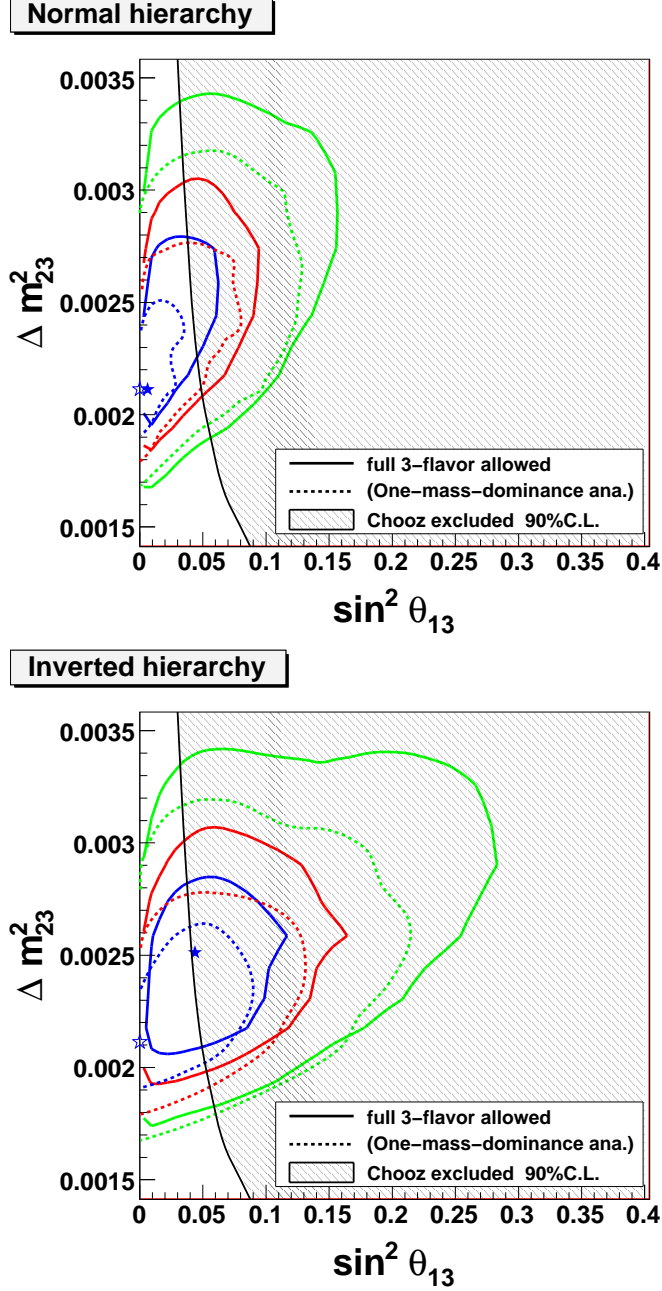
Figure 6.23: Contours of $\Delta m_{23}^2$ and $\sin^2 2\theta_{23}$ parameter allowed regions for normal hierarchy (upper panel) and inverted hierarchy (lower panel). Solid lines show the new results obtained by this full 3-flavor analysis; each colored lines indicate the allowed regions at 68 % C.L., 90 % C.L. and 99 % C.L. defined as $\Delta\chi^2 = 2.3$, 4.6 and 9.2, respectively. The stars show the best-fit parameter points. 90 % C.L. allowed regions from other analysis are also overlaid. Dotted lines show SK 2-flavor analysis using the zenith angle, dashed lines show SK L/E analysis and dash-dotted lines show MINOS results [32].
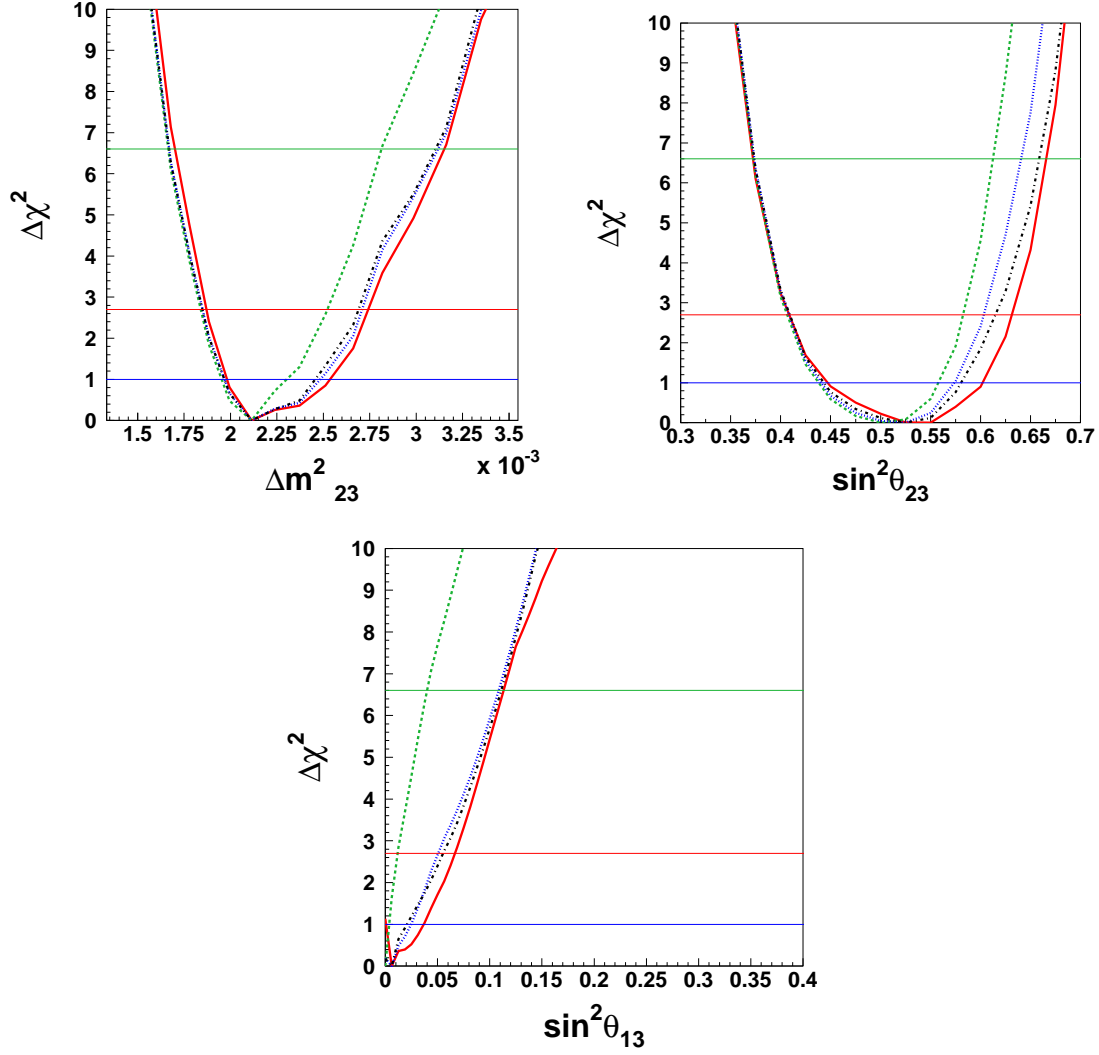
Figure 6.24: The $\Delta\chi^2$ distributions for CP phase values fixed at $0°$ (dashed line), $140°$ (dotted line), $220°$ (solid line) and $300°$ (dash-dotted line) for the normal hierarchy case. The three horizontal lines indicate 68 % C.L., 90 % C.L. and 99 % C.L. ($\Delta\chi^2 = 1.0$, 2.7 and 6.6).

Figure 6.25: Contours of $\Delta m_{23}^2$ and $\sin^2 \theta_{13}$ parameter allowed regions for normal hierarchy (upper panel) and inverted hierarchy (lower panel). Solid lines show the new results obtained by this full 3-flavor analysis; each colored lines indicate the allowed regions at 68 % C.L., 90 % C.L. and 99 % C.L. defined as $\Delta \chi^2 = 2.3$, 4.6 and 9.2, respectively. The solid stars show the best-fit parameter points. The results from the past 3-flavor analysis with one-mass-scale-dominant scheme are shown by dashed lines and hollow stars. The shaded regions show Chooz 90 % C.L. excluded region.
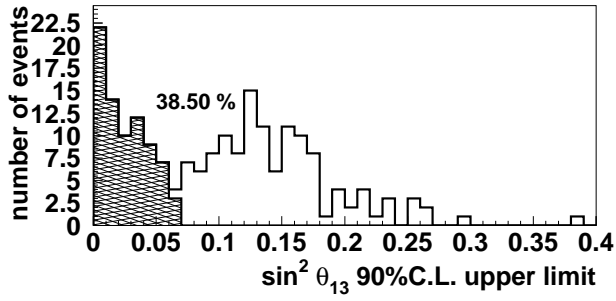
Figure 6.26: $\sin^2 \theta_{13}$ 90 % C.L. upper limit distribution made by 200 toy MC calculations. The hatched histogram indicates $\sin^2 \theta_{13} < 0.066$.
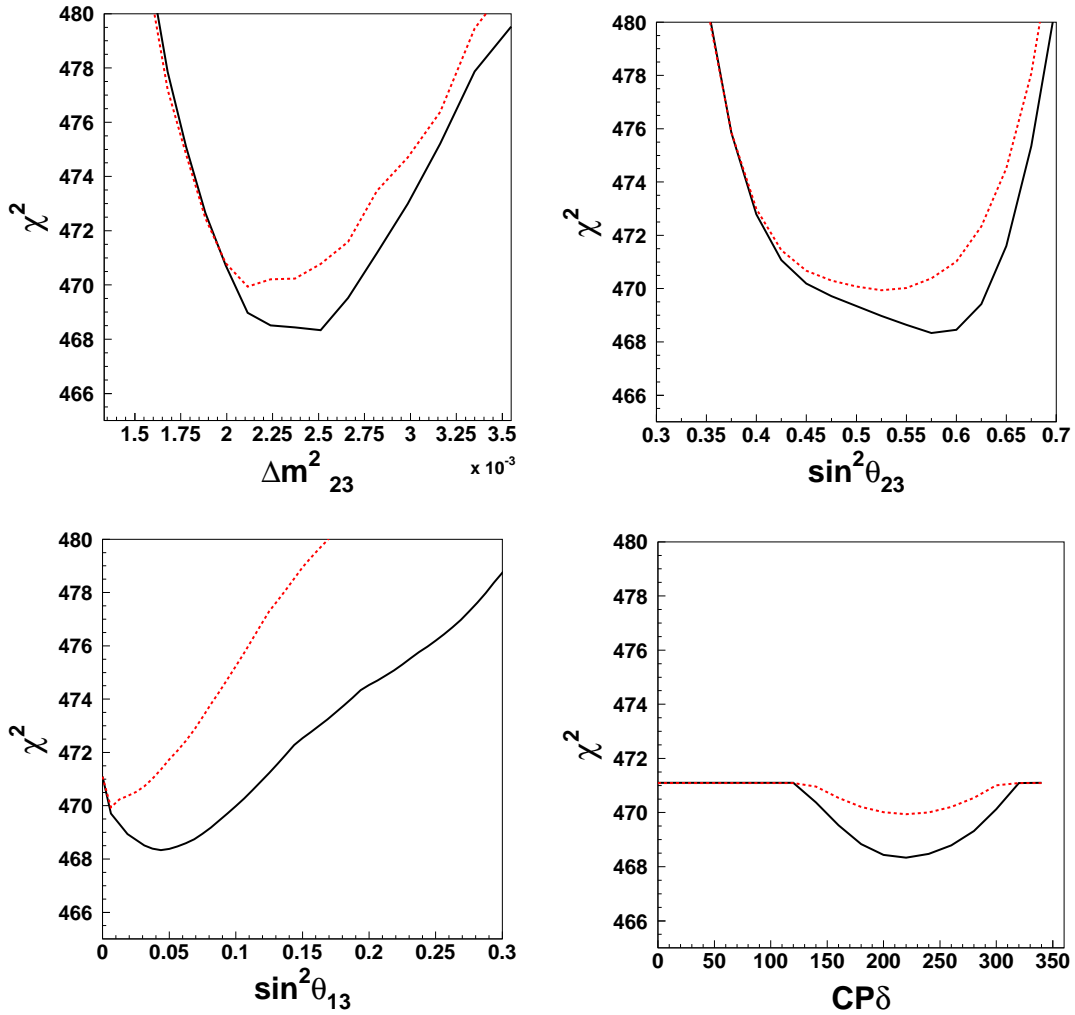


Figure 6.27: The $\chi^2$ distributions of each $\Delta m^2_{23}$, $\sin^2 \theta_{23}$, $\sin^2 \theta_{13}$ and $\delta_{cp}$ parameter for both normal (dashed line) and inverted (solid line) mass hierarchy cases.
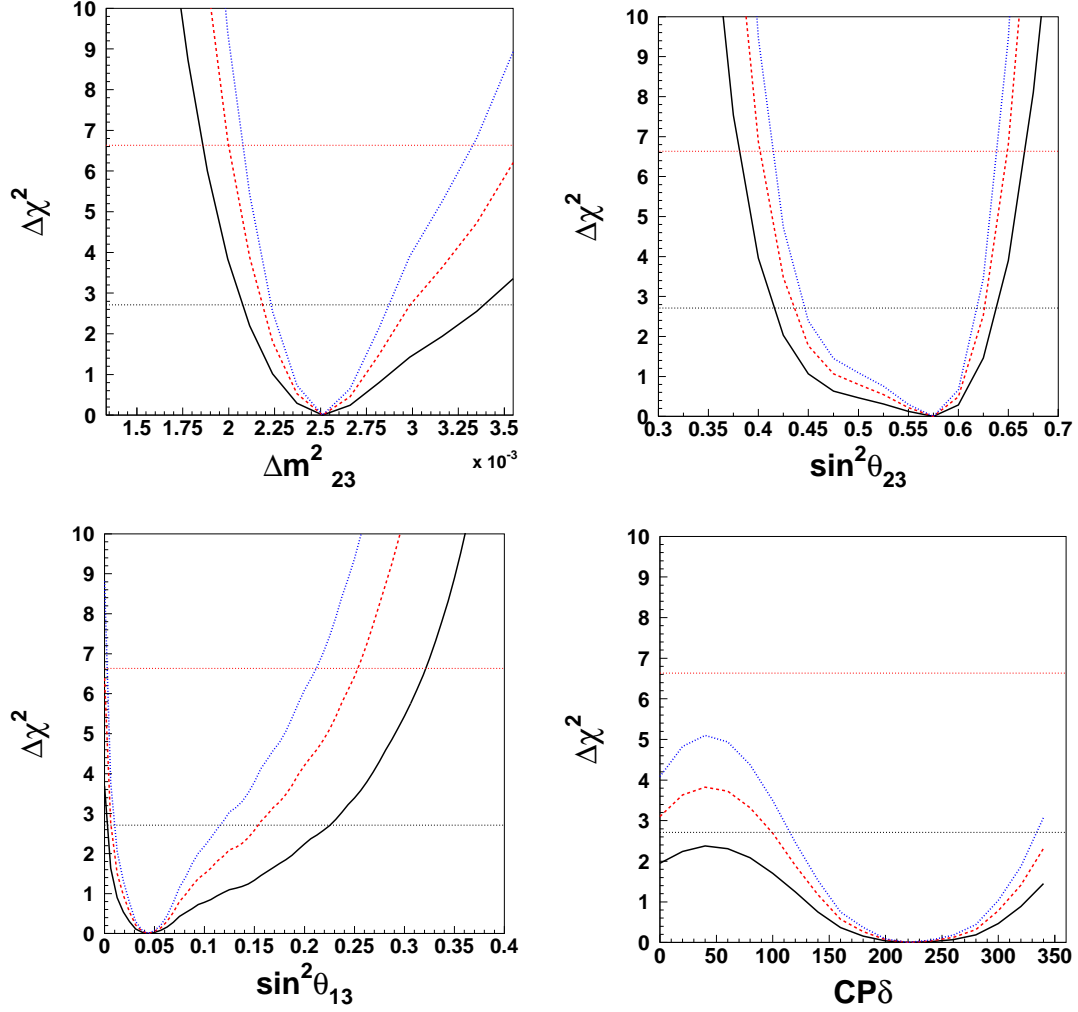
Figure 6.28: The expected $\Delta\chi^2$ distributions of each $\Delta m^2_{23}$, $\sin^2\theta_{23}$, $\sin^2\theta_{13}$ and $\delta_{cp}$ parameter using the oscillated Monte Carlo events of a 10 years (solid line), 20 years (dashed line) and 30 years (dotted line) exposure with the true oscillation parameters of the best-fit by this analysis, $(\Delta m^2_{23},\ \sin^2\theta_{23},\ \sin^2\theta_{13},\ \delta_{cp}) = (-2.5\times10^{-3},\ 0.575,\ 0.043,\ 220°)$. The two horizontal lines at $\Delta\chi^2 = 2.7$ and 6.6 indicate 90 % C.L. and 99 % C.L., respectively.

# Chapter 7

# Conclusion

The full neutrino oscillation analysis was performed for the first time with the atmospheric neutrino data observed in Super-Kamiokande. All data observed in SK-I (1489.2 days exposure for FC and PC, 1645.9 days for UPMU), SK-II (798.6 days exposure for FC and PC, 827.7 days for UPMU), and SK-III (518.1 days exposure for FC and PC, 635.6 days for UPMU) periods through Apr. 1996 to Sep. 2008 were used.

In the normal mass hierarchy case, $\Delta m_{23}^2$, $\sin^2 \theta_{23}$ and $\sin^2 \theta_{13}$ are constrained to $1.88 \times 10^{-3} < \Delta m_{23}^2 < 2.75 \times 10^{-3}$ eV$^2$, $0.406 < \sin^2 \theta_{23} < 0.629$, $\sin^2 \theta_{13} < 0.066$ at 90 % C.L.. In the inverted mass hierarchy case, $\Delta m_{23}^2$, $\sin^2 \theta_{23}$ and $\sin^2 \theta_{13}$ are constrained to $1.98 \times 10^{-3} < \Delta m_{23}^2 < 2.81 \times 10^{-3}$ eV$^2$, $0.425 < \sin^2 \theta_{23} < 0.644$, $\sin^2 \theta_{13} < 0.122$ at 90 % C.L.. This full 3-flavor analysis gives consistent results on the oscillation parameters with the past 2-flavor analysis and show that the allowed parameter regions are less restricted taking account of the effects from the parameters such as $\delta_{cp}$ $\sin^2 \theta_{13}$ parameter is also consistent with the results obtained in the past reactor experiment.

Although it was shown that the analysis has sensitivity, no significant constraint on CP phase at 90 % C.L. was obtained for both mass hierarchies and there is no clear preference of mass hierarchy. However, the present analysis demonstrated the usefulness of high statistics of the atmospheric neutrino data for the understanding of $\theta_{13}$, $\delta_{cp}$ and mass hierarchy as well as the measurement of $\Delta m_{23}^2$ and $\sin^2 2\theta_{23}$.

# Bibliography

[1] M. Fukugita, T. Yanagida, Phys. Lett. B **174** 45 (1986).

[2] J.H. Christenson *et al.*Phys. Rev. Lett. **80** 13 (1964).

[3] S.L. Glashow, Nucl. Phys. **22**, 579 (1961).

[4] S. Weinberg, Phys. Rev. Lett. **19**, 1264 (1967).

[5] A. Salam, In *Proceedings of the 8th Nobel Symposium on Elementary particle theory, relativistic groups and analyticity*, edited by N. Svartholm (1969).

[6] Ch. Kraus *et al.*, Euro. Phys. J. C **40**, 447 (2005).

[7] K.A. Assamagan *et al.*, Phys. Rev. D **53**, 6065 (1996).

[8] R. Barate *et al.*, Euro. Phys. J. C **2**, 395 (1998).

[9] Z. Maki, M. Nakagawa, and S. Sakata, Prog. Theo. Phys. **28**, 870 (1962).

[10] B. Pontecorvo, Sov. Phys. JETP **26**, 984 (1968).

[11] R. Davis Jr., D.S. Harmer, and K.C. Hoffman, Phys. Rev. Lett. **20**, 1205 (1968).

[12] K.S. Hirata *et al.*, Phys. Rev. Lett. **63**, 16 (1989);
K.S. Hirata *et al.*, Phys. Rev. D **44**, 2241 (1991), Erratum-ibid. **D45**, 2170 (1992).

[13] J.N. Bahcall and M.H. Pinsonneault, Rev. Mod. Phys. **64**, 885 (1992).

[14] A.I. Abazov *et al.*, Phys. Rev. Lett. **67**, 3332 (1991);
J.N. Abdurashitov *et al.*, JETP **95**, 181 (2002).

[15] P. Anselmann *et al.*, Phys. Lett. B **285**, 376 (1992);
W. Hampel *et al.*, Phys. Lett. B **447**, 127 (1999).

[16] S. Fukuda *et al.*, Phys. Lett. B **539**, 179 (2002);
M.B. Smy *et al.*, Phys. Rev. D **69**, 011104 (2004).

[17] Q.R. Ahmad *et al.*, Phys. Rev. Lett. **89**, 011301 (2002);
S.N. Ahmed *et al.*, Phys. Rev. Lett. **92**, 181301 (2002);
B. Aharmin *et al.*, Phys. Rev. C **72**, 055502 (2005).

[18] J. Hosaka *et al.*, Phys. Rev. D **73**, 112001 (2006).

[19] B. Aharmin *et al.*, Phys. Rev. Lett. **101**, 111301 (2008).

[20] S.Abe *et al.*, Phys. Rev. Lett. **100**, 221803 (2008).

[21] S.P. Mikheyev and A.Y. Smirnov, Sov. Jour. Nucl. **42**, 913 (1985); L. Wolfenstein, Phys. Rev. D **17**, 2369 (1978).

[22] M. Honda *et al.*, Phys. Rev. D **75**, 043006 (2007).

[23] K.S. Hirata *et al.*, Phys. Lett. B **205**, 416 (1988).

[24] K.S. Hirata *et al.*, Phys. Lett. B **280**, 146 (1992).

[25] D. Casper *et al.*, Phys. Rev. Lett. **66**, 2561 (1991).

[26] R. Becker-Szendy *et al.*, Phys. Rev. D **46**, 3720 (1992).

[27] M. C. Sanchez *et al.*, Phys. Rev. D **68**, 113004 (2003).

[28] Y. Fukuda *et al.*, Phys. Lett. **81**, 1562 (1998).

[29] The MACRO collaboration, Phys. Lett. B **434**, 451 (1998).

[30] Y.Fukuda *et al.*, Phys. Rev. Lett. **82** 2644 (1999).

[31] M.H. Ahn *et al.*, Phys. Rev. D **74** 072003 (2006).

[32] P. Adamson *et al.*, Phys. Rev. Lett. **101** 131802 (2008).

[33] Y. Ashie *et al.*, Phys. Rev. Lett. **93** 101801 (2004).

[34] J. Hosaka *et al.*, Phys. Rev. D **74** 032002 (2006).

[35] R. Wendell, In *proceedings of 11th nternational conference on Topics in Astroparticle and Underground Physics*, (2009)

[36] M. Apollonio *et al.*, Phys. Lett. B **466** 415 (1999).

[37] T. Schwetz, M. Tortola, J.W.F. Valle New J.Phys. **10** 113011 (2008), hep-ph/0808.2016.

[38] G. L. Fogli, E. Lisi, A. Marrone and A. Palazzo Prog. Part. Nucl. Phys. **57** 742 (2006), hep-ph/0506083.

[39] O. L. G. Peres and A. Y. Smirnov, Nucl. Phys. B **680** 479 (2004).

[40] I. Frank and I.Tamm, C. R. Acad. Sci. USSR **14**, 109 (1937).

[41] H. Kume *et al.*, Nucl. Inst. and Meth. **205**, 443 (1983).

[42] A. Suzuki *et al.*, Nucl. Inst. and Meth. A **329**, 299 (1993).

[43] Y. Takeuchi *et al.*, Phys. Lett. **452**, 418 (1999).

[44] H. Ikeda *et al.*, Nucl. Inst. and Meth. A **320**, 310 (1992).

[45] T. Tanimori *et al.*, IEEE Trans. Nucl. Sci. **NS-36**, 497 (1989).

[46] J. George, Ph.D. Thesis, University of Washington (1998).

[47] M. Honda *et al.*, Phys. Rev. D **64**, 053001 (2001).

[48] M. Honda *et al.*, Phys. Rev. D **70**, 043008 (2004).

[49] G.Battistoni *et al.*, Astropart.Phys. **19** 269 (2003) [Erratum-ibid. **19** 291 (2003)]. (http://www.mi.infn.it/ battist/neutrino.html)

[50] G. Barr *et al.*, Phys. Rev. D **70**, 0423006 (2004).

[51] L.V. Volkova, Sov. J. Nucl. Phys. **31**, 784 (1980).

[52] T. Sanuki *et al.*, Astrophys. J. **545** 1135 (2000).

[53] J.Alcarez *et al.*, Phys. Lett. B **490** 27 (2000).

[54] W.R. Webber, R.L. Golden and S.A. Stephens, In *Proceedings of the 20th International Cosmic Ray Conference* (1987).

[55] E.S. Seo *et al.*, Astrophys. J. **378** 763 (1991).

[56] P. Pappini *et al.*, In *Proceedings of the 23rd International Cosmic Ray Conference* (1993).

[57] M. Boezio *et al.*, Astrophys. J. **518** 457 (1999).

[58] W. Menn *et al.*, Astrophys. J. **533** 281 (2000).

[59] M.J. Ryan, J.F. Ormes and V.K. Balasubrahmanyan, Phys. Rev. Lett. **28** 985 (1972).

[60] K. Asakamori *et al.*, Astrophys. J. **502** 985 (1998).

[61] I.P. Ivanenko *et al.*, In *Proceedings of the 23rd International Cosmic Ray Conference* (1993).

[62] Y. Kawamura *et al.*, Phys. Rev. D **40** 729 (1989).

[63] A.V. Apanasenko *et al.*, Astropart. Phys. **16** 13 (2001).

[64] http://modelweb.gsfc.nasa.gov/atmos/usstandard.html.

[65] http://www.ngdc.noaa.gov/IAGA/vmod/igrf.html.

[66] K. Hänssget and J. Ranft, Comput. Phys. **39** 37 (1986).

[67] S. Roesler, R. Engel, and J. Ranft, Phys. Rev. D **57** 2889 (1998).

[68] M.Motoki *et al.*, Astropart.Phys. **19** 113 (2003).

[69] P. Achard *et al.*(L3 Collaboration), Phys. Lett. B **598**, 15 (2004).

[70] M. Honda *et al.*, Phys. Rev. D **75**, 043005 (2007).

[71] S. Haino *et al.*(BESS Collaboration), Phys. Lett. B **594**, 35 (2004).

[72] T. Sanuki *et al.*, Phys. Lett. B **541**, 234 (2002).

[73] O. C. Allkofer *et al.*, Nucl. Phys. B **259**, 1 (1985).

[74] S. Matsuno *et al.*, Phys. Rev. D **29**, 1 (1984).

[75] G. Battistoni *et al.*, Astopart. Phys. **12**, 315 (2000).

[76] Y. Hayato, Nucl. Phys. Proc. Suppl. **112**, 171 (2002).

[77] G. Mitsuka, AIP Conf. Proc. **967**:208-211 (2007), AIP Conf. Proc. **981**:262-264 (2008).

[78] C. H. Llewellyn Smith, Phys. Rep. **3**, 261 (1972).

[79] R. Gran, E. J. Jeon *et al.*, Phys. Rev. D **74**, 052002 (2006).

[80] A.A. Aguilar-Arevalo *et al.*, Phys. Rev. Lett. **100**, 032301 (2008).

[81] F. Sanchez, Talk at Fifth International Workshop on Neutrino-Nucleus Interactions in the Few-GeV Region(NuInt07), http://conferences.fnal.gov/nuint07/

[82] R. A. Smith and E. J. Moniz, Nucl. Phys. B **43**, 605 (1972). [Erratum-ibid. B **101**, 547 (1975).]

[83] J. Nieves *et al.*, Phys. Rev. C **70**, 055503 (2004).

[84] H. Nakamura *et al.*, Nucl. Phys. B (Proc. Suppl.) **112**, 197 (2002).

[85] C.H. Albright *et al.*, Phys. Rev. D **14**, 1780 (1976).

[86] K. Abe *et al.*, Phys. Rev. Lett. **56**, 1107 (1986).

[87] S. Barish *et al.*, Phys. Rev. D **16**, 3103 (1977).

[88] S. Bonetti *et al.*, Nouvo Cimento **38**, 260 (1977).

[89] M. Pohl *et al.*, Nuovo Cimento **26**, 332 (1979);
N. Arimenise *et al.*, Nucl. Phys. B **152**, 365 (1979).

[90] A.S. Vovenko *et al.*, Yad. Fiz. **30**, 1014 (1979).

[91] S. Belikov *et al.*, Z. Phys. **320**, 625 (1985).

[92] J.Brunner *et al.*, Z. Phys. C **45**, 551 (1990).

[93] D. Rein and L.M. Sehgal, Ann. of Phys. **133**, 1780 (1981).

[94] D. Rein, Z. Phys. C **35**, 43 (1987).

[95] T. Kitagaki *et al.*, Phys. Rev. D **34**, 2554 (1986).

[96] S.K. Singh, M.J. Vicente-Vacas and E.Oset, Phys. Lett. B **416**, 23 (1998).

[97] H. Faissne *et al.*, Phys. Lett. B **125**, 230 (1983).

[98] W. Krenz *et al.*, Nucl. Phys. B **135**, 45 (1978).

[99] M. Glück, E. Reya and A. Vogt, Eur. Phys. J. C **5**,461 (1998).

[100] A. Bodek and U.K. Yang, hep-ex/0308007

[101] P. Musset and J.P. Vialle, Phys. Rep. C **39**, 1 (1978).

[102] J.E. Kim *et al.*, Rev. Mod. Phys. **53**, 211 (1981).

[103] S.J. Barish *et al.*, Phys. Rev. **D17**, 1 (1978).

[104] S. Barlag *et al.*, Z. Phys. C **11**, 283 (1982).

[105] T. Sjöstrand *et al.*, CERN-TH-7112-93 (1994).

[106] D. Rein and L.M. Sehgal, Nucl. Phys. B **233**, 29 (1983).

[107] M. Hasegawa *et al.*, Phys. Rev. Lett. **95**, 252301 (2005).

[108] D. Rein and L.M. Sehgal, Phys. Lett. B. **657**, 207 (2007).

[109] R. Woods and D. Saxon, Phys. Rev. **95**, 577 (1954).

[110] L. Salcedo *et al.*, Nucl. Phys. A **484**, 557 (1988).

[111] G. Rowe *et al.*, Phys. Rev. C **18**, 584 (1978).

[112] D. Ashery *et al.*, Phys. Rev. C **23**, 2173 (1981).

[113] C. Ingram *et al.*, Phys. Rev. C **27**, 1578 (1983).

[114] B. R. Martin and M. K. Pidcock, Nuc. Phys. B **126**, 266 (1977).

[115] B. R. Martin and M. K. Pidcock, Nuc. Phys. B **126**, 285 (1977).

[116] J. S. Hyslop *et al.*, Phys. Rev. D **46**, 961 (1992).

[117] D. A. Sparrow, Proc. of the Conf. on the intersection between partivle and nuclear physics, 1019 (1984).

[118] H. W. Bertini *et al.*, Phys. Rev. C **6**, 631 (1972).

[119] S. J. Lindenbaum *et al.*, Phys. Rev. **105**, 1874 (1957).

[120] GEANT, CERN Program Library Long Writeup W5013 (1994).

[121] C. Zeitnitz and T.A. Gabriel, Nucl. Inst. and Meth. A **349**, 106 (1994).

[122] M. Nakahata *et al.*, J. Phys. Soc. Jpn. **55**, 3786 (1986).

[123] E. Bracci *et al.*, CERN/HERA 72-1 (1972).

[124] A.S. Carrol *et al.*, Phys. Rev. C **14**, 635 (1976).

[125] A. Morel *et al.*, Luminology and Oceanography 22, **709**, (1977).

[126] D. Groom *et al.*, Atomic Data and Nuclear Data Tables **78**, 044 (201).

[127] S. Desai, Ph.D. Thesis, Boston University (2004).

[128] Y. Takenaga, Ph.D. Thesis, University of Tokyo (2008).

[129] P. Hanggi *et al.*, Phys. Lett. B **51**, 119 (1974).

[130] M. Yamada *et al.*, Phys. Rev. D **44**, 617 (1991).

[131] Hirokazu Ishino, PhD Thesis, University of Tokyo, (1999).

[132] E. R. Davies, *Machine Vision: Theory, Algorithms, Practicalities*, Academic Press, San Diego (1997).

[133] G. Ambrosini *et al.*, Phys. Lett. B **420**, 225 (1998).

[134] A. E. Hedin, J. Geophys. Res. **96**, 1159 (1991),

[135] Dziewonski and Anderson, Phys. Earth. Planet. Int. **25**, 297-356 (1981).

[136] Barszczak, T., University of California, Irvine,(2005)

[137] D. Casper, Nucl. Phys. Proc. Suppl. **112**, 161 (2002).

[138] C.H. Albright and C. Jarlskog, Nucl. Phys. B **84**, 467 (1975).

[139] Y. Fukuda *et al.*, Phys. Lett. B **433**, 9 (1998).

[140] S.Baker and R.D. Cousins, Nucl. Inst. and Meth. **221**, 437 (1984).

[141] E. Hernandez *et al.*, Phys. Rev. D **76**, 033005 (2007).

[142] A. Capella *et al.*, Phys. Lett. B **337**, 358 (1994). M.H.Reno, Phys. Rev. D **74**, 033001 (2006).

[143] K. Hagiwara *et al.*, Nucl. Phys. B **668**, 364 (2003).

[144] V. Barger *et al.*, Phys. Rev. D **22**, 2718 (1980).

[145] B. T. Cleveland *et al.*, Astrophys. J. **496**, 505 (1998).

[146] J. N. Abdurashitov *et al.*, J. Exp. Theor. Phys. **95**, 181 (2002).

[147] B. Aharmim *et al.*, Phys. Lett. B **616**, 174 (2005).

[148] G.L. Fogli *et al.*, hep-ph/0905.3549

[149] P. Adamson *et al.*, hep-ex/0909.4996

[150] M. Altmann *et al.*, hep-ex/0910.2984

[151] Y. Itow *et al.*, hep-ex/0106019

[152] C. Palomares *et al.*, hep-ex/0911.3227

[153] W. Wang *et al.*, hep-ex/0910.4605

# Appendix A

# Oscillation analysis

## A.1   Solar terms effect

The results of the oscillation analysis with different solar terms are checked. Since the global-best of $\Delta m_{12}^2$ and $\sin^2 \theta_{12}$ parameters is obtained by [37] with $1\sigma$ allowed region, two parameter sets, which are selected in the allowed region, are used for this check :

$$
\begin{aligned}
(\Delta m_{12}^2, \ \sin^2 \theta_{12}) &= (7.45 \times 10^{-5}, 0.288) \quad \cdots \quad \text{A} \\
&= (7.89 \times 10^{-5}, 0.326) \quad \cdots \quad \text{B}.
\end{aligned}
$$

The analysis fitting process is performed in the same way described in Section 6 for both of the above two sets of solar parameters. Figure A.1 shows the $\Delta m_{23}^2$ and $\sin^2 \theta_{13}$ parameters allowed region obtained by the analysis using the two solar parameters together with the global-best solar parameters, $(\Delta m_{12}^2, \sin^2 \theta_{12}) = (7.65 \times 10^{-5}, 0.304)$. These allowed regions are exactly the same for these analyses with different solar parameter sets. It is obvious that the results of this analysis are not affected by the solar parameters within the parameter error size.

## A.2   Zenith angle distributions

From Figure A.2 to Figure A.7 the zenith angle distributions together with the best-fit distributions in the normal hierarchy case for each SK run period are shown.

## A.3   Best-fit systematic uncertainties

The systematic error parameters ($\epsilon_j$) for the best fit point are summarized in a bar graph which indicates the error parameters ($\epsilon_j$) in units of the estimated $1\sigma$ error ($\sigma_j^{sys}$) value for each systematic error term. From Figure A.8 to Figure A.10 the best-fit results in normal hierarchy case are shown and from Figure A.11 to Figure A.13 the best-fit results in inverted hierarchy case are shown.
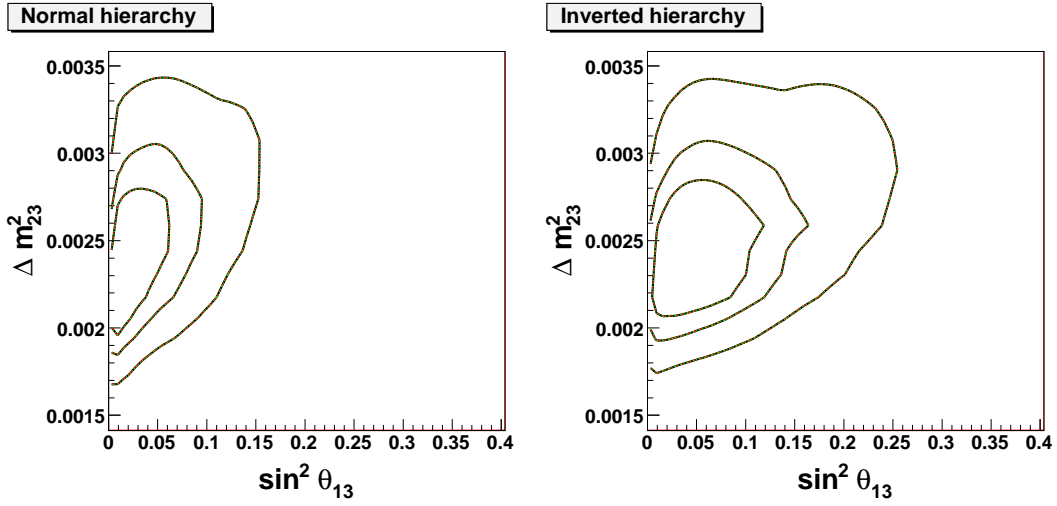
Figure A.1: The allowed region contour of $\sin^2 \theta_{13}$ and $\Delta m_{23}^2$ parameters obtained by the oscillation analyses with the different solar parameters, global-best (black-solid lines), parameter set A (red-dashed lines) and parameter set B (green-dotted lines), in normal hierarchy (left) and inverted hierarchy (right). A contour indicates 68 %, 90 % and 99 % C.L. allowed regions by three lines. Since there is no difference on the results among the three analyses, all lines overlap.
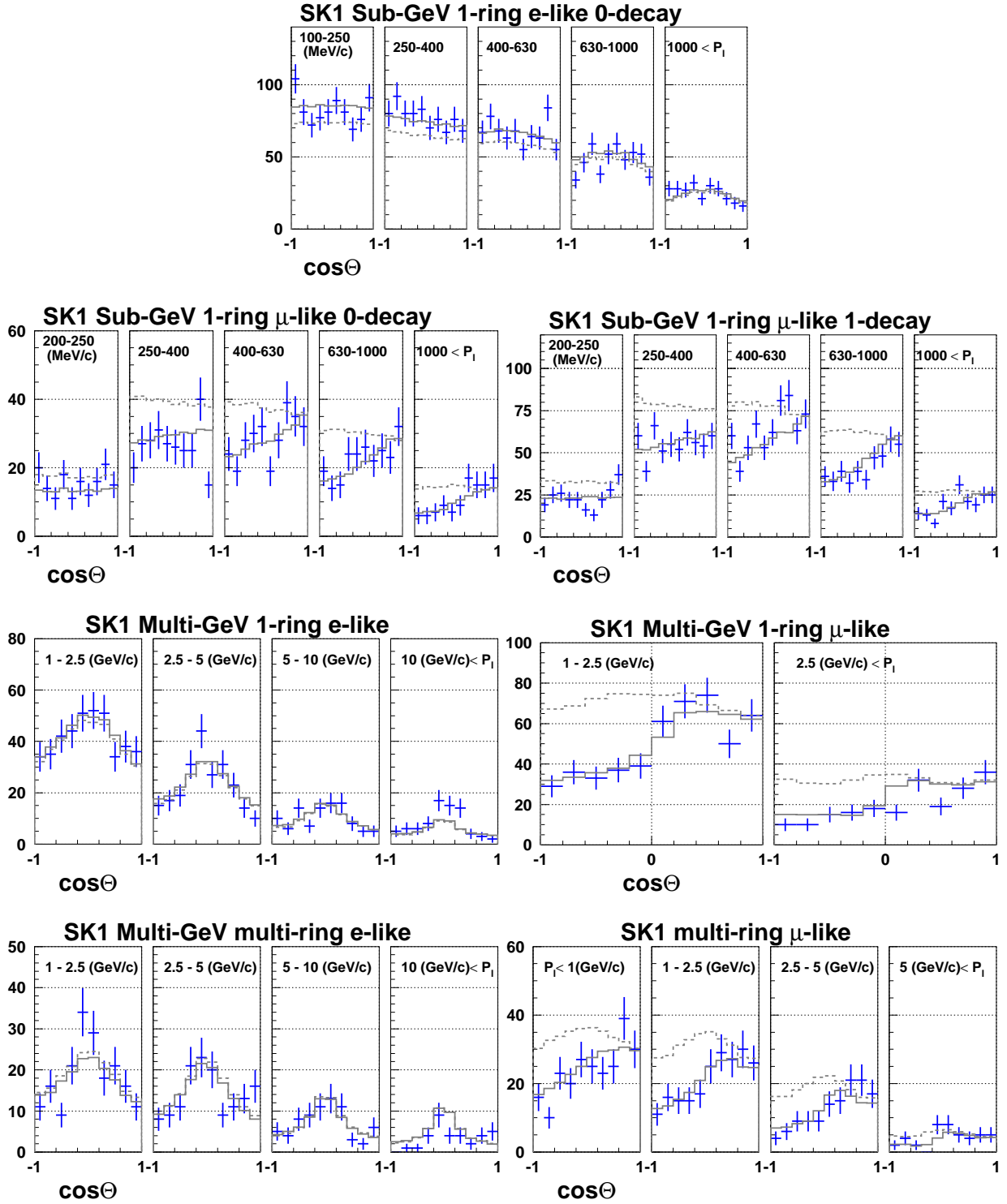
Figure A.2: SK-I zenith angle distributions for FC events for data (line with error bar) and MC assuming no oscillation (dashed line) and the best-fit results (solid line). Normal hierarchy is assumed.
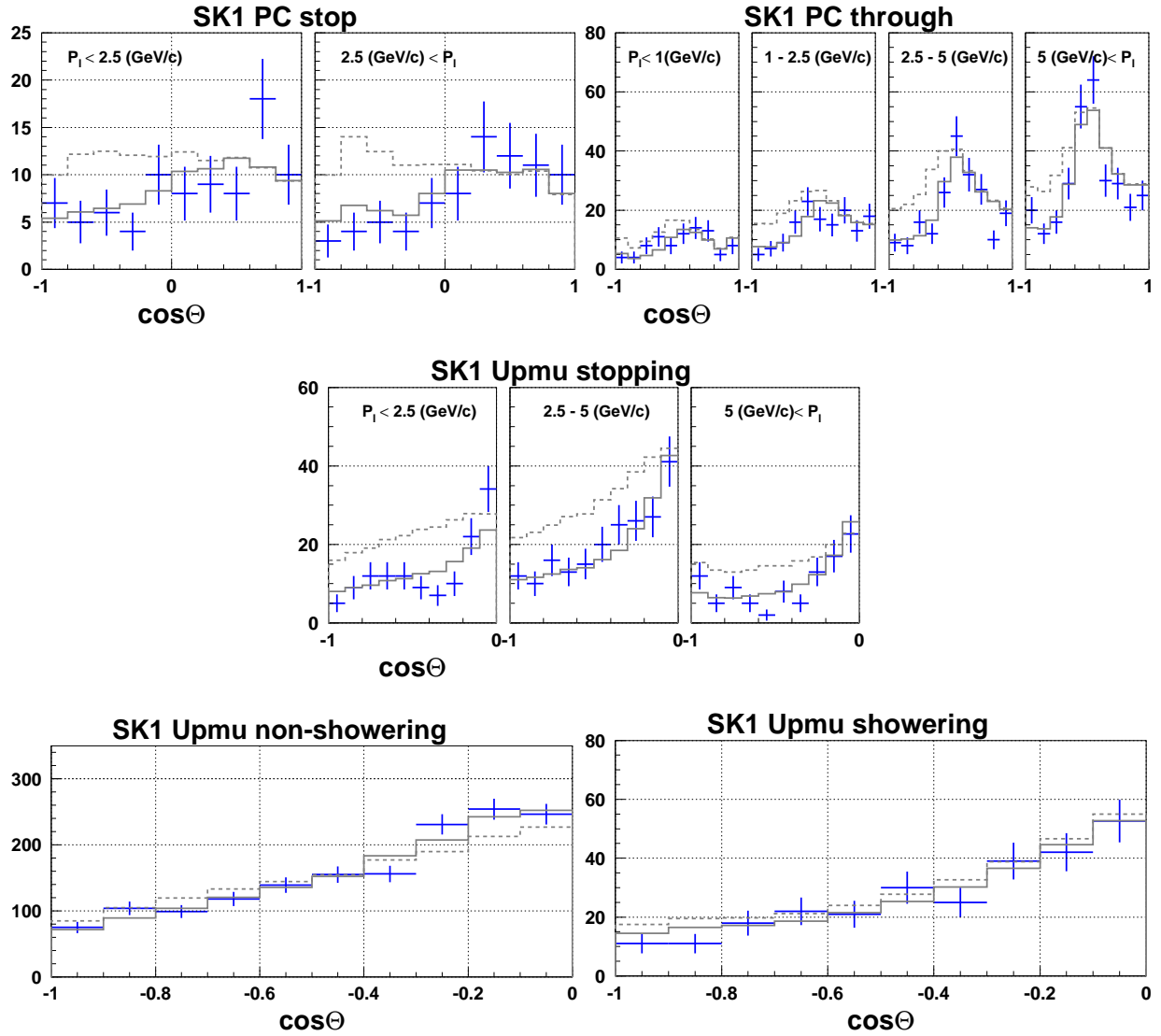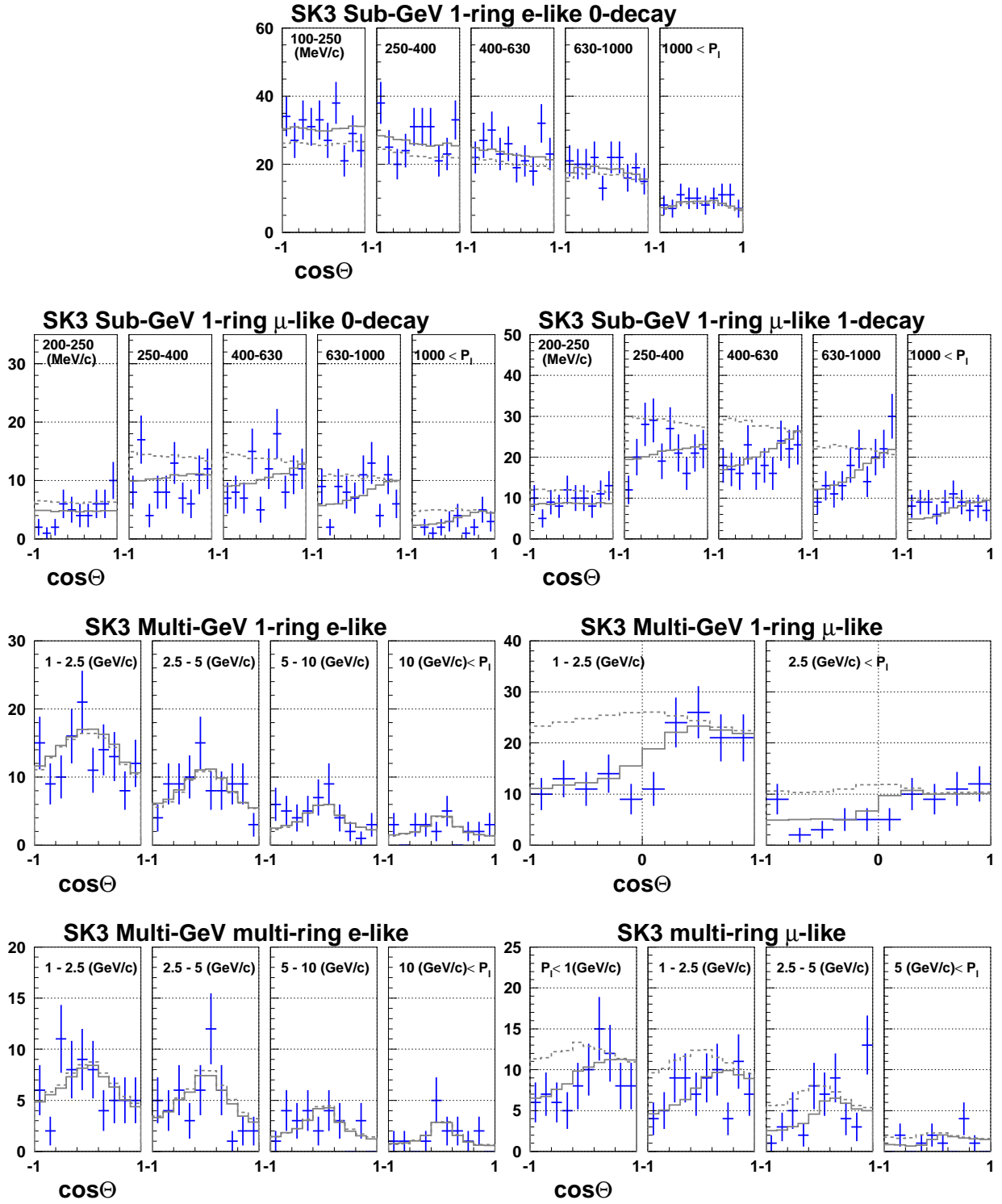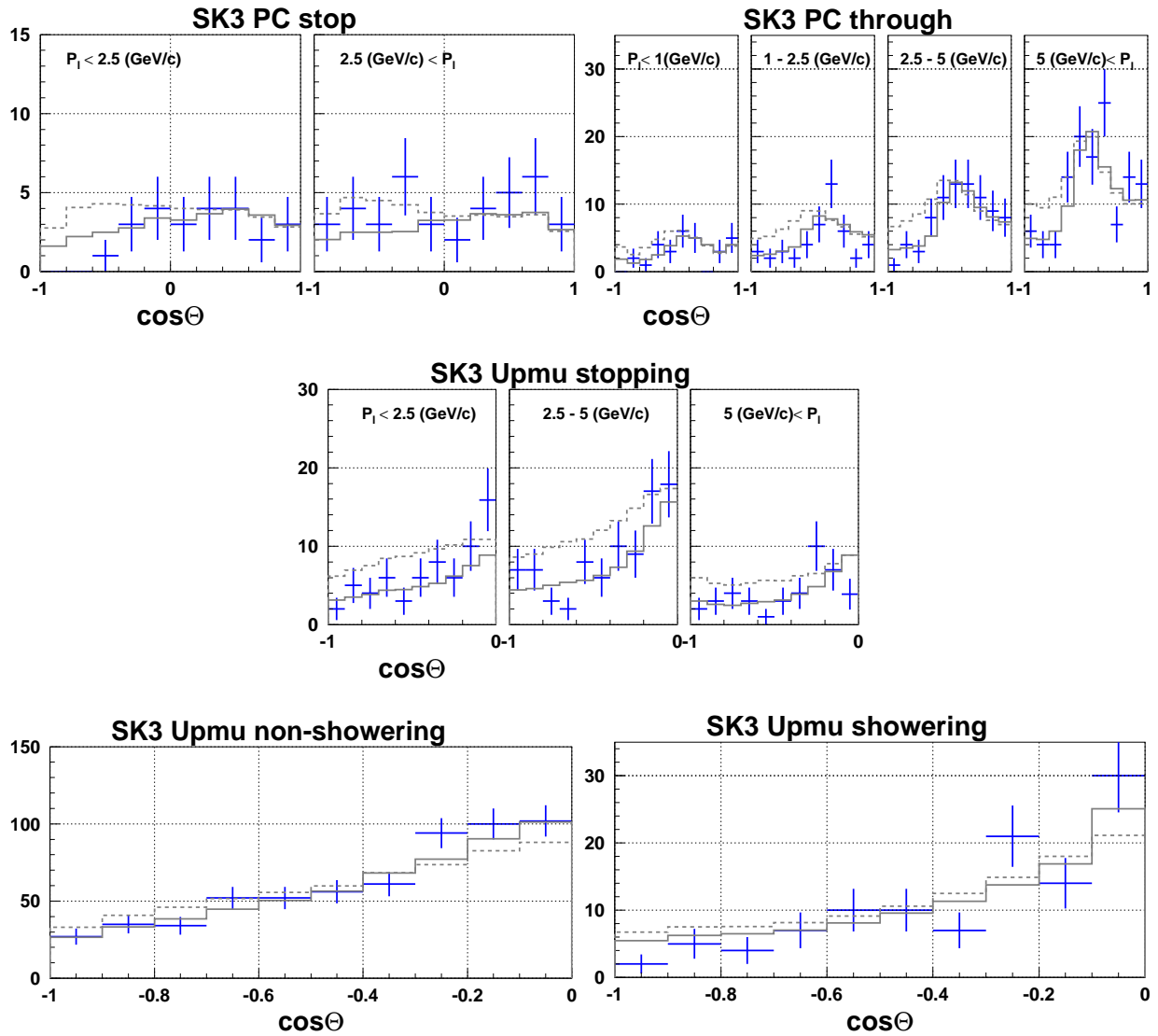
Figure A.3: SK-I zenith angle distributions for PC and UPMU events for data (line with error bar) and MC assuming no oscillation (dashed line) and the best-fit results (solid line). Normal hierarchy is assumed.
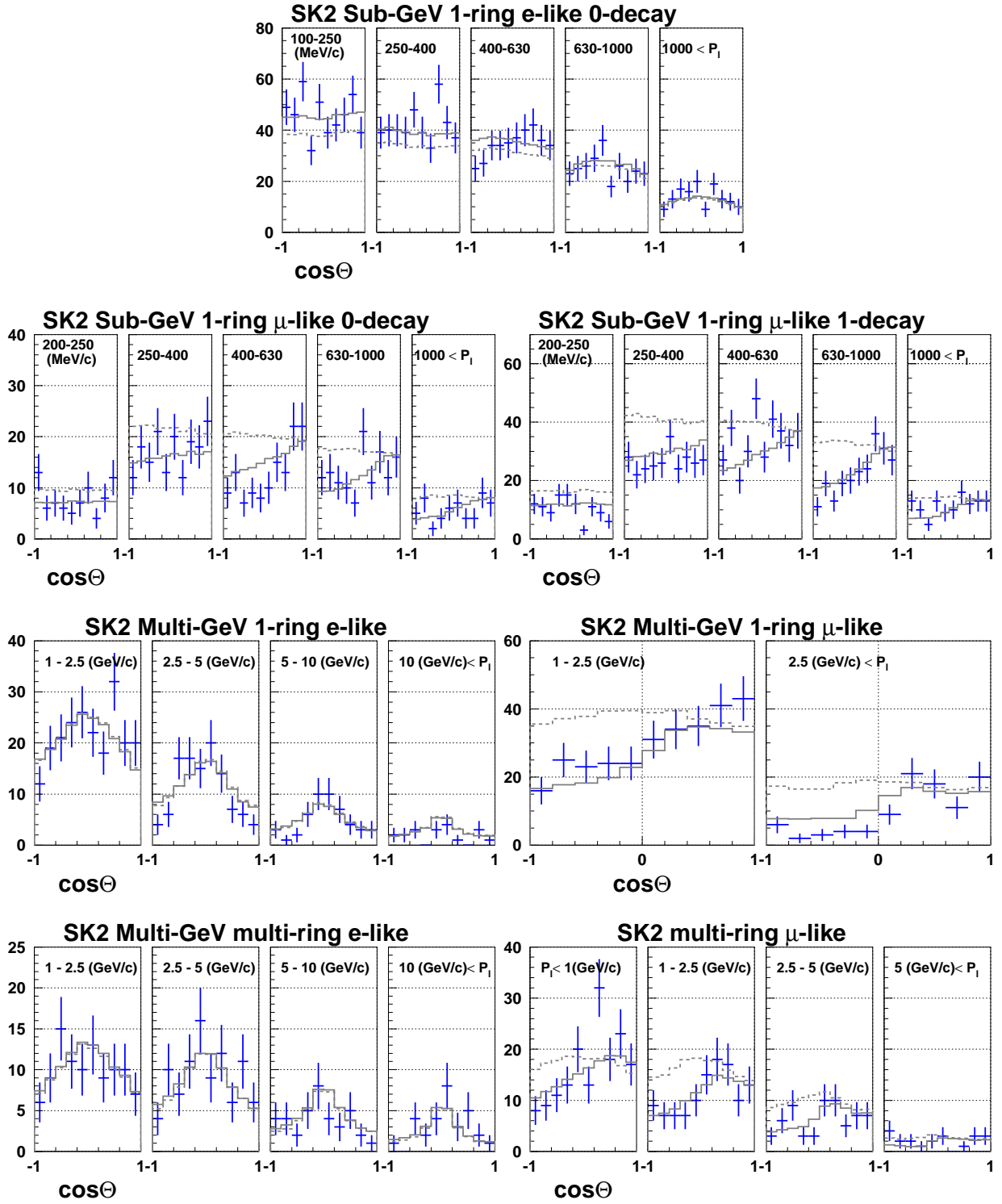
Figure A.4: SK-II zenith angle distributions for FC events for data (line with error bar) and MC assuming no oscillation (dashed line) and the best-fit results (solid line). Normal hierarchy is assumed.
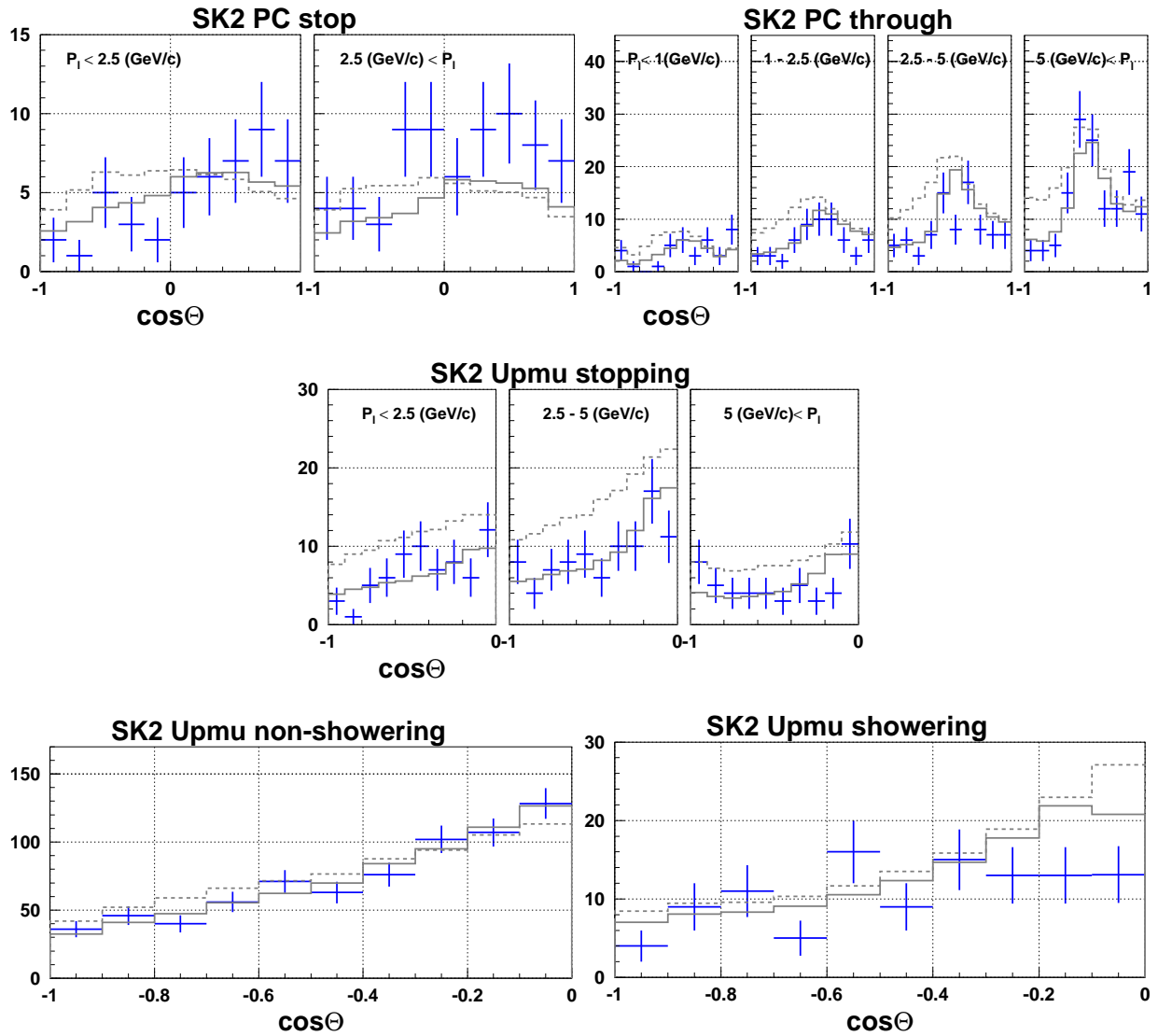
Figure A.5: SK-II zenith angle distributions for PC and UPMU events for data (line with error bar) and MC assuming no oscillation (dashed line) and the best-fit results (solid line). Normal hierarchy is assumed.

Figure A.6: SK-III zenith angle distributions for FC events for data (line with error bar) and MC assuming no oscillation (dashed line) and the best-fit results (solid line). Normal hierarchy is assumed.

Figure A.7: SK-III zenith angle distributions for PC and UPMU events for data (line with error bar) and MC assuming no oscillation (dashed line) and the best-fit results (solid line). Normal hierarchy is assumed.
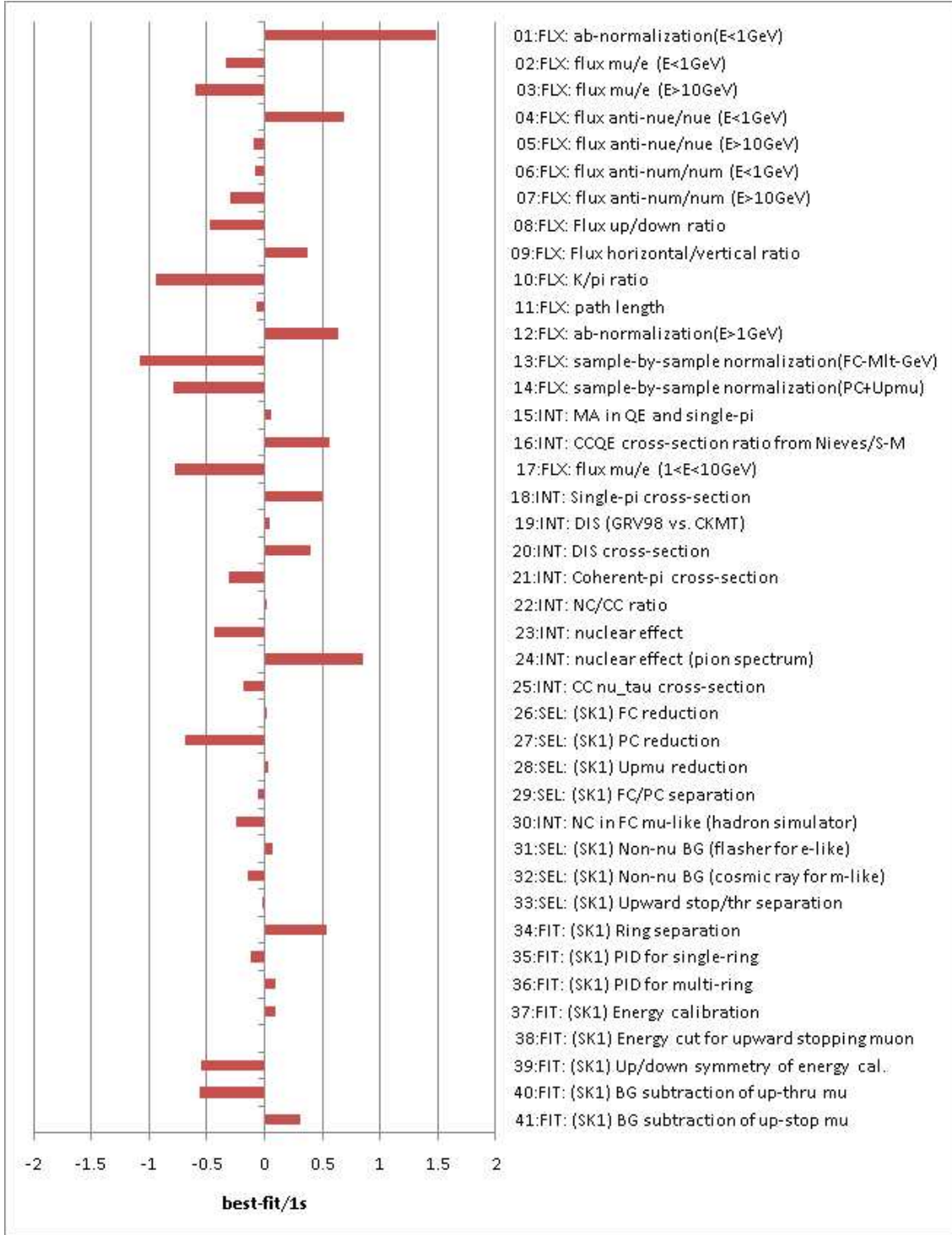
Figure A.8: (Normal hierarchy, No.1) The best-fit value of the systematic error parameter $\epsilon_j$ in units of the estimated $1\sigma$ error value for each systematic error term shown in the right column.
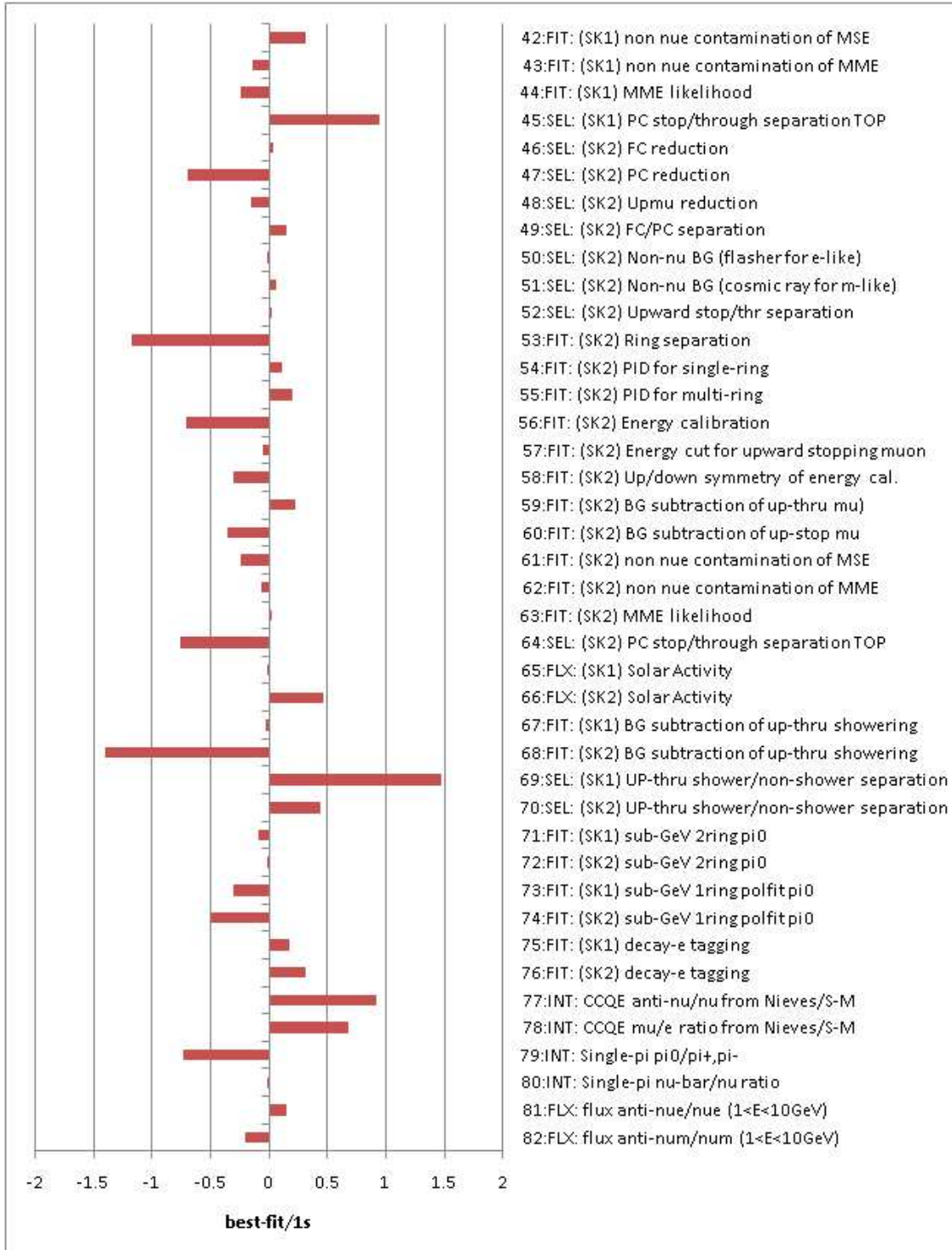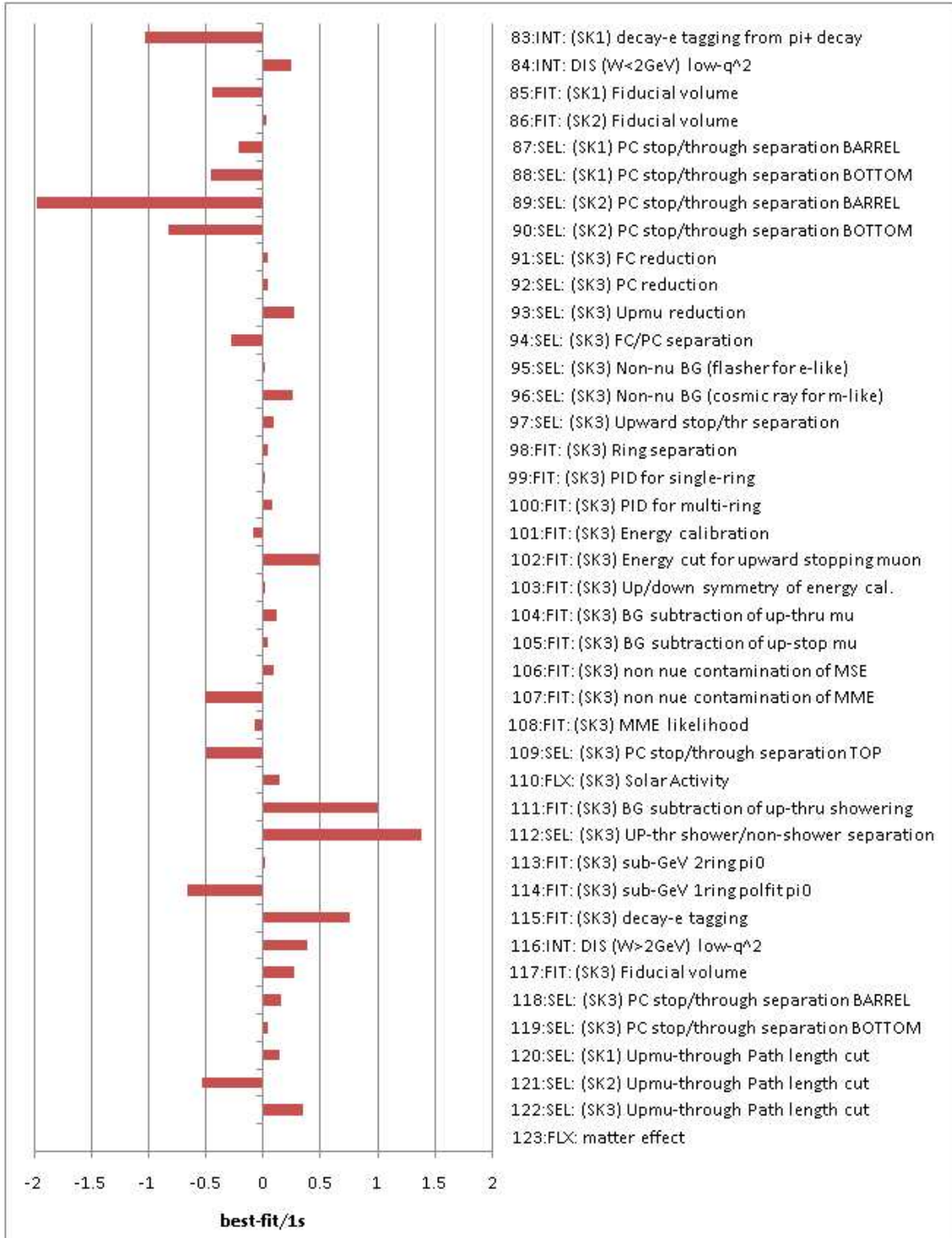
Figure A.9: (Normal hierarchy, No.2) The best-fit value of the systematic error parameter $\epsilon_j$ in units of the estimated $1\sigma$ error value for each systematic error term shown in the right column.

Figure A.10: (Normal hierarchy, No.3) The best-fit value of the systematic error parameter $\epsilon_j$ in units of the estimated $1\sigma$ error value for each systematic error term shown in the right column.
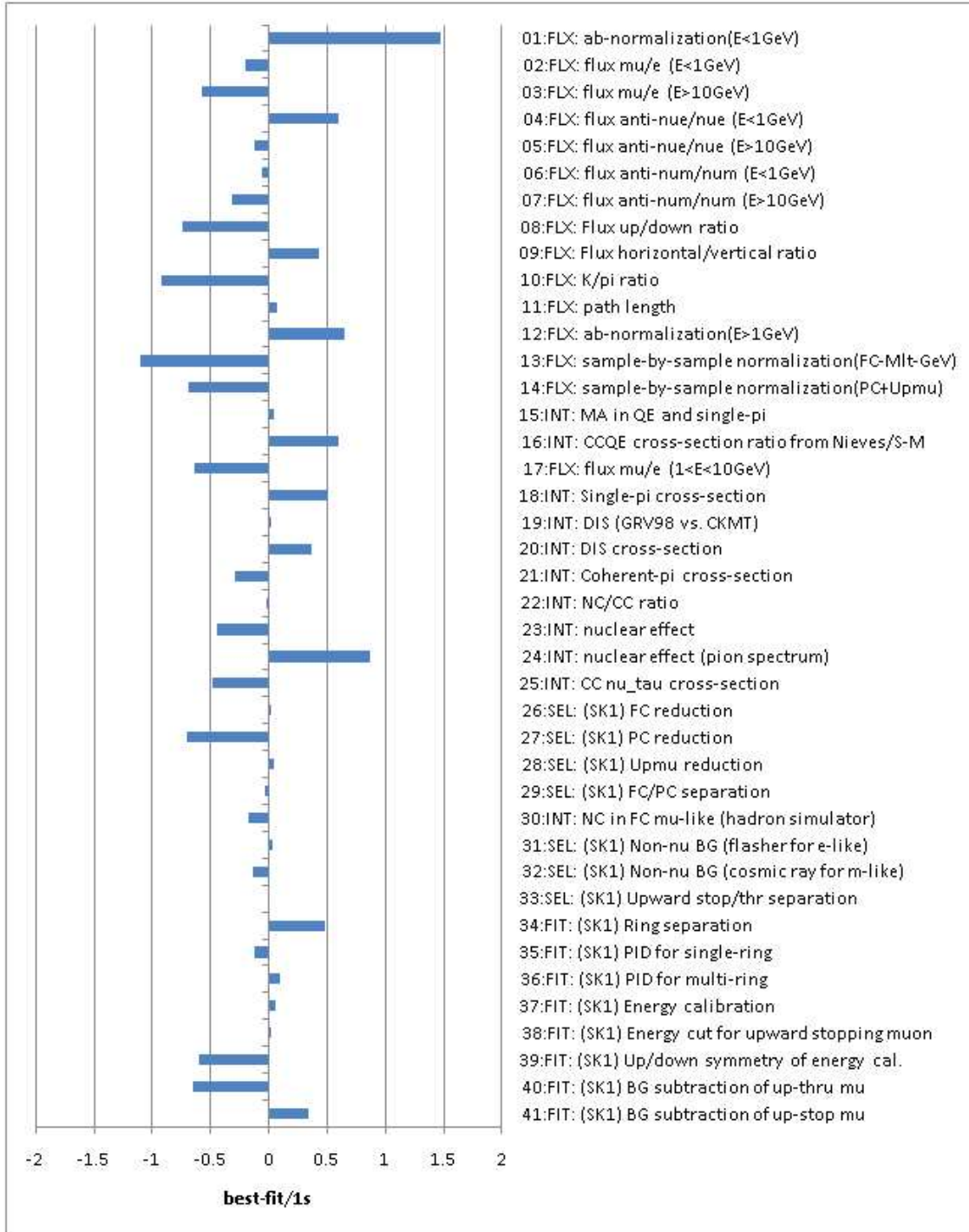
Figure A.11: (Inverted hierarchy, No.1) The best-fit value of the systematic error parameter $\epsilon_j$ in units of the estimated $1\sigma$ error value for each systematic error term shown in the right column.
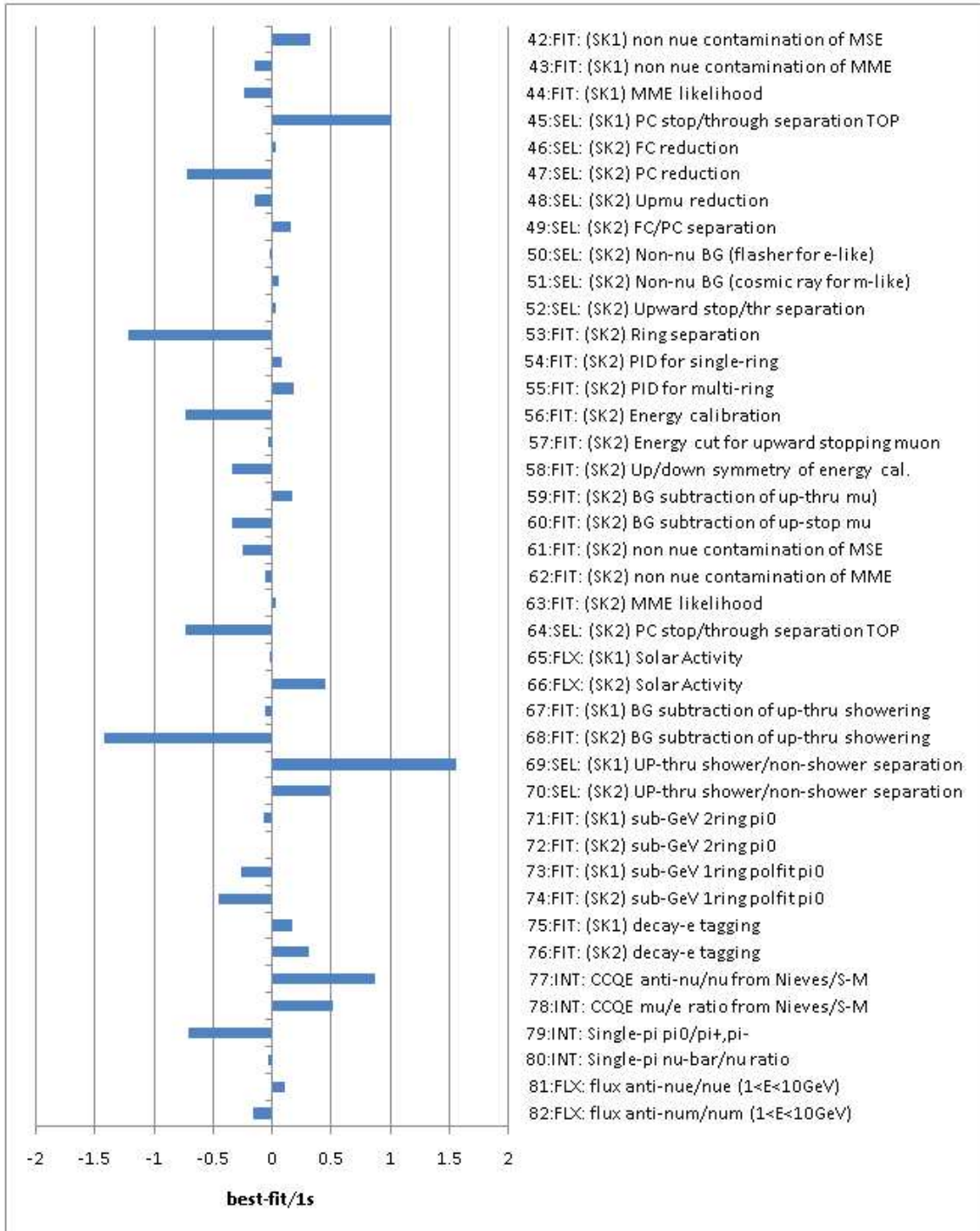
Figure A.12: (Inverted hierarchy, No.2) The best-fit value of the systematic error parameter $\epsilon_j$ in units of the estimated $1\sigma$ error value for each systematic error term shown in the right column.
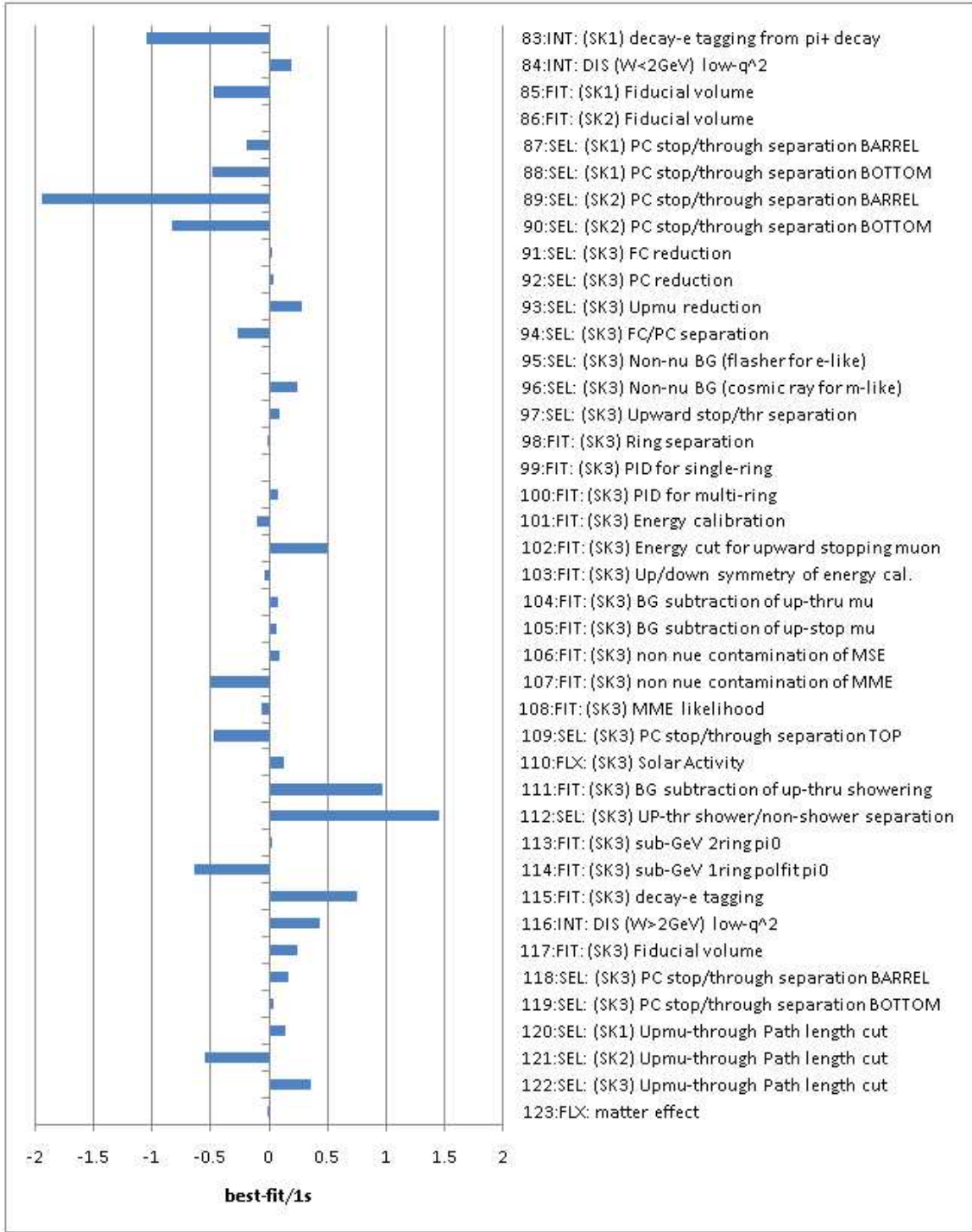
Figure A.13: (Inverted hierarchy, No.3) The best-fit value of the systematic error parameter $\epsilon_j$ in units of the estimated $1\sigma$ error value for each systematic error term shown in the right column.

179